Habitability through Time: Photochemistry and Aerosols of Planetary Atmospheres

Thesis by
Danica Adams

In Partial Fulfillment of the Requirements for the
Degree of
Doctor of Philosophy

CALIFORNIA INSTITUTE OF TECHNOLOGY
Pasadena, California

2023
Defended May 16, 2023

Danica Adams
ORCID: 0000-0001-9897-9680

I dedicate this thesis to my cat, Stella, who attended nearly every zoom research meeting by my side during and after the pandemic.

ACKNOWLEDGEMENTS

Desire. Dedication. Determination.

These attributes are what have guided me through this journey so far, and they are also the philosophy of my lifelong swim team, Terrapins. Coach Ray, Coach Dan, and Coach Doug: I am grateful for your teaching me how to embody these words since the age of eight.

I am grateful for the warmth of the MAVEN team and SSL staff. It is there that I first discovered my desire to become a Martian, as an undergraduate at UC Berkeley. I will never forget my first PSG meeting in 2016 – I remember being completely mesmerized by the great depth of science that the mission team had accomplished. At SSL, from getting to visit instruments before they launched to the nonchalant conversations in our office, my more senior colleagues showed me how much fun life in the planetary sciences would be. I am grateful for my continued collaborations and friendships: Dr. David Mitchell, Dr. Shaosui Xu, Dr. Matt Fillingm, Dr. Rob Lillis, Dr. Shannon Curry, Dr. Phyllis Whittlesey, Patrick Dunn, Dr. Ali Rahmati, Dr. Janet Luhmann, Dr. David Larson, Gwen Hanley, Melissa Marquette, Eryn Cangi, Dr. Mike Chaffin, Dr. Paul Withers, Dr. Bruce Jakosky, and the MAVEN team and SSL staff. At UC Berkeley, I am also grateful for the teaching opportunities Professor Raymond Jeanloz and Professor Courtney Dressing provided me in EPS C12, the research mentorship of Professor Imke de Pater and Dr. Peter Gao, and the academic mentorship of Professor Burkhard Militzer.

I cannot believe it has been nearly five years since I first met the many cows along Highway 5, en route to Pasadena. I never thought I'd say this, but I'll miss that drive between my two homes.

Yuk, I am grateful for how flexible your mentoring style has been – for allowing me to explore many projects, work with many students and collaborators, and tackle some research questions of my own. Heather, not only have you been an exceptional research and academic advisor, but I also thank you for your unwavering support from quals prep to postdoc apps and everything in between. Thank you both for being a role model for the scientist and mentor I hope to become, including cultivating such collaborative research groups. The graduate students and staff in both of your groups have become my closest friends in the department, and I am grateful to all of you for supporting me in both science and life: Dr. Yangcheng Luo, Dr. Stuart

Bartlett, Jiani Yang, Sihe Chen, Dr. Jiazheng Li, Dr. Siteng Fan, Dr. Tianho Le, Dr. Jiazheng Li, Lixiang Gu, Dr. Michael Wong, Dr. Peter Gao, Professor Yuan Wang, Professor Zhao-Cheng Zeng, Professor Chao Liu, Dr. Cheng Li, Dr. Run-Lie Shia, Julie Inglis, Dr. Jessica Spake, Dr. Michael Zhang, Dr. Nicole Wallack, Mike Greklek-McKeon, Morgan Saidel, Dr. Aida Behmard, Dr. Yayaati Chachan, Kim Paragas, Jonathan Gomez, Dr. Fei Dai, Dr. Shreyas Vissapragada, and Dr. Sarah Blunt.

The most influential person during my graduate career was someone I overlapped with at Caltech for only a few months. Mike, you are always rooting for every one of your colleagues and friends, understanding of the hardships faced by the earlier career students, and excited to hear about new science. These attributes brought out the best scientist in me when you taught me KINETICS during my first summer, and that experience taught me the importance of adopting these attributes in my own student mentorships later on. It has been tremendous fun to co-mentor students with you, and I hope to continue our collaboration over the remainder of our careers.

I am very grateful to the many undergraduate and high school students who have taken a chance on me, as it has been incredible fun working with each of you: Maddy Christensen, Kayla Smith, Jaylen Shawcross, Camilla Power, Rachel Caulfield, Tracy Xia, Lulu Tierney, Katerina Gorou, Kimia Hassibi, Peter Shen, Catherine Zhang, and Schuyler Dick. I am thankful to Dr. Natasha Batalha and Dr. Peter Gao for your mentorship in exoplanet atmospheres; your programming skills are something I will admire for years to come, and I have learned so much from you both. I am also grateful to Professor Mitchio Okumura, Greg Jones, Doug Ober, Hannah Szentkuti, and Katerina Gorou for adopting me into your research group, helping me learn chemistry, and for your great discussions during our Mars reading group. Furthermore, I must thank the numerous collaborators whom have shared invaluable science with me: Dr. Renyu Hu, Dr. Tiffany Kataria, Dr. Pin Chen, Dr. Chris Blaszczak-Boxe, Dr. Laurie Barge, Dr. Scott Perl, Dr. Mark Swain, Dr. Markus Scheucher, Trent Thomas, Dr. Frank Mills, Dr. Karen Willacy, Dr. Joe Pinto, Dr. Eliot Young, Dr. Vijay Natraj, Dr. Gael Roudier, Dr. Dave Crisp, Dr. King-Fai Li, Dr. Stanley Sander, Dr. Armin Kleinboehl, Dr. Florian Schwandner, Dr. Max Coleman, Dr. Sally Newman, Dr. Rob Lillis, Dr. Chuanfei Dong, Patrick Dunn, Dr. Shaosui Xu, Dr. Ed Thiemann, Dr. Bruce Jakosky, Dr. Mike Chaffin, Professor Imke de Pater, Dr. Caroline Morley, Hemani Kalucha, Dr. Eva Scheller, and Professor Bethany Ehlmann.

About halfway through my graduate career, COVID hit. While COVID was a tragic time for the world, COVID also taught me that science knows no distance. I thank the powers of Zoom for allowing me to emerge from COVID with new student mentorships, and for allowing Stella (my cat) to join most of my research meetings both during and after the pandemic. Maddy, Kayla, Jaylen, Rachel, Camilla, Kimia, and Tracy: I will always remember how amazing it was the first time to meet you in person after zooming week-after-week from different states! My first experiences TA-ing also occurred during COVID, and I am grateful for the opportunity to have TAed and guest lectured for Professor Yuk Yung's Astrobiology class.

I emerged from COVID with new friendships, new science ideas, and new collaborations. Upon returning to Pasadena, I am grateful for the adventures I have had in Southern California. I thank the sharks and fishies for choosing not to eat me, having swum at nearly every beach between Santa Barbara and San Diego. From discovering my love for open water swimming at Naples Island, to seeing musicals at Pantages, and to dislocating my kneecap onstage at the Grove, I can truly smile, laugh, and say that I have experienced Southern California.

I am grateful to the swim community for acting as a second home. I grew up at the Concord pool, and returning to Terrapins during the pandemic, reminded me why I swim: the people and the life lessons. I am extremely grateful to Coach Ray Mitchell, Coach Dan Cottam, and Coach Doug Reed for always welcoming me back home to the turtle pond, for cultivating such a special team culture, and for truly being there for me during the highs and lows over these past 15 years. You showed me how to dream and work toward goals, and you taught me who I wanted to be in the face of both hardships and success. I am grateful for the memories and life-long friendships I have made in Concord and at our travel meets. I am also thankful to the members of the Caltech Tri Club and all of my swim and ballet friends in Southern California for all of your support. Finally, I am very grateful to Coach Jeff Julian and Coach Kristine Julian of Mission Viejo Nadadores for being so welcoming this year, for cultivating a spectacular "TEAM" culture, and for sharing such contagious positivity. I thank all of my Nadadore teammates for such wonderful camaraderie and friendships.

I am finally most grateful to my family for acting as my full-time cheerleaders 100% of the time. Thank you for cultivating a childhood of curiosity and heart, and for supporting me in chasing all of my childhood dreams through the years. Your frequent visits to SoCal, our kayak-swim adventures, and our RV trips have made

the past few years during my graduate career so much fun.

ABSTRACT

The unique geologic preservation of much of Mars' ancient surface provides a window into its earliest history, and hence the early history of the solar system. Extensive geological and mineralogical evidence suggest that ancient Mars once had large volumes of surface liquid water (Carr and J. W. Head, 2003; Clifford and Parker, 2001; Di Achille and Hynek, 2010; Kurokawa et al., 2014), which likely persisted over timescales of $10^5 - 10^7$ years during the Noachian era (Barnhart, Howard, and Moore, 2009; Hoke, Hynek, and Tucker, 2011; Schon, J. Head, and Fassett, 2012). Explaining this evidence for surface liquid water is challenging, however, because of Mars's distant orbit and the lower luminosity of the young Sun 3-4 billion years ago. The faint young Sun paradox is an important problem in planetary science that challenges our ability to understand atmospheric evolution in general, including Earth, Mars, and rocky exoplanets (Sagan and Mullen, 1972).

The precise composition and climate of the early atmosphere overtime largely remains an open question. In 2014, it was first recognized that early Mars could have been episodically warmed by the greenhouse effects of H_2 in a CO_2 atmosphere; however, no sustained source of H_2 was identified in the literature (noting that volcanism would have been short lived) (Ramirez et al., 2014; Wordsworth, Kalugina, et al., 2017). Chapter 2 presents a solution: crustal hydration (the loss of surface water to reduced iron and hydrated minerals) likely supplied large fluxes of H_2. Over a timescale of 10^7 years (the upper limit for the duration of large volumes of surface liquid water), crustal hydration provides a flux of H_2 into the atmosphere large enough to sustain a surface temperature >273 K in a $\geq$ 1 bar Noachian atmosphere. Importantly, Mars was likely warm over only a fraction of its early history, and cold early atmospheres likely also existed during early Mars' history. In cool climates, I find that a loss of atmospheric oxidants to the ground (to oxidize surface reduced iron) caused CO_2 to convert to CO in agreement with the results of (Zahnle et al., 2008). Furthermore, a warm and wet climate suggests early Mars may have been similar to early Earth; however, the climate alone is not enough to suggest that early Mars may have been habitable. In Chapters 3 and 4, I investigate whether Mars may have had a nitrogen cycle, which would be important for nitrogen fixation. I used KINETICS, the Caltech-JPL 1D photochemical model, to explain present day deposits in Mars' soil samples. The Sample Analysis at Mars instrument onboard Mars Science Laboratory (MSL) has baked several volatile species out of the unique

rock record at Mars, including nitrate (J. C. Stern et al., 2015; B. Sutter et al., 2017; Jennifer C. Stern et al., 2018; Glavin et al., 2013). The formation of these species would originate in the atmosphere as a result of photochemistry. In Chapter 3, I discover that nitrogen fixation in a warm and wet climate with lightning is able to explain the weight percent of nitrate measured by the MSL; lightning-induced NOx forms nitric acid in the atmosphere, and this nitric acid may dissolve in water, rain out to the surface, and undergo photoreduction in shallow surface waters. In Chapter 4, I discover a comparable amount of pernitric acid may be explained from formation in an icy climate; SEP-induced $N(^2D)$ attacks CO_2 to form NO_x which reacts with HO_2 to form HO_2NO_2.

The relatively new subfield of comparative planetology between Mars' evolution and exoplanet evolution (specifically, close-in super-Earths) will soon open, in the new era of the James Webb Space Telescope (JWST). I have prepared for this subfield by working with a suite of established numerical models to investigate the formation of prebiotic species in the reduced atmospheres of super-Earths (in Chapter 5) and the aerosols at warm gas Giants. In Chapter 6, I discover that aggregate hazes at warm sub-Neptunes, which result from methane photolysis, can explain the observed flat exoplanet spectra and muted spectral features, including the observations of GJ 1214b. In Chapter 7, I discover that the atmospheric dynamics of hot Jupiters cause patchy clouds of forsterite, iron, and titanium dioxide, and the 3D structure of the clouds helps explain the phase-integrated albedos of six worlds observed by HST.

PUBLISHED CONTENT AND CONTRIBUTIONS

Adams, Danica, Markus Scheucher, et al. (in prep). "Crustal Hydration Primed Early Mars with Warm and Habitable Conditions".
D.J.A identified the original research question and method approach, and D.J.A. and R.H. later improved the method approach and interpreted results. D.J.A modified and ran the photochemical model, and M.S. ran the climate model. E.S. assisted D.J.A. in converting water sinks (m GEL) to hydrogen fluxes. D.J.A. drafted the initial manuscript and all authors participated in revisions to the manuscript. In preparation.

Adams, Danica, Yuk Yung, et al. (in prep). "Explaining Nitrogen Fixation at Paleo-Mars by Investigating Diurnal and Heterogeneous Nitrogen Chemistry".
D.J.A added heterogeneous reactions to and ran the photochemical model with assistance of R.L.S., computed soil nitrate and nitrite weight percents, interpreted results, and drafted the initial manuscript. K.F.L. added the diurnal mode to the photochemical model, and reactions and rate coefficients were updated by F.M. and S.S. A.K. provided MCS ice data, and Y.L.Y. identified the research concept. In preparation.

Adams, Danica, Yangcheng Luo, and Yuk L. Yung (2022). "Hydrocarbon chemistry in the atmosphere of a Warmer Exo-Titan". In: *Frontiers in Astronomy and Space Science* 9.
D.J.A. and Y.L.Y. developed the research conept together, and D.J.A. ran the photochemical model KINETICS and estimated detectability with Pandexo. Y.L. computed the synthetic spectra. DOI: 10.3389/fspas.2022.823227.

Adams, Danica J. et al. (2022). "Spatially Resolved Modeling of Optical Albedos for a Sample of Six Hot Jupiters". In: *The Astrophysical Journal* 926.2.
D.J.A. ran the cloud models Virga and CARMA and the radiative transfer model Picaso. T.K. ran the GCMs. H.K. identified the research question. N.B. provided instructions and assistance to D.J.A. in running Virga and Picaso, and P.G. helped interpret cloud results. D.J.A. drafted the initial manuscript, and all authors helped with revisions., p. 157. DOI: 10.3847/1538-4357/ac3d32.

Adams, Danica, Yangcheng Luo, Michael L Wong, et al. (2021). "Nitrogen Fixation at Early Mars". In: *Astrobiology* 21.8.
D.J.A modified and ran the photochemical model KINETICS and the thermochemical model CEA, and D.J.A. developed the steady state aqueous chemistry model. Y.L. computed CAPE from established GCM results. C.D. and P.D. ran the Geant4 simulation, and M.C. improved the aqueous chemistry model. Y.L.Y and M.L.W developed the research concept., pp. 968–980. DOI: 10.1089/ast.2020.2273.

Adams, Danica, Peter Gao, et al. (2019). "Aggregate Hazes in Exoplanet Atmospheres". In: *The Astrophysical Journal* 874.1.

D.J.A. ran the microphysical model CARMA and computed the optical properties of haze particles. P.G. provided assistance to D.J.A. in these models and computed the synthetic spectra. D.J.A drafted the initial manuscript, and all authors provided revisions., p. 61. DOI: 10.3847/1538-4357/ab074c.

TABLE OF CONTENTS

LIST OF ILLUSTRATIONS

Number *Page*

NOMENCLATURE

Aerosols. Solid or liquid particles suspended in a gaseous atmosphere, often belonging to one of the following three categories: dust, hazes, or clouds.

Amazonian era. A geologic era at Mars which spans 3 Gya to the present day, characterized by the cold and dry climate in addition to infrequent bombardment by meteorites.

Cloud condensation nuclei (CCN). Small aerosols (often referred to as seed particles or cloud seeds) upon which other species may heterogeneously nucleate.

Clouds. Collections of particles forming in the atmosphere under thermochemical equilibrium, often from condensation or as products of thermochemical reactions.

Crustal Hydration. A potential loss mechanism for surface liquid water at Mars, largely due to the oxidation of crustal Fe(II) via the reaction $2FeO + H_2O \rightarrow Fe_2O_3 + H_2$.

Dust. Particles lifted from the surface into the atmosphere.

Fixed Nitrogen. The chemical product of nitrogen fixation, a chemical processes which splits the strong triple covalent bond of N_2 to produce N-bearing compounds useful to potential life such as NO_x, NH_3, or related species.

Global Equivalent Layer (GEL). A unit of volume, defined as the depth a global ocean would be if a specified volume of water were spread uniformly across the Martian surface. Although a global ocean (especially of uniform thickness) is unlikely, this unit is frequently used to describe the volume of water remaining in the crust today and/or the history of water escape through time.

Goldilocks zone. A term to describe what worlds are likely to have surface liquid water and thereby may be habitable, depending on their distance to and the brightness of their host star.

Haze. Particles formed directly from an energy input such as stellar photons, which are often the product of a complex chemical network.

Hesperian era. A transitional geologic era at Mars which occurred 3.7-3.0 Gya. During this time, Mars likely evolved from the warmer world of the Noachian to the cold and dry planet of the Amazonian (seen today).

Heterogeneous Nucleation. Nucleation onto a cloud condensation nuclei, often favorable to cloud species with high surface tensions.

Hot Jupiter. An exoplanet of similar size to Jupiter with a short orbital period and subsequently high equilibrium temperature.

Hubble Telescope. A space telescope that was launched in the 1990s and observes primarily in the visible and UV wavelengths.

James Webb Space Telescope (JWST). A space infrared telescope launched in December 2021. One of the main uses is to study the atmospheres of exoplanets, primarily using transit spectroscopy.

Noachian era. A geologic era at Mars which occurred 3.7-4.1 Gya, characterized by periods likely abundant of liquid water which suggest a warmer climate and thicker atmosphere. This era is also characterized by the frequent bombardments by meteorites.

Nucleation. The initial phase change of a gaseous species to a solid or liquid state.

Primary Eclipse. Occurs when a transiting exoplanet crosses in front of the host star as viewed from Earth, allowing starlight to transmit through the atmosphere.

Secondary Eclipse. Occurs when a transiting exoplanet crosses behind the host star as viewed from Earth, causing the planet's thermal radiation to disappear to the observer.

Spitzer Telescope. A space telescope that was launched in 2003 and observes primarily in the infrared wavelengths.

Super-Earth. An exoplanet whose radius is larger than earth-like planets (of 0.8-1.2 R_e and smaller than sub-Neptunes (of 2-4 R_e).

Tidally locked. A planet whose gravitational interaction with its host star caused the length of its day to match the length of its year, requiring that the same side of the planet is always facing its host star.

Transiting Exoplanet. A planet that crosses in front of its host star during its orbit as viewed from Earth.

Window Region. A range of wavelengths in which radiation passes through the atmosphere with little absorption and contributes little to atmospheric warming.

Chapter 1

INTRODUCTION

In exoplanet science, we use the term "Goldilocks zone" to describe the range of orbital separations where orbiting planets may be 'just right' for habitability, namely which worlds are likely to have surface liquid water depending on their distance to and the brightness of their host star. But, in the Goldilock's story, one can imagine that the porridge must cool over time. *When* she arrives at the porridge determines which bowl she will deem 'just right'. Similarly, planets evolve through time too, and when we observe them determines our interpretation of which may be 'just right' for habitability. Mars' surface is an excellent example of this. We have photos of ancient riverbeds carved into the surface, which tell us that the planet has changed profoundly (Wordsworth, 2016; Michael H Carr and James W Head, 2003; Clifford and Parker, 2001; Grotzinger, Gupta, et al., 2015). The atmosphere today is too cold and too thin to allow surface liquid water. Deciphering how Mars evolved and what early Mars was like will help us understand the habitability and evolution of many worlds (e.g., Dong et al., 2018). In the exciting new era of the James Webb Space Telescope (JWST), the exploration of exoplanets' atmospheres is on the rise (Team and al., 2023). JWST will observe young planets just having formed, old planets with older host stars, and everything in between, requiring us to question how planets change and evolve in order to learn if they have ever been habitable or ever will be. Yet, understanding our own neighbor's evolution remains a challenge. What happened to the water? Where did the atmosphere go?

1.1 Mars Evolution

Extensive geological evidence, including fluvial features and hydrated minerals, on present-day Mars suggests that a 100-1500m global equivalent layer (GEL) in meters of surface liquid water once flowed on the ancient Mars' surface during the late Noachian (>3.7 Ga) (Michael H Carr and James W Head, 2003; Clifford and Parker, 2001; Di Achille and Hynek, 2010; Kurokawa et al., 2014). Orbital imagery of fluvial features indicates that the surface liquid water and corresponding warmer atmosphere must have persisted for long timescales, up to $10^5 - 10^7$ years (Barnhart, Howard, and Moore, 2009; Hoke, Hynek, and Tucker, 2011; Schon, J. Head, and C. Fassett, 2012). Despite the evidence for a warm, wet early Mars, even a zero-albedo

early Mars would have had an equilibrium temperature of only 210 K, far too cold to allow liquid water (e.g., Wordsworth, 2016). This begged the question "can we warm early Mars with a simple greenhouse?".

The present-day 7 mbar atmosphere of Mars is predominately CO2; early models therefore considered whether or not a thicker CO2 atmosphere would have been enough to warm the surface. However, James F Kasting (1991) demonstrated that a 0.5-2 bar CO_2 atmosphere alone was insufficient to warm early Mars. Later works considered the effect of CO_2 and water clouds (Forget and Pierrehumbert, 1997; Urata and Toon, 2013; R. M. Ramirez and James F. Kasting, 2017), as well as sulfur-rich volcanic emissions (e.g., Halevy and James W Head, 2014); however, these hypotheses also did not result in a strong enough greenhouse effect to warm early Mars. Finally, more recent studies pointed out that trace amounts of reduced gases, H_2 and CH_4, could induce a strong greenhouse in 1-2 bar atmospheres (R. Ramirez et al., 2014; Wordsworth et al., 2017). Although these gases are weak infrared absorbers on their own, as their symmetry means they lack a dipole moment, collisions with CO_2 induce a transient dipole and cause infrared absorption in the CO_2 opacity windows where the atmosphere would otherwise be mostly transparent. However, both H2 and CH4 are relatively short-lived in Mars' atmosphere, and published studies therefore argued that they must be continuously outgassed from the interior by some unknown mechanism. We examine this problem in more detail in Chapter 2, and propose a novel solution.

It is clear that early Mars was very different than the cold, barren Mars we see today. The most recent 3 Ga are referred to the Amazonian period, which has largely been characterized as cold and dry other than some geological evidence for potential anomalous briny flows of localized liquid water (Michael H. Carr and James W. Head, 2010; C. I. Fassett et al., 2014; Tanaka et al., 2014). This is in striking contrast to the large volumes of liquid water that appear to have been present during the Noachian (3.7-4.1 Ga). During the transition from the Noachian (periods of a warm and wet climate) to the Amazonian (cold and dry), the Hesperian period (3-3.7 Ga) may have experienced more limited but active outflow channels and lake environments (e.g., Ehlmann et al., 2011; Grotzinger, D Y Sumner, et al., 2014). One may ask where such volumes of water and atmospheric materials went over time. There are only two possibilities: into the ground or away to space. Mars's present-day atmosphere is enriched in heavy isotopes, and carbonate deposits on the surface appear to be rare. This suggests that the atmosphere was likely lost to space.

However, the history of Mars' water is not as easily explained. Extensive geological evidence, including fluvial features and hydrated minerals, on present-day Mars suggests that a total volume of 100-1500m global equivalent layer (GEL) in meters of liquid water once existed on the surface. Photochemical models predict loss to space may account for 20-220 m GEL (Alsaeed and Jakosky, 2019; Cangi, Chaffin, and Deighan, 2020) and interpretation of D/H isotope measurements suggests large volumes of water may have been lost to crustal hydration, largely via the reaction $2FeO + H_2O \rightarrow Fe_2O_3 + H_2$ (Scheller et al., 2021). This evolution may have influenced early Mars' atmospheric chemistry, which I investigate in Chapter 2.

It is currently unknown whether the surface of early Mars was habitable (or inhabited). Habitability for earth-like life requires not only a warm atmosphere and near-surface liquid water, but also prebiotic chemistry; in particular, it requires fixed nitrogen, which is required for protein synthesis. In Chapters 3 and 4 of this thesis, I investigate the early Mars' nitrogen cycle.

1.2 Exoplanet Observations

An improved understanding of Mars' evolution is interesting not only for learning about the habitability of its ancient surface but also for comparative planetology. A transiting exoplanet, or a planet that crosses in front of its host star during its orbit as viewed from Earth, provide two opportunities to observe the atmosphere. First, during the primary eclipse, starlight is transmitted through the atmosphere. The depth of the transit, or the amount of starlight blocked by the planet, varies with wavelength, as the atmosphere absorbs light at some wavelengths and less/none at others. This transmission spectrum has a signal proportional to the scale height of the atmosphere ($H \sim kT/\mu g$, where T is the temperature, g is the surface gravity, and μ is the mean molecular weight of the atmospheric constituents). The second opportunity comes just before the secondary eclipse: starlight is reflected off the atmosphere and a planet's thermal radiation appears, and these sources of radiation disappear when the planet passes completely behind the star during secondary eclipse. Recent space telescopes, including Hubble and Spitzer, made the first spectral measurements from space of exoplanet atmospheres, and soon the recently-launched James Webb Space Telescope (JWST) will allow atmospheric measurements of many rocky Mars-like worlds. Chapter 5 investigates a chemical network of reduced species to study the formation of N-bearing prebiotic chemistry at warm Super Earths with H_2-dominated atmospheres in preparation for interpreting future JWST measurements.

Exoplanet transmission spectra that display subdued molecular features and scattering slopes are seen across a wide swath of planet types, from Super Earths to hot Jupiters (e.g., Sing et al., 2016; Crossfield and Kreidberg, 2017), and optical reflected light measurements also demonstrate that hot Jupiters exhibit a wide range of albedos (e.g., Adams et al., 2021). The relatively high albedos of some hot Jupiters suggest the potential presence of reflective aerosols in their dayside atmospheres. The formation and composition of aerosols are closely tied to the chemistry, dynamics, and radiative transfer in planetary atmospheres, making them a critical component to understanding planetary atmospheres as a whole. For example, water clouds at Earth and dust at Mars influence the surface climates; organic hazes at Titan, Pluto, and warm giant exoplanets are chemical products originating from methane photolysis and dominate the heating and cooling rates in the cooler worlds' atmospheres (e.g., Zhang, Strobel, and Imanaka, 2017); sulfuric acid clouds at Venus are a result of a complex chemical network and result in a high optical albedo (Mills, Esposito, and Yung, 2007); and the atmospheric dynamics of hot Jupiters appear to influence the longitudes at which silicate clouds form (e.g., Vivien Parmentier et al., 2016).

The composition of aerosols is diverse, and most fall into three categories: dust, hazes, and clouds. Dust is defined as particles lifted from the surface into the atmosphere. The formation of hazes requires an energy input, and these particles form directly from photochemistry and energetic particle bombardment. The dissociation of simple species such as methane, carbon monoxide, nitrogen, and hydrogen sulfide at low pressures commonly creates radicals and ions, which are highly reactive, and through a complex chemical network, small particles (or "monomers") are eventually formed (e.g., Lavvas et al., 2013; Horst, He, and Lewis, 2018). In warm exoplanet atmospheres ($T < 950K$), photochemical hazes which result from methane photolysis are expected (e.g., Gao, Wakeford, et al., 2021), and their presence results in scattering slopes and muted spectral features, thereby influencing the interpretation of spectral observations. In Chapter 6, the effect of hazes on exoplanet spectra is investigated.

Clouds are defined as collections of particles forming in the atmosphere under thermochemical equilibrium (Gao, Wakeford, et al., 2021). They may form directly from condensation (such as gaseous water changing phases to liquid or ice water), or they may form as products of thermochemical reactions. The formation of silicate clouds, commonly found at hot Jupiters, are a good example of the latter; forsterite

(Mg_2SiO_4) does not exist in the gas phase but reactions with gaseous magnesium, silicon monoxide and water result in the formation of forsterite cloud particles (e.g., Gao, Wakeford, et al., 2021). The formation of different aerosol species depends on the local temperature-pressure, atmospheric composition, and surface tension of condensable species. Importantly, the temperature-pressure profiles of many hot Jupiters cross the condensation curves of a diverse number of potential cloud species including: KCl, ZnS, Na_2S, MnS, Cr, $MgSiO_3$, Mg_2SiO_4, Fe, TiO_2, and Al_2O_3 (e.g., Vivien Parmentier et al., 2016; Powell et al., 2018; Gao, Thorngren, et al., 2020). However, only a select few of these species are expected to form in significant quantities, as a result of their varying material properties (e.g., Gao, Wakeford, et al., 2021).

Particle nucleation, which refers to the initial phase change of a gaseous species to a solid or liquid state, may occur heterogeneously or homogeneously. This depends on the energy barrier associated with nucleation, which is largely sensitive to the species' surface tension and molecular weight as well as the availability of seeds or cloud condensation nuclei (CCNs). Species with low surface tension and molecular weight may undergo homogeneous nucleation more easily, and these species may act as the CCNs to others which may require heterogeneous nucleation for efficient formation (e.g., Powell et al., 2018). In the atmospheres of hot Jupiters, for example, TiO_2 nucleates at high temperatures (2000 K), and they become CCNs when the rate of heterogeneous nucleation of other materials such as forsterite and iron overtakes their own growth rate. Commonly at these worlds, TiO_2 cloud masses persist at higher pressure levels and the heterogeneous clouds take over in the lower pressure regimes (e.g., Gao, Thorngren, et al., 2020). Importantly, some species have such high surface tensions that even heterogeneous nucleation is too slow for them to become dominant cloud species. For example, the sulfide species that are predicted to form in hot Jupiter atmospheres have high surface tensions that may preclude their condensation in practice. The atmospheres of hot Jupiters with equilibrium/atmospheric temperatures between 950-2100 K are predicted to be dominated by $Mg_2SiO_4$4 clouds, with Al_2O_3 and TiO_2 forming as well. For close-in gas giants cooler than 950 K, hazes are expected to dominate, and for gas giants with temperatures higher than 2100 K, models predict relatively clear atmospheres (e.g., Gao, Wakeford, et al., 2021).

Hot Jupiters are expected to be tidally locked as a result of their short orbital periods, which can lead to significant day-night temperature gradients (e.g., Guillot and A. P.

Showman, 2002). For these worlds, the hottest region on the dayside is shifted east of the substellar point by eastward equatorial winds which transport heat to the planet's nightside (e.g., Adam P. Showman, Tan, and V. Parmentier, 2020, and references therein). This patchy temperature structure affects the cloud distribution. As exoplanets begin to cross behind their host stars during secondary eclipse, overtime the fraction of the planet's surface area blocked by the star increases. This allows for measurements of the planet's optical albedo as a function of longitude, known as an optical phase curve. To date, three of the four planets with observed reflected-light phase curves appear to have patchy clouds which preferentially form in the western (cooler) hemisphere (e.g., Desert et al., 2011; Demory et al., 2013; Angerhausen et al., 2014; Esteves, De Mooij, and Jayawardhana, 2015; Shporer and Hu, 2015; von Paris et al., 2016; Niraula et al., 2018). Importantly, the global albedos of hot Jupiters near effective temperatures of $\sim$ 1600 K do not appear to track with equilibrium temperature. In Chapter 7, I investigate whether the 3D patchiness of hot Jupiter clouds may explain these observations.

References

Adams, Danica et al. (2021). "Nitrogen Fixation at Early Mars". In: *Astrobiology* 21.8.
D.J.A modified and ran the photochemical model KINETICS and the thermochemical model CEA, and D.J.A. developed the steady state aqueous chemistry model. Y.L. computed CAPE from established GCM results. C.D. and P.D. ran the Geant4 simulation, and M.C. improved the aqueous chemistry model. Y.L.Y and M.L.W developed the research concept., pp. 968–980. DOI: 10.1089/ast.2020.2273.

Alsaeed, N. R. and B. M. Jakosky (2019). "Mars Water and D/H Evolution From 3.3 Ga to Present". In: *Journal of Geophysical Research: Planets* 124.12, pp. 3344–3353. DOI: https://doi.org/10.1029/2019JE006066. eprint: https://agupubs.onlinelibrary.wiley.com/doi/pdf/10.1029/2019JE006066. URL: https://agupubs.onlinelibrary.wiley.com/doi/abs/10.1029/2019JE006066.

Angerhausen, Daniel et al. (2014). "Occultation Spectrophotometry of Extrasolar Planets with SOFIA". In: *Formation, Detection, and Characterization of Extrasolar Habitable Planets, Proceedings of the International Astronomical Union, IAU Symposium* 293. DOI: 10.1017/S1743921313013343.

Barnhart, Charles, Alan Howard, and Jeffrey Moore (2009). "Long-term precipitation and late-stage valley network formation: Landform simulations of Parana Basin, Mars". In: *J. Geophys. Res.* 114.E1. DOI: 10.1029/2008JE003262.

Cangi, E. M., M. S. Chaffin, and J. Deighan (2020). "Higher Martian Atmospheric Temperatures at All Altitudes Increase the D/H Fractionation Factor and Water Loss". In: *Journal of Geophysical Research: Planets* 125.12. e2020JE006626 2020JE006626, e2020JE006626. DOI: https://doi.org/10.1029/2020JE006626. eprint: https://agupubs.onlinelibrary.wiley.com/doi/pdf/10.1029/2020JE006626. URL: https://agupubs.onlinelibrary.wiley.com/doi/abs/10.1029/2020JE006626.

Carr, Michael H and James W Head (2003). "Oceans on Mars: An assessment of the observational evidence and possible fate". In: *J. Geophys. Res. Planets* 108.E5. DOI: 10.1029/2002JE001963.

– (2010). "Geologic history of Mars". In: *Earth and Planetary Science Letters* 294.3. Mars Express after 6 Years in Orbit: Mars Geology from Three-Dimensional Mapping by the High Resolution Stereo Camera (HRSC) Experiment, pp. 185–203. ISSN: 0012-821X. DOI: https://doi.org/10.1016/j.epsl.2009.06.042. URL: https://www.sciencedirect.com/science/article/pii/S0012821X09003847.

Clifford, Stephen M and Timothy J Parker (2001). "The evolution of the Martian hydrosphere: Implications for the fate of a primordial ocean and the current state of the northern plains". In: *Icarus* 154, pp. 40–79. DOI: 10.1006/icar.2001.6671.

Crossfield, I. J. M. and L. Kreidberg (2017). "Trends in Atmospheric Properties of Neptune-size Exoplanets". In: *The Astronomical Journal* 154.6. DOI: 10.3847/1538-3881/aa9279.

Demory, Brice-Olivier et al. (2013). "Inference of Inhomogeneous Clouds in an Exoplanet Atmosphere". In: *The Astrophysical Journal Letters* 776. DOI: 10.1088/2041-8205/776/2/L25.

Desert, Jean-Michel et al. (2011). "The Atmospheres of the Hot Jupiters Kepler-5b and Kepler-6b Observed during Occultations with Warm Spitzer and Kepler". In: *The Astrophysical Journal Supplement* 197. DOI: 10.1088/0067-0049/197/1/11.

Di Achille, Gaetano and Brian Hynek (2010). "Ancient ocean on Mars supported by global distribution of deltas and valleys". In: *Nature Geoscience* 3, pp. 459–463. DOI: 10.1038/ngeo891.

Dong, Chuanfei et al. (2018). "The Dehydration of Water Worlds Via Atmospheric Losses". In: *The Astrophysical Journal Letters* 847.1. DOI: 10.3847/2041-8213/aa8a60.

Ehlmann, Bethany et al. (2011). "Subsurface water and clay mineral formation during the early history of Mars". In: *Nature* 479.7371, pp. 53–60. DOI: 10.1038/nature10582.

Esteves, Lisa J., Ernst J. W. De Mooij, and Ray Jayawardhana (2015). "Changing Phases of Alien Worlds: Probing Atmospheres of Kepler Planets with High-precision Photometry". In: *The Astrophysical Journal* 804. DOI: 10.1088/0004-637X/804/2/150.

Fassett, Caleb I. et al. (Sept. 2014). "An extended period of episodic northern mid-latitude glaciation on Mars during the Middle to Late Amazonian: Implications for long-term obliquity history". In: *Geology* 42.9, pp. 763–766. ISSN: 0091-7613. DOI: 10.1130/G35798.1. eprint: https://pubs.geoscienceworld.org/gsa/geology/article-pdf/42/9/763/3546867/763.pdf. URL: https://doi.org/10.1130/G35798.1.

Forget, François and Raymond Pierrehumbert (1997). "Warming early Mars with carbon dioxide clouds that scatter infrared radiation". In: *Science* 278.5341, pp. 1273–1276.

Gao, Peter, Daniel P Thorngren, et al. (2020). "Aerosol composition of hot giant exoplanets dominated by silicates and hydrocarbon hazes". In: *Nature Astronomy* 4.10, pp. 951–956. DOI: 10.1038/s41550-020-1114-3.

Gao, Peter, Hannah R. Wakeford, et al. (2021). "Aerosols in Exoplanet Atmospheres". In: *Journal of Geophysical Research: Planets* 126.4. e2020JE006655 2020JE006655, e2020JE006655. DOI: https://doi.org/10.1029/2020JE006655. eprint: https://agupubs.onlinelibrary.wiley.com/doi/pdf/10.1029/2020JE006655. URL: https://agupubs.onlinelibrary.wiley.com/doi/abs/10.1029/2020JE006655.

Grotzinger, John P, Sanjeev Gupta, et al. (2015). "Deposition, exhumation, and paleoclimate of an ancient lake deposit, Gale crater, Mars". In: *Science* 350.6257.

Grotzinger, John P, D Y Sumner, et al. (2014). "A Habitable Fluvio-Lacustrine Environment at Yellowknife Bay, Gale Crater, Mars". In: *Science* 343.6169. DOI: 10.1126/science.1242777.

Guillot, T. and A. P. Showman (2002). "Evolution of 51 Pegasus b-like Planets". In: *Astronomy and Astrophysics* 385. DOI: 10.1051/0004-6361:20011624.

Halevy, Itay and James W Head (2014). "Episodic warming of early Mars by punctuated volcanism". In: *Nature Geoscience* 7, pp. 865–868.

Hoke, Meredith, Brian Hynek, and Gregory Tucker (2011). "Formation timescales of large Martian valley networks". In: *Earth and Planetary Science Letters* 312, p. 1. DOI: 10.1016/j.epsl.2011.09.029.

Horst, Sarah M., Chao He, and Nikole K. Lewis (2018). "Haze production rates in super-Earth and mini-Neptune atmosphere experiments". In: *Nature Astronomy* 2, pp. 303–306. DOI: 10.1038/s41550-018-0397-0.

Kasting, James F (1991). "CO2 condensation and the climate of early Mars". In: *Icarus* 94, pp. 1–13.

Kurokawa, Hidenori et al. (2014). "Evolution of water reservoirs on Mars: Constraints from hydrogen isotopes in Martian meteorites". In: *Earth Planet. Sci. Lett.* 394, pp. 179–185. DOI: 10.1016/j.epsl.2014.03.003.

Lavvas, Panayotis et al. (2013). "Aerosol growth in Titan's ionosphere". In: *Proceedings of the National Academy of Sciences* 110.8, pp. 2729–2734. DOI: 10.1073/pnas.1217054110.

Mills, Franklin P, Larry W Esposito, and Yuk L Yung (2007). "Atmospheric composition, chemistry, and clouds". In: *Exploring Venus as a Terrestrial Planet*. Ed. by Larry W Esposito, Ellen R Stofan, and Thomas E Cravens. Washington, DC, USA: American Geophysical Union, pp. 73–100. DOI: 10.1029/176GM06.

Niraula, Prajwal et al. (2018). "Discovery of Six Optical Phase Curves with K2". In: *arXiv preprint arXiv:1812.09227*.

Parmentier, Vivien et al. (2016). "Transitions in the Cloud Composition of Hot Jupiters". In: *The Astrophysical Journal* 828. DOI: 10.3847/0004-637X/828/1/22.

Powell, Diana et al. (June 2018). "Formation of Silicate and Titanium Clouds on Hot Jupiters". In: *The Astrophysical Journal* 860.1, p. 18. DOI: 10.3847/1538-4357/aac215. URL: https://doi.org/10.3847/1538-4357/aac215.

Ramirez, Ramses et al. (2014). "Warming early Mars with CO2 and H2". In: *Nature Geoscience* 7.1, pp. 59–63.

Ramirez, Ramses M. and James F. Kasting (2017). "Could cirrus clouds have warmed early Mars?" In: *Icarus* 281, pp. 248–261. ISSN: 0019-1035. DOI: https://doi.org/10.1016/j.icarus.2016.08.016. URL: https://www.sciencedirect.com/science/article/pii/S001910351630495X.

Scheller, Elisa et al. (2021). "Long-term drying of Mars by sequestration of ocean-scale volumes of water in the crust". In: *Science* 372.6537.

Schon, Samuel, James Head, and Caleb Fassett (2012). "An overfilled lacustrine system and progradational delta in Jezero crater, Mars: Implications for Noachian climate". In: *Planetary and Space Science* 67, p. 1. DOI: 10.1016/j.pss.2012.02.003.

Showman, Adam P., X. Tan, and V. Parmentier (2020). "Atmospheric Dynamics of Hot Giant Planets and Brown Dwarfs". In: *Space Science Reviews* 216. DOI: 10.1007/s11214-020-00758-8.

Shporer, Avi and Renyu Hu (2015). "Studying Atmosphere-dominated Hot Jupiter Kepler Phase Curves: Evidence that Inhomogeneous Atmospheric Reflection is Common". In: *The Astronomical Journal* 150. DOI: 10.1088/0004-6256/150/4/112.

Sing, David K et al. (2016). "A continuum from clear to cloudy hot- Jupiter exoplanets without primordial water depletion". In: *Nature* 529.7584, pp. 59–62. DOI: 10.1038/nature16068.

Tanaka, K.L. et al. (2014). "The digital global geologic map of Mars: Chronostratigraphic ages, topographic and crater morphologic characteristics, and updated resurfacing history". In: *Planetary and Space Science* 95. Planetary Geology Field Symposium, Kitakyushu, Japan, 2011: Planetary Geology and Terrestrial Analogs, pp. 11–24. ISSN: 0032-0633. DOI: https://doi.org/10.1016/j.pss.2013.03.006. URL: https://www.sciencedirect.com/science/article/pii/S0032063313000652.

Team, JWST Transiting Exoplanet Community Early Release Science and et al. (2023). "Identification of carbon dioxide in an exoplanet atmosphere". In: *Nature* 614.7945, pp. 649–652. DOI: 10.1038/s41586-022-05269-w.

Urata, R.A. and O.B. Toon (2013). "Simulations of the Martian hydrologic cycle with a general circulation model: Implications for the ancient Martian climate". In: *Icarus* 226, pp. 229–250. DOI: 10.1016/j.icarus.2013.05.016.

von Paris, P. et al. (2016). "Inferring heat recirculation and albedo for exoplanetary atmospheres: Comparing optical phase curves and secondary eclipse data". In: *Astronomy & Astrophysics* 587. DOI: 10.1051/0004-6361/201526297.

Wordsworth, Robin (2016). "The Climate of Early Mars". In: *Annual Review of Earth and Planetary Sciences* 44, pp. 381–408.

Wordsworth, Robin et al. (2017). "Transient reducing greenhouse warming on early Mars". In: *Geophysical Research Letters* 44.2, pp. 665–671. DOI: 10.1002/2016GL071766.

Zhang, Xi, Darrell Strobel, and Hiroshi Imanaka (2017). "Haze heats Pluto's atmosphere yet explains its cold temperature". In: *Nature* 551.7679, pp. 352–355. DOI: 10.1038/nature24465.

Chapter 2

CRUSTAL HYDRATION PRIMED EARLY MARS WITH WARM AND HABITABLE CONDITIONS

Extensive geological evidence, including fluvial features and hydrated minerals, on present-day Mars suggests that a ~ 100-1500m global equivalent layer (GEL) in meters of surface liquid water once flowed on the ancient Mars' surface during the late Noachian (Carr and J. W. Head, 2003; Clifford and Parker, 2001; Di Achille and Hynek, 2010; Kurokawa et al., 2014). Orbital imagery of fluvial features indicates that the surface liquid water and corresponding warmer atmosphere must have persisted for long timescales, up to $10^5 - 10^7$ years (Barnhart, Howard, and Moore, 2009; Hoke, Hynek, and Tucker, 2011; Schon, J. Head, and Fassett, 2012). Despite the evidence for a warm, wet early Mars, even a zero-albedo early Mars would have hosted an equilibrium temperature of only 210 K, far too cold to allow liquid water (e.g., Wordsworth, 2016, and references therein). Importantly, the young Sun 3-4 Gya would have been less luminous, highlighting the problem of the faint young sun paradox (FYSP) which challenges our understanding of atmospheric evolution at Earth, Mars, and exoplanets (Sagan and Mullen, 1972). A thicker atmosphere enriched with greenhouse gases at Mars is likely required to explain the evidence for flowing liquid water and aqueous chemical alteration, which, in combination with measurements of enriched heavy isotopes, suggests the atmosphere of Mars has evolved over time (e.g., Bruce Jakosky et al., 2017; B. M. Jakosky et al., 2018; T. M. Donahue, 1995; Webster et al., 2013; Greenwood et al., 2008; Hu, Kass, et al., 2015; Hu and T. Thomas, 2022). Several bar of CO_2 can be accounted for via escape and geologic processes (Bruce Jakosky, 2019), but Pollack et al. (1987) finds that CO_2 alone, regardless of mass, is unable to sufficiently warm the climate. Recent work suggests the paleoatmosphere had a large abundance of N_2 (Hu and T. Thomas, 2022), which could contribute to warming the climate (Ramirez et al., 2014; Paris et al., 2013; Wordsworth, Kalugina, et al., 2017). In the early atmosphere, collision induced absorption (CIA) of CO_2 with CH_4 and H_2, due to both transient induced dipole and dimer effects could provide sufficient climate forcing to allow at least transient liquid water on the early Martian surface (Ramirez et al., 2014; Paris et al., 2013; Wordsworth, Kalugina, et al., 2017). However, these gases can escape to space or be removed by photochemical processes in an oxidized CO_2 atmosphere,

and thus require continuous production to sustain. The production fluxes of these species have previously been thought to be from transient processes such as impacts and explosive volcanism (Paris et al., 2013; Wordsworth, Kalugina, et al., 2017; Batalha et al., 2015), inconsistent with the evidence for surface liquid water spread across geologic time and may have persisted in episodes of a few thousand to several million years (e.g., Olsen and Rimstidt, 2007; Grotzinger et al., 2014).

We propose crustal hydration as a long-lasting source of H_2 in the early atmosphere during warm climates. Crustal hydration would have released large fluxes of H_2 into the atmosphere as a result of aqueously incorporating OH to oxidize surface reduced iron and to form hydrated minerals. Water loss to oxidized iron primarily occurs by electron transfer between Fe and H during the redox reaction (e.g., Tosca et al., 2018): $2FeO + H_2O \longleftrightarrow Fe_2O_3 + H_2$ (Scheller et al., 2021) estimates that ~100-900m GEL and ~10-100m GEL of water may have been lost to the crust during the Noachian and Hesperian periods respectively, a finding grounded in recent observations which suggest the hydration of Mars' upper crust may have been extensive during the Noachian and persisted in localized regions during the Hesperian period (Mustard, 2019; Murchie et al., 2009; Sun and R. E. Milliken, 2015). The estimates of Scheller et al. (2021) include three water sinks: (1) water lost to oxidizing 10-60 percent of all Fe(II) to Fe(III), requiring 0.5 mol O per mol Fe, in the full crustal reservoir at depths of 5-10 km globally; (2) water lost to forming hydrated minerals, constrained by remote sensing observations of hydrated minerals in crustal depths of 7-10 km in the walls of tectonic features (Wernicke and B. Jakosky, 2019; Murchie et al., 2009; Sun and R. E. Milliken, 2015); (3) water lost to the crust, constrained by observations revealing crustal water content from 0.5-3 wt percent (e.g., Mustard, 2019; Wernicke and B. Jakosky, 2019) up to 5-15 percent (Vaniman and al., 2014; B. Sutter et al., 2017; N. H. Thomas and al., 2020; Audouard and al., 2014; Maurice and al., 2011). We equivalently express the ground sinks of water reported above (Scheller et al., 2021) as fluxes of hydrogen of geologic origins into the atmosphere. We assume 2-25% of the H_2O lost to the crust released H_2, which is applicable to serpentine (Chassefière and al., 2013; Chassefière, Lasue, et al., 2016), and we assume that crustal hydration rates were constant during the respective epochs. The fluxes we consider are as follows: $2x10^{10}$ – $2x10^{12}$ molec $H_2 cm^{-2} s^{-1}$ during the Noachian and $1.2x10^{9}$ – $1.2x10^{11}$ molec $H_2 cm^{-2} s^{-1}$ during the Hesperian period.

In the present-day atmosphere, MAVEN observations confirm the early hypothesis

that oxygen and hydrogen escape to space at nearly a 2:1 ratio (e.g., Webster et al., 2013; McElroy and T. Donahue, 1972; McElroy, Kong, and Y. Yung, 1977). Water photolysis and subsequent HO_x chemistry drives hydrogen formation near the surface, which then thermally escapes after diffusing above the exobase. Oxygen escapes primarily via dissociative recombination after being ionized at high altitudes. At present day, this 2:1 escape rate helps balance the redox budget. Additionally, at present day, the CO_2 content is regulated by similar HO_x chemistry, in which photolysis, $CO_2 + hv \rightarrow CO + O$, is balanced by a recycling reaction, $CO + OH \rightarrow CO_2 + H$. We hypothesize the reduced iron on the early surface would likely have modified this redox balance at ancient Mars by either encouraging crustal hydration in early warm climates with surface liquid water (Scheller et al., 2021) which then supply large hydrogen fluxes, or by acting as an oxidant sink in cool dry climates with limited surface liquid water (Zahnle et al., 2008).

2.1 A Comprehensive Photochemical and Climate Model

We build a model to comprehensively consider radiative transfer and photochemistry on early Mars, the latter including effects of all H, C, and O sinks. This tool allows us to investigate how atmospheric and water sinks controlled early Mars' atmospheric chemistry and climate. Recent efforts (e.g., Ramirez et al., 2014; Paris et al., 2013; Wordsworth, Kalugina, et al., 2017) have shown that the warming of early Mars may have been possible through a complex interplay of climate and atmospheric chemistry. A reasonable solution may only be obtained by including the radiative effects of CIAs (e.g. H_2-CO_2), together with atmospheric escape of H, C, and O species, as well as sophisticated interplay of the atmosphere with a potential surface ocean and photochemical treatment of surface sources, such as H_2 from crustal hydration.

We adapt KINETICS, the Caltech/JPL 1D photochemical and transport model (Allen, Y. L. Yung, and Waters, 1981; Nair et al., 1994) (details in S1), to consider an initial set of five atmospheric pressures and bulk compositions for early Mars. This set represents slices in time during the Noachian and Hesperian periods and uncertainty in N_2:CO_2 composition (Hu and T. Thomas, 2022). We consider two scenarios for each of the potential atmospheres: with and without surface liquid water. For those with surface liquid water, we range the flux of hydrogen from crustal hydration according to the assigned epoch: $2x10^{10} - 2x10^{12}$ molec $H_2 cm^{-2} s^{-1}$ during the Noachian and $1.2x10^{9} - 1.2x10^{11}$ molec $H_2 cm^{-2} s^{-1}$ during the Hesperian period. For those without surface liquid water, we range the dry oxidant sinks as

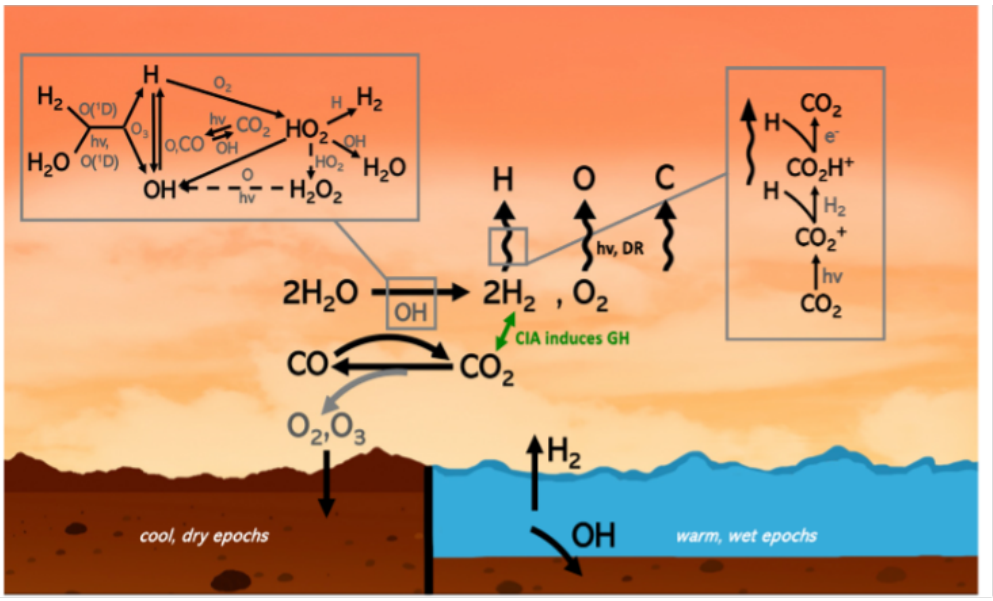

Figure 2.1: Mars H, C, O chemistry including ground sinks and escape processes. Destruction of water vapor results in a production of H_2 (upper left inset) and O_2. Upon diffusing and reacting with ion species (right inset), H may undergo thermal escape. Oxygen primarily escapes from dissociative recombination (DR), where after becoming ionized, the exothermic reaction of recombining with an electron often gives hot O atoms the energy to escape. Carbon species may also be lost to space through sputtering or photochemical loss. During warm, wet epochs, OH is aqueously lost to the crust, resulting in large fluxes of H_2 which may sustain a warm greenhouse (GH) via collision induced absorption (CIA) with CO_2. During cool, dry epochs, atmospheric oxygen may oxidize this reduced iron (though at a much slower rate). These chemical sinks and atmospheric escape rates were large early in the planet's history and have large implications for the climate and redox chemistry.

a free parameter across lesser values of up to $10^6 - 10^9 O_2 cm^{-2} s^{-1}$. Although this loss is likely kinetically inhibited, several works identify a similar mechanism likely occurred at early Earth and highlight the need for future laboratory measurements (e.g., Payne et al., 2020; Herwartz et al., 2021). Our model considers chemical production and loss, and vertical transport with both molecular and eddy diffusion. The main chemical networks are demonstrated in Figure 2.1 and described in the following sections. We solve for the thermal escape of hydrogen (e.g., Hunten, 1973), escape of oxygen to dissociative recombination including electron impact ionization (e.g., Lillis, Deighan, et al., 2017; Lillis, Xu, et al., 2021), and photochemical escape of carbon (according to Daniel Y Lo, Yelle, and Lillis (2020)). We parametrize sputtering for carbon species (Hu, Kass, et al., 2015) at the upper boundary condition, and we implement crustal hydration (in warm cases) or oxidant

sinks (in cool cases) at the lower boundary condition. We iterate KINETICS with REDFOX , a correlated-k radiative-convective 1D climate module (Scheucher et al., 2020) which we use to solve for the temperature profiles at pressures larger than 1 microbar. REDFOX includes CIA of H_2-H_2, CO_2-H_2, CO_2-CH_4 and CO_2-CO_2, as well as MTCKD for H_2O continuum absorption. We add N_2-H_2 collision-induced absorption (Borysow and Frommhold, 1986) to REDFOX for this study, making it particularly suitable to investigate the effect of H_2 from crustal hydration on the early Mars climate.

2.2 Crustal Hydration: A Sustained Source of Atmospheric H_2

We first consider the set of five potential atmospheres with no crustal hydration as a basis for comparison; these atmospheres contain 200 mbar – 1.3 bar of background CO_2 and up to 300 mbar N_2. Hydrogen is photochemically produced through water photolysis, which produces H and OH. The HO_x radicals (H, OH, and HO_2) quickly reach steady state through fast reactions primarily involving O_x. A self-terminating reaction among H and HO_2 ultimately forms H_2, while another self-terminating reaction among OH and HO_2 recycles the HO_x back to water. This H_2 is primarily formed near the surface where water photolysis is fast, as water vapor becomes limited in the upper atmosphere due to cold trapping which we represent in our model by assigning a constant mixing ratio above the cold trapped layer and assigning a mixing ratio that corresponds to the saturation vapor pressure of water at and below the cold trapped layer. The H_2 diffuses on timescales of 10^5 years or may be attacked by $O(^1D)$ which would then restart the HO_x cycle. We ignore the effect of dust storms due to their transient nature, but we acknowledge their inclusion would increase the H escape rate on short timescales. The steady state mixing ratio of H_2 in cases with only photochemical production as the source is less than 10^{-6} in all early atmospheric pressures we consider, which is too low for a sufficient warming effect. In a 1 bar atmosphere, this corresponds to a surface temperature of 230 K. These surface temperatures and species mixing ratios are presented in Figure 2.2 and the full temperature-pressure profiles are shown in Figure 2.4.

In all atmospheric pressures, we find that crustal hydration supplies fluxes much larger than the photochemical production rate of hydrogen, and on long timescales we find notably increased steady state abundances. We consider a 500 mbar – 1.3 bar atmosphere and the Noachian crustal hydration rates, and we find surface mixing ratios of hydrogen of up to 17%. In agreement with Ramirez et al. (2014)

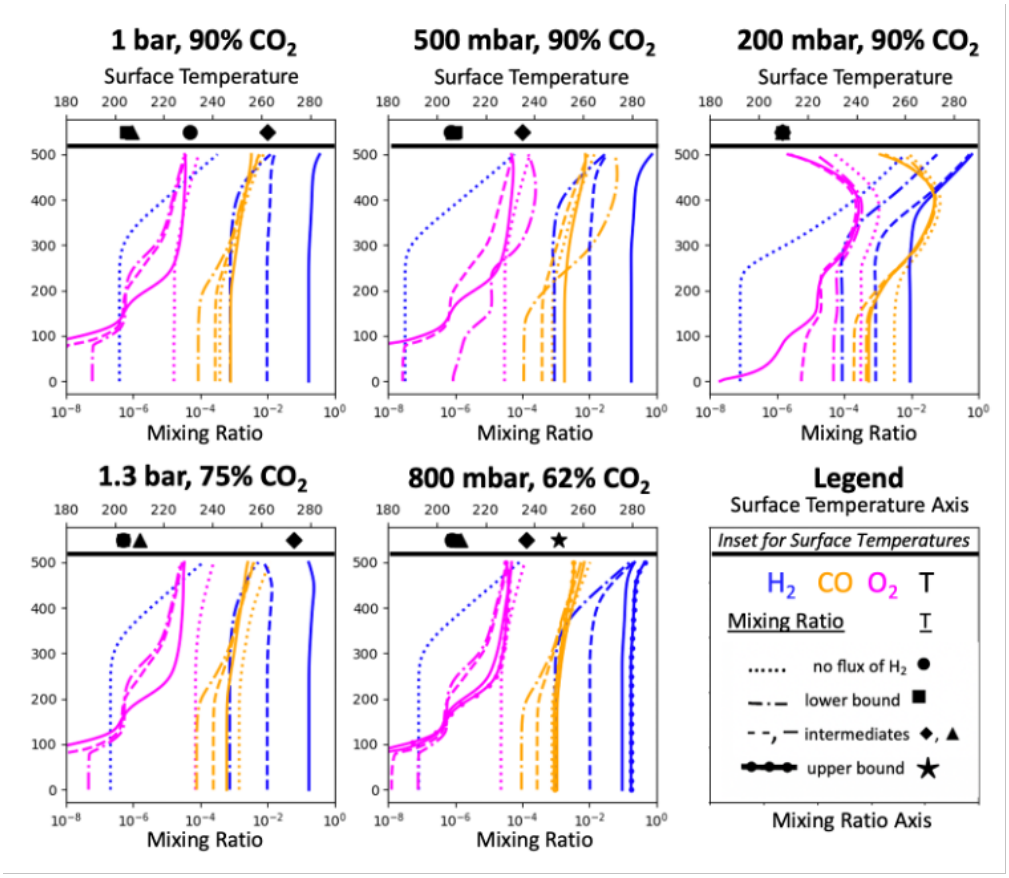

Figure 2.2: Mixing ratio profiles of H_2 (blue), O_2 (magenta), and CO (orange) in five atmospheres: 1 bar 90% CO_2 (upper left), 500 mbar 90% CO_2 (upper middle), 200 mbar 90% CO_2 (upper right), 1.3 bar 75% CO_2 (lower middle), 800 mbar 62% CO_2 (lower left). The complementary component of the atmosphere is N_2. A legend is shown in the lower right. For all except the 200 mbar case, the range of ground sinks shown spans 0 (dots), $1x10^{10}cm^{-2}s^{-1}$ (dash dot), $10^{11}cm^{-2}s^{-1}$ (dashed), $10^{12}cm^{-2}s^{-1}$ (solid), and $2x10^{12}cm^{-2}s^{-1}$ (solid with dots). We assume the 200 mbar atmosphere would not have persisted in the Noachian and therefore only a lower range of sinks: 0 (dots), $1x10^{9}cm^{-2}s^{-1}$ (dash dot), $10^{10}cm^{-2}s^{-1}$ (dashed), $10^{11}cm^{-2}s^{-1}$ (solid), and $3x10^{11}$ (solid with dots). Models are run to steady state ($> 10^8$ years, after which there is negligible variation in specie concentration over time).

and Wordsworth, Kalugina, et al. (2017), we find that mixing ratios of 10% and larger are sufficient to warm the climate above 270 K in the 1 bar atmosphere. The crustal hydration rates incorporated in our model assume consistent crustal hydration rates over the 400 Myr Noachian era. The H_2 production fluxes may have been episodically larger than those presented here. Since the chemical lifetime of hydrogen is 10^5 years, episodically larger rates of hydration would increase the H_2

and surface temperature on shorter timescales than we consider here.

From these results, we can infer a minimum surface pressure that could have supported large volumes of surface liquid water; cases with global mean surface temperatures cooler than 250 K are deemed unlikely to support local temperatures above 270 K and thus also unlikely to support large amounts of surface liquid water. The surface pressure during the warm epochs of the Noachian era was likely at minimum near 800 mbar, as thinner atmospheres are unable to sustain sufficiently warm surface temperatures. This constraint on pressure is in agreement with the results of an isotope evolution model (Hu, Kass, et al., 2015) which finds surface pressures of up to 1.5 bar during the Noachian, as well as a recent CO_2 budget model which accounts for loss of 1.5-3 bar CO_2 total, although not likely all at the same moment in time (Bruce Jakosky, 2019). A subset of nitrogen isotope evolution models motivate our cases that include 300 mbar N_2, as those models account for 60-740 mbar N_2 with a median pressure value of 310 mbar (Hu and T. Thomas, 2022). The 500 mbar CO_2, 300 mbar N_2 with H_2 is an attractive option for forming a warm, wet early climate, because it fits both C and N isotopic evolution without incurring too much carbonate formation.

We find that the lower geological estimates of crustal hydration are not supported by our chemical and climate model if crustal hydration was in fact the major source of H_2, as low hydrogen fluxes yield surface temperatures that are too cool for surface liquid water. If crustal hydration occurred consistently on long timescales during the Noachian, we can conclude that the total amount of water lost to the crust is near the upper range of geological estimates. Although, we acknowledge that the total time elapsed of the warm climate remains unknown.

2.3 Volcanic Fluxes Are Too Low to Sustain Large Ratios of H_2

Previous works have considered volcanism as a potential source of H_2. Since the lifetime of H_2 is 10^5 years, volcanic outgassing would need to be frequent and H_2-rich in order to supply large mixing ratios of atmospheric H_2 on long timescales. T. B. Thomas, Hu, and Daniel Y. Lo (2023), show that a more reduced Martian mantle is required to recreate the modern abundances and isotopic composition of N_2, CO_2, and Ar in Mars's atmosphere. They estimate that the magma oxygen fugacity was at the the Iron-Wustite buffer or one log unit below it, which is favorable for high H_2 volcanic outgassing rates. However, the maximum H_2 outgassing rates estimated in Thomas et al., in revision, are still insufficient to warm the surface to host liquid

water. During the Noachian, the maximum rate is $1.34x10^{10}cm^{-2}s^{-1}$ and in 1 and 1.3 bar atmospheres a flux of $10^{10}cm^{-2}s^{-1}$ does not sustain surface temperatures warmer than 240 K. Others have estimated higher H_2 outgassing rates on the order of $10^{11}cm^{-2}s^{-1}$, but they are based on highly uncertain scaling of modern Earth's H_2 outgassing rate (e.g., Wordsworth, Kalugina, et al., 2017; Liggins and al., 2020). In later epochs, the volcanic flux decreases and the atmosphere thins, yielding cooler surface temperatures than volcanism in the Noachian would have supported.

2.4 Cool, Dry CO_2 Atmospheres Are Photochemically Unstable in Early Epochs

In putative cool, dry epochs, little to no surface water would have been available, and therefore water-rock reactions sourcing H_2 would slow or cease. Although the majority of Fe oxidation was likely a result of crustal hydration (releasing H_2 in a warm climate), slower Fe oxidation may have still occurred during periods of a cool, dry climate which would lack of surface aqueous systems. Early in Mars' history, a lack of surface liquid water would expose reduced Fe(II) to the atmosphere, resulting in a loss of atmospheric oxidants to the ground; this scenario was previously considered by (Zahnle et al., 2008). Atmospheric oxidation of 2.7-Ga-old iron-nickel micrometeorites potentially via high abundances of upper atmospheric O2 (Tomkins et al., 2016; Rimmer, Shorttle, and Rugheimer, 2019) suggests early Mars may have undergone a similar loss of atmospheric oxidants to the ground. Chemical rates for iron oxidation by O2 have been measured at >1000 K (Abuluwefa, Guthrie, and Ajersch, 1997); however, the rate of iron oxidation by atmospheric oxidants is poorly constrained at temperatures relevant to the early Mars surface and are likely to be slow. In this work we vary the sink of oxygen from $10^6cm^{-2}s^{-1}$ to $10^9cm^{-2}s^{-1}$, with a lower bound representing a flux with negligible influence on the atmospheric chemistry and an upper bound within the range of oxidation weathering considered by (Hunten, 1973). Under this climate, we assume crustal hydration (which we acknowledge may still occur in localized underground systems) is negligible during these cold periods.

We consider one case with no oxidant sinks as a basis for comparison. In this case, the photochemical results differ from the assumed warm scenarios as CO deposition to the ground goes to zero due to no aqueous processes. With no sink to the ground, CO mixing ratios are of a few percent in the 1 bar atmosphere and are near 10% in thinner atmospheres. CO is more abundant in thinner atmospheres due to less water availability. In all cases, we initialize water to the saturation vapor pressure,

and in colder thinner atmospheres, less water is available to the recycling reaction: $CO + OH \rightarrow CO_2 + H$.

When ground sinks of oxygen are introduced, we find that the hydrogen escape rate increases. The loss of hydrogen to water in a 2:1 ratio seems to occur while the system has sufficient water to balance the oxygen sinks. However, once the oxidant sinks are increased beyond a rate that hydrogen diffusion can match (near $10^9 cm^{-2} s^{-1}$), the hydrogen escape rate can no longer increase to balance the oxygen sinks. Instead, sinking oxygen begins to be pulled off of CO_2 and the CO mixing ratio begins to rise. Zahnle et al. (2008) comes to a similar conclusion that oxidant sinks result in a CO runaway in initially thick CO_2-dominated atmospheres. Here, we improve the work with a more comprehensive model, including updated photochemical loss of carbon and coupling to a 1D climate model. Importantly, we find that the CO_2 instability only occurs on timescales of $> 10^8$ years. This suggests that the response to obliquity variations (10^5 years) and to transient H_2 sources (10^5 years) likely would have temporarily interrupted the evolution towards a CO atmosphere as the climate cooled. We find a CO-dominated atmosphere to be cooler (see Figure 2.4). The anharmonic mode coupling terms are small for CO because it is a diatomic molecule, resulting in fewer strong lines; CO has only an absorption band in the 5 micron region (which is far shortward of the main thermal distribution of a blackbody near 210 K) and a pure rotational band at longer wavelengths. Thus the main climate effect of CO would come from pressure-broadening of absorption by other gas species.

The behavior of 3D processes could have transported water to the upper atmosphere (such as periods of strong convection, variations in surface pressure, and obliquity changes), allowing rapid H escape. We investigate the effects of the water transport in only a 1D sense but find the oxidation of the surface to be faster than this oxidation of the atmosphere, maintaining relatively low O_2 and large CO abundances (see Table S1). We find that the mechanism of a CO runaway may also be self-limiting. The loss of atmospheric oxidants severely slows the recycling reaction $CO+OH \rightarrow CO_2+H$, yielding a CO-dominated atmosphere in cases of larger H_2 flux. The loss of a CO_2-dominated atmosphere removes the main photochemical production pathway for O_2, effectively placing an upper limit on the rate of O2 loss to oxidizing the surface. Larger sinks of O_2 to the ground would therefore likely not be sustained on long timescales of $> 10^8$ years.

We hypothesize two possible mechanisms to destroy or prevent a CO-dominated

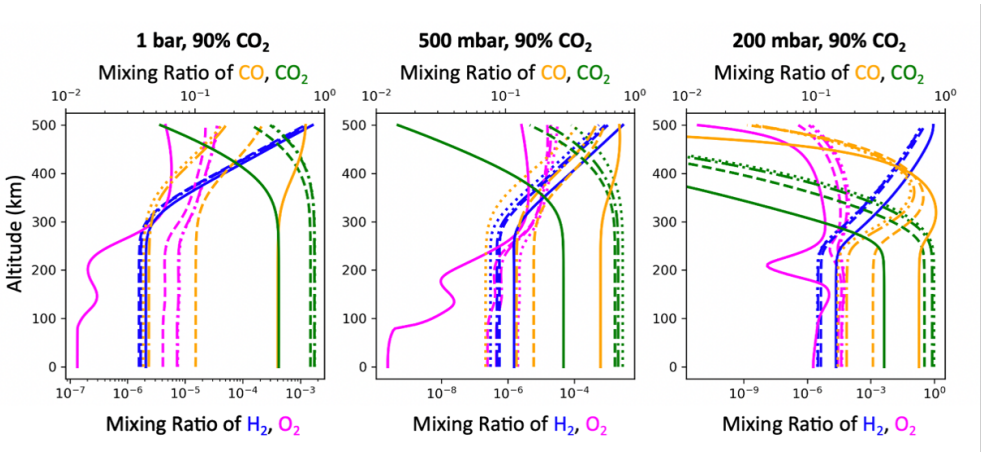

Figure 2.3: Mixing ratio profiles of H_2 (blue), O_2 (magenta), CO (orange), and CO_2 (green) in three atmospheres: 1 bar 90% CO_2 (left), 500 mbar 90% CO_2 (middle), 200 mbar 90% CO_2 (right). For all cases, the range of oxidant ground sinks shown are as follows 0 (dots), $10^7 cm^{-2}s^{-1}$ (dash dot), $10^8 cm^{-2}s^{-1}$ (dashed). We vary the upper limit (solid) as a function of surface pressure: $10^9 cm^{-2}s^{-1}$ (1 bar), $5x10^8$ (500 mbar), $2x10^8$ (200 mbar). Models are run for the duration of the Noachian era (400 Myr), and the resulting profiles after 400 Myr are shown.

atmosphere. First, on long timescales, the surface iron will become largely oxidized and thus sinks of atmospheric oxidants to the ground will slow. During the Amazonian era, the ground sink of oxygen would have been on average an order of magnitude less than the present-day atmospheric escape rate (Scheller et al., 2021). Therefore, iron oxidation would minimally impact the atmospheric chemistry, and CO_2 would be photochemically stable, as it is at present-day Mars. Second, a CO-runaway is most likely to occur in long-standing cool climates. Geologic events could have helped episodically warm a thinning atmosphere (on short timescales of 105 years), thereby slowing the onset of the CO runaway.

We acknowledge that catalytic chemistry involving chlorine radicals is known to prevent a CO-runaway at Venus (e.g., Y. Yung and Demore, 1982). However, at present-day Mars, the HCl abundance is only a few ppb (Korablev and al., 2021), which we predict would be insufficient to fully balance the CO runaway. The presence of present-day surface perchlorates (e.g., B. Sutter et al., 2017) implies the relevance of Cl- chemistry at early Mars and volcanism would likely have transiently increased HCl abundances to larger values; however, the HCl abundance at early Mars is poorly constrained and including Cl- chemistry in photochemical models would induce large error bars (spanning several orders of magnitude). For these reasons, we ignore catalytic chlorine chemistry, while also acknowledging its

importance on the chemistry of other solar system worlds. Similarly, due to our focus on atmospheric chemistry and climate, we do not solve aqueous processes such as the potential for chlorates to oxidize ferrous iron at early Mars (Kaushik Mitra and Catalano, 2019).

2.5 Implications for Early Mars' Redox Chemistry

Our coupled photochemical-climate model finds two plausible chemical and climate states for early Mars on long timescales for two different climate assumptions: [I] A warm climate capable of sustaining surface liquid water could have been maintained by large mixing ratios of H_2 supplied by crustal hydration; [II] a cool climate could have runaway to a cooler, CO-dominated atmosphere which results from large, dry oxidant sinks to the surface. The evolution of Mars' atmosphere remains uncertain, likely impacted by transient events on the atmospheric chemistry and climate. Geology predicts localized crustal hydration may have occurred during the Hesperian era, and several previous works have suggested the climate was not warm and wet consistently for the entire duration of the Noachian era (e.g., Fastook and al., 2012; N. Mangold and al., 2012; Wordsworth, Knoll, et al., 2021). Geologic events, including but not limited to obliquity changes (Kite et al., 2020), impacts, and volcanism (Wordsworth, Knoll, et al., 2021), may have sharply influenced the climate (Wordsworth, Knoll, et al., 2021; Kite et al., 2020) and facilitated abrupt climate transitions. We predict that Mars' atmosphere may not have always been in chemical steady state, meaning these two solutions describe end-of-range cases. Instead, it is plausible that Mars' atmosphere underwent abrupt redox changes by alternating from highly oxidized (CO_2-rich), to mildly reduced (CO_2-H_2) and warm, and to reduced and cold (CO-dominant). This hypothesis is grounded in the following recent observations.

First, Mars surface generally lacks surface carbonates (e.g., Ehlmann and Edwards, 2014), which are expected to form in the presence of neutral pH water and a CO_2 dominated atmosphere. If a CO runaway persisted for long periods, it could be a potential explanation for the global lack of carbonates. Second, a reducing CO-dominated atmosphere may also help to explain the recently observed C-13 isotope fractionation (Yoshida et al., 2023). However, since the CO atmosphere cannot sustain surface liquid water or crustal hydration, it is not likely to be the only early atmospheric composition and climate. The evidence for surface liquid water highlights the importance of the warm CO_2-H_2 solution. Alternating redox conditions could therefore help explain the lack of carbonates, $\delta^{13}C$ observations,

and the evidence for surface liquid water.

Mars' lack of tectonics has preserved geologic clues about the ancient climate and chemistry, and they have been geochemically analyzed. Interestingly, there are both reduced species including chlorobenzene (Glavin et al., 2013), trichloromethane (Glavin et al., 2013), H_2S (J. C. Stern et al., 2015; Glavin et al., 2013), and nitriles (Jennifer C. Stern et al., 2018), and oxidized species including perchlorate (B. Sutter et al., 2017; Glavin et al., 2013), nitrate (B. Sutter et al., 2017; J. C. Stern et al., 2015; Jennifer C. Stern et al., 2018), and sulfate (Jennifer C. Stern et al., 2018; B. Sutter et al., 2017) in the soils, and we term this the "redox dichotomy" as it suggests the surface of Mars is far from equilibrium. Similar to how Earth underwent a Great Oxidation Event (due to biological processes), this redox dichotomy may suggest that Mars underwent a photochemically driven redox transition or potentially a series of fluctuating redox conditions driven by both photochemistry and geologic events. The steady state photochemical results of this work may thus be end-member cases of the redox states Mars has experienced. While many of these species are of atmospheric origins, upon delivery to the surface, aqueous alteration would have also influenced the deposits seen today. For example, hypotheses of perchlorate formation include not only atmospheric oxidation of chlorine species (Catling et al., 2010) but also formation from brines (Steele et al., 2018) or irradiation of chlorine-bearing parent materials (Carrier and Kounaves, 2015). Similarly, halogen cycling may have contributed to oxidizing dissolved Mn(II) in Mars-like fluids (Kaustav Mitra et al., 2023), opposed to requiring a highly oxidizing atmosphere to explain MnO formation (Liu et al., 2021; Lanza, Woodward W. Fischer, et al., 2014; Lanza, Roger C. Wiens, et al., 2016). Hence, full interpretation of the redox paradox allows our hypothesis of alternating redox states to be testable, but requires careful consideration of both atmospheric and aqueous mechanisms.

2.6 Supporting Information: Materials and Methods

Photochemical Model, KINETICS

We adapt the Caltech/JPL photochemical and transport model, KINETICS, for the early Mars atmosphere. Additional input and output files from our study can be found in the Caltech online repository (see acknowledgements). The KINETICS software is described in the original references (Allen, Y. L. Yung, and Waters, 1981; Nair et al., 1994), and the work can be reproduced with all reactions and rate constants used in this study which are included in the provided output files. We consider the chemistry of 28 species linked by 172 reactions on an altitude grid

spaced on average with three bins per scale height that extends to 500 km (well above the exobase for our five atmospheric pressures considered). Our model calculates and outputs chemical abundances for each species at every level by computing the chemical production and loss rates at each altitude as well as the diffusive flux between each altitude grid with the 1-D continuity equation:

$$\frac{dn_i}{dt} = P_i - L_i - \frac{\partial \phi_i}{\phi z} \tag{2.1}$$

where n_i is the number density of species i, ϕ_i the vertical flux, P_i the chemical production rate, and L_i the chemical loss rate, all evaluated at time t and altitude z. The vertical flux is given by:

$$\phi_i = -D_i(\frac{\partial n_i}{\partial z} + \frac{n_i}{H_i} + \frac{1-\alpha_i}{T}\frac{\partial T}{\partial z}n) - K(\frac{\partial n_i}{\partial z}\frac{n_i}{H_i} + \frac{1}{T}\frac{\partial T}{\partial z}n) \tag{2.2}$$

where D_i is the species' molecular diffusion coefficient, H_i the species' scale height, H_{atm} the atmospheric scale height, α_i the thermal diffusion parameter, Kzz the vertical eddy diffusion coefficient, and T the temperature (Y. Yung and Demore, 1982). The flux consists of molecular diffusion (which can be derived from the molecular theory of ideal gases) and eddy transport. We calculate the eddy diffusion coefficient profile according to the formulation in (Ackerman and Marley, 2001).

Radiative Transfer Model, REDFOX

REDFOX calculates radiative transfer for discrete intervals in the spectral range from v = 0 to 10^5 cm^{-1}. We individually studied the temperature responses to including CO_2-H_2, H_2-H_2, as well as N_2-H_2 CIA in our scenarios, and even in the two cases of added 300 mbar of N_2 we found the latter to affect surface temperatures less than 2 K. Surface temperature changes between the 5 atmospheres considered are mainly attributed to variations in surface pressure opposed to the compositional variations. This is in agreement with (Wordsworth, Kalugina, et al., 2017), which found that the more heterogeneous electron density distribution of the major atmospheric constituent CO_2 strengthens the multipole moments and increases the polarizability leading to a stronger CIA effect in comparison to that of any added N_2. This result is in contrast to the early Earth study by (Wordsworth, Francois Forget, et al., 2013), which had found N_2-H_2 to significantly increase their temperatures. The difference lies mainly in the large amounts of CO_2 in early Mars, with major absorption bands in the same wavelength range as the N_2-H_2 CIA. See Scheucher et al. (2020) for a

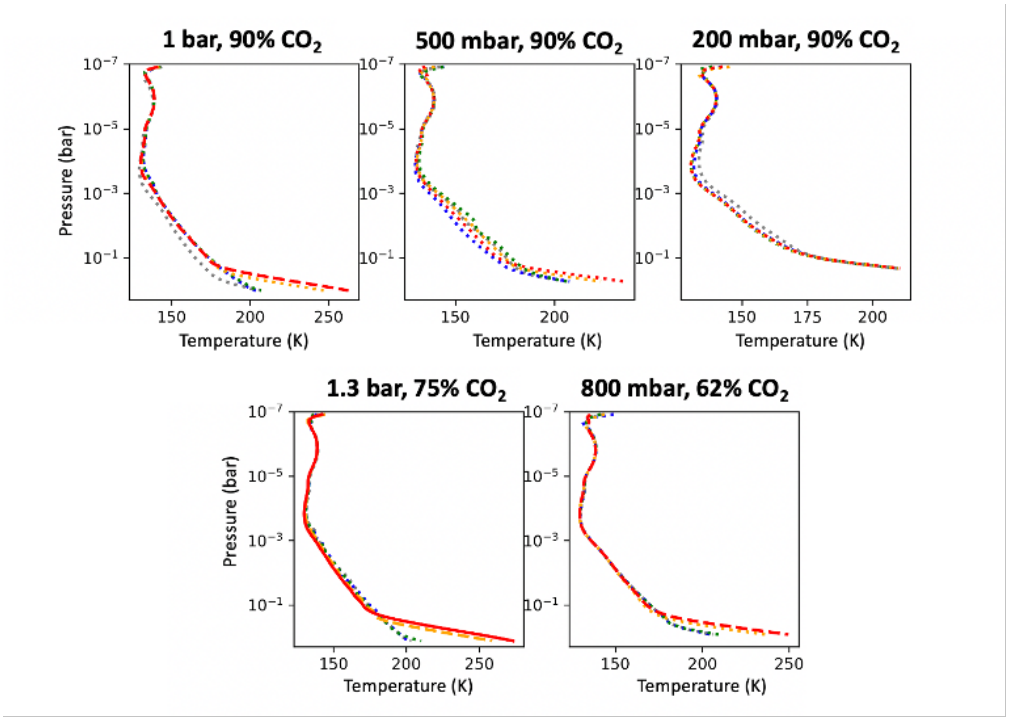

Figure 2.4: Temperature-pressure profiles computed by REDFOX after iteration with KINETICS. The top three panels assume a background CO_2 atmosphere with 10% N_2 in a 1 bar atmosphere (left), 500 mbar atmosphere (center), and 200 mbar atmosphere (right). The lower left panels show the cases with 300 mbar N_2 added to 1 bar and 500 mbar of CO_2. Cases with no hydrogen source are plotted in grey, lower limit H_2 fluxes in blue, intermediates in green and orange, and upper limit H_2 fluxes in red. Cases with surface temperatures cooler than 250 K are plotted in a dotted linestyle, greater than 250 K are plotted in a dashed linestyle, and greater than 270 K in a solid linestyle.

full list of atmospheric absorbers included in our correlated-k radiative transfer and for details about the cross sections. Water concentrations in convective regions in the troposphere are adjusted to follow modern Earth-like relative humidity profiles after (Manabe and Wetherald, 1967) with surface $R_H = 0.77$, including the potential presence of a liquid water ocean.

Figure 2.4 shows the temperature-pressure profiles as computed by REDFOX after iteration with KINETICS. The temperature profiles are similar in the upper regions, where the atmospheric density is not large enough for significant longwave absorption. The near-surface temperature shows the greatest response to near-surface photochemistry and surface interactions, and the thicker atmospheres show a warming of up to 60 K compared to our thinner atmospheres.

Note for our coldest resulting tropospheres without added N_2, such as in the case of 200 mbar atmospheres and the 500 mbar atmosphere with lowest H_2 fluxes, CO_2 may partially freeze out in parts of the troposphere. A caveat of 1D models is the global treatment of such freeze out, potentially leading to artificial full atmospheric collapse in such cases (e.g., F. Forget et al., 2013). In an effort to compare all our cases with the intended surface pressure, we prevented global CO_2 freeze out.

Relating Hydration to an Atmospheric Hydrogen Source

Clay minerals and other hydrated minerals will incorporate OH-groups and H_2O-groups, and the case of OH groups can be thought of as an oxygen sink since one H is liberated for every OH-group that is incorporated. The ratio of OH:H_2O groups incorporated is dependent on the mineral, and in this work we make the assumption that it is serpentine-like. With the simplifying assumption that 2 OH must be incorporated for one release of H_2, for serpentine, the ratio of H_2O incorporated to H_2 released is 4-40 (Chassefière and al., 2013; Chassefière, Lasue, et al., 2016). Scheller et al. (2021) finds that 100-900m GEL water is lost to crustal hydration during the Noachian and 10-100m GEL during the Hesperian.

Crustal hydration is not the only source of water loss. We base assumptions on Fe(II) to Fe(III) oxidation depths on Scheller et al. (2021): 10-5 km during the Noachian and 5-1 km during the Hesperian. Regular basalt at Mars contains 20 wt% FeO, and the Fe^{3+}/Fe_T is $< 0.2 - 0.3$ for relatively unaltered basalts and 0.6-0.9 for highly altered basalts (**morris2006**). Therefore, assuming 10-60% of all Fe(II) becomes oxidized to Fe(III), which requires 0.5 mol O per Fe, this relates to 32-382m GEL lost during the Noachian and 6-192m GEL during the Hesperian.

Furthermore, oxidation of FeS minerals to sulfate contributes as a third relevant mechanism, and SNC meteorites show 0.2-0.3 wt% FeS (McLennan and Grotzinger, 2008). Meanwhile Fe oxidation via chlorates may also be efficient (Kaushik Mitra and Catalano, 2019). However, neither of these aqueous mechanisms would release H_2, and therefore we ignore them in our work. With similar assumptions as iron oxidation, we acknowledge the former contributes 2-29m GEL water loss during the Noachian and 0.5-15m GEL loss during the Hesperian.

The total water lost (in units of m GEL) can be related to a flux lost (in units of molecules $cm^{-2}s^{-1}$) with another simplifying assumption that loss was approximately constant over a respective era:

$$F_{waterloss} = D \cdot A \cdot \rho \cdot \frac{1}{mu_{water}} \cdot N_A \cdot \frac{1}{t} \cdot 1A \cdot 1n \tag{2.3}$$

where D is the depth of water in cm GEL, A is the surface area of Mars (cm2), ρ is the density (g/cm3) of water, μ_{water} is the mean molecular weight of water (18 g/mol), N_A is Avogadro's constant, and t is the duration of a given epoch. This flux may then be related to the flux of hydrogen released according to the ratio, n, of 4-40 for H_2O loss : H_2 release. This relates to a range of hydrogen released to the atmosphere between $10^{10} - 2x10^{12}\ H_2 cm^{-2} s^{-1}$ during the Noachian and $10^9 - 3x10^{11}\ H_2 cm^{-2} s^{-1}$ during the Hesperian.

Effect of Water Photolysis Rates on CO Runaway

CO runaway at Mars occurs when the production of HO_x radicals is limited. At present-day Mars, dust storms are known to increase hydrogen escape via lofting water into the stratosphere. At early Mars, a similar effect may result from periods of strong convection. Here, we demonstrate that lofting water into the stratosphere supplies an insufficient amount of HOx to balance the CO runaway.

Additionally, it was recently found that the extended tail region for the photolysis cross section of water is non-negligible due to the solar spectrum hosting an increased number of photons at longer wavelengths (Ranjan, Sasselov, and Lewis, 2020). Here, we demonstrate that the effect of the faster water photolysis (i.e., faster supply of HO_x) is also insufficient to balance the CO runaway.

O_2 sink	0 O_2/cm^2/s	0 O_2/cm^2/s	10^8 O_2/cm^2/s	10^8 O_2/cm^2/s	10^9 O_2/cm^2/s	10^9 O_2/cm^2/s
Modification:	convection	photolysis	convection	photolysis	convection	photolysis
% change in [CO] near surface:	-2.4%	-13.4%	-1.3%	-15.6%	-0.05%	-9.0%
% change in [CO] in stratosphere:	-2.4%	-13.4%	-1.3%	-15.6%	-0.05%	-9.0%

Figure 2.5: Percent change in surface and stratospheric CO concentrations due to periods of strong convection or the inclusion of the tail region in the water photolysis cross sections.

References

Abuluwefa, H T, R I L Guthrie, and F Ajersch (1997). "Oxidation of low carbon steel in multicomponent gases: Part I. Reaction mechanisms during isothermal oxidation". In: *Metallurgical and Materials Transactions A* 28.8, pp. 1633–1641.

Ackerman, Andrew S and Mark S Marley (2001). "Precipitating Condensation Clouds in Substellar Atmospheres". In: *The Astrophysical Journal* 556.2. DOI: 10.1086/321540.

Allen, Mark, Yuk L Yung, and Joe W Waters (1981). "Vertical transport and photochemistry in the terrestrial mesosphere and lower thermosphere (50-120f km)". In: *Journal of Geophysical Research* 86.A5, pp. 3617–3627.

Audouard, J. and et al. (2014). "Water in the Martian regolith from OMEGA/Mars Express". In: *Journal of Geophysical Research: Planets* 119, pp. 1969–1989.

Barnhart, Charles, Alan Howard, and Jeffrey Moore (2009). "Long-term precipitation and late-stage valley network formation: Landform simulations of Parana Basin, Mars". In: *J. Geophys. Res.* 114.E1. DOI: 10.1029/2008JE003262.

Batalha, Natasha et al. (2015). "Testing the early Mars H2-CO2 greenhouse hypothesis with a 1-D photochemical model". In: *Icarus* 258, pp. 337–349.

Borysow, A. and L. Frommhold (1986). "Theoretical collision-induced rototranslational absorption spectra for modeling Titan's atmosphere: H2-N2 pairs". In: *AJ* 303, p. 495.

Carr, Michael H and James W Head (2003). "Oceans on Mars: An assessment of the observational evidence and possible fate". In: *J. Geophys. Res. Planets* 108.E5. DOI: 10.1029/2002JE001963.

Carrier, Brandi L. and Samuel P. Kounaves (2015). "The origins of perchlorate in the Martian soil". In: *Geophysical Research Letters* 42.10, pp. 3739–3745. DOI: https://doi.org/10.1002/2015GL064290.

Catling, D. C. et al. (2010). "Atmospheric origins of perchlorate on Mars and in the Atacama". In: *Journal of Geophysical Research: Planets* 115.E1. DOI: https://doi.org/10.1029/2009JE003425.

Chassefière, E. and et al. (2013). "The fate of early Mars' lost water: The role of serpentinization". In: *Journal of Geophysical Research: Planets* 118.

Chassefière, E., J. Lasue, et al. (2016). "Early Mars serpentinization-derived CH4 reservoirs, H2-induced warming and paleopressure evolution". In: *Meteoritics and Planetary Science* 51.11, pp. 2234–2245. DOI: https://doi.org/10.1111/maps.12784.

Clifford, Stephen M and Timothy J Parker (2001). "The evolution of the Martian hydrosphere: Implications for the fate of a primordial ocean and the current state of the northern plains". In: *Icarus* 154, pp. 40–79. DOI: 10.1006/icar.2001.6671.

Di Achille, Gaetano and Brian Hynek (2010). "Ancient ocean on Mars supported by global distribution of deltas and valleys". In: *Nature Geoscience* 3, pp. 459–463. DOI: 10.1038/ngeo891.

Donahue, T. M. (1995). "Evolution of water reservoirs on Mars from D/H ratios in the atmosphere and crust". In: *Nature* 374, pp. 432–434.

Ehlmann, Bethany L and Christopher S Edwards (2014). "Mineralogy of the Martian Surface". In: *Annual Review of Earth and Planetary Sciences* 42, pp. 291–315.

Fastook, J. and et al. (2012). "Early Mars climate near the Noachian-Hesperian boundary: independent evidence for cold conditions from basal melting of the south polar ice sheet (Dorsa Argentea Formation) and implications for valley network formation". In: *Icarus* 219.

Forget, F. et al. (2013). "3D modelling of the early Martian climate under a denser CO2 atmosphere: Temperatures and CO2 ice clouds". In: *Icarus* 222, pp. 81–99. DOI: 10.1016/j.icarus.2012.10.019.

Glavin, Daniel P et al. (2013). "Evidence for perchlorates and the origin of chlorinated hydrocarbons detected by SAM at the Rocknest aeolian deposit in Gale Crater". In: *Journal of Geophysical Research: Planets* 118.10, pp. 1955–1973.

Greenwood, J. P. et al. (2008). "Hydrogen isotope evidence for loss of water from Mars through time". In: *Geophysical Research Letters* 35.5.

Grotzinger, John P et al. (2014). "A Habitable Fluvio-Lacustrine Environment at Yellowknife Bay, Gale Crater, Mars". In: *Science* 343.6169. DOI: 10.1126/science.1242777.

Herwartz, Daniel et al. (2021). "A CO2 greenhouse efficiently warmed the early Earth and decreased seawater 18O/16O before the onset of planet tectonics". In: *Proceedings of the National Academy of Sciences* 118.14, e2022620118.

Hoke, Meredith, Brian Hynek, and Gregory Tucker (2011). "Formation timescales of large Martian valley networks". In: *Earth and Planetary Science Letters* 312, p. 1. DOI: 10.1016/j.epsl.2011.09.029.

Hu, Renyu, David Kass, et al. (2015). "Tracing the fate of carbon and the atmospheric evolution of Mars". In: *Nature Communications* 6, p. 10003. DOI: 10.1038/ncomms10003.

Hu, Renyu and Tommaso Thomas (2022). "A nitrogen-rich atmosphere on ancient Mars consistent with isotopic evolution models". In: *Nature Geoscience* 15.2.

Hunten, Donald M (1973). "The escape of light gases from planetary atmospheres". In: *Journal of Atmospheric Sciences* 30.8, pp. 1481–1494.

Jakosky, Bruce (2019). "The CO2 Inventory on Mars". In: *Planetary and Space Science* 175, pp. 52–59.

Jakosky, Bruce et al. (2017). "Mars' atmospheric history derived from upper-atmosphere measurements of 38Ar/36Ar". In: *Science* 355.633.

Jakosky, Bruce M et al. (2018). "Loss of the Martian atmosphere to space: Present-day loss rates determined from MAVEN observations and integrated loss through time". In: *Icarus* 315, pp. 146–157. DOI: 10.1016/j.icarus.2018.05.030.

Kite, E. et al. (2020). "Atmosphere Origins for Exoplanet Sub-Neptunes". In: *The Astrophysical Journal* 891.2. DOI: 10.3847/1538-4357/ab6ffb.

Korablev, O. and et al. (2021). "Transient HCl in the atmosphere of Mars". In: *Science* 7.

Kurokawa, Hidenori et al. (2014). “Evolution of water reservoirs on Mars: Constraints from hydrogen isotopes in Martian meteorites”. In: *Earth Planet. Sci. Lett.* 394, pp. 179–185. DOI: 10.1016/j.epsl.2014.03.003.

Lanza, Nina L., Woodward W. Fischer, et al. (2014). “High manganese concentrations in rocks at Gale crater, Mars”. In: *Geophysical Research Letters* 41.16, pp. 5755–5763. DOI: https://doi.org/10.1002/2014GL060329.

Lanza, Nina L., Roger C. Wiens, et al. (2016). “Oxidation of manganese in an ancient aquifer, Kimberley formation, Gale crater, Mars”. In: *Geophysical Research Letters* 43.14, pp. 7398–7407. DOI: https://doi.org/10.1002/2016GL069109.

Liggins, F. and et al. (2020). “Can volcanism build hydrogen-rich early atmospheres?” In: *Earth and Planetary Science Letters* 550.

Lillis, Robert J, Justin Deighan, et al. (2017). “Photochemical escape of oxygen from Mars: First results from MAVEN in situ data”. In: *Journal of Geophysical Research: Space Physics* 122.3, pp. 3559–3571.

Lillis, Robert J, Shaosui Xu, et al. (2021). “Ionization efficiency in the dayside ionosphere of Mars: Structure and variability”. In: *Journal of Geophysical Research: Planets* 126.12, e2021JE006981.

Liu, Yang et al. (2021). “Manganese oxides in Martian meteorites Northwest Africa (NWA) 7034 and 7533”. In: *Icarus* 364, p. 114471. ISSN: 0019-1035. DOI: https://doi.org/10.1016/j.icarus.2021.114471.

Lo, Daniel Y, Roger V Yelle, and Robert J Lillis (2020). “Carbon photochemistry at Mars: Updates with recent data”. In: *Icarus* 352, p. 113984.

Manabe, Syukuro and Richard T Wetherald (1967). “Thermal equilibrium of the atmosphere with a given distribution of relative humidity”. In: *Journal of Atmospheric Sciences* 24.3, pp. 241–259.

Mangold, N. and et al. (2012). “The origin and timing of fluvial activity at Eberswalde crater, Mars”. In: *Icarus* 220.

Maurice, S. and et al. (2011). “Mars Odyssey neutron data: 1. Data processing and models of water-equivalent-hydrogen distribution”. In: *Journal of Geophysical Research: Planets* 116 (E11).

McElroy, M. and T. Donahue (1972). “Stability of the Martian Atmosphere”. In: *Science* 177.4045, pp. 986–988.

McElroy, M., T. Kong, and Y. Yung (1977). “Photochemistry and evolution of Mars’ atmosphere: A Viking perspective”. In: *Journal of Geophysical Research* 82.28, pp. 4329–4339.

McLennan, Scott M and John P Grotzinger (2008). “The sedimentary rock cycle of Mars”. In: *The Martian Surface: Composition, Mineralogy, and Physical Properties*. Cambridge University Press, pp. 541–577.

Mitra, Kaushik and Jeffrey G. Catalano (2019). "Chlorate as a Potential Oxidant on Mars: Rates and Products of Dissolved Fe(II) Oxidation". In: *Journal of Geophysical Research: Planets* 124.11, pp. 2893–2916. DOI: https://doi.org/10.1029/2019JE006133.

Mitra, Kaustav et al. (2023). "Formation of manganese oxides on early Mars due to active halogen cycling". In: *Nature Geoscience* 16, pp. 133–139.

Murchie, Scott L et al. (2009). "A synthesis of Martian aqueous mineralogy after 1 Mars year of observations from the mars Reconnaissance Orbiter". In: *J. Geophys. Res. Planets* 114.E2.

Mustard, John F (2019). "Sequestration of volatiles in the Martian crust through hydrated minerals: A significant planetary reservoir of water". In: *Volatiles in the Martian Crust*. 2nd ed. Amsterdam, Netherlands: Elsevier, pp. 247–264.

Nair, H. et al. (1994). "A photochemical model of the Martian atmosphere". In: *Icarus* 111.1, pp. 124–150.

Olsen, Amanda Albright and J. Donald Rimstidt (2007). "Using a mineral lifetime diagram to evaluate the persistence of olivine on Mars". In: *American Mineralogist* 92.4, pp. 598–602. DOI: 10.2138/am.2007.2462.

Paris, Philip von et al. (2013). "N2-assisted surface warming on early Mars". In: *Planetary and Space Science* 82-83, pp. 149–154.

Payne, Richard J et al. (2020). "Oxidized micrometeorites suggest either high pCO2 or low pN2 during the Neoarchean". In: *Proceedings of the National Academy of Sciences* 117.47, pp. 29272–29278.

Pollack, James et al. (1987). "The case for a wet, warm climate on early Mars". In: *Icarus* 71.2.

Ramirez, Ramses et al. (2014). "Warming early Mars with CO2 and H2". In: *Nature Geoscience* 7.1, pp. 59–63.

Ranjan, Sukrit, Dimitar D. Sasselov, and Nikole K. Lewis (2020). "Photochemistry of anoxic abiotic habitable planet atmospheres: Impact of new H2O photolysis cross sections". In: *AJ* 896.2, p. 148. DOI: 10.3847/1538-4357/ab90f1.

Rimmer, Paul B, Oliver Shorttle, and Sarah Rugheimer (2019). "Oxidised micrometeorites as evidence for low atmospheric pressure on the early Earth". In: *Geochemical Perspectives Letters* 9, pp. 38–42. DOI: 10.7185/geochemlet.1923.

Sagan, Carl and George Mullen (1972). "Earth and Mars: Evolution of Atmospheres and Surface Temperatures". In: *Science* 177.4043, p. 52. DOI: 10.1126/science.177.4043.52.

Scheller, Elisa et al. (2021). "Long-term drying of Mars by sequestration of ocean-scale volumes of water in the crust". In: *Science* 372.6537.

Scheucher, M. et al. (2020). "Consistently simulating a wide range of atmospheric scenarios for K2-18b with a flexible radiative transfer module". In: *AJ* 898.1.

Schon, Samuel, James Head, and Caleb Fassett (2012). "An overfilled lacustrine system and progradational delta in Jezero crater, Mars: Implications for Noachian climate". In: *Planetary and Space Science* 67, p. 1. DOI: 10.1016/j.pss.2012.02.003.

Steele, Andrew et al. (2018). "Organic synthesis on Mars by electrochemical reduction of CO2". In: *Science Advances* 4.10.

Stern, J. C. et al. (2015). "Evidence for indigenous nitrogen in sedimentary and aeolian deposits from the Curiosity rover investigations at Gale crater, Mars". In: *Proceedings of the National Academy of Sciences of the United States of America* 112.14, pp. 4245–4250. DOI: 10.1073/pnas.142.

Stern, Jennifer C. et al. (2018). "Major Volatiles Evolved From Eolian Materials in Gale Crater". In: *Geophysical Research Letters* 45.19, pp. 10240–10248. DOI: https://doi.org/10.1029/2018GL079059.

Sun, V. Z. and R. E. Milliken (2015). "The geology of mineralogy of Ritchey crater, Mars: Evidence for post-Noachian clay formation". In: *Journal of Geophysical Research: Planets* 119, pp. 810–836.

Sutter, B. et al. (2017). "Evolved gas analyses of sedimentary rocks and eolian sediment in Gale Crater, Mars: Results of the Curiosity Rover's sample analysis at Mars instrument from Yellowknife Bay to the Namib Dune". In: *Journal of Geophysical Research: Planets* 122.11, pp. 2574–2609. DOI: 10.1002/2016JE005225.

Thomas, N. H. and et al. (2020). "Hydrogen Variability in the Murray Formation, Gale Crater, Mars". In: *Journal of Geophysical Research: Planets* 125.e2019JE006289.

Thomas, Trent B., Renyu Hu, and Daniel Y. Lo (Mar. 2023). "Constraints on the Size and Composition of the Ancient Martian Atmosphere from Coupled CO2–N2–Ar Isotopic Evolution Models". In: *The Planetary Science Journal* 4.3, p. 41. DOI: 10.3847/PSJ/acb924. URL: https://dx.doi.org/10.3847/PSJ/acb924.

Tomkins, Andrew et al. (2016). "Ancient micrometeorites suggestive of an oxygen-rich Archaean upper atmosphere". In: *Nature* 533.7602, pp. 235–238. DOI: 10.1038/nature17678.

Tosca, Nicholas J et al. (2018). "Magnetite authigenesis and the warming of early Mars". In: *Nature Geoscience* 11.9, pp. 635–639.

Vaniman, D. T. and et al. (2014). "Mineralogy of a mudstone at Yellowknife Bay, Gale crater, Mars". In: *Science* 343 (6169).

Webster, Christopher R et al. (2013). "Isotope ratios of H, C, and O in CO2 and H2O of the Martian atmosphere". In: *Science* 341.6143.

Wernicke, L. and B. Jakosky (2019). "Quantifying the Water Stored in Hydrated Minerals on Mars". In: *AGU Fall Meeting Abstracts*. Vol. 2019, P41C–3462.

Wordsworth, Robin (2016). “The Climate of Early Mars”. In: *Annual Review of Earth and Planetary Sciences* 44, pp. 381–408.

Wordsworth, Robin, Francois Forget, et al. (2013). “Global modelling of the early Martian climate under a denser CO2 atmosphere: Water cycle and ice evolution”. In: *Icarus* 222.1, pp. 1–19. DOI: 10.1016/j.icarus.2012.10.026.

Wordsworth, Robin, Yulia Kalugina, et al. (2017). “Transient reducing greenhouse warming on early Mars”. In: *Geophysical Research Letters* 44.2, pp. 665–671. DOI: 10.1002/2016GL071766.

Wordsworth, Robin, Andrew Knoll, et al. (2021). “A coupled model of episodic warming, oxidation and geochemical transitions on early Mars”. In: *Nature Geoscience* 14.3, pp. 167–173.

Yoshida, Tatsuya et al. (Mar. 2023). “Strong Depletion of 13C in CO Induced by Photolysis of CO2 in the Martian Atmosphere, Calculated by a Photochemical Model ”. In: *The Planetary Science Journal* 4.3, p. 53. DOI: 10.3847/PSJ/acc030. URL: https://dx.doi.org/10.3847/PSJ/acc030.

Yung, Y. and W. Demore (1982). “Photochemistry of the stratosphere of Venus: implications for atmospheric evolution”. In: *Icarus* 51.

Zahnle, K. et al. (2008). “Photochemical instability of the ancient Martian atmosphere”. In: *Journal of Geophysical Research: Planets* 113.E11, n/a–n/a.

Chapter 3

NITROGEN FIXATION AT EARLY MARS

Adams, Danica et al. (2021). "Nitrogen Fixation at Early Mars". In: *Astrobiology* 21.8.

D.J.A modified and ran the photochemical model KINETICS and the thermochemical model CEA, and D.J.A. developed the steady state aqueous chemistry model. Y.L. computed CAPE from established GCM results. C.D. and P.D. ran the Geant4 simulation, and M.C. improved the aqueous chemistry model. Y.L.Y and M.L.W developed the research concept., pp. 968–980. DOI: 10.1089/ast.2020.2273.

3.1 Introduction

The Mars Science Laboratory (MSL) recently discovered 70–260 and 330–1100 ppm of nitrate in the Klein and Cumberland Noachian-aged mudstone deposits, respectively, at Yellowknife Bay (Stern et al., 2015). Subsequent measurements of 0.002 to 0.05 wt% of nitrate in sediments near Gale Crater were also reported (Sutter et al., 2017). One possible mechanism for nitrate deposition is through HNOx formation and rain-out in the atmosphere, for which lightning-induced NO is the fundamental source (e.g., Schuman and Huntrieser, 2007; Ducluzeau et al., 2009). At early Mars, electrical discharges would have heated local air parcels to tens of thousands of Kelvin, encouraging the following chemical processes (e.g., Wong, Charnay, et al., 2017):

$$CO_2 \rightarrow CO + O$$

$$O + N_2 \rightarrow NO + N$$

$$N + CO_2 \rightarrow NO + CO$$

Photochemical pathways then produce HNOx from NO and oxidizing species, followed by subsequent rain-out into a depositional environment. Wong, Charnay, et al. (2017) investigated the production and precipitation of HNOx via this pathway in early Earth environments. This mechanism is likely applicable to early Mars, as extensive geological and mineralogical evidence at the present surface suggests that liquid water once flowed and precipitated on the surface during the late Noachian

(e.g., Baker, 2006; Bibring et al., 2006; Grotzinger et al., 2015; McEwen et al., 2013; Milliken, Grotzinger, and Thomson, 2010).

HCN may be produced as a dissociation product of N_2 and CH_4 (i.e., in the presence of lightning, as well as solar energetic particle events). HCN is also soluble, and we expect it would have also precipitated to the early Mars surface during times of a warm, wet climate. We thus also examine the surface flux of HCN rain-out. Multiple pathways to produce HCN from radicals have been suggested (Pearce, Ayers, and Pudritz, 2019). The dominant formation mechanisms in this work are summarized in Fig. 3.7, and the complete reaction table (with rate constants and column rates) are provided in Appendix 1.

The nitrogen cycle at early Mars remains a long-standing question of significant astrobiological relevance; specifically, lightning-induced production of HCN and nitrogen oxides may have been key to the onset of both early terrestrial and possibly Martian life.

Astrobiological Implications of HCN

HCN production may have been relevant to synthesizing prebiotic molecules (e.g., D. Ritson and J. D. Sutherland, 2012; D. J. Ritson and J. D. Sutherland, 2013; J. Sutherland, 2017). It has been hypothesized that prebiotic synthesis of adenine from HCN may have made adenine readily available in early terrestrial environments (e.g., Holm and Neubeck, 2009). The purine coding elements of RNA, adenine in particular, can be synthesized in an efficient process from HCN (Oro, 1960; Oro, 1961). While this synthesis would have required high concentrations of HCN ($> 0.01M$), strong absorption via zeolites (Fripiat et al., 1972) and other concentrating mechanisms have been suggested to allow for synthesis via compartmentalization in an otherwise more dilute solution of HCN (e.g., Holm and Neubeck, 2009). In this work we investigate the HCN produced by lightning and photochemistry involving radicals produced from solar energetic particle (SEP) events, but we acknowledge that formation could have also been encouraged by UV radiation and geothermal energy sources.

Astrobiological Implications of NOx

It has been hypothesized that nitrogen oxides may have acted as high-potential electron acceptors for early metabolic processes (e.g., Mancinelli and McKay, 1988). Nitrate (NO_3^-) and nitrite (NO_2^-) could have provided the free energy gradient to drive the first metabolic pathway via oxidizing hydrothermal CH_4 while hydrogenat-

ing CO_2 at alkaline hydrothermal vents (e.g., Ducluzeau et al., 2009; Nitschke and M. J. Russell, 2013; Shibuya, M. Russell, and Takai, 2016). In order for this mechanism to proceed, nitrogen oxides are required as high potential electron acceptors. First, their presence would help set up the initial disequilibrium required to activate methane, which is converted to methanol as nitrate and nitrite are re-reduced to nitric oxide, NO (Nitschke and M. J. Russell, 2013). Second, they could potentially facilitate electron bifurcation, in which the acceptance of an outer shell molybdenum electron would be coupled to the reduction of CO_2 (the low-potential electron acceptor) to CO (Schoepp-Cothenet et al., 2012; Nitschke and M. J. Russell, 2013; Helz, Erickson, and Vorlicek, 2014). The astrobiological relevance of lightning-induced nitrogen fixation in the early terrestrial atmosphere has been considered and was motivated by these mechanisms in (Wong, Charnay, et al., 2017).

Relevance of the Early Mars Climate

As mentioned above, its present-day surface morphology indicates that early Mars was likely warm and wet during the late Noachian, suggesting a drastically different early climate than the present. This climate is key to inferring the nature of the early Mars nitrogen cycle. Since this paper seeks to examine HCN and HNOx production, it is critical to first understand the nature of the early atmosphere in which these molecules would have formed. Despite the evidence for a warm, wet early Mars, a zero-albedo early Mars would have hosted an equilibrium temperature of only 210 K, far from the phase transition for liquid water. With a semi-major axis of 1.524 AU, Mars only receives 43% of the solar flux received by Earth. The early Sun (at 3.8 Ga) contributed to this cool temperature as it was only 75% as luminous as the present-day Sun; the energy output of stellar cores increases with time as they contract due to the increasing mean molecular weight yielded from hydrogen fusion (Gough, 1981). Hence, this evidence for surface water is paradoxical and begs the question: what early Mars climate was capable of sufficiently warming the surface?

It has been hypothesized that early Mars likely hosted a much thicker atmosphere enriched with greenhouse gases. James F Kasting (1991) demonstrated that a CO_2–H_2O atmosphere (i.e., an atmosphere dominated by greenhouse gases) would have increased the planetary albedo via Rayleigh scattering and cloud condensation, and would thus be insufficient to warm early Mars. Other surface warming processes have been investigated but yielded insufficient surface warming; these include but are not limited to: cirrus clouds (e.g., R. M. Ramirez and James F. Kasting, 2017), water clouds (e.g., Urata and O. Toon, 2013), CO_2 clouds (e.g., François Forget

and Pierrehumbert, 1997), sulfur dioxide from volcanic outgassing (e.g., Halevy and James W Head, 2014), and orbital obliquity and eccentricity variations and/or diurnal variations (Wordsworth, Francois Forget, et al., 2013). While the present Mars atmosphere is oxidizing due to efficient hydrogen escape, it has recently been suggested that the early atmosphere may have been more reducing. Collisionally induced absorption (CIA) of CO_2 with CH_4 and H_2, due to both induced dipole and dimer effects (Gruszka and Borysow, 1997; Baranov, Lafferty, and Fraser, 2004),could provide sufficient climate forcing to allow at least transient liquid water on the early martian surface (e.g., R. Ramirez et al., 2014; Wordsworth, Kalugina, et al., 2017). The climate model presented in Wordsworth et al. (2017) produces global mean surface temperatures >273 K with atmospheric pressures below 2 bar. This atmospheric pressure is consistent with estimates of carbon isotope fractionation (Hu, Kass, et al., 2015), an upper limit derived from surface crater distributions (Kite et al., 2014), and the estimated time-integrated atmospheric loss derived from MAVEN (the Mars Atmospheric and EvolutioN mission) (Bruce M Jakosky et al., 2018). We consider it likely that H_2 and CH_4 were important greenhouse gases on early Mars; however, their early abundances are still highly uncertain.

Throughout this work, we assume a background 1 bar CO_2 atmosphere and vary the abundances of N_2, H_2, and CH_4 from 1–10%. The precise phase space is summarized in Figure 3.1.

These mixing ratios of reduced gases are motivated in part by their contribution to the greenhouse effect, but also by geochemistry. Note that these geochemical sources – serpentinization-induced CH_4 fluxes of $10^{10\sim}10^{12} cm^{-2}s^{-1}$ (Etiope and Sherwood Lollar, 2013; Wordsworth, Kalugina, et al., 2017), in combination with release from methane clathrates, impact degassing, and volcanic outgassing – would have competed with atmospheric escape and photochemical destruction for H_2 and CH_4, respectively. Methane clathrates may have formed in the presence of surface ice and serpentine (Lasue et al., 2015). Theoretical equilibrium calculations of carbonaceous chondrite impactors suggest methane as the dominant C-bearing specie outgassed (Schaefer and Fegley, 2007). The interior of Mars may not have reached the temperature and pressure required to undergo the spinel-to-perovskite transition at 1900 K and 24 GPa (Chudinovskikh and Boehler, 2001) which would make the interior more reduced; if Mars had a lower oxygen fugacity mantle, magmatic outgassing could have yielded a CH_4 rich atmosphere (Wadhwa, 2001). Relatively low mixing ratios would have been likely, due to the competition of

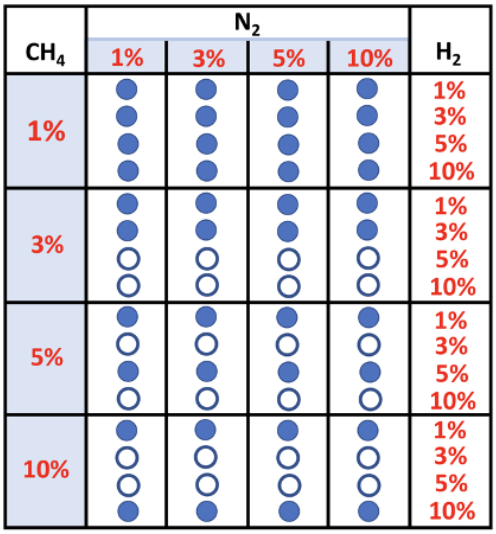

Figure 3.1: Summary of the 40 atmospheric compositions we consider. CH_4 composition is indexed on the left (blocks of four rows), H_2 on the right (one value per row), and N_2 by each column. Composition combinations that are considered are shown by filled (blue) circles, and those not considered are shown by open (white) circles.

photochemistry with geochemical sources, and Wordsworth, Kalugina, et al. (2017) finds that mixing ratios <10% are able to sufficiently warm early Mars to sustain transient surface liquid water. Wordsworth, Kalugina, et al. (2017) notes that the mixed CO_2-CH_4-H_2 composition would likely persist over timescales of 100,000s years, which is long enough to explain the formation of deposits in Gale crater (Grotzinger et al., 2015) and agrees with the timescale estimated by some valley network formation models if a high discharge frequency is assumed (Rosenberg et al., 2015). We caution the reader that the abundance of nitrogen in early Mars' atmosphere remains poorly constrained, and in the discussion section we outline future steps that may be taken to improve this understanding. Note that isotopic fractionation of nitrogen implies a greater abundance of N_2 in the early atmosphere, but few constraints have been made regarding the abundance of nitrogen in the early Mars atmosphere.

We investigate the production of HCN and nitrogen oxides in a phase space of potential early Mars climates. In Section 2, we compute lightning-induced fluxes of HCN and NO at early Mars. In Section 3, we compute N and $N(^2D)$ flux profiles that Solar Energetic Particle (SEP) events may have yielded at early Mars. In Section 4, we input these fluxes into a photochemistry and transport model to

examine precipitation rates of nitrogen oxide. In Section 5, oceanic concentrations are derived considering loss via hydrolysis and photoreduction, and astrobiological relevance is investigated. In Section 6, we estimate nitrate precipitation to the surface. In Section 7, we discuss future work, and in Section 8 we summarize conclusions.

3.2 Photochemistry due to Lightning at Early Mars

While lightning has not been observed in the present-day Mars to date, extraterrestrial lightning associated with water clouds has been observed at Jupiter and Saturn, and lightning attributed to sulfuric acid clouds has been observed at Venus. A warm early Mars climate likely held more water in its atmosphere, supporting the assumption that lightning may have been active. Lightning is sufficiently energetic to split the triple bond of N_2, thereby transforming N_2 into a form which can be metabolized by most organisms. Here, we calculate a theoretical lightning flash rate in Section 2.1, which is used in Section 2.2 to compute the associated production flux of NO and HCN in the lower atmosphere.

Parametrizing the Lightning Flash Rate on Early Mars

We adopt the parametrization for the lightning flash rate, F, from Romps et al. (2014):

$$F = \frac{\eta}{E} \cdot CAPE \cdot P \tag{3.1}$$

where η is a dimensionless parameter that describes the efficiency of lightning discharge energy, E is the energy released per flash, P is the precipitation rate per unit area, and $CAPE$ is the convective available potential energy. CAPE quantifies the convective instability of the atmosphere by measuring the maximum kinetic energy that an ascending air parcel can gain during convection. Larger CAPE gives rise to higher ascending velocity in a convective zone. Although Romps et al. (2014) did not propose a specific charging mechanism, they identified a correlation between higher updraft speeds and higher flash rates. We adopt the coefficient value, $/E$, from Romps, Seeley, et al. (2014) of $1.3x10^{-11}J^{-1}$. The parametrization of $CAPEP$ describes the maximum change in kinetic energy that water droplets in an ascending parcel of air may undergo. Note that we presently lack a thorough analysis of lightning on the scale of comparative planetology; we acknowledge this parametrization was originally derived over a localized region in the context of only terrestrial data (Romps, Seeley, et al., 2014). We discuss these assumptions in Section 6.1.

We use the 3-D general circulation model (GCM) results of Wordsworth, Kerber, et al. (2015) to inform P and CAPE. Wordsworth, Kerber, et al. (2015) applied the Laboratorie de Meterologie Dynamique GCM in a transient warm, wet climate, which was likely applicable on transient timescales. The horizontal resolution of the GCM is 3.75° in latitude by 5.625° in longitude, corresponding to a grid dimension of 220 km by 330 km at the equator and 220 km by 165 km at 60° latitude. In a 1 bar CO_2 atmosphere, the H_2O mixing ratio was governed by the moist convection scheme and a grey-gas absorber was used to alter the broadband IR opacity in order to warm the surface temperature to 300 K. Surface topography 2.54 km below the geoid was considered to comprise a potential transient northern ocean (Wordsworth, Kerber, et al., 2015; Di Achille and Hynek, 2010).

We compute CAPE based on the GCM-simulated atmosphere of early Mars. We note that the concept of CAPE has been applied extensively extraterrestrially, including to the present-day Mars atmosphere (e.g., Colaprete and O. B. Toon, 2003; Hu, Cahoy, and Zuber, 2012). Physically, CAPE is determined by the abundance of moisture at the surface and the vertical profile of atmospheric temperature. In our calculation, for each grid point at each timestep in the course of the GCM simulation, an arbitrary air parcel is lifted from the surface, as defined by the initial properties of surface temperature, pressure, and specific humidity. As the air parcel ascends, the evolution of its temperature follows the dry adiabatic lapse rate ($\Gamma_d = g/c_p$, where g is the gravitational acceleration and c_p is the specific heat capacity of CO_2, assumed constant at $744 J kg^{-1} K^{-1}$) before saturation. After saturation is reached, the temperature profile follows the moist adiabatic lapse rate. We assume a clean atmosphere free of ice nuclei, requiring that nucleation can only happen homogeneously. Note that heterogeneous nucleation, allowing the phase transition from water vapor to water ice, would release more latent heat than homogeneous nucleation, further warming up the air parcel, and making CAPE larger. Accordingly, the condensate is assumed to be liquid water if the parcel temperature is above -38°C; it is assumed to be water ice if the parcel temperature is below this temperature threshold, which is the highest temperature at which homogeneous nucleation takes place. This assumption provides a lower bound of the estimated CAPE.

We derive a global mean value of 5179 J/kg, which is 1 order of magnitude larger than typical values for the terrestrial atmosphere (Romps, Seeley, et al., 2014) and more than two orders of magnitude greater than that on the present-day Mars

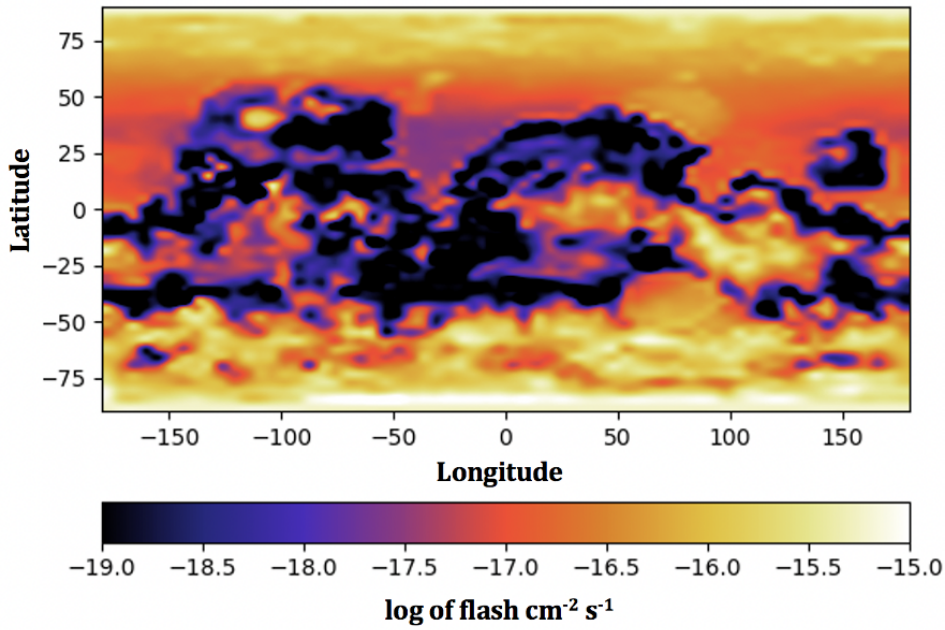

Figure 3.2: Annual mean lightning flash rate (log-scale, flash $cm^{-2}s^{-1}$) in a warm, wet, early Mars climate, assuming a global northern ocean for topography at an altitude of -2.54 km. Despite significant temporal variability (not shown here), we show the annual mean here since we seek to model the average early Mars environment in this work. This figure has been interpolated from the 64x49 grid of the GCM presented in Wordsworth, Kerber, et al. (2015).

during polar night (Hu, Cahoy, and Zuber, 2012). Analytical terrestrial estimations demonstrate that CAPE increases in direct response to higher surface temperatures (Romps, Charn, et al., 2016), and the 30 K warmer surface temperature of this GCM (313 K) compared to the terrestrial global mean temperature is a likely contributor to the larger global mean CAPE. CAPE is generally larger over the northern ocean than surface topography (by a factor of 2), consistent with the terrestrial trends identified in Romps, Charn, et al. (2016).

The precipitation rates exhibit significant temporal variability but are on average larger by factors of 10 and 5 at the northern and southern poles, respectively, in comparison to the mid-to-low latitude regions ($< |60^o|$). The global mean flash rate is considered in the later calculations in this paper, and we derive a value of $5.2x10^{-17}$ flash $cm^{-2}s^{-1}$ (for details regarding this derivation please refer to Appendix 4), which is comparable to the present-day terrestrial rate and early earth rate (as determined by the Generic LMDZ 3D global climate model; (Wong, Charnay, et al., 2017)). The derived lightning flash rate also exhibits large temporal

variability due to the effect of the precipitation rate. The annual mean flash rate is demonstrated in Figure 3.1, with larger values over the poles (explained by high precipitation rates) and more frequent mid-latitude ($30 - 50^o$) flashes in the north due to the larger CAPE over the northern oceans.

Nitrogen Fixation via Lightning

Lightning is known to have profound local effects on atmospheric chemistry. During a lightning flash, the current-carrying channel is heated to 3x104 K, and UV radiative photodissociation produces radicals and complex chemistry in the vicinity of the channel. The shock wave associated with thermal expansion of the gas yields overpressures that drive the shock outward, heating surrounding gas to several thousand kelvin. At these temperatures, the atmospheric constituents are broken into radicals which recombine to form molecules stable at temperatures of several thousand kelvin, such as NO_x and HCN for early Mars. The gas cools at $10^6 K/s$, and the cool atmospheric temperature quenches the gas composition out of equilibrium, but the compositions remain nearly frozen in since the reactions involved in driving the atmosphere back to equilibrium are kinetically inhibited (e.g., Desch et al., 2002, and references therein).

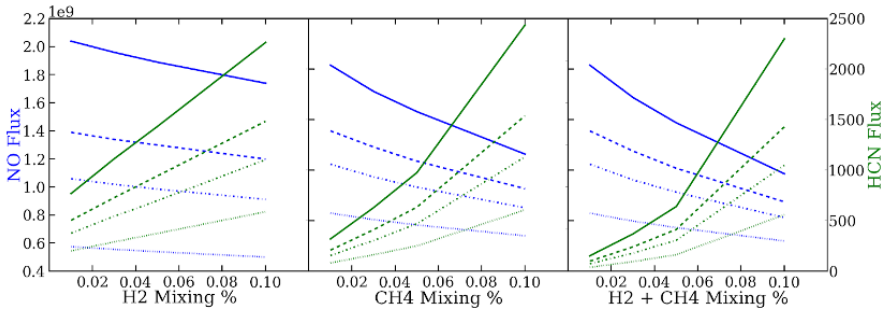

Figure 3.3: Lightning-induced fluxes of NO (blue) and HCN (green) (molecules $cm^{-2}s^{-1}$) produced by lightning in a CO_2 background atmosphere with varied amounts of N_2 (1% dotted; 3% dot-dash; 5% dash; 10% solid), H_2 (1-10% x-axis of A + C), and CH_4 (1-10% x-axis of B + C). In panels (a) and (b), CH_4 and H_2 (respectively) are fixed at 1%. While the molecular fluxes respond to atmospheric composition, all cases vary by less than one order of magnitude.

We calculate the NO and HCN mixing ratios from local thermodynamic equilibrium in the presence of lightning (approximated as 2000 K) using the Chemical Equilibrium and Applications program (McBride and S. Gordon, 1996). In the potential early climates considered, we find that lightning yields fluxes of NO and HCN

of 10^9 molecules $cm^{-2}s^{-1}$ and 10^3 molecules $cm^{-2}s^{-1}$ (as shown in Figure 3.2). The former is comparable to the fluxes of NO on early Earth estimated by Wong, Charnay, et al. (2017) and James F. Kasting, Holland, and Pinto (1985), and may have profound astrobiological implications, which we investigate further in Section 4 when considering precipitation rates.

The NO flux is found to decrease when the abundances of reduced species are increased, while the HCN flux is found to increase due to the more reduced state, as shown in Figure 3.2. Notice that neither flux varies by orders of magnitude; these are small variations that would likely not significantly affect the habitability of early Mars in the greater scheme of current uncertainties.

3.3 Dissociation of N_2 by Solar Energetic Particle Events

We use the simulation platform Geant4 (e.g., Agostinelli et al., 2003) to approximate the response of the Martian atmosphere to a coronal mass ejection (CME) and the associated SEP events. The planetary surface is represented by a uniform non-magnetized sphere with radius 3400 km composed of only iron for simplicity with an STP density of 7.9 gcm^{-3}. The atmosphere is represented by a grid of 66 altitude layers extending to 110 km composed of pure CO_2. Below 60 km, the atmospheric temperature and eddy diffusivity (Kzz) profiles are informed by the GCM output. At higher altitudes, the temperature profile is assumed isothermal and the Kzz profile is calculated following the methods of Ackerman and Marley (2001). These profiles are also used to inform the photochemical model that follows in Section 5, which is where they are shown in Fig. 3.4. We subject the Mars atmosphere to an isotropic distribution of particles with energies ranging from 10 MeV to 10 GeV. The energy for each particle was assigned randomly, with an algorithm designed to create a logarithmically uniform distribution. Particles are sourced from a sphere enclosing both Mars and its atmosphere; we ran two simulations with spheres of different radii, 3250 and 5280 km, to validate that the result was independent of the arbitrary value selected. We record the initial energy of each particle and resulting energy deposited at each altitude layer. We binned the data by initial energy in logarithmic increments of 0.025 (40 bins per order of magnitude) for 120 bins ranging from 10 MeV to 10 GeV, and we obtain the average deposit on a 120x66 grid over energy and altitude. We calculated the energy deposit geometric factor matrix (units of MeV cm2 ster) by multiplying this energy deposit matrix by $4\pi^2r^2$ (where r is the radius of the spherical particle source). We multiplied this with the flux distribution to obtain a total energy deposit rate (MeV/sec) at each altitude. For our simulated event, we

used the differential flux from the October 29, 2003 CME event as displayed in Figure 3.5 of Mewaldt et al. (2012). The data from the figure was extrapolated out to 6 GeV, assuming the linear log-log relation shown in the figure, and we assume zero flux for energies greater than 6 GeV. The differential flux was converted to an actual flux and run through our atmospheric response matrix in order to obtain the energy deposit at each altitude. This describes the theoretical response of the Martian atmosphere to the October 29, 2003 event.

The frequency of CMEs from the young Sun and other active stars has been estimated from their association with solar/stellar flares. SOHO/LASCO and STEREO observations show strong association of energetic and fast (>1000 km/s) CMEs with powerful solar flares. Empirical correlations for present solar events allow CME occurrence frequencies to be estimated from Kepler observations of the frequency of stellar superflare events at active and young K-G type main sequence stars. Lingam et al. (2018) analyzed this correlation to determine that early Mars may have experienced a few CMEs per day. In this work, we assume, on average, early Mars experienced one event per terrestrial day, each with a duration of 1 terrestrial day.

We compared the energy deposition rate at each altitude layer with the ionization rates of CO_2, the dominant atmospheric constituent, and N_2. We assume a 50:50 branching ratio for the products of N_2 dissociation to yield N and N(2D) in order to derive profiles of N and $N(^2D)$ production rates induced by SEP events, as shown in Fig. 3.3 below.

3.4 Photochemical Production and Precipitation of HNOx and HCN

In order to calculate the equilibrium concentration and rainout of HNOx and HCN, we adapt KINETICS, the Caltech/JPL chemical transport model (e.g., Allen, Yung, and Waters, 1981), to the early Mars environment. Other versions of this model have been validated across numerous planetary bodies, such as Jupiter (e.g., Moses et al., 2005), Titan (e.g., C. Li et al., 2014), and Pluto (e.g., Wong, Yung, and Gladstone, 2015), and a similar model was considered for the early Earth in Wong, Charnay, et al. (2017).

The lightning-induced fluxes for NO and HCN are injected to the lowest atmospheric level, which extends from 0 to 1.4 km. The N and $N(^2D)$ fluxes resulting from SEP events are input as fixed altitude-dependent profiles. We consider the chemistry of 50 species linked by 495 reactions on an altitude grid with 1-2 km spacing, having updated the chemical network to include all 118 reactions consid-

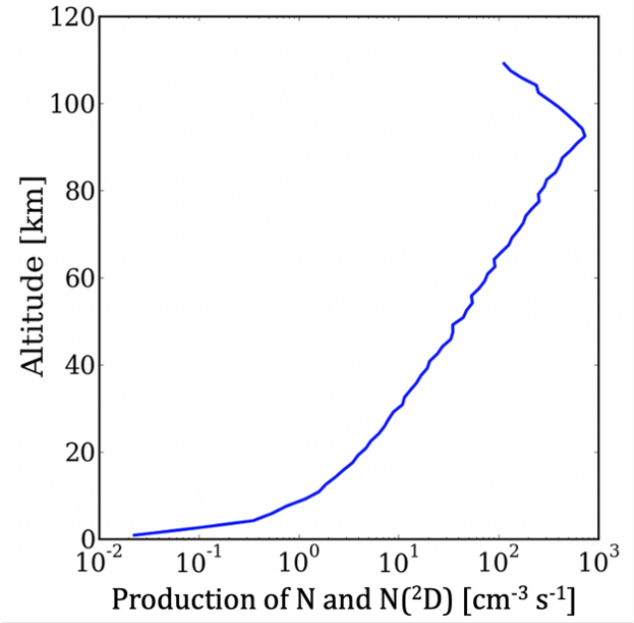

Figure 3.4: N and $N(^2D)$ production rates (atoms $cm^{-3}s^{-1}$) that result from SEP events as a function of altitude, for an atmospheric composition of 10% N_2.

ered by Airapetian (2016), which examined terrestrial nitrogen fixation. The model calculates the chemical production and loss rates at each altitude as well as the diffusive flux between each altitude grid by solving the 1-D continuity equation. We consider a solar spectrum from 4.4 Ga (Claire et al., 2012). For a complete list of chemical reactions and rates, model boundary conditions, and details regarding these equations, we refer the reader to Appendix 1 and 2 respectively.

Below 60 km, the atmospheric temperature and K_zz profiles are informed by the GCM output. At higher altitudes, the temperature profile is assumed isothermal and the K_zz profile is calculated following the methods of Ackerman and Marley (2001). The water vapor concentration is fixed to the saturation vapor pressure. Homogeneous nucleation of water condensation is assumed; please refer to appendix 2. These profiles are shown in Figure 3.4 below.

Our model calculates and outputs chemical abundances for each species at every level. The vertical profiles of photochemically derived NO, NO_2, N_2O, HNO, HNO_3, and HCN in atmospheric compositions of 10% N_2, 1% CH_4 and H_2, and 10% N_2, 10% CH_4 and H_2 are shown in Fig. 3.5.

The resulting precipitation column rates of HNO, HNO_2, HNO_3, HO_2NO_2, and HCN are found to be $10^8, 10^2, 10^6, 10^3, and 10^5$ molecules $cm^{-2}s^{-1}$, respectively.

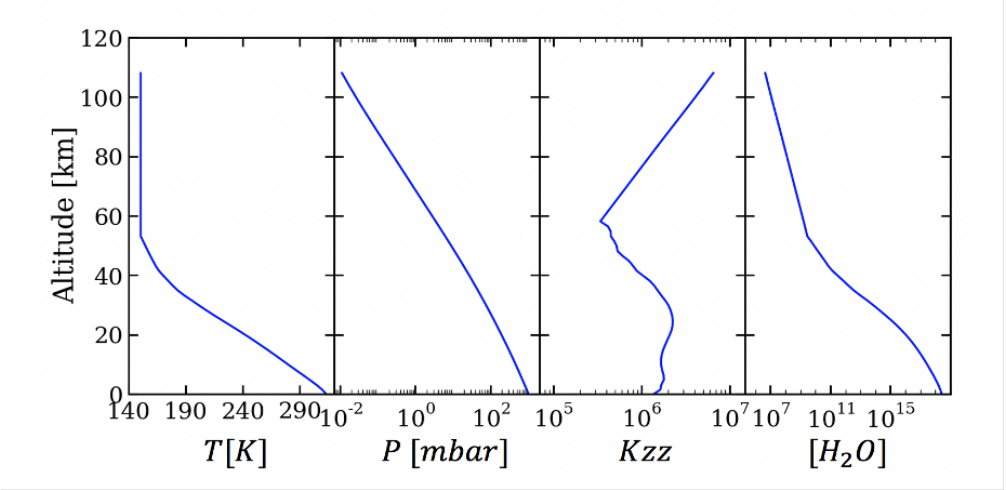

Figure 3.5: (a) Temperature (K), (b) pressure (mbar), (c) eddy diffusion coefficient (cm^2s^{-1}), and (d) water vapor concentration profiles (cm^{-3}) of our model atmosphere. The inversion feature in the K_{zz} profile corresponds to the tropopause, as defined by the temperature profile.

These fluxes also respond to variations in the abundances of H_2 and CH_4, as shown in Figure 3.6. These responses are discussed below, and the photochemical pathways governing such behavior is demonstrated in Figure 3.6.

The precipitation rates of HNO appear to increase as H_2 and N_2 are added to the initial atmospheric abundance. The dominant formation pathway for HNO, summarized in Fig. 3.7, is via NO reacting with HCO, and the latter is a result of $H + CO$. By this process, greater initial abundances of H_2 enhance HCO concentrations, increasing the production rate of HNO. Likewise, greater initial N_2 abundances directly correspond to increased lightning-induced NO fluxes (as shown in Fig. 3.2), and therefore also increase the HNO production rate.

HNO_3 is dominantly formed via NO reacting with HO_2, and therefore displays similar trends in N_2 abundances. However, production of HNO_3 decreases as the initial abundance of reduced gases is increased. Atmospheres with high abundances of reduced gases yield less O_2, which limits HO_2 (produced via $HCO + O_2$) and hence the formation of HNO_3. We note an additional formation mechanism via N_2O5 reacting on atmospheric ice particles; this formation mechanism dominantly occurs at night, although this can only be done in a future model that includes diurnal variation.

HNO_2 and HO_2NO_2 are both formed via NO_2 reacting with HO_2, as shown in

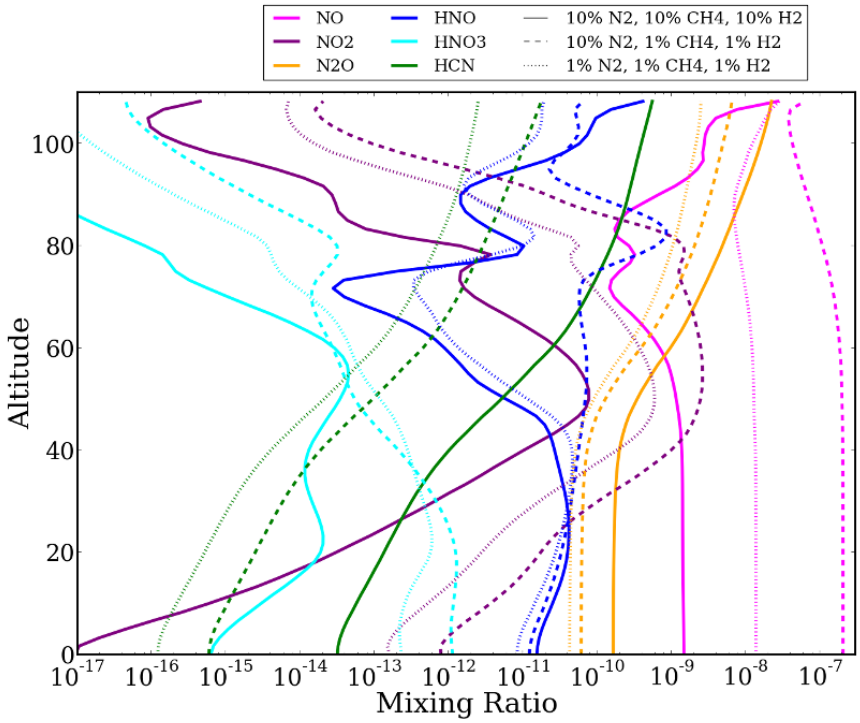

Figure 3.6: Mixing ratio profiles of NO (pink), NO2 (purple), N_2O (yellow), HNO (blue), HNO3 (cyan), and HCN (green) in two atmospheric compositions: 10% N_2, 10% CH_4, 10% H_2 (dashed) and 10% N_2, 1% CH_4, 1% H_2 (solid).

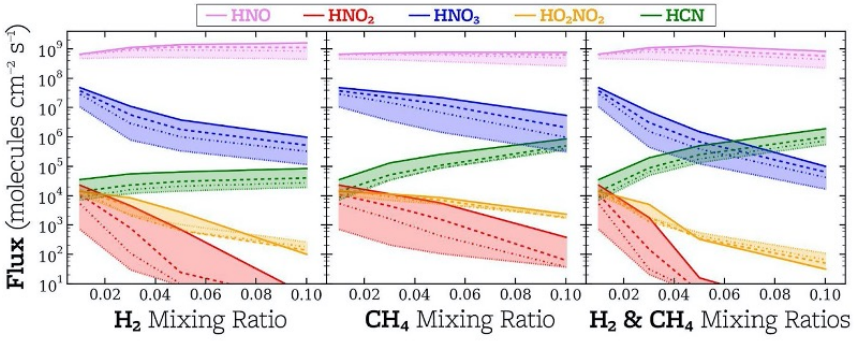

Figure 3.7: Precipitation rates (fluxes) of HNO, HNO_2, HNO_3, and HCN (molecules $cm^{-2}s^{-1}$) (shown in pink, red, blue, and green, respectively) in atmospheres with varying mixing ratios of H_2 (a), CH_4 (b), and $H_2 + CH_4$ (c). In panels (a) and (b), CH_4 and H_2 (respectively) are fixed at 1%. In all panels N_2 is varied as the line style: 1% (dots), 3%(dot-dash), 5% (dashes), and 10% (solid line). 1 bar atmosphere is considered with a background composition of CO_2.

Fig. 3.7. From Fig. 3.6, it is apparent that the production of both decreases in the presence of reduced gases, though the magnitude of this behavior depends on the presence of N_2. HO_2 again behaves as a limiting reactant in the presence of high reduced gas abundances, as in the formation of HNO_3. But an important N_2 dependence is that HCO may form either HNO (in the high-N_2 regime) or HO2 by reacting with $O2$. Hence in high N_2 atmospheres, NO is readily abundant, and HCO is lost to HNO rainout, making HO_2 further limited. Hence, the abundance of NO affects the slope at which the reduced gas abundance decreases HO2 production and thereby the production rate of HNO_2 and HO_2NO_2.

HCN increases by 1 order of magnitude within the N_2 range considered. HCN is formed dominantly via H_2CN, which is created from atomic N reacting with the methyl radical. CH3 is a result of $N(2D)$ reacting with methane. (Recall that both N and $N(^2D)$ are products of N_2 dissociation via solar events.) This mechanism is summarized in Fig. 3.7. The production rate of HCN therefore depends on the concentrations of both N and $N(^2D)$, yielding an increased dependence on initial N_2 abundance. The inclusion of SEP events results in a factor of 2 increase in HCN production.

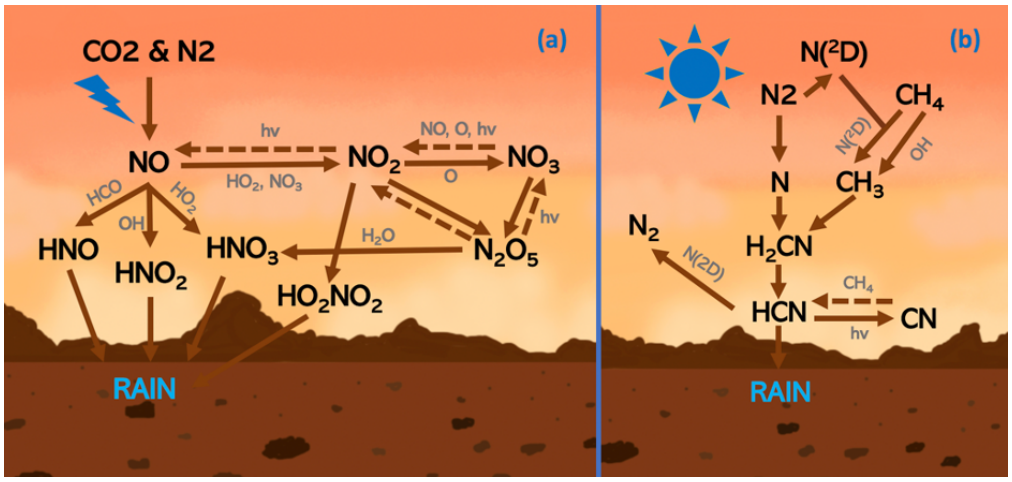

Figure 3.8: Photochemical pathways describing (a) the production of HNO_x and (b) the production and loss of HCN. HNO_x is produced mainly by oxidizing lightning-induced NO, and HCN is produced mainly through radicals, including N and CH_3, that result from SEP events.

3.5 Oceanic Concentrations and Astrobiological Implications

To assess the possibility of whether nitrate and nitrite may have acted as high potential electron acceptors, we solve for the equilibrium concentration of nitrate

in a putative global northern ocean. The putative northern ocean is motivated by a shoreline of deltaic deposits north of the dichotomy boundary (Di Achille and Hynek, 2010). We consider photoreduction (Ranjan et al., 2019) and hydrolysis (Miyakawa, James Cleaves, and Miller, 2002) as dominant loss mechanisms of nitrate and cyanide respectively; we compare this nitrate loss to the assumption of hydrothermal vent circulation dominating nitrate loss (e.g., Wong, Charnay, et al., 2017). After raining out, HNO is of great interest due to the relatively high rainout rates computed. It has been suggested that via the following aqueous reactions, HNO will likely produce nitrate and nitrite (Summers and Khare, 2007):

$$HNO \rightarrow H^+ + NO^-$$

$$NO^- + NO \rightarrow N_2O_2^-$$

$$N_2O_2^- + NO \rightarrow N_3O_3^-$$

$$N_xO_x^- \rightarrow NO_3^- + NO_2^- + N_2O$$

HNO_2 and HNO_3 will dissociate into H^+ and NO_2^- or NO_3^- respectively, and HO_2NO_2 will deoxygenate rapidly to produce nitrite and O_2. Hu and Diaz (2019) analyzed the kinetic rates of aqueous-phase chemistry and determined that the mechanism above should be inefficient in Archean Earth's ocean. Here, we adopt the former mechanism of Summers and Khare (2007) for early Mars and discuss its impact on our results in Section 6.

HCN can be destroyed via hydrolysis, and the first product would be formamide. The stability of formamide has not been exhaustively studied, but it is a potential solvent for prebiotic reactions it can be concentrated and is itself a prebiotic reagent. However, the consideration of this specie is beyond the scope of our work. We fit the laboratory hydrolysis rates of Miyakawa, James Cleaves, and Miller (2002) to an Arrhenius equation to find a hydrolysis kinetic rate of $2.265x10^{-12}$ molec $cm^{-2}s^{-1}$, which corresponds to a temperature of 273 K.

Intense heating (to nearly 700 K) as ocean water circulates through acidic hydrothermal vents would have acted as a significant loss process. Heterogeneous distributions of zinc and gypsum veins suggest aqueous alteration via impact generated hydrothermal vents in the terrains of early Mars (e.g., Squyres et al., 2012). At these high temperatures, iron minerals within the crusts would have reduced nitrate and nitrite to N_2. Additional reduction via cooler serpentinization-driven alkaline springs may have likely yielded ammonia, adding alkaline vents to the loss as well

(A. D. Gordon et al., 2013). To consider hydrothermal vent circulation alone, we derive resulting oceanic concentrations, following the methods of Wong, Charnay, et al. (2017), as:

$$C = \frac{f_{atm} A_M \tau_{HTV}}{V_{ocean}} \tag{3.2}$$

where f_{atm} is the HNO_x flux from the atmosphere (molecules $cm^{-2}s^{-1}$), A_M is the area of Mars, τ_{HTV} is the timescale for cycling through high-temperature vents, and V_{ocean} is the volume of the northern ocean, which we approximate in our work as the full northern hemisphere. Notice that $\tau_{HTV} = V_{ocean}/F_{HTV}$, where F_{HTV} is the mass flux of water through high-temperature hydrothermal vents for which we adopt the current terrestrial water mass flux from high-temperature vents, 7.210^12 kg/year. The equilibrium concentration may then be expressed as:

$$C = \frac{f_{atm} A_M}{F_{HTV}} \tag{3.3}$$

With hydrothermal vent circulation acting as the only source of nitrate destruction in early surface waters, concentrations of $0.001 - 0.01M$ nitrate are found, which is slightly lower than the concentration expected at early earth of 0.024 M under this same assumption (Wong, Charnay, et al., 2017).

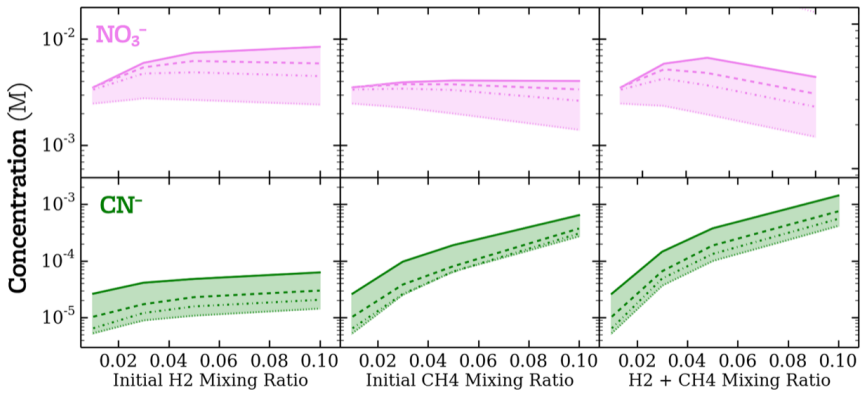

Figure 3.9: Concentrations of nitrate (top) and cyanide (bottom) assuming hydrothermal vent circulation as the only loss mechanism for both species (as in Wong et al., 2017). The following are varied from 1-10%: (a) H_2, (b) CH_4, and (c) both H_2 and CH_4. In panels (a) and (b), CH_4 and H_2 (respectively) are fixed at 1%. In all panels N_2 is varied as the line style: 1% (dots), 3% (dot-dash), 5% (dashes), and 10% (solid line). 1 bar atmosphere of background CO_2 is considered.

However, the concentration expressed in eq. 5 would overestimate the concentration of nitrate, which undergoes further destruction in surface waters. We therefore also incorporate photodestruction in order to compute a concentration of nitrate in surface waters. Photolysis by UV radiation reduces nitrate to nitrite and nitrite to gaseous NO, which may directly escape to the atmosphere or become reduced to N_2O before escaping (e.g., Ranjan et al., 2019):

$$NO_3^- + hv \rightarrow NO_2^- + 1/2O_2$$
$$NO_2^- + H_2O + hv \rightarrow NO + OH + OH^-$$

These processes have been measured in present-day terrestrial oceans to have median rate constants of $k_{NO_3^-}$, $hv = 2.3x10^{-8}\ s - 1$ and $k_{NO_2^-}$, $hv = 1.2x10^{-6}s^{-1}$ for nitrate and nitrite respectively (Mack and Bolton, 1999). Although OH may oxidize nitrite to nitrate, nitrite is lost with 20-100% efficiency in the presence of bicarbonate, Br^-, and other OH scavengers (e.g., Zafiriou and True, 1979). We assume surface water temperatures of 273 K, and we note that the photolysis rates increase by a factor of up to 4 had we assumed a temperature up to 50 K greater (Ranjan et al., 2019). Further, we acknowledge that the incident solar flux at the early Mars surface would differ from that at present-day earth, attributed to both the change in solar spectrum over time and the different atmospheric optical depths due to the two differing compositions. To account for this, we use a KINETICS output adapted to present-day Earth (K.-F. Li et al., 2017) to compare the two incident fluxes between 200 and 400 nm (the dominant wavelengths that contribute to photoreduction). Early Mars, accounting for the faint young sun and attenuation through an atmosphere of different optical depth, is found to experience a flux that is 27.2x greater than present-day Earth, and we linearly scale the rates above. Hence, we consider the following rate constants for our calculation: $k_{NO_3^-}$, $hv = 6.26x10^{-7}s^{-1}$ and $k_{NO_2^-}$,hv = $3.26x10^{-5}s^{-1}$.

We find nitrate and cyanide concentration values of $0.1 - 2nM$ and $0.01 - 2mM$ (respectively) in a putative northern ocean at early Mars. Note that despite a much less efficient rainout of HCN compared to HNO_x, the slower loss mechanism (or, the lack of photodestruction) generally allows a greater concentration of cyanide in the surface waters than nitrate. For both species, the variation attributed to the different atmospheric compositions considered are linearly comparable to the rainout fluxes shown in Figure 3.8, and are again due to the photochemical processes described in Section 4.

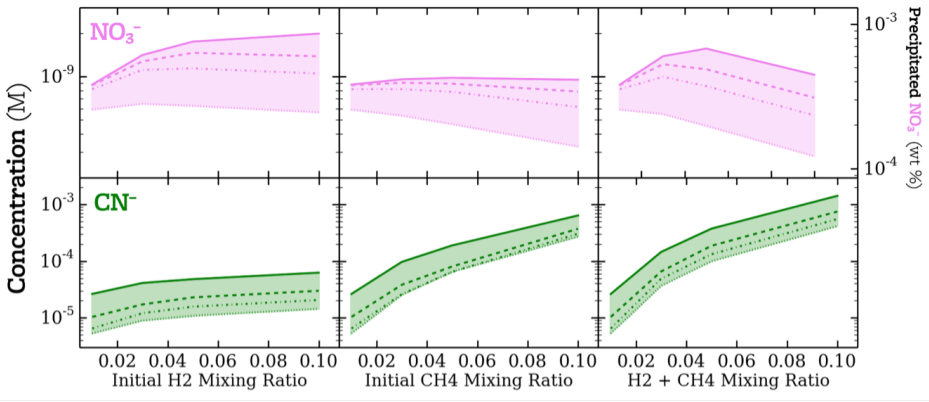

Figure 3.10: Concentrations of CN- (green) and NO3- (pink) in oceans are shown (y-axis) are compared across varied atmospheric compositions (x-axis, linestyle). The following are varied from 1-10%: (a) H_2, (b) CH_4, and (c) both H_2 and CH_4. In panels (a) and (b), CH_4 and H_2 (respectively) are fixed at 1%. In all panels N_2 is varied as the line style: 1% (dots), 3% (dot-dash), 5% (dashes), and 10% (solid line). 1 bar atmosphere of background CO_2 is considered.

Recall from Section 1 that NO3- and HCN may have been astrobiologically relevant in concentrations of 1 μmol and 0.01 mol respectively. Both concentrations derived in our model are significantly more dilute. It is likely that secondary concentrating processes of HCN would be required for the production of adenine or amino acids, as expected by previous terrestrial work (e.g., Holm and Neubeck, 2009). We suggest that future work, particularly laboratory experiments, could investigate the relevance of more dilute nitrate concentrations in scenarios thought to be important to the onset of metabolism. Future studies may also draw comparisons with the nitrate-deposits identified previously by the MSL (Stern et al., 2015; Sutter et al., 2017).

3.6 Estimating Nitrate Precipitation

We next consider what these results imply about expected concentrations of nitrate in the martian regolith. We assume salts would precipitate to the surface from the acids after evaporation of surface waters, likely during the Amazonian eon, and we make several assumptions to calculate the concentration of salts that would have deposited. The concentration of acids can be expressed in terms of column mass of nitrate per unit surface area, spread over the northern hemisphere in the putative northern ocean assumed throughout this paper. We assume the nitrates would have deposited in the first 2 meters of the Mars soil, which is the mean of three e-folding depths of the 0.51-0.85m 1/e mixing depths that small post-Noachian impactors

would have churned the soil (Zent, 1998). We assume a soil density of 1 g/cc (Moore and Bruce M. Jakosky, 1989).

We compute the weight percent of nitrate precipitates that may have formed in each climate composition considered, and we find values between 1-8x10^{-4} weight percent. The nitrate precipitation concentrations demonstrate a similar response to climate composition as the formerly presented aqueous concentrations, since the response of both are determined by the response of the rainout fluxes to the atmospheric composition.

Sutter et al. (2017) measured present-day surface nitrate abundances of 0.002 to 0.05 weight percent, and Stern et al. (2015) measured 70-260 and 330-1100 ppm. The largest range of values from our model thus agree with the lowest range measured by Stern et al. (2015), and are a factor of two from the lowest range in Sutter et al. (2017). The best match is represented by an atmospheric composition rich in hydrogen, or by a moderate (3% each) combination of hydrogen and methane in the atmosphere.

We compute salt precipitation directly from the equilibrium oceanic acid concentrations, but this assumption neglects the following processes. First, photoreduction of aqueous nitrates is efficient only above the photic depth, which we define to be two thirds of the present-day terrestrial photic depth at the equator of 5m (the scaling to average over latitude). Evaporation would not be instantaneous, and once water evaporates to be shallower than the photic depth, acids may be more concentrated in this near-surface layer. In this case, photoreduction would become more efficient, decreasing the amount of nitrate precipitation that would form on the surface. Second, since evaporation would not be instantaneous, assuming the entire northern hemisphere as the depositing surface area may be an overestimate. In the absence of an ocean (eg, ponds), photodestruction would be more efficient (since they would be shallower), but the surface area of deposition would decrease. Third, in the early case of a deep ocean, nitrates may either react with dissolved cations to sink and precipitate to the ocean floor. Similarly, if nitrates were involved in biologic processes, the death of oceanic creatures would also result in the sinking and deposition of nitrate-bearing compounds to the ocean floor. The sinking and burial of nitrates would protect them from photoreduction, decreasing the efficiency of loss and thus increasing the concentration of surface precipitates.

3.7 Discussion

Parametrizing Lightning on Global Scales across Comparative Planetology

Romps, Seeley, et al. (2014) derived Eq. 1 as an approximation to estimate lightning over the United States (a localized region), and deviations within an order of magnitude are known to exist over the continents versus oceans (Romps, Charn, et al., 2016). We acknowledge that this parametrization lacks mechanistic underpinnings, while the true flash rate may depend on the atmospheric scale height, atmospheric constituents, the presence/absence of a mixed-phase region in the deep convection, and the gravitational constant through its impact on particle fall speeds. Some of these parameters (scale height, constituents, and surface gravity) are included in the GCM and may be captured by the dependence of F on CAPE and P. This parametrization has been used in previous works regarding early Earth (Wong, Charnay, et al., 2017). We solve for CAPE and P directly, and we assume E is comparable to that of present day Earth noting that the electrostatic breakdown field is thought to not vary strongly with the local composition of the gas (Helling et al., 2013). However, the constant η in eq. 1 is likely not a best fit on global scales at other worlds, which makes the scaling relation in this parametrization likely valid only to an order of magnitude; η is not physically motivated but is a best fit parameter (Romps, Seeley, et al., 2014) and therefore the uncertainty in applying this relation to other worlds is large (David Romps, private communication). Since no constraints can be made to date, we accept the parametrization and suggest future work investigate parametrizing lightning globally on other worlds.

In calculating the lightning flash rate, we obtain the precipitation rate and derive CAPE from GCM outputs of Wordsworth, Kerber, et al. (2015), which considered a 1 bar CO_2 atmosphere with a grey-gas absorber to explain a fairly high surface temperature of 300 K. A grey-gas absorber cannot be considered in kinetics models, but the reducing gases we consider (1-10% H_2 and CH_4, which are excluded from the GCM) have a similar warming effect due to collision-induced-absorption (Wordsworth et al., 2017). We also consider 1-10% abundances of N_2, though no N_2 was considered in the GCM. Despite the exclusion of trace gases from the GCM, since the bulk composition (CO_2) is the same in both the GCM and our models, we expect that our model set up is not far from self-consistent, and uncertainties from the small difference are likely small.

It is necessary to note that results of CAPE calculation depend on the convection scheme in the GCM, and the LMD GCM in this study only employs a simple

convection scheme as described in Manabe and Strickler (1964), in which convective adjustments are applied where the radiation-determined temperature profiles are convectively unstable. Therefore, we interpret the CAPE results in this study as an order-of-magnitude estimate. Future studies with more realistic GCM simulations using mesoscale models such as PlanetWRF (Richardson, Toigo, and Newman, 2007) need to be conducted to provide a more accurate estimate of CAPE on early Mars and validate the conclusions in the present study.

Fixed Nitrogen in Surface Waters

In addition to surface delivery via rainout, Hu and Diaz (2019) calculated nitrate deposition by considering aqueous chemistry in the ocean and atmosphere–ocean equilibrium. This work derives a flux of nitrate deposition comparable to that in Wong, Charnay, et al. (2017) but demonstrates that oceanic feedback to the gaseous deposition will remove HNO prior to the formation of nitrates. Hence, our oceanic concentrations are likely upper limits for the derived nitrate flux into surface waters. We intend for future work to incorporate the feedback mechanism of Hu and Diaz (2019) to determine its impact on early Mars' nitrate formation.

Nitrate reduction by reactions with iron (e.g., Buchwald et al., 2016), have been identified as an additional loss mechanism. The neglection of this loss is motivated by present-day terrestrial measurements, in which dissolved ferrous iron is able to circulate thousands of kilometers from hydrothermal vent sites, in the presence of abundant nitrate and nitrite (Fitzsimmons, Boyle, and Jenkins, 2014). Further, Ranjan et al. (2019) examined the relevance of this loss in the context of hydrothermal vent circulation and photoreduction; the reaction rates for reduction by iron are poorly constrained and yield uncertainties of >8 orders of magnitude, and the mechanism would only change our result should it be faster than photoreduction. We suggest future lab work constrain these reaction rates to improve uncertainties.

Cyanide in surface waters would likely also react with iron to form ferrocyanic salts. Toner and Catling (2019) investigated the fate of varied fixed partial pressures of atmospheric HCN gas (ignoring rainout to aqueously deliver cyanide). They found that ferrocyanic salts would form from gaseous HCN reacting with surface iron, and subsequent thermal decomposition of the salts would release cyanide to the waters in equilibrium. We deem an aqueous chemistry model is beyond the scope of this work, but we predict that aqueously delivered cyanide to early Mars surface waters would lead to an equilibrium composition of both aqueous cyanide and ferrocyanic

salts.

Throughout this work, we assume a putative northern ocean at early Mars. While some evidence has been explored (e.g., Di Achille and Hynek, 2010), the presence of an ancient ocean is still highly uncertain and debated (e.g., Palumbo and James W. Head, 2018). Surface lakes and/or ponds are a plausible scenario (e.g., Grotzinger et al., 2015); however, investigating fixed nitrogen concentrations in smaller bodies of water would require some estimate of the fraction of early Mars' surface area covered by this water (which presently is poorly constrained). HCN hydrolysis is not sensitive to depth, and would approximately be homogeneous throughout any body of water (although the rate of destruction would respond to water pH, (Miyakawa, James Cleaves, and Miller, 2002). Hence, the concentration of HCN in small bodies of water would inversely scale with the total volume of surface water across the planet. Photoreduction of NOx is sensitive to depth, and primarily only occurs above a photic depth of 100s cm. Hence, destruction of nitrates would be more rapid in small ponds, yielding a more dilute concentration (e.g., Ranjan et al., 2019). However, for both species, the catchment area feeding into a lake/pond would introduce significant uncertainty, as would weather, mineralogy, and proximity to a volcano. Hence, it is difficult to model such systems using global models such as ours.

3.8 Conclusions

The nitrogen cycle remains one of the long-standing questions regarding early Mars habitability and has strong ties to profound astrobiological implications. We estimated NO and HCN lightning-induced fluxes of 10^9 and 10^3 $cm^{-2}s^{-1}$ respectively, by computing thermochemical equilibrium with Chemical Equilibrium with Applications in regions of lighting, parametrized following the methods of Romps et al. (2014). We computed N and $N(^2D)$ flux profiles (peaking nearly at $10^3 cm^{-3}s^{-1}$) yielded by solar energetic particle events with a Geant4 simulation platform. Using KINETICS (the Caltech/JPL model that considers photochemistry and transport), we derived precipitation rates of HNOx and HCN (of 10^9 and 10^5 respectively). In a putative northern ocean at early Mars, assuming loss via hydrothermal vent circulation we find concentrations of 3-20 mM nitrate and 0.01-2 mM cyanide, and assuming nitrate loss via photodestruction we find nitrate concentrations of 0.1-2 nM. We suggest future work investigate the astrobiological relevance of these concentrations. Following the evaporation of surface waters, these acids may have precipitated out as salts which would correspond to precipitates of $1 - 8x10^{-4}$

weight percent.

3.9 Appendix 1: KINETICS Model

We assume an upper boundary condition flux of 0 for all species, except for N and N(2D), whose downward traveling fluxes at the upper boundary are determined from these SEP events as $-1.6x10^9$ molecules $cm^{-2}s^{-1}$. At the lower boundary, a zero flux is considered for $O, O(^1D), H, OH, HO_2, N, N(^2D), NO_2, NO_3, N_2O_5, C, CH, {}^1CH$, CH_2, CH_3, C_2H, C_2H_3, andC_2H_5; a deposition velocity of $10^{-6}cms^{-1}$ for O2; and a deposition velocity of 10^{-2} for all remaining species. N_2 and CO_2 are considered as fixed species (not solved as time dependent species). This means that the removal of N_2 to form fixed nitrogen species is replenished to maintain the N_2 profile constant overtime. The column concentration of fixed nitrogen is 7 orders of magnitude smaller than the column concentration of N_2, and the column rainout rate of fixed nitrogen of 10^9 molecules $cm^{-2}s^{-1}$ (dominated by HNO) corresponds to a loss over 100,000 years of 3e21 molecules cm^{-2}, which is only 1 ppt of the total N_2 budget. While the outgassing rate of N_2 is widely unknown for early Mars, even in the case of no outgassing, the assumption to resupply the N_2 budget does not notably affect our result.

We use a fixed mixing ratio at the lower boundary condition for H_2 and CH_4, which requires that KINETICS solve for a steady state flux to resupply these species as they are transported or destroyed from the lowest bin:

$$\frac{dn_i}{dt} = P_i - L_i - \frac{\partial \phi_i}{\phi z} \tag{3.4}$$

where n_i is the number density of species i, ϕ_i the vertical flux, P_i the chemical production rate, and L_i the chemical loss rate, all evaluated at time t and altitude z. The vertical flux is given by:

$$\phi_i = -D_i(\frac{\partial n_i}{\partial z} + \frac{n_i}{H_i} + \frac{1-\alpha_i}{T}\frac{\partial T}{\partial z}n) - K(\frac{\partial n_i}{\partial z}\frac{n_i}{H_i} + \frac{1}{T}\frac{\partial T}{\partial z}n) \tag{3.5}$$

where D_i is the species' molecular diffusion coefficient, H_i the species' scale height, H_{atm} the atmospheric scale height, α_i the thermal diffusion parameter, Kzz the vertical eddy diffusion coefficient, and T the temperature Yung and DeMore (1999). The flux consists of two parts: (1) molecular diffusion which can be derived from the molecular theory of ideal gases and (2) eddy transport. We calculate the eddy diffusion coefficient profile by using the formulation in the work of Ackerman and

Marley (2001). A critical difference between the two terms is the scale height: in the isothermal case, molecular diffusion drives the system toward diffusive equilibrium since each species follows its own scale height, H_i, while eddy diffusion drives the system toward a well mixed state since all species follow the bulk atmospheric scale height, H_a.

3.10 Appendix 2: GCM Outputs

Global maps of (top) surface temperature and (b) surface relative humidity over the annual mean as computed by the warm, wet GCM scenario from Wordsworth, Kerber, et al. (2015).

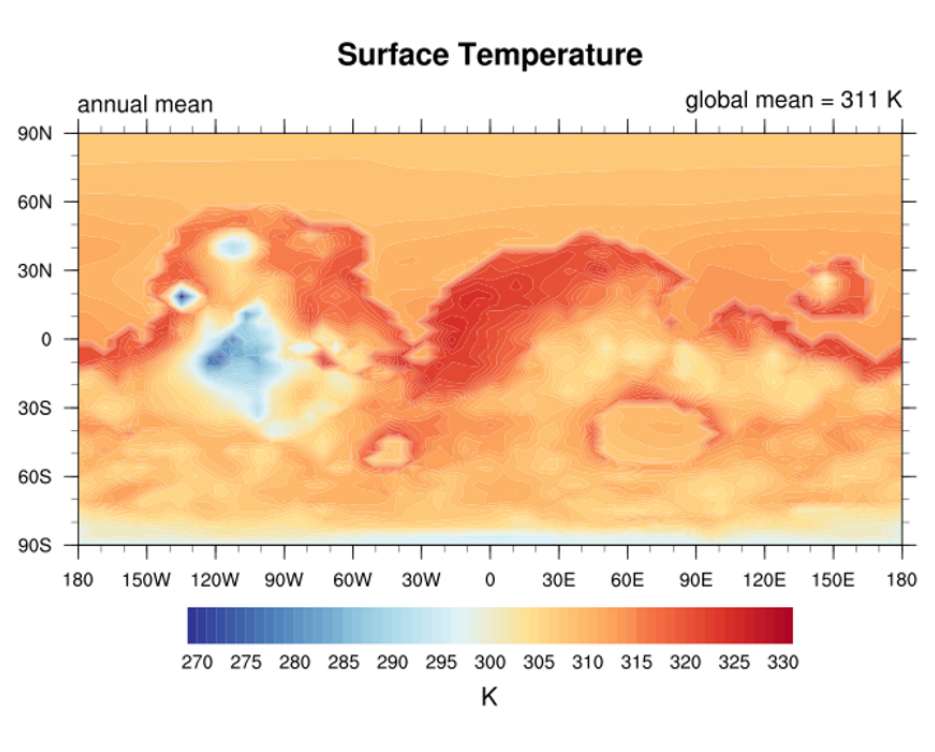

3.11 Appendix 3: Lightning-Induced Fluxes of NO and HCN

The general circulation model outputs precipitation rate on a 49x64 grid over 373 timesteps. The annual-mean globally averaged precipitation rate in the GCM from Wordsworth, Kerber, et al. (2015) is 7.8e-6 kg $m^{-2}s^{-1}$, which is equivalent to 246 kg $m^{-2}yr^{-1}$ or 0.246 myr^{-1}. The annual-mean globally averaged convective available potential energy is 5179 J/kg. The flash rate (as in eq. 1) is thus:

$$F = (5179J/kg)*(7.810^{-6}kgm^{-2}s^{-1})*(1.310^{-11}J^{-1}) = 5.2310^{-13}m^{-2}s^{-1} = 5.2310^{-}17cm^{-2}s^{-1} \quad (3.6)$$

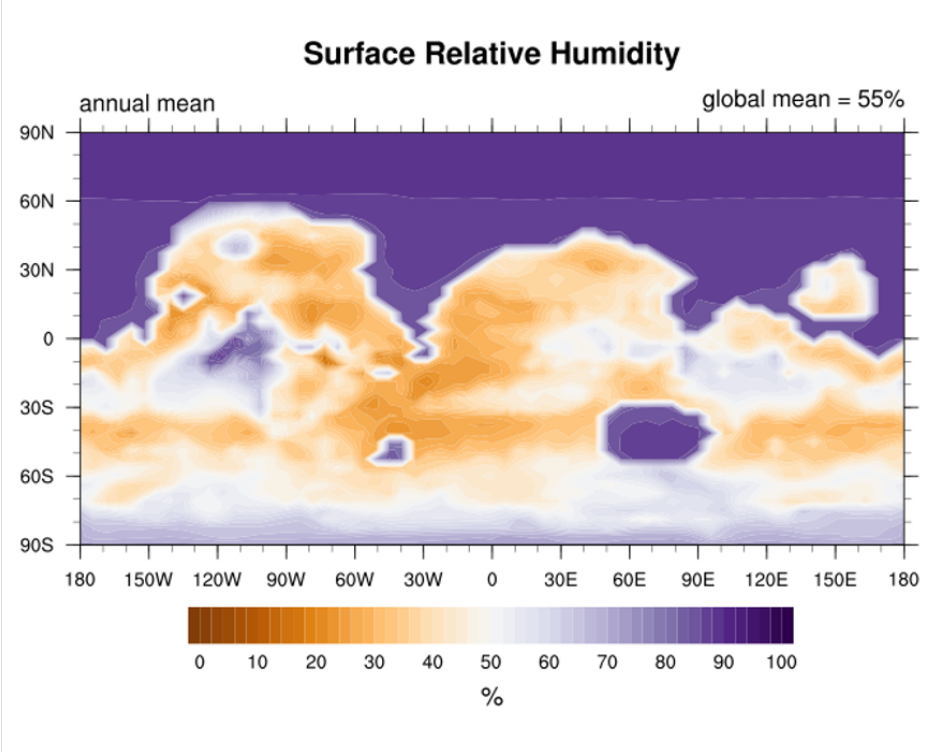

The current-carrying channel released from a lightning flash results in a shock wave associated with thermal expansion of the gas, and this yields overpressures that drive the shock outward, heating surrounding gas to several thousand Kelvin. At these temperatures, we assume this atmospheric gas takes on a thermochemical equilibrium composition which we compute with CEA, Chemical Equilibrium with Applications. This model outputs mixing ratios of the new local composition.

To determine global fluxes of NO and HCN from these mixing ratios, we must consider the mass of atmospheric gas that experiences this heating per lightning event. We then scale by the global lightning flash rate to determine fluxes. This conversion is done with the following equation:

$$P_i = F \frac{E_f}{(c_p \Delta T)} \frac{1}{/} (\mu m_p) \chi_i \tag{3.7}$$

where P_i is the production flux of species i, F is the lightning flash rate, E_f is the energy released per flash (we assume a terrestrial-like value of 5 GJ), c_p is the heat capacity, ΔT is the temperature increase (from the background atmospheric temperature to 2000 K, the assumed near-lightning temperature), μ is the atmospheric mean molecular weight, m_p is the mass of a proton, χ_i is the equilibrium mixing ratio output by CEA of species i.

Parameter	Units	Value
P	kg m-2 s-1	7.8e-6
CAPE	J/kg	5179
η/E	1/J	1.3e-11
F	cm-2 s-1	5.23e-17
Ef	GJ	5
cp	J / (g K)	~8.4*

References

Ackerman, Andrew S and Mark S Marley (2001). "Precipitating Condensation Clouds in Substellar Atmospheres". In: *The Astrophysical Journal* 556.2. DOI: 10.1086/321540.

Agostinelli, S. et al. (2003). "Geant4—a simulation toolkit". In: *Nuclear Instruments and Methods in Physics Research Section A: Accelerators, Spectrometers, Detectors and Associated Equipment* 506.3, pp. 250–303. ISSN: 0168-9002. DOI: https://doi.org/10.1016/S0168-9002(03)01368-8.

Airapetian, Vladimir S (2016). "The Environment of the Young Earth in the Perspective of a Young Sun". In: *Living Around Active Stars, Proceedings IAU Symposium No. 328*. DOI: 10.1017/S1743921317004288.

Allen, Mark, Yuk L Yung, and Joe W Waters (1981). "Vertical transport and photochemistry in the terrestrial mesosphere and lower thermosphere (50-120f km)". In: *Journal of Geophysical Research* 86.A5, pp. 3617–3627.

Baker, Victor R (2006). "Geomorphological Evidence for Water on Mars". In: *Elements* 2.3, pp. 139–143. DOI: 10.2113/gselements.2.3.139.

Baranov, Yuri I, Walter J Lafferty, and GT Fraser (2004). "Infrared spectrum of the continuum and dimer absorption in the vicinity of the O2 vibrational fundamental in O2/CO2 mixtures". In: *Journal of Molecular Spectroscopy* 228.2, pp. 432–440. DOI: 10.1016/j.jms.2004.04.010.

Bibring, JP et al. (2006). "Global Mineralogical and Aqueous Mars History Derived from OMEGA/Mars Express Data". In: *Science* 312.5772, pp. 400–404. DOI: 10.1126/science.1122659.

Buchwald, Carolyn et al. (2016). "Constraining the role of iron in environmental nitrogen transformations: Dual stable isotope systematics of abiotic NO2 reduction by Fe(II) and its production of N2O". In: *Geochimica et Cosmochimica Acta* 186, pp. 1–12. DOI: 10.1016/j.gca.2016.03.009.

Chudinovskikh, L. and R. Boehler (2001). "High-pressure polymorphs of olivine and the 660-km seismic discontinuity". In: *Nature* 411.6837, pp. 574–577.

Claire, Mark W. et al. (Sept. 2012). "THE EVOLUTION OF SOLAR FLUX FROM 0.1nm TO 160m: QUANTITATIVE ESTIMATES FOR PLANETARY STUDIES". In: *The Astrophysical Journal* 757.1. DOI: 10.1088/0004-637X/757/1/95.

Colaprete, Anthony and Owen B. Toon (2003). "Carbon dioxide clouds in an early dense Martian atmosphere". In: *Journal of Geophysical Research: Planets* 108.E4. DOI: https://doi.org/10.1029/2002JE001967.

Desch, Steven J. et al. (2002). "Progress in Planetary Lightning". In: *Reports on Progress in Physics* 65.6, pp. 955–997.

Di Achille, Gaetano and Brian Hynek (2010). "Ancient ocean on Mars supported by global distribution of deltas and valleys". In: *Nature Geoscience* 3, pp. 459–463. DOI: 10.1038/ngeo891.

Ducluzeau, Anne-Lise et al. (2009). "Was nitric oxide the first deep electron sink?" In: *Trends in Biochemical Sciences* 34, pp. 9–15.

Etiope, Giuseppe and Barbara Sherwood Lollar (2013). "ABIOTIC METHANE ON EARTH". In: *Reviews of Geophysics* 51.2, pp. 276–299. DOI: https://doi.org/10.1002/rog.20011.

Fitzsimmons, Jessica N., Edward A. Boyle, and William J. Jenkins (2014). "Distal transport of dissolved hydrothermal iron in the deep South Pacific Ocean". In: *Proceedings of the National Academy of Sciences of the United States of America* 111.46, pp. 16654–16661.

Forget, François and Raymond Pierrehumbert (1997). "Warming early Mars with carbon dioxide clouds that scatter infrared radiation". In: *Science* 278.5341, pp. 1273–1276.

Fripiat, JJ et al. (1972). "Zeolite as catalysts for the synthesis of amino acids and purines". In: *Clays Clay Miner* 20.5, pp. 331–339.

Gordon, Alexander D et al. (2013). "Reduction of nitrite and nitrate on nano-dimensioned FeS". In: *Origins of life and evolution of the biosphere* 43.4-5, pp. 305–322.

Gough, Douglas O (1981). "Solar interior structure and luminosity variations". In: *Solar Physics* 74.1, pp. 21–34.

Grotzinger, John P et al. (2015). "Deposition, exhumation, and paleoclimate of an ancient lake deposit, Gale crater, Mars". In: *Science* 350.6257.

Gruszka, Michal and Aleksandra Borysow (1997). "Roto-translational collision-induced absorption of CO2 for the atmosphere of Venus at frequencies from 0 to 250 cm-1, at temperatures from 200 to 800 K". In: *Icarus* 129.1, pp. 172–177.

Halevy, Itay and James W Head (2014). "Episodic warming of early Mars by punctuated volcanism". In: *Nature Geoscience* 7, pp. 865–868.

Helling, Christiane et al. (2013). "Dust cloud lightning in extraterrestrial atmospheres". In: *Planetary and Space Science* 77. Surfaces, atmospheres and magnetospheres of the outer planets and their satellites and ring systems: Part VIII, pp. 152–157. ISSN: 0032-0633. DOI: https://doi.org/10.1016/j.pss.2012.07.003.

Helz, George R, Brittany E Erickson, and Thomas P Vorlicek (2014). "Stabilities of thiomolybdate complexes of iron; implications for retention of essential trace elements (Fe, Cu, Mo) in sulfidic waters". In: *Metallomics* 6, pp. 1131–1140.

Holm, Nils and Anna Neubeck (2009). "Reduction of nitrogen compounds in oceanic basement and its implications for HCN formation and abiotic organic synthesis". In: *Geochemical Transactions* 10.1, p. 9. DOI: 10.1186/i467-4866-10-9.

Hu, Renyu, Kerri Cahoy, and Maria T. Zuber (2012). "Mars atmospheric CO2 condensation above the north and south poles as revealed by radio occultation, climate sounder, and laser ranging observations". In: *Journal of Geophysical Research: Planets* 117.E7. DOI: https://doi.org/10.1029/2012JE004087.

Hu, Renyu and Hector Delgado Diaz (Nov. 2019). "Stability of Nitrogen in Planetary Atmospheres in Contact with Liquid Water". In: *The Astrophysical Journal* 886.2, p. 126. DOI: 10.3847/1538-4357/ab4cea.

Hu, Renyu, David Kass, et al. (2015). "Tracing the fate of carbon and the atmospheric evolution of Mars". In: *Nature Communications* 6, p. 10003. DOI: 10.1038/ncomms10003.

Jakosky, Bruce M et al. (2018). "Loss of the Martian atmosphere to space: Present-day loss rates determined from MAVEN observations and integrated loss through time". In: *Icarus* 315, pp. 146–157. DOI: 10.1016/j.icarus.2018.05.030.

Kasting, James F (1991). "CO2 condensation and the climate of early Mars". In: *Icarus* 94, pp. 1–13.

Kasting, James F., Heinrich D. Holland, and Joseph P. Pinto (1985). "Oxidant abundances in rainwater and the evolution of atmospheric oxygen". In: *Journal of Geophysical Research: Atmospheres* 90.D6, pp. 10497–10510. DOI: https://doi.org/10.1029/JD090iD06p10497.

Kite, Edwin et al. (2014). "Low paleopressure of the Martian atmosphere estimated from the size distribution of ancient craters". In: *Nature Geoscience* 7.5, pp. 335–339.

Lasue, Jeremie et al. (2015). "Methane storage capacity of the early martian cryosphere". In: *Icarus* 260, pp. 205–214. ISSN: 0019-1035. DOI: https://doi.org/10.1016/j.icarus.2015.07.010.

Li, Cheng et al. (2014). "A non-monotonic eddy diffusivity profile of Titan's atmosphere revealed by Cassini observations". In: *Planetary and Space Science* 104, pp. 48–58. DOI: 10.1016/j.pss.2013.10.009.

Li, Ke-Feng et al. (2017). "Resolving Model-Observation Discrepancy in the Mesospheric and Stratospheric HOx Chemistry". In: *Earth and Space Science* 4. DOI: 10.1002/2017EA000283.

Lingam, Manasvi et al. (2018). "The propitious role of solar energetic particles in the origin of life". In: *The Astrophysical Journal* 853.1, p. 10. DOI: 10.3847/1538-4357/aaa1b9.

Mack, James and James R Bolton (1999). "Photochemistry of nitrite and nitrate in aqueous solution: a review". In: *Journal of Photochemistry and Photobiology A: Chemistry* 128, pp. 1–13. DOI: 10.1016/S1010-6030(99)00131-9.

Manabe, Syukuro and Raymond F Strickler (1964). "Thermal equilibrium of the atmosphere with a convective adjustment". In: *Journal of the Atmospheric Sciences* 21.4, pp. 361–385. DOI: 10.1175/1520-0469(1964)021<0361:TEOTAW>2.0.CO;2.

Mancinelli, Rocco L and Christopher P McKay (1988). "The evolution of nitrogen cycling". In: *Origins of Life and Evolution of the Biosphere* 18.4, pp. 311–325. DOI: 10.1007/BF01808213.

McBride, Bonnie and Sanford Gordon (1996). *Computer program for calculation of complex chemical equilibrium compositions and applications*. Tech. rep. 1311. NASA Reference Publication.

McEwen, Alfred S et al. (2013). "Recurring Slope Lineae in Equatorial Regions of Mars". In: *Nature Geoscience* 7, pp. 53–58. DOI: 10.1038/ngeo2014.

Mewaldt, R A et al. (2012). "ACE observations of energetic particle radiation in the heliosphere". In: *Space Science Reviews* 171, pp. 97–120. DOI: 10.1007/s11214-012-9884-2.

Milliken, Ralph E, John P Grotzinger, and Bradley J Thomson (2010). "Paleoclimate of Mars as Captured by the Stratigraphic Record in Gale Crater". In: *Geophysical Research Letters* 37. DOI: 10.1029/2009GL041870.

Miyakawa, Satoko, H James Cleaves, and Stanley L Miller (2002). "The Cold Origin of Life: A. Implications Based On The Hydrolytic Stabilities Of Hydrogen Cyanide And Formamide". In: *Origins of Life and Evolution of Biospheres* 32.3, pp. 195–208. DOI: 10.1023/A:1016514305984.

Moore, Henry J. and Bruce M. Jakosky (1989). "Viking landing sites, remote-sensing observations, and physical properties of Martian surface materials". In: *Icarus* 81.1, pp. 164–184. ISSN: 0019-1035. DOI: https://doi.org/10.1016/0019-1035(89)90132-2.

Moses, Julianne I et al. (2005). "Photochemistry and diffusion in Jupiter's stratosphere: Constraints from ISO observations and comparisons with other giant planets". In: *Journal of Geophysical Research: Planets* 110.E8. DOI: 10.1029/2005JE002411.

Nitschke, Wolfgang and Michael J. Russell (2013). "Beating the acetyl coenzyme A-pathway to the origin of life". In: *Philosophical Transactions of the Royal Society B: Biological Sciences* 368.1622, p. 20120258.

Oro, J. (1960). "Synthesis of adenine from hydrogen cyanide". In: *Biochemical and Biophysical Research Communications* 2.6, pp. 407–412.

– (1961). "Mechanisms of synthesis of adenine from hydrogen cyanide under possible primitive Earth conditions". In: *Nature* 191.4792, pp. 1193–1194.

Palumbo, Ashley M. and James W. Head (2018). "Early Mars Climate History: Characterizing a "Warm and Wet" Martian Climate With a 3-D Global Climate Model and Testing Geological Predictions". In: *Geophysical Research Letters* 45.19, pp. 10, 249–10, 258. DOI: https://doi.org/10.1029/2018GL079767.

Pearce, Ben K. D., Paul W. Ayers, and Ralph E. Pudritz (2019). "A consistent reduced network for HCN chemistry in early Earth and Titan atmospheres: quantum calculations of reaction rate coefficients". In: *The Journal of Physical Chemistry A* 123.9, pp. 1861–1873. DOI: 10.1021/acs.jpca.8b113323.

Ramirez, Ramses et al. (2014). "Warming early Mars with CO2 and H2". In: *Nature Geoscience* 7.1, pp. 59–63.

Ramirez, Ramses M. and James F. Kasting (2017). "Could cirrus clouds have warmed early Mars?" In: *Icarus* 281, pp. 248–261. ISSN: 0019-1035. DOI: https://doi.org/10.1016/j.icarus.2016.08.016. URL: https://www.sciencedirect.com/science/article/pii/S001910351630495X.

Ranjan, Sukrit et al. (2019). "Nitrogen oxide concentrations in natural waters on early Earth". In: *Geochemistry, Geophysics, Geosystems* 20.3, pp. 2021–2039. DOI: 10.1029/2018GC008082.

Richardson, Mark I., Anthony D. Toigo, and Claire E. Newman (2007). "PlanetWRF: A general purpose, local to global numerical model for planetary atmospheric and climate dynamics". In: *Journal of Geophysical Research: Planets* 112.E9.

Ritson, Dougal and John D Sutherland (2012). "Prebiotic synthesis of simple sugars by photoredox systems chemistry". In: *Nature Chemistry* 4.11, p. 895.

Ritson, Dougal J and John D Sutherland (2013). "Synthesis of aldehydic ribonucleotide and amino acid precursors by photoredox chemistry". In: *Angewandte Chemie International Edition* 52.22, pp. 5845–5847.

Romps, David M, Alexander B Charn, et al. (2016). "CAPE times P explains lightning over land but not the land-ocean contrast". In: *Geophysical Research Letters* 45, pp. 12623–12630.

Romps, David M, Jacob T Seeley, et al. (2014). "Projected increase in lightning strikes in the United States due to global warming". In: *Science* 346.6211, pp. 851–854.

Schaefer, L. and Bruce Fegley (2007). "Outgassing of ordinary chondritic material and some of its implications for the chemistry of asteroids, planets, and satellites". In: *Icarus* 186, pp. 462–483. DOI: 10.1016/j.icarus.2006.09.002.

Schoepp-Cothenet, B. et al. (2012). "The ineluctable requirement for the trans-iron elements molybdenum and/or tungsten in the origin of life". In: *Sci Rep* 2, pp. 1–5.

Schuman, U. and H. Huntrieser (2007). "The global lightning induced nitrogen oxides source". In: *Atmos Chem Phys Discuss* 7, pp. 2623–2818.

Shibuya, T., M.J. Russell, and K. Takai (2016). "Free energy distribution and hydrothermal mineral precipitation in Hadean submarine alkaline vent systems: importance of iron redox reactions under anoxic conditions". In: *Geochim Cosmochim Acta* 175, pp. 1–19.

Squyres, S. et al. (2012). "Ancient Impact and Aqueous Processes at Endeavour Crater, Mars". In: *Science* 336, pp. 570–575. DOI: 10.1126/science.1220476.

Stern, J. C. et al. (2015). "Evidence for indigenous nitrogen in sedimentary and aeolian deposits from the Curiosity rover investigations at Gale crater, Mars". In: *Proceedings of the National Academy of Sciences of the United States of America* 112.14, pp. 4245–4250. DOI: 10.1073/pnas.142.

Summers, D.P. and B. Khare (2007). "Nitrogen fixation on early Mars and other terrestrial planets: experimental demonstration of abiotic fixation reactions to nitrite and nitrate". In: *Astrobiology* 7.2, pp. 333–341. DOI: 10.1089/ast.2006.0056.

Sutherland, J.D. (2017). "Opinion: Studies on the origin of life—the end of the beginning". In: *Nature Reviews Chemistry* 1.2, pp. 1–7. DOI: 10.1038/s41570-017-0022.

Sutter, B. et al. (2017). "Evolved gas analyses of sedimentary rocks and eolian sediment in Gale Crater, Mars: Results of the Curiosity Rover's sample analysis at Mars instrument from Yellowknife Bay to the Namib Dune". In: *Journal of Geophysical Research: Planets* 122.11, pp. 2574–2609. DOI: 10.1002/2016JE005225.

Toner, J.D. and D.C. Catling (2019). "Alkaline lake settings for concentrated prebiotic cyanide and the origin of life". In: *Geochimica et Cosmochimica Acta* 260, pp. 124–132. ISSN: 0016-7037. DOI: https://doi.org/10.1016/j.gca.2019.06.031. URL: https://www.sciencedirect.com/science/article/pii/S0016703719303801.

Urata, R.A. and O.B. Toon (2013). "Simulations of the Martian hydrologic cycle with a general circulation model: Implications for the ancient Martian climate". In: *Icarus* 226, pp. 229–250. DOI: 10.1016/j.icarus.2013.05.016.

Wadhwa, Meenakshi (2001). "Redox state of Mars' upper mantle and crust from Eu anomalies in shergottite pyroxenes". In: *Science* 291.5508, pp. 1527–1530. DOI: 10.1126/science.1057594.

Wong, Michael L, Benjamin D Charnay, et al. (2017). "Nitrogen oxides in early Earth's atmosphere as electron acceptors for life's emergence". In: *Astrobiology* 17.10, pp. 975–983. DOI: 10.1089/ast.2016.1473.

Wong, Michael L, Yuk L Yung, and G Randall Gladstone (2015). "Pluto's Implications for a Snowball Titan". In: *Icarus* 246, pp. 192–196. DOI: 10.1016/j.icarus.2014.05.019.

Wordsworth, Robin, Francois Forget, et al. (2013). "Global modelling of the early Martian climate under a denser CO2 atmosphere: Water cycle and ice evolution". In: *Icarus* 222.1, pp. 1–19. DOI: 10.1016/j.icarus.2012.10.026.

Wordsworth, Robin, Yulia Kalugina, et al. (2017). "Transient reducing greenhouse warming on early Mars". In: *Geophysical Research Letters* 44.2, pp. 665–671. DOI: 10.1002/2016GL071766.

Wordsworth, Robin, Laura Kerber, et al. (2015). "Comparison of "warm and wet" and "cold and icy" scenarios for early Mars in a 3-D climate model". In: *Journal of Geophysical Research: Planets* 120.6, pp. 1201–1219. DOI: 10.1002/2015JE004787.

Yung, Yuk L and William B DeMore (1999). *Photochemistry of planetary atmospheres*. Oxford University Press.

Zafiriou, Oliver C. and Mary B. True (1979). "Nitrite photolysis as a source of free radicals in productive surface waters". In: *Geophysical Research Letters* 6.2, pp. 81–84. DOI: https://doi.org/10.1029/GL006i002p00081.

Zent, Aaron P. (1998). "On the thickness of the oxidized layer of the Martian regolith". In: *Journal of Geophysical Research: Planets* 103.E13, pp. 31491–31498. DOI: https://doi.org/10.1029/98JE01895.

Chapter 4

EXPLAINING NITROGEN FIXATION AT PALEO-MARS BY INVESTIGATING DIURNAL AND HETEROGENEOUS NITROGEN CHEMISTRY

4.1 Introduction

Evolved gas analyses measurements of Mars' soils made by the SAM instrument on board the Mars Science Laboratory (MSL) recently discovered 70-260 and 330-1100 ppm of nitrate in the Klein and Cumberland Noachian-aged mudstone deposits respectively at Yellowknife Bay (Stern et al., 2015). Subsequent measurements of 0.002 to 0.05 wt% of nitrate in sediments near Gale Crater were also reported (Sutter et al., 2017). The presence of nitrate suggests a nitrogen cycle during Mars' history, which would be of high astrobiological relevance; nitrogen fixation is required for nitrogen to be useful to terrestrial life. However, the precise mechanism of the nitrogen cycle at early Mars remains debated.

Mancinelli (1996) predicted the formation of nitrates at early Mars would arise via the following complex chemical network. First, photodissociation of N_2 and ion-neutral reactions are known to form odd nitrogen radicals in the thermosphere, and upon transporting downwards, these species may then be oxidized to form nitric acid (e.g., Krasnopolsky, 1993; Yung et al., 1977). Smith et al. (2014) considered this mechanism and subsequent dry deposition of gaseous nitric acid to estimate the rate of nitrate delivery to the surface. However, they ignored heterogeneous chemistry and diurnal variations, which are known to influence terrestrial NOx deposition.

Adams et al. (2021) was the first work to explain the abundance of nitrate observed by the MSL; however, their mechanism required lightning-induced nitrogen fixation in a warm and wet climate. These assumptions may be valid; significant geochemical and geomorphological evidence exists to suggest warm, wet periods persisted for 105-107 years during the Noachian likely due to a thicker atmosphere enriched in reduced greenhouse gases (e.g., Grotzinger et al., 2014; 5-7 in warm mars paper; Wordsworth et al., 2017). In addition, although no lightning has been observed at present-day Mars, which is now cold and dry, lightning has been observed at planets other than Earth including Venus, Jupiter, and Saturn. However, the surface deposits of nitrate predicted by Adams et al. (2021) are only in agreement with the lower

limits of the MSL measurements, and the climate would have likely only been warm and wet for a brief window of Mars' history. The question still remains whether nitrates can form and deposit in a cold, dry Martian atmosphere at rates relevant to the MSL observations.

In terrestrial models, it has been shown that heterogeneous chemistry involving ice reactions with N_2O5 and HNO3 are important to nitrate formation, especially when diurnal effects are included since N_2O5 is unstable to photolysis on the dayside (e.g., Li et al., 2021). There, three main sources contribute to increasing NOx during the daytime: (1) photolysis of reservoir species HNO3 and N_2O5; (2) destruction of N_2O via reacting with O(1D) which results from O3 photolysis ; (3) a small source through NO3 photolysis. In this work, we examine whether the addition of diurnal chemistry and heterogeneous reactions may increase the rate of nitric acid deposition in cold, dry Martian climates.

4.2 Methods

We adapt KINETICS, the Caltech/JPL chemical transport model (eg., Allen et al., 1981), to the present-day Mars environment as in Nair et al. (1994). Other versions of this model have been validated across numerous planetary bodies, such as Jupiter (eg., Moses et al., 2005), Titan (eg., Li et al., 2014), and Pluto (see, e.g., Wong et al., 2015), and a similar model was considered for the early Earth in Wong et. al. (2017) and for the early Mars in Adams et al. (2021). The model calculates the chemical production and loss rates at each altitude as well as the diffusive flux between each altitude grid by solving the 1-D continuity equation:

$$\frac{dn_i}{dt} = P_i - L_i - \frac{\partial \phi_i}{\phi z} \tag{4.1}$$

where n_i is the number density of species i, ϕ_i the vertical flux, P_i the chemical production rate, and L_i the chemical loss rate, all evaluated at time t and altitude z. The vertical flux is given by:

$$\phi_i = -D_i\left(\frac{\partial n_i}{\partial z} + \frac{n_i}{H_i} + \frac{1-\alpha_i}{T}\frac{\partial T}{\partial z}n\right) - K\left(\frac{\partial n_i}{\partial z}\frac{n_i}{H_i} + \frac{1}{T}\frac{\partial T}{\partial z}n\right) \tag{4.2}$$

where D_i is the species' molecular diffusion coefficient, H_i the species' scale height, H_{atm} the atmospheric scale height, α_i the thermal diffusion parameter, Kzz the vertical eddy diffusion coefficient, and T the temperature. The flux consists of two parts: (1) molecular diffusion which can be derived from the molecular theory

of ideal gases and (2) eddy transport. We calculate the eddy diffusion coefficient profile by using the formulation in the work of Ackerman and Marley (2001). A critical difference between the two terms is the scale height: in the isothermal case, molecular diffusion drives the system toward diffusive equilibrium since each species follows its own scale height, H_i, while eddy diffusion drives the system toward a well mixed state since all species follow the bulk atmospheric scale height, H_a.

We consider the chemistry of the following species linked by 152 reactions on an altitude grid with 1-2 km spacing: O, $O(^1D)$, O_2, O_3, H_2O, H, H_2, OH, HO_2, H_2O_2, N, $N(^2D)$, N_2, NO, NO_2, NO_3, N_2O, N_2O_5, HNO_2, HNO_3, HO_2NO_2, CO, CO_2, O^+, O_2^+, CO_2+, CO_2H^+, and electrons. Unless otherwise stated, we consider a zero flux at the boundary condition. At the lower boundary, we fix the concentration of water vapor to the concentration equivalent to the saturation vapor pressure and the concentration of all ion species to zero. We fix the mixing ratio at the lower boundary for O2, H_2, N_2, CO, and CO_2 to agree with measurements of the present-day atmosphere. At the upper boundary, we fix the escape flux of O to 1.210^8 molecules $cm^{-2}s^{-1}$ (Nair et al., 1994) which is in agreement with present-day observations (e.g., Jakosky et al., 2018; references therein), and we fix the escape velocity of H and H_2 to $3.08x10^3$ and 3.3910^1 molecules $cm^{-2}s^{-1}$ according to diffusion limited escape theory (e.g., Hunten et al., 1972). We ignore the dry deposition of HNOx, as previous works have found the dry deposition rate to be small. Instead, heterogeneous reactions on ice particles are assumed to be the dominant loss of HNOx to the surface in our model.

A cartoon of the dominant production and loss mechanisms in the odd nitrogen cycle is shown in Figure 4.1. Solar energetic particles have sufficient energy to dissociate N_2, and subsequent oxidation of N radicals forms NO and NOx. At night, photolysis (largely of NO_x and N_2O_5) severely slows, causing a buildup of N_2O_5 and HNO_3, and heterogeneous reactions on ice particles may deplete these reservoirs.

We invoke diurnal variations in KINETICS, and the model runs through simulated time until the diurnal cycle of the stratospheric NO_2 becomes stationary. During the progression through time, the pressure and temperature profiles are fixed and do not vary with time; the incident photon flux drives the diurnal variations. We prescribe a rate coefficient for loss of a species through heterogeneous reactions with ice aerosols as:

$$J' = 0.25\gamma v \sigma N_{ice} \tag{4.3}$$

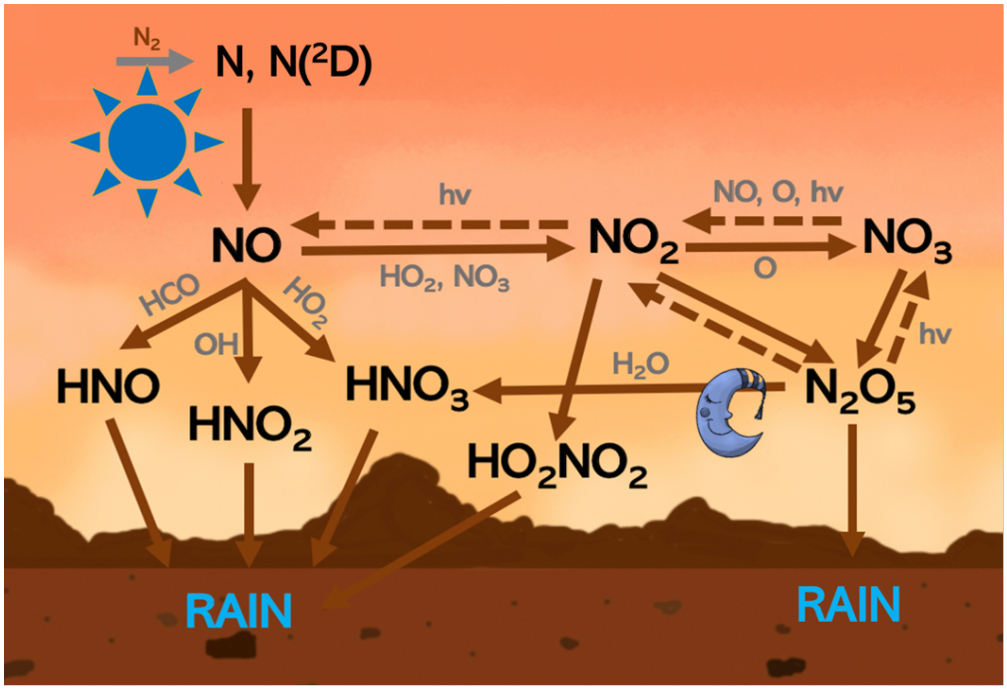

Figure 4.1: Cartoon of the relevant odd-nitrogen chemistry in Mars' atmosphere.

where γ describes the sticking coefficient, v describes the thermal velocity of the gas, σ describes the average cross section (area) of the ice particle, and N_ice describes the number density of the ice particles. We consider a γ of 0.01 according to Michelangeli et al. (1989), and we compute the cross section according to a mean particle radius of 1.41 microns based on the particle size distributions of Kleinbohl et al. (2011). We compute the number density of ice particles by temporally averaging MCS observations for Mars years 29-33 for the 5 Ls periods 0-5, 45-50, 90-95, 135-140, and 175-180. The computed time-averaged J profile is plotted in black in Figure 4.2, and the temporal variations are overlaid behind in various colors.

4.3 Diurnal Cycle of NOy Reservoirs

The dominant loss for nitrogen from the atmosphere is the formation of HNO3, which is eventually deposited. During the daytime, HNO3 is produced via oxidation of NO2 by OH, but overnight, heterogeneous hydrolysis of N_2O5 on ice particles leads to HNO3 formation as well:

$$NO2 + OH \rightarrow HNO3$$

$$N_2O_5 + H_2O_{(s)} \rightarrow 2HNO_3$$

The availability of N_2O5 in R2 is sensitive to diurnal variations. N_2O5 is thermally

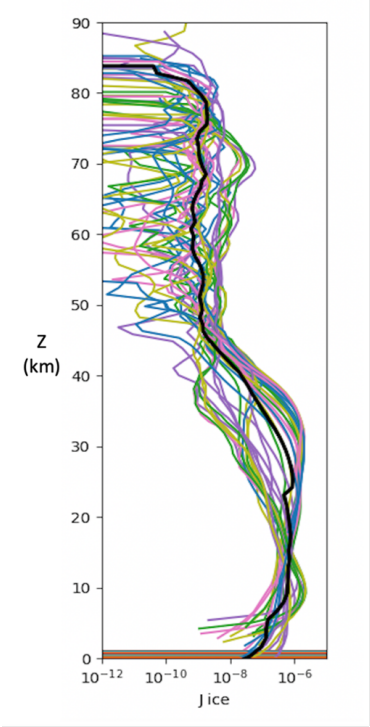

Figure 4.2: Vertical profiles of J, the rate coefficient for loss of a species through heterogeneous reactions with ice particles, derived from a temporal average of MCS observations taken during Mars years 29-33.

unstable and decomposes back to NO2 and NO3. The presence of NO3 is characteristic of night chemistry, as on the dayside it quickly photolyzes to NO2; however, when it builds up at night from the slowed loss, NO2 and NO3 may react to form N_2O5 again:

$$N_2O_5 \rightarrow NO_2 + NO_3$$

$$NO_3 + h\nu \rightarrow NO_2 + O$$

$$NO_2 + NO_3 \rightarrow N_2O_5$$

This cycle requires that N_2O5 be in thermal equilibrium with NO2 and NO3, and therefore the concentration of N_2O5 shows a diurnal variation. We discover a 15% increase in N_2O5 overnight from Mars dusk to Mars dawn.

4.4 Heterogeneous Removal of NOy

Heterogeneous chemistry has demonstrated to be a significant contribution to total HNOx and N_2O5 loss. The steady state mixing ratio of both species decreases by a factor of 2 with the inclusion of ice particles with a number density informed from the temporal average of four Mars years of MCS data. N_2O5 converts to HNO3

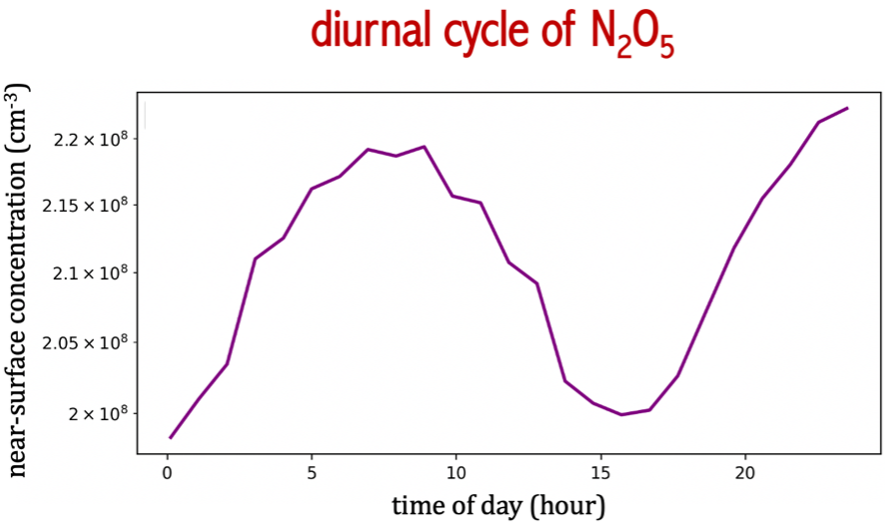

Figure 4.3: Diurnal cycle of N_2O_5 at Mars which derives from the diurnal variation in NO3, a species sensitive to photolysis on the dayside.

through reactions on ice particles, and despite the faster production of HNO3, heterogeneous reactions with ice encourage the removal of HNOx from the Mars atmosphere which results in a decrease in the HNO3 mixing ratio profile.

We acknowledge that the ice densities are highly variable over time, and as a sensitivity study we consider a third case with ice densities enhanced by a factor of 3; in this case, the steady state mixing ratios decrease again by a factor of 2.

4.5 Deposition Rate of HNOx on Ice Particles

Our photochemical model finds a deposition rate of 5.3e5 HNOx molecules cm-2 s-1, which is a two-fold increase in comparison to the results of Smith et al. (2014) that did not include heterogeneous chemistry. Figure 4.5 summarizes the flux of the relevant NOy species to the Martian surface.

Interestingly, the deposition rate of pernitric acid is faster than that of nitric acid, which differs from terrestrial chemistry. The formation of nitric acid requires that NO2 become oxidized by OH; however, the water vapor abundance at Mars is low due to the cool temperatures and hence OH production is limited. Meanwhile, HO2NO2 forms faster due to the temperature-dependence of the rate coefficient for its main production reaction, R, which is inversely related to temperature:

$$HO2 + NO2 + M \rightarrow HO2NO2 + M$$

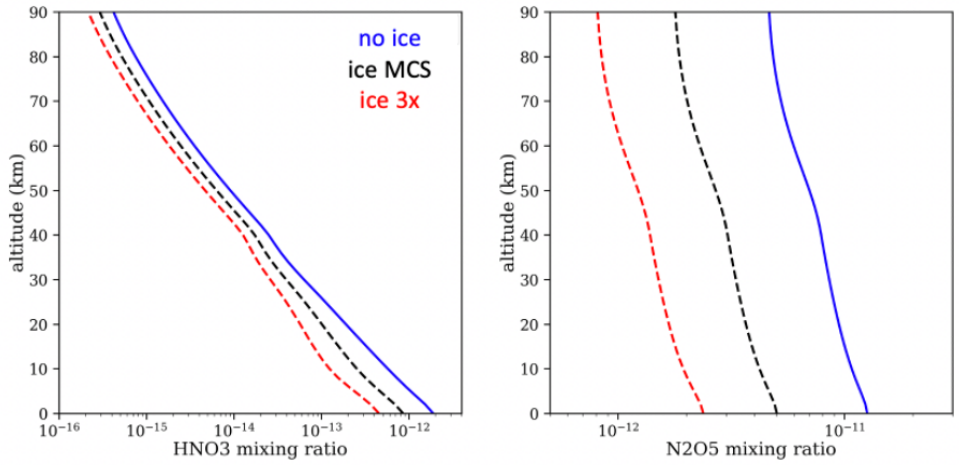

Figure 4.4: Steady-state mixing ratio of HNO_3 and N_2O_5. We consider one case with no heterogeneous chemistry (blue; labeled "no ice") as a control to compare with the scenario considering heterogeneous chemistry with ice data informed from MCS (black). In a third scenario, we acknowledge the ice number densities vary overtime and consider a scenario with ice densities enhanced by three-fold.

	DRY FLUX	FLUX ON ICE
N_2O_5	0.165	0.278
HNO_2	0.573	2.442
HNO_3	0.088	0.233
HO_2NO_2	1.245	2.098
TOTAL N	2.235*Y	5.329

Figure 4.5: Comparison of dry deposition versus deposition through rainout on ice particles. Fluxes are shown in units of 1e5 molec cm-2 s-1. Y represents a factor to consider the inefficiency of adsorption into the ground, which may be less than unity.

With several assumptions, we can approximate to an order of magnitude the concentration of salts that have accumulated in the Mars soil. We take a similar approach as Smith et al. (2014): We approximate the duration of the icy climate as the duration of the Amazonian eon. Upon deposition on ice, we assume the soils mixed throughout a shallow depth due to post-Noachian impactors. We consider 2m which represents three e-folding depths (Zent 1998). We also assume a soil density of 1 g/cc (Moore and Jakosky, 1989). We assume the loss rates of nitrate and nitrite upon deposition would be negligible, unlike aqueous systems. Under these assump-

tions, our resulting deposition fluxes correspond to the following weight percents: 0.03 wt% nitrate, 0.6 wt% nitrite (considering both nitrous acid and pernitric acid decompose into nitrite).

4.6 Interpreting the Formation of MSL-Measured Volatiles

We find that icy climates are able to form and deposit nitric acid fast enough to explain the MSL-measured nitrates as global averages, although we acknowledge that the MSL measurements may not be globally representative (e.g., ices and/or NOx could transport to locally collect in some regions).

Our result does not rule out the formation of nitrates in warm and wet climates, however, it suggests the nitrates measured by MSL could be formed by two mechanisms at different epochs in time. Future measurements of N-isotopes in the Martian nitrates could help constrain when the nitrates formed. Over Mars' history, the atmospheric isotopic record became enriched in heavy isotopes due to atmospheric loss to space; since nitrate formation originates with atmospheric chemistry under both regimes, nitrates formed during the warm and wet climate would likely be older and thus of lighter isotopic signatures than nitrates formed during the cool, icy climate.

In addition, it is noteworthy that our results demonstrate that the deposition of pernitric acid may have been faster than that of nitric acid. The fate of pernitric acid upon deposition may be analogous to its fate in aqueous systems, in which its destruction would result in nitrite salts on the surface (e.g., Regimbal and Mozurkewich, 1997; Slusher et al., 2002). Nitrite salts are unlikely to convert to nitrate via reactions with magnetite, hematite, and geothite (Li et al., 2020). However, Sutter et al. (2017) reports only detections of nitrate at Mars from the SAM instrument, inferred from multiple NO releases from soil samples in the evolved gas analysis (EGA) experiment; they suggest NO peaks at various temperatures may result from the sensitivity of NO evolved from Fe-bearing nitrates (relatively lower temperatures) and Mg-, Ca-, Na- and K-bearing nitrates (at relatively higher temperatures).

It may be interesting to question whether the evolved NO could suggest the presence of nitrite. Navarro-González et al. (2018) discovered that both nitrite and nitrate are extremely labile in the presence of iron perchlorates decomposing at temperatures below 270 C; however, in the presence of magnesium and calcium chlorates or perchlorates, NO_2^- decomposes below 400 C and nitrate decomposes above 400 C. The EGA results of Sutter et al. (2017) show NO peaks at temperatures below 400

C in the Cumberland, John Klein, and Rocknest samples; NO peaks at temperatures greater than 400 C are in several samples. We suggest future work investigate the thermal decomposition of nitrite- and nitrate- bearing species in Mars-like soil samples in order to place better constraints on interpreting the presence or absence of nitrite.

Chapter 5

HYDROCARBON CHEMISTRY IN THE ATMOSPHERE OF A WARMER EXO-TITAN

5.1 Introduction

Titan is the only moon in the solar system demonstrated to have complex organic chemistry occurring in an earth-like atmospheric envelope (1.5 bar), which is a result of its unique atmospheric properties: a N_2 atmosphere with a reducing composition, energy sources to drive disequilibrium chemistry, and an aerosol layer to shield the surface from solar UV radiation (eg., Yung et al., 1984; Wilson and Atreya, 2004; Willacy et al., 2016). This world draws parallels to an early Earth-like world which may have been reducing (eg., Lunine 2005; Lorenz and Mitton 2008), and these characteristics make it an appealing object of study when exploring planetary habitability.

To date, over 5000 exoplanets have been discovered, primarily due to NASA's Kepler mission which searched for and discovered transiting exoplanets. Hot-Jupiters were the easiest planets to detect at first, but today small (1-4 Re), low mass (< 20 Me) and short period (P < 100 days) planets are the most common type of exoplanet known today (eg., Bean et al., 2019). The atmospheres of small close-in planets are vulnerable to rapid escape; however, it has been recently suggested that during planet formation of super-Earth planets, H_2 may not have accumulated as a thick gaseous envelope, but instead would dissolve in the interior magma (Chachan et al., 2019; Kite et al., 2020). Outgassing of a reduced secondary atmosphere may be plausible and has been suggested to explain the observed atmospheric spectra of GJ 1132b, a super-Earth orbiting an M-Dwarf at a close-in orbit at 0.01 AU, a super-Earth orbiting an M-Dwarf at a close-in orbit at 0.01 AU (Swain et al., 2021). Recent Hubble Space Telescope (HST) observations suggest a surface pressure between 1 and 10 bars, a surface temperature of 950 K, a stratospheric temperature of 480 K, and an H_2-dominated atmosphere with nitrogen and hydrocarbon chemistry (Swain et al., 2021). Although, recent works have also disputed the observations, suggesting either that photochemical hazes muted the spectral features or that no atmosphere was present (Mikal-Evans et al., 2021; Libby-Roberts et al., 2021).

The photochemistry in the reduced atmospheres of close-in, rocky planets may be

unique from the solar system worlds. Previous studies have primarily examined the surface climate and atmospheric circulation of earth-like exoplanets (eg, Kaspi Showman 2015; Shields et al., 2013; 2016; Merlis Shneider 2010; Kopparapu et al., 2013), but fewer investigations have explored the range of possible conditions at exoplanets with photochemical hazes, reduced atmospheres, and/or different equilibrium temperatures (eg., Morley et al., 2015; Lora et al., 2018). Lora et al. (2018) examines the response of a Titan-like atmosphere to different host stars and finds (in agreement with results presented here in Section 3) that the greater shortwave activity but lower luminosity of M-Dwarves both result in a lesser production of hydrocarbons. Here we investigate the response of a Titan-like atmosphere to a larger swath of planetary parameters than previously considered in order to more closely adapt known atmospheric chemistry to the conditions of close-in super-Earths: to a warmer temperature, larger irradiation flux, different stellar type, and different background H_2:N_2 ratios. We term these planets exo-Titan due to their similarities in atmospheric composition (reduced, N-bearing chemistry), although we acknowledge the differences in interior composition, planetary radius, and temperature.

5.2 Methods

We adapt the Titan KINETICS model presented in Willacy et al. (2021) to various Exo-Titan atmospheres orbiting Sun-like and M-Dwarf host stars. The model considers 111 species linked by 1143 reactions in order to calculate the chemical production and loss rates at each altitude as well as the diffusive flux between each altitude grid by solving the 1D continuity equation.

We consider Titan and GJ 1132b as our two end members, and consider a swath of theoretical intermediates between in order to examine the photochemical response to four parameters: (1) the stellar type, M-Dwarf vs K-star vs Sun-like host star; (2) close-in orbit, ranged from a Titan-like distance of 9.55 AU to 0.01 AU; (3) temperature, from a Titan temperature (94 K at the surface and 170 K in the stratosphere) to a GJ 1132b temperature (950 K at the surface and 480 K in the stratosphere); and (4) initial H_2:N_2 ratio, varied from Titan-like (or <1% H_2) to GJ 1132b-like (10% N_2 and 90% H_2).

The TP profile at Titan comes from Willacy et al. (2022), and for orbits at the same equilibrium temperature at different host stars we maintain the same TP profile. The TP profile at the 9.5 AU at dimmer stars is scaled according to the differing equilibrium temperatures. The TP profile of GJ 1132b comes from Swain et al.

(2021).

The stellar type (M-Dwarf) and properties of GJ 1132 are very similar to those of GJ 1214 (with a temperature of 3000 K and mass of 0.15 solar masses), which is a stellar spectrum that has been well studied. Figure 5.1 compares the incident radiation at 1 AU of this star and the Sun.

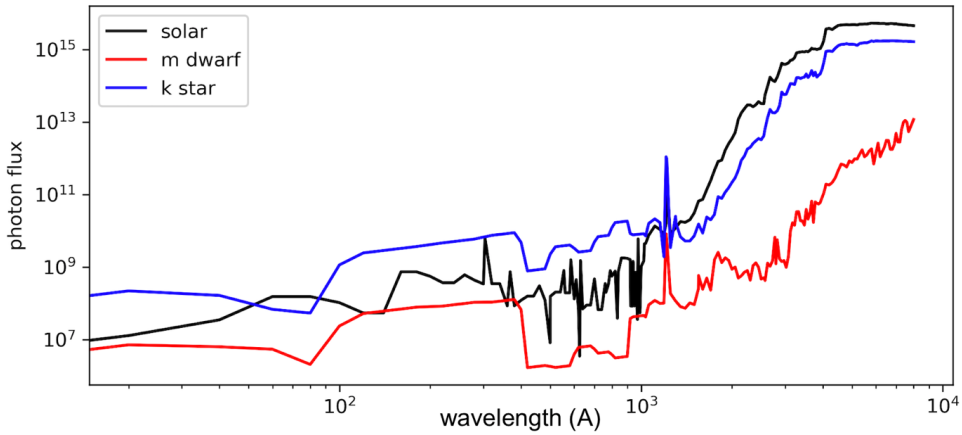

Figure 5.1: Stellar spectra of the Sun (black), an M4.5 host star (red), and a K star (blue), all shown at 1 AU. We obtain the K and M star spectra from the MUSCLES database (France et al., 2016), and we adapt the solar flux from Gladstone et al. (2010). In all cases shown, we have binned to a coarser resolution than the original datasets to minimize model runtime.

We compute synthetic spectra of the predicted photochemical results in order to consider potential detectability. We use Exo-Transmit (Kempton et al., 2016), an open-source radiative transfer code, that calculates atmospheric transmission spectrum of transiting exoplanets. In this study, we include eleven species – C, CH_4, C2H_2, C2H4, C2H6, H, HCN, H_2, N, N_2, and NH3. Then, Exo-Transmit finds atmospheric opacity by interpolating between single-molecule cross section data for CH_4, C2H_2, C2H4, C2H6, HCN, N_2, and NH3 between a predefined temperature-pressure grid (temperature ranging from 100 K to 3000 K with a spacing of 100 K, pressure ranging from 10-4 Pa to 108 Pa with a spacing of one order of magnitude) and collision-induced-absorption opacity data for CH_4–CH_4, H_2–H_2, H_2–H, H_2–CH_4, N_2–CH_4, N_2–H_2, and N_2–N_2 between the same temperature grid, solve the radiative transfer equation line by line, and generates wavelength-dependent transit depths. The wavelength range is 300 nm to 30 m. Exo-Transmit considers the oblique path of light through the planetary atmosphere along a distant observer's light of sight. It also accounts for opacity caused by Rayleigh scattering. All opacity

data in Exo-Transmit is taken from Freedman et al. (2008), Freedman et al. (2014), and Lupu et al. (2014).

We carry out Exo-Transmit calculations for 10-5 to 103 mbar of the modelled atmosphere. Exo-Transmit has a resolving power $\lambda/\Delta\lambda$ of 1000. For visual clarity, we perform a running average with a resolving power of 50. It is worth noting that some of the modelled atmospheres have altitude ranges with temperatures lower than 100 K where Exo-Transmit does not have opacity data. We manually set the opacity for 70–100 K the same as that for 100 K. Sensitivity tests show that the transmission spectra are robust against different approaches of extrapolation.

5.3 Results

Stellar Irradiance on Hydrocarbon Chemistry

The production of hydrocarbons is driven by methane photolysis, which makes the incident photon flux a critical driver of hydrocarbon chemistry. An M-Dwarf host star is more active in the shortwave region than longwave, compared to the Sun. However, the star is less luminous making the total incident radiation at 2 AU orbit comparable to the 9.5 AU orbit around the Sun.

Here, we consider the hydrocarbon chemistry at five worlds: Titan around the Sun, Titan around an M-Dwarf at an orbit of 2 AU and 9.5 AU, and Titan around a K star at an orbit of 5.6 AU and 9.5 AU. A similar investigation is presented in Lora et al. (2018), and our results presented in this section largely agree with theirs. Understanding these cases is imperative to understanding the novel results presented later in this work.

Ethane, C2H6

At all cases, the production of C2H6 is dominated by 2CH3 + M, where M is the third body (Fig. 5.3). At the same equilibrium temperatures (close-in orbits of 5.6 AU and 2.0 AU around the K and M star respectively), the photolysis of methane is comparable to that of Titan around the Sun (Fig. 5.3). However, the enhanced flux of short wavelength (λ<80nm) photons of the M-Dwarf encourages faster N_2 dissociation (Fig. 5.3), allowing N+CH3 (Fig. 5.3) to act as an additional sink of CH3.

At all cases, the dominant loss of ethane are reactions to C2H and C3N, and these are both important in the M-Dwarf cases as well. At a distant orbit of 9.5 AU around an M-Dwarf, methane photolysis is slowed but N_2 photolysis is still enhanced,

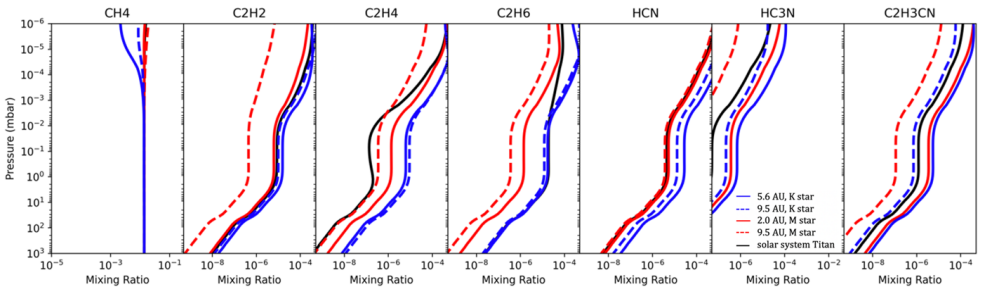

Figure 5.2: Response to stellar type and irradiation; all cases are at a Titan-like temperature and N_2-dominated atmosphere. Black line: Sun-like star at 9.55 AU; solid red line: M-Dwarf star at 2.0 AU; dashed red line: M-Dwarf star at 9.5 AU; solid blue line: K star at 5.6 AU; dashed blue line: K star at 9.5 AU. Note that the total irradiation at 2.0 AU from an M-Dwarf host star and 5.6 AU from a K star are both comparable to the total irradiation a world experiences at 9.55 AU from a Sun-like star. From left to right, the panels show CH_4, C2H_2, C2H4, C2H6, HCN, HC3N, and C2H3CN.

and thus production of ethane is limited. Methane photolysis results from slightly longer wavelength photons (770-1600 A) than N_2 photons (680-980 A). A distant orbit means all photon fluxes are reduced compared to a close-in orbit. However, since M Dwarves emit more photons in the smaller wavelengths (relative to longer wavelengths), the slowed photolysis effect is lesser for N_2 photolysis.

Acetylene, C2H_2, and Ethylene, C2H4

At Titan, the concentration of acetylene is influenced by production via C2H + CH_4 and CH_2 + CH_2 balanced by destruction via photolysis which yields C2H + H. However, in the upper atmosphere with an M-Dwarf host star, H+C2H3 and CH3+C2H3 and CH3+C3H_2 become dominant, where the cycling among C2H_2, C2H3, and C3H_2 balances the C2H_2 concentration. Around an M-Dwarf, upper atmospheric C2H_2 is lost to reactions with CN, and photolysis of C2H_2 is the dominant lower atmosphere destruction reaction.

At all cases CH + CH_4 is the dominant production, and photolysis is the dominant destruction. At a comparable effective temperature (2 AU around the M-Dwarf), the greater flux of energetic photons results in faster methane photolysis and thereby a faster production of ethylene. From the same distance (9.5 AU), photolysis of both methane (production) and C2H4 (loss) are slowed and therefore the steady state mixing ratios at Titan and the 9.5 orbit around an M-Dwarf are comparable.

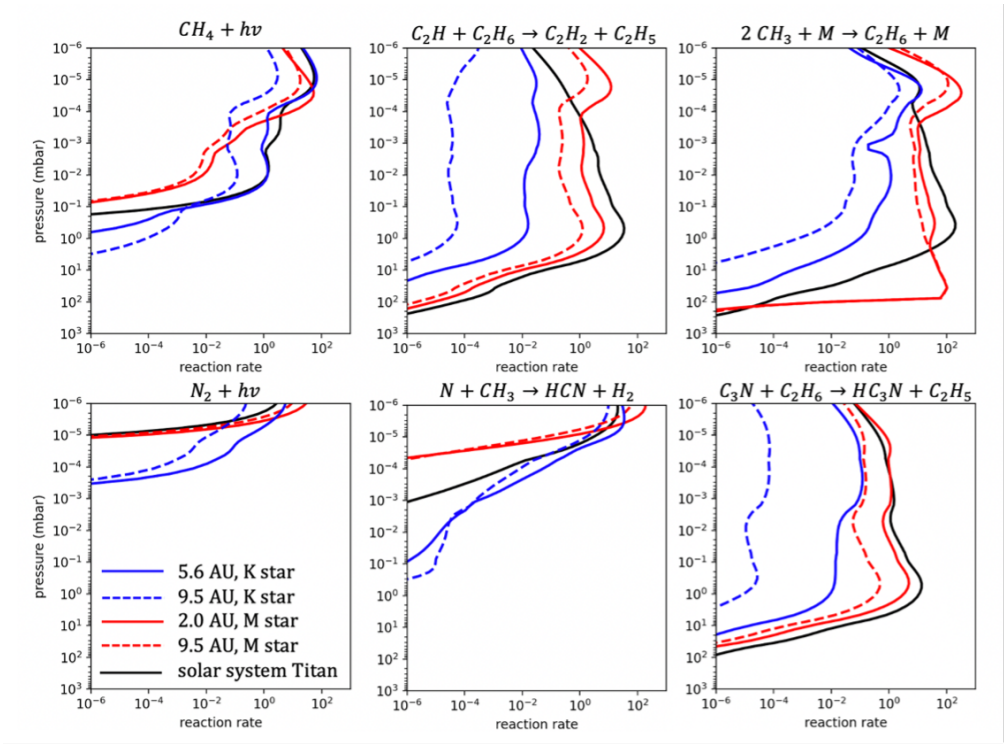

Figure 5.3: Reaction rates (cm-3 s-1) of dominant production and destruction reactions for C2H6. Black lines represent solar system Titan, solid red lines represent Titan around an M-Dwarf at 2 AU, dashed red lines represent Titan around and M-Dwarf at 9.5 AU, solid blue lines represent Titan around a K star at 5.6 AU, and dashed blue lines represent Titan around a K star at 9.5 AU.

-CN species

The greater photon flux in the shortwave spectral region emitted by the K star yields a greater abundance of N and thereby a faster production of HCN. However, HCN photolysis rate is comparable between the K star and sun as lyman-alpha photons are able to dissociate HCN, and the Ly-A of the two stars is more comparable. As a result, the HCN abundance is greatest at a 5.6 AU orbit around a K star, where production is faster. Dissociation of N_2 and HCN are both faster around the M star, and these effects balance each other out and thereby yield a comparable HCN concentration as that at solar system Titan. Photolysis of HCN, the primary loss mechanism, results in CN which may form C2H3CN via reactions with C2H4; although, CN may also cycle back to HCN via reactions with the hydrocarbons. For the same reasons that HCN is larger around the K star at the same equilibrium temperature as solar system Titan (5.6 AU), HC3N and C2H3CN are largest around the K star. Meanwhile, in the 9AU orbit around the M star, slowed photolysis due to a

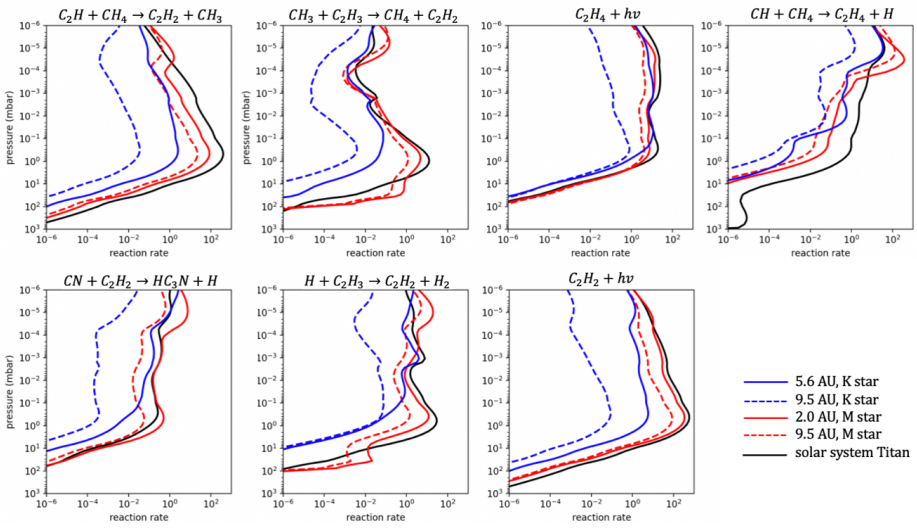

Figure 5.4: Reaction rates (cm-3 s-1) of dominant production and destruction reactions for C2H_2 and C2H4. Black lines represent solar system Titan, solid red lines represent Titan around an M-Dwarf at 2 AU, dashed red lines represent Titan around an M-Dwarf at 9.5 AU, solid blue lines represent Titan around a K star at 5.6 AU, and dashed red lines represent Titan around a K star at 9.5 AU.

lower photon flux in total, limits the presence of N and CH3. HCN loss to photolysis is similarly slowed, however, resulting in a similar steady state concentration.

Temperature and H_2 Composition on Hydrocarbon Chemistry

With the same solar host star and at the same orbit of 9.5 AU, we now investigate the hydrocarbon chemistry in a cold N_2 atmosphere (Titan), a cold H_2 dominated atmosphere, and a warm H_2 dominated atmosphere (eg, a sub-Neptune or close-in super Earth). The H_2-dominated atmospheres are motivated by the recognized H_2-dominated atmosphere of GJ 1132b (Swain et al., 2021) and predicted reduced interiors of close-in super Earths described in Section 1.

Methane, CH_4, and Ethane, C2H6

The reaction H+CH_4 $\rightarrow$ CH3+H_2 is well known to be a mechanism for methane destruction at Titan, other than methane photolysis. Both this reaction and its back reaction, H_2 + CH3 $\rightarrow$ CH_4 + H, are highly temperature dependent, and in the warmer atmosphere these reactions recycle CH3 back into CH_4, which will limit hydrocarbon production. H+CH3+M is a second important reaction to destroy CH3, and this reaction also becomes faster in the H_2 atmospheres due to the greater

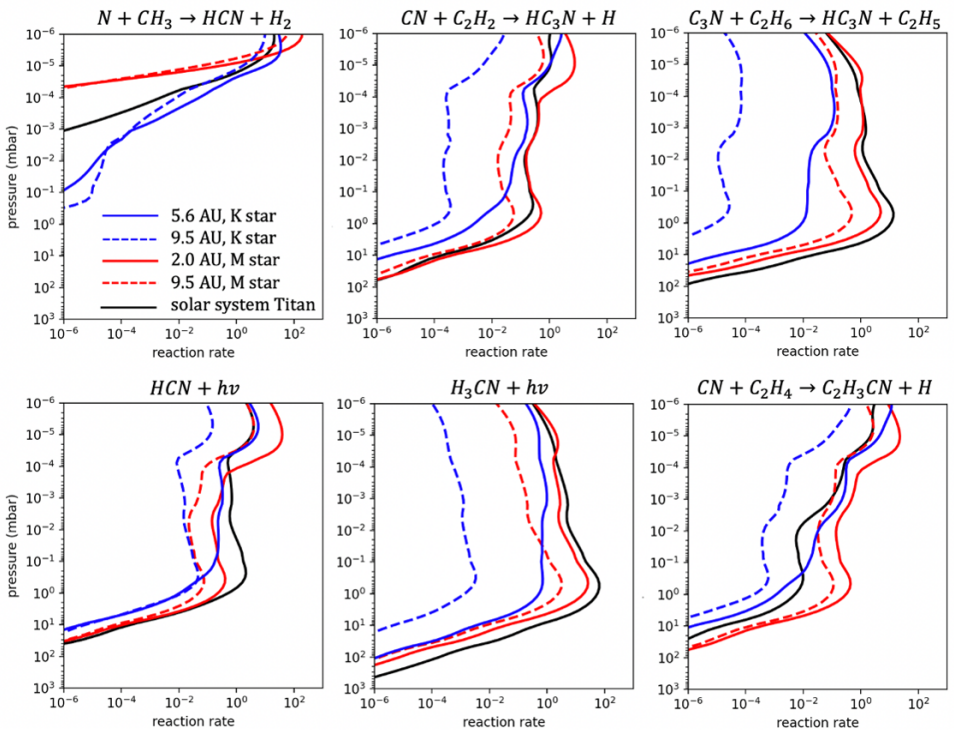

Figure 5.5: Reaction rates (cm-3 s-1) of dominant production and destruction reactions for -CN species. Black lines represent solar system Titan, solid red lines represent Titan around an M-Dwarf at 2 AU, dashed red lines represent Titan around an M-Dwarf at 9.5 AU, solid blue lines represent Titan around a K star at 5.6 AU, and dashed red lines represent Titan around a K star at 9.5 AU.

concentrations of H.

In the N_2-dominated atmosphere, photolysis of methane becomes severely photon limited above 0.1 mbar since shortwave photons are lost to N_2. In both H_2-dominated atmospheres, however, the atmosphere is less opaque to incident stellar photons and photolysis of methane extends down to the near-surface. The CH3 produced from methane photolysis recycles back into methane. However, the photolysis branch of CH_2+H acts as a longer-lived sink of methane, and this CH_2 may then be photolyzed to CH to kick off subsequent hydrocarbon chemistry described in the following sections.

This cycling does not directly affect the methane profile, but the faster destruction of CH3 is important to the larger hydrocarbons that are shown next.

For all three cases, the production of C2H6 is dominated by the reaction 2CH3 $\rightarrow$ C2H6. At Titan, ethane is largely destroyed to reactions with C2H and secondly to

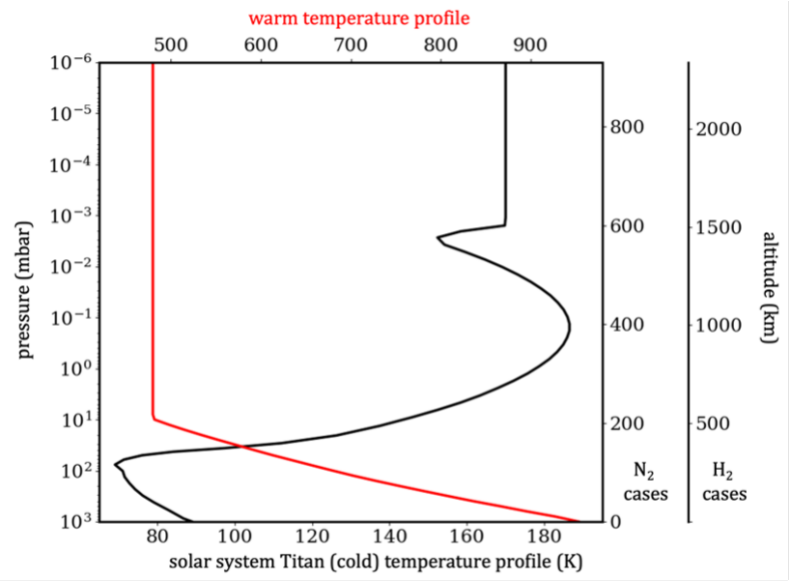

Figure 5.6: Temperature-pressure-altitude profiles of the cold solar system Titan N_2 atmosphere (black) and warm Exo-Titan H_2 atmosphere (red). Notice the altitude scale changes for the Exo-Titan, which is a result of the warmer temperature and puffy nature (large scale height) of H_2 atmospheres.

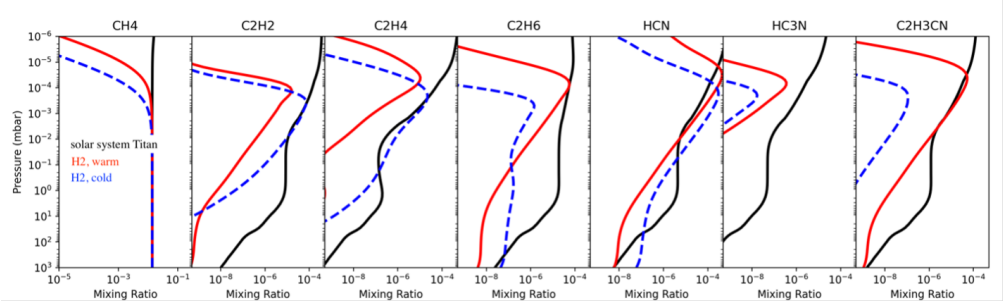

Figure 5.7: Response to temperature and H_2 content; all cases are around a Sun-like star at 9.5 AU. Solid black lines: Titan temperature, N_2 dominated atmosphere; red lines: warm, H_2 dominated atmosphere; blue lines: Titan temperature (cold), H_2 dominated atmosphere. From left to right, the panels show CH_4, C2H_2, C2H4, and C2H6.

reactions with C3N. However, in an H_2-dominated atmosphere, loss is dominated by H+C2H6 $\rightarrow$ C2H5+H_2. The slower production in the warm case in combination with a faster loss rate to atomic hydrogen in both cases results in a depleted C2H6 profile in the H_2-dominated atmospheres.

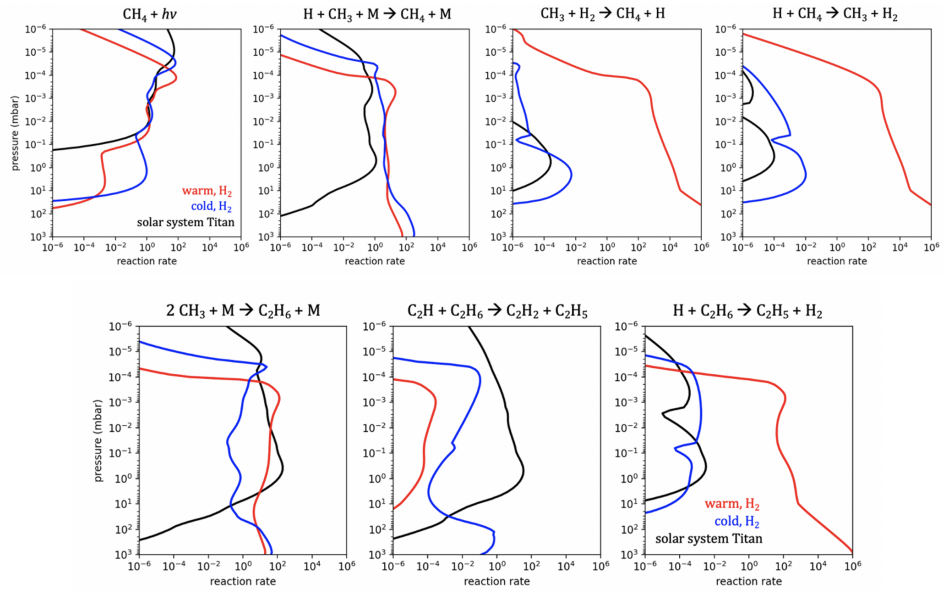

Figure 5.8: Reaction rates (cm-3 s-1) of CH_4-CH3 recycling and dominant production and destruction reactions for C2H6. Black lines represent a cold N_2 atmosphere (Titan), blue lines represent a cold H_2 atmosphere, and red lines represent a warm H_2 atmosphere.

Acetylene, C2H_2

At Titan, C2H_2 is known to form from C2H + CH_4 in the upper atmosphere and is destroyed via photolysis to form C2H + H, and these reactions lead to the autocatalytic destruction of methane. Importantly, C2H is a chemical product of destruction of larger hydrocarbons, so we note another relevant production of C2H_2 directly from methane photochemical products is CH+CH_2 $\rightarrow$ C2H_2+H. In an H_2-dominated atmosphere, the main production of C2H_2 occurs via C2H+H_2 instead of with CH_4 (as at Titan), and the main destruction is again via photolysis to form C2H+H occurs in the upper atmosphere.

In the H_2-dominated atmospheres, faster production and loss reactions occur in an inner cycle between C2H_2, C2H3, and C2H4 via reactions with H and H_2. Importantly, this exchange is imperfect; in the full profile C2H_2 reacts to form C2H3, which cycles back into C2H_2 only in the upper atmosphere. In the middle and lower atmospheres C2H3 reacts with H_2 to build C2H4 instead of C2H_2. C2H4 photolysis sources C2H_2 in the middle atmosphere.

In the middle atmosphere, most of these inner cycle reaction rates are comparable to the rates at Titan. However, the photolysis of C2H_2 is faster at Titan due

to a larger steady state concentration of C2H_2, and the production of C2H_2 via C2H+CH_4 is faster than C2H4 photolysis. Therefore, the inner cycle reactions are small compared to the main production/destruction reactions at Titan. At the H_2 dominated atmospheres though, the inner cycle is more important, where the photolysis rate is comparable to the inner cycle reaction rates.

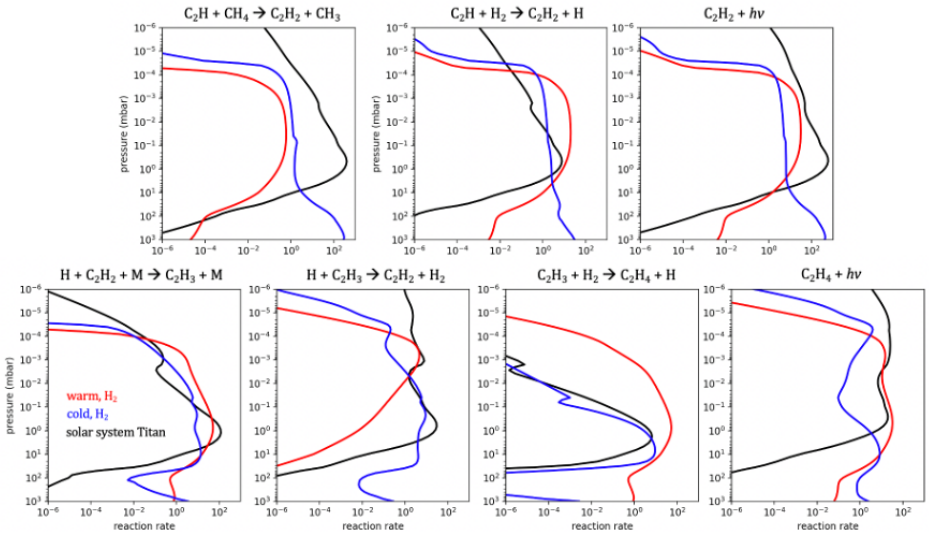

Figure 5.9: Rates (cm-3 s-1) of dominant production and loss reactions for C2H_2 in the top panel. Rates of exchange reactions between C2H_2-C2H3-C2H4 in the bottom panel. Black lines represent a cold N_2 atmosphere (Titan), blue lines represent a cold H_2 atmosphere, and red lines represent a warm H_2 atmosphere.

-CN species

In the mid-atmosphere, HCN loss to C2H3 becomes faster in the H_2-dominated warm atmosphere due to the faster formation of this radical via H+C2H_2 (Figure 5.10), resulting in a lower concentration 1 mbar. Photolysis of HCN still yields CN, yet in the H_2-dominated atmospheres, reactions to C2H_2 act as the primary production pathway to HC3N and C2H3CN, resulting in a narrower production peak near 0.1 microbar (due to the results of C2H_2 shown in 3.2.3).

Ethylene, C2H4

At Titan, C2H4 is formed from the reaction CH + CH_4 and lost to photolysis which yields C2H_2 and either H_2 or 2H. The CH3-CH_4 exchange described in 3.2.1 encourages the production of CH, thereby increasing the production rate of C2H4 in the warm H_2 atmosphere.

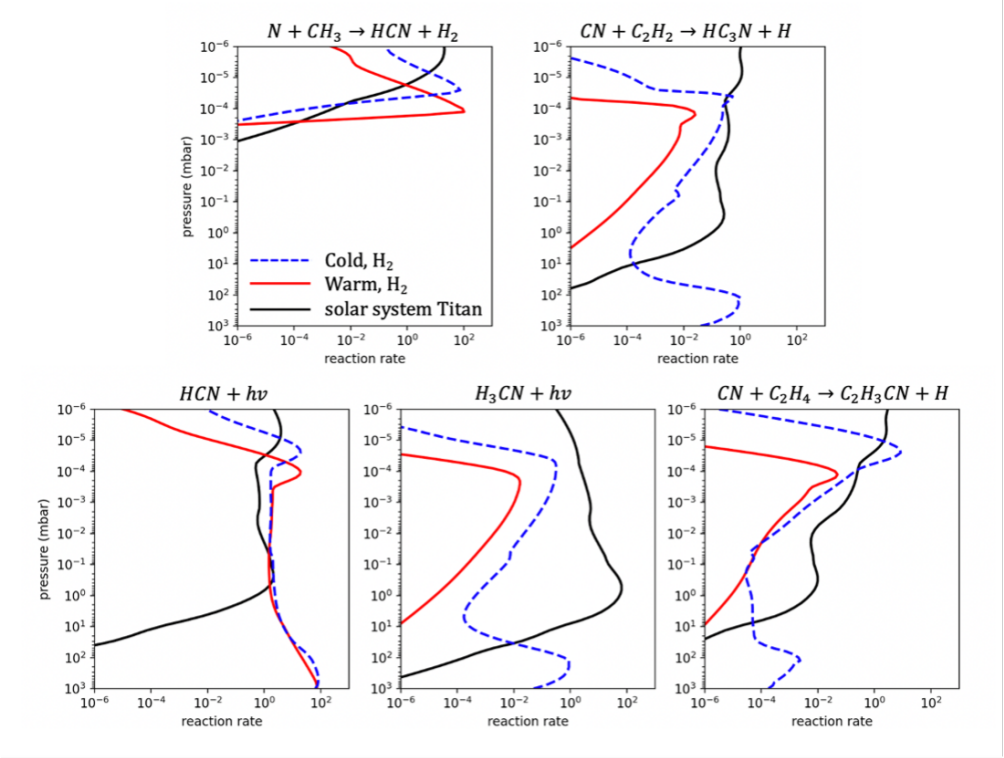

Figure 5.10: Rates (cm-3 s-1) of dominant production and loss reactions for -CN species. Black lines represent a cold N_2 atmosphere (Titan), blue lines represent a cold H_2 atmosphere, and red lines represent a warm H_2 atmosphere.

In addition to photolysis, in the H_2 atmospheres, C2H4 is lost to reactions with H_2 to form C2H5, and in the upper atmosphere, the latter reacts with H to form 2CH3. In the warm H_2 atmosphere, the CH3 may cycle back to methane, photolyze, and further encourage the production reaction CH+CH_4.

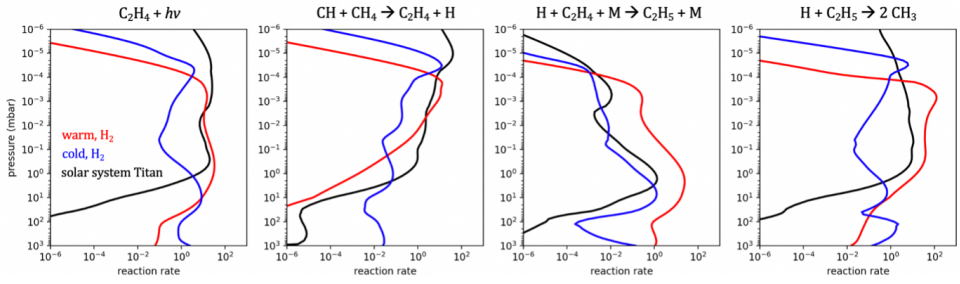

Figure 5.11: Rates (cm-3 s-1) of dominant production and loss reactions for C2H4. Black lines represent a cold N_2 atmosphere (Titan), blue lines represent a cold H_2 atmosphere, and red lines represent a warm H_2 atmosphere.

5.4 GJ 1132b: A Warm H_2 Atmosphere at a Close-In Orbit Around an M-Dwarf

Thus far we have examined, individually, the effect of changing the temperature, host star, semi-major axis, and stellar type. GJ 1132b is an interesting world with all of these parameters differing from the solar system Titan. Hubble Space Telescope (HST) observations revealed a warm (stratospheric T of 480 K), H_2-dominated atmosphere in an otherwise Titan-like atmosphere (90% H_2, 8.9% N_2, 0.3% HCN, 0.3% CH_4, 0.3% CO; Swain et al., 2021), and the world orbits an M-Dwarf at a close-in orbit of 0.01 AU (Bonfils et al., 2018).

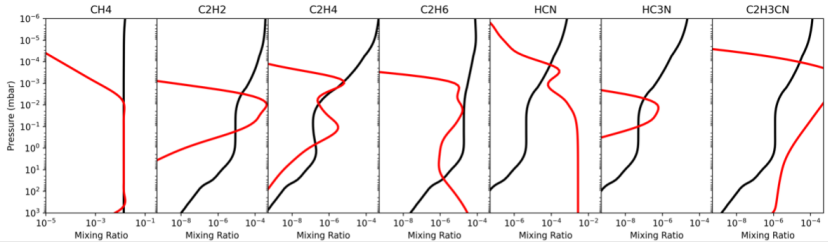

Figure 5.12: GJ 1132b (red lines; warm, H_2 dominated atmosphere at 0.01 AU away from an M-Dwarf host star) vs Titan (black lines; cold, N_2 dominated atmosphere at 9.55 AU away from the Sun). From left to right, the panels show C2H_2, C2H4, and C2H6.

The C2H_2 profile peaks just above 0.1 mbar, or near 1000 km. Above the peak, the rate of formation is limited by the rate of methane photolysis (due to a low number density). Centered near the peak, the fate C2H_2 is photolysis to C2H, which may cycle back into C2H_2. But, below the peak C2H_2 is lost to reactions with H to yield C2H3, which may either cycle back to C2H_2 or build larger hydrocarbons. The latter means reactions with H act as a more efficient net loss of C2H_2 than photolysis, hence decreasing the mixing ratio profile of C2H_2 in the regions below.

The C2H4 profile is comparable to that at Titan. At a close-in orbit around an M-Dwarf, photolysis of methane is efficient and thus synthesis of C2H4 via CH+CH_4 is fast. Meanwhile, photolysis of C2H4 (the main loss) is also efficient. Hence, the production and loss rates have been altered comparably and hence the steady state abundance of C2H4 is not majorly changed.

We find a depletion in the C2H6 profile due to the CH3-H_2 exchange reactions which efficiently recycle CH3 back to methane before two CH3 molecules may react to form C2H6.

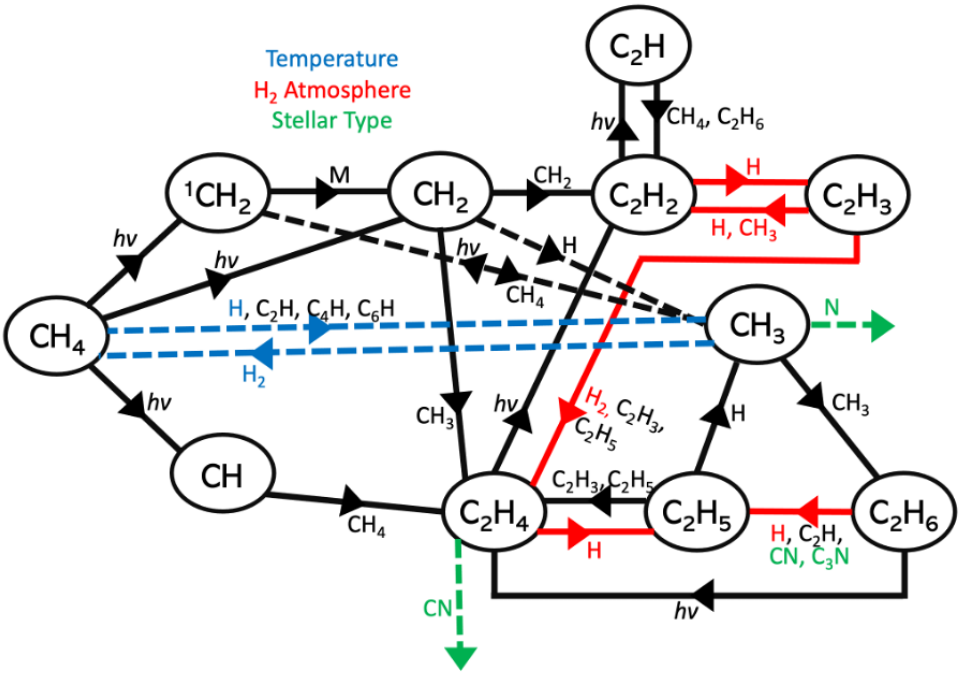

Figure 5.13: Diagram of important reactions relevant to hydrocarbon chemistry at Exo-Titans, based off the Titan chemistry presented in Yung et al. (1984). Reactions highlighted in blue show those with a large temperature dependence, thus dominating the chemistry in warmer atmospheres. Reactions highlighted in red show those which become significant in H_2-dominant atmospheres. Reactions highlighted in green show those which become significant at worlds around M-Dwarves.

5.5 Discussion

Model Validation

In this work, we extrapolate the known photochemistry of Titan (e.g., Willacy et al., accepted) to putative super-Earth conditions which will become testable in the new JWST era. In order to ensure valid predictions, we validate our model against atmospheric observations of the Titan atmosphere (Figure 5.15). Our lower boundary conditions of CH_4 are based on observations, forcing the lower atmosphere to agree with near-surface observations. The resulting photochemically produced hydrocarbons and N-bearing species roughly agree with the measurements from ALMA and Cassini. Our model overestimates the HCN profile in the lower atmosphere, which we speculate may be related to condensation processes, but the profile roughly matches in the upper atmosphere. Overall, the success of our model reproducing the observations in most regions demonstrates that our predictions of putative super-Earth atmospheres are grounded in a complete photochemical model.

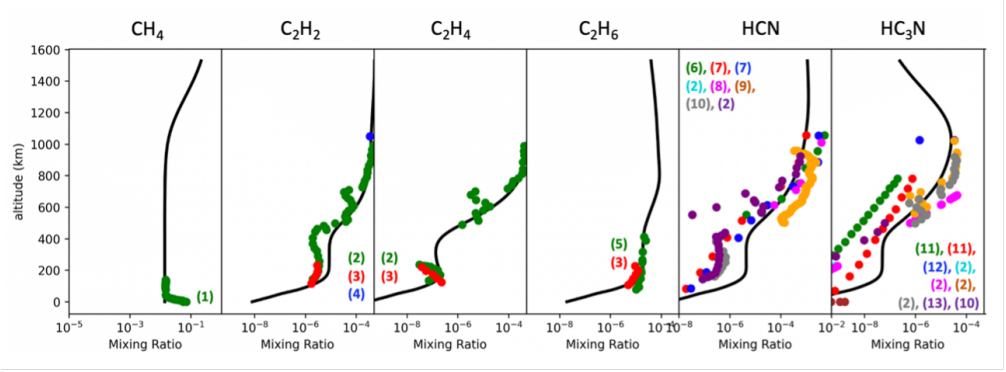

Figure 5.14: Mixing ratio profiles of CH_4, C2H_2, C2H4, C2H6, HCN, and HC3N at Titan. Model results are in black and overplotted dots show a comparison to recent observations in the literature: (1) Niemann et al. (2010); (2) Koskinen et al. (2011); (3) Nixon et al. (2013); (4) Magee et al. (2009); (5) Lombardo et al. (2019); (6) Adrian et al. (2011); (7) Kim et al. (2005); (8) Shemansky et al. (2005); (9) Vervack et al. (2004); (10) Vinatier et al. (2010); (11) Cordiner et al. (2014); (12) Cui et al. (2009); (13) Marteen et al. (2005)

Aerosols

Photochemical hazes are common in reducing atmospheres, as a result of methane and hydrocarbon destruction by solar UV photons and high-energy ions and neutrals, followed by polymerization of the radical species products. Hazes play important roles in radiative transfer, atmospheric dynamics, and atmospheric composition (e.g., Zhang et al., 2017), and they are predicted in atmospheres cooler than 1000 K (e.g., Gao et al., 2020). Therefore, hazes are common at solar system worlds with reduced atmospheric chemistry, having been revealed at Titan by Voyager (West et al., 1983; West and Smith, 1991) and Cassini (e.g., Tomasko et al., 2008; Lavvas et al., 2009; 2010), Pluto by New Horizons (e.g., Gao et al., 2017; Cheng et al., 2017; Fan et al., 2021), and Triton (e.g., Ohno et al., 2021). Photochemical hazes are also common at exoplanets and influence observables by acting as grey absorbers and muting spectral features (e.g., Adams et al., 2019; Kawashima Ikoma, 2019; Zahnle et al., 2016; Marley et al., 2013).

Our photochemical models predict notable photochemical production rates of haze material, assuming a soot (hydrocarbon-based) or tholin (N-bearing, hydrocarbon-based) composition. We find rates similar to the production rate at Titan regardless of stellar type or H_2 atmospheric content: 2.2e9 molecules/cm2/s at Titan; 2.5e9 molecules/cm2/s at a 2AU orbit around an M Dwarf; 1.2e9 molecules/cm2/s at a 5.6 AU orbit around a K star; 3.4e9 molecules/cm2/s for a warm H_2 atmosphere;

and 3.4e9 molecules/cm2/s for a cool H_2 atmosphere. However, the close-in orbits (e.g., GJ 1132b) host large photolysis rates of 8.0e13 molecules/cm2/s due to the greater flux of incident photons. The particle sizes are known to scale with production rate (controlled by this preceding photochemistry), which the role of hazes on radiative transfer is dependent on. A larger production rate could lead to more particles available to coagulate, resulting in larger particles. This result may skew observations by muting spectral features, although we note that other parameters may influence the microphysics of particle growth (such as gravity influencing sedimentation, dynamics influencing upward diffusion, and particle fractal dimensions influencing radiative transfer).

Predicted Observability

The new era of JWST begs the question of whether the predicted concentrations and chemistry found in this work are potentially testable. We find that the predicted concentrations at solar system Titan and Titan around an M-Dwarf are both not likely to be detected due to their atmospheres' small scale height. However, the larger scale height of the H_2 dominated atmospheres encourage a more feasible detection of the hydrocarbons and nitrile species. GJ 1132b is an especially interesting world: the large scale height, close-in orbit to a relatively smaller star, and greater concentration of HCN makes for potentially more feasible detections. We find that solar system Titan would yield spectral features of order 1 ppm, while GJ 1132b could yield spectral features of up to >150 ppm in a hazy sky and up to 1000 ppm in a clear sky.

We present results assuming both a hazy sky and clear sky at all worlds. As discussed in section 5.2, observations of Titan reveal tholin-like hazes which would mute spectral features, and our photochemical model predicts a haze production rate several orders of magnitude larger at GJ 1132b thereby worsening the outlook for detectability. A flat or sloped spectrum may be capable of muting the large spectral features predicted for GJ 1132b shown in Figure 5.15. In these results, we do not solve for the haze parameters, but instead assume an optically thick haze layer whose top is located at 10 Pa (motivated by the vertical extent of Titan's hazes; e.g., Rages Pollack, 1983; West et al., 2018). Exo-Transmit only considers extinction caused by the atmosphere above this pressure level. However, we note that the larger haze production rate at GJ 1132b (see section 5.2) may influence the haze properties to deviate from those at Titan.

We adapted Pandexo, an open source code which determines the noise floor of

JWST observations (Batalha et al., 2017), to GJ 1132b, and we find a noise floor of 400 ppm for NIRCAM's G395H instrument (acknowledging this value varies with wavelength dependences). Comparing to Figure 5.15 (bottom left panel), we predict the aerosols would mute spectral features below the noise floor for potential detection at GJ 1132b. The molecular features for the species presented in our work would be detectable in a clear sky at GJ 1132b (bottom right panel); however, we find those conditions to be unlikely provided the large haze production rate (see Section 5.2). While JWST detections of these predictions may be challenging, detection of these signals will likely be possible with future instruments dedicated for atmospheric characterization of transiting exoplanets.

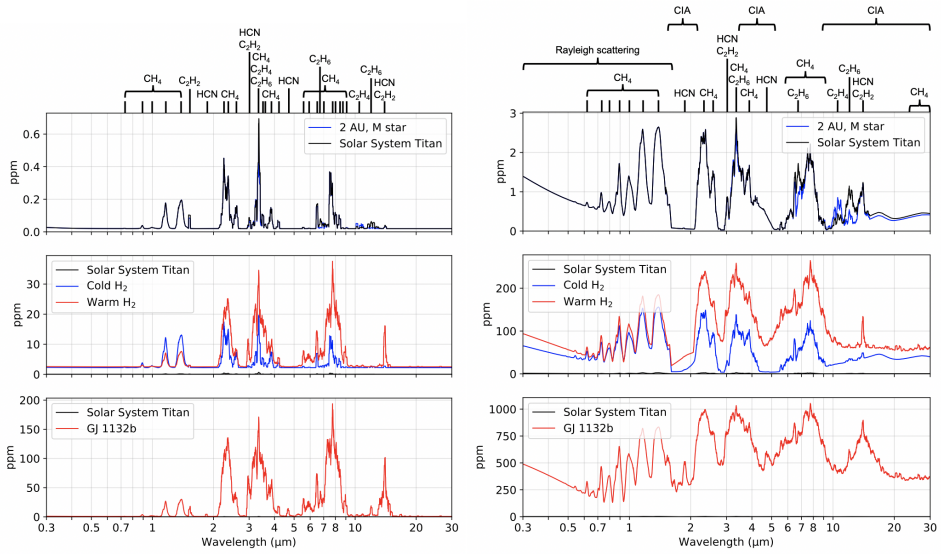

Figure 5.15: Computed transmission spectra for the bookend exo-Titan cases presented in this paper: (upper) solar system Titan vs. a 2 AU orbit around an M star; (middle) solar system Titan vs. a cold H_2-dominated atmosphere (blue) vs. a warm H_2 dominated atmosphere (red); (lower) solar system Titan vs. GJ 1132b. Notice the different y-axis scales, where the spectral features in the upper panel are well below detection thresholds and spectral features in the middle and the lower panels are much larger and potentially detectable with JWST. The absorption regions of detectable species are labeled above the uppermost panel. CIA, collision-induced absorption.

5.6 Conclusion

A larger H_2 abundance and warmer temperature increases the rate of the back reaction H_2 + CH3 $\rightarrow$ CH_4 + H, and the temperature dependence is so great that CH3 recycles back into CH_4 instead of forming C2H6. A larger H_2 abundance and warmer temperature also encourages interesting cycling between C2H_2, C2H3, and

C2H4 via reactions with atomic H. This results in a decreased column abundance of C2H6 and C2H_2 and relatively larger column abundance of C2H4 at close-in Exo-Titans with warm, H_2-dominant atmospheres than Titan, at a more distant orbit with a cool, N_2-dominant atmosphere. Meanwhile, close-in orbits around stars with greater shortwave photon emission result in faster N_2 photolysis and a greater availability of HCN, HC3N, and C2H3CN. We find these abundances may be detectable at close-in, H_2 dominated atmospheres (e.g., GJ 1132b) should these worlds have clear skies, but we caution the reader of large haze production rates which may mute these spectral features.

Chapter 6

AGGREGATE HAZES IN EXOPLANET ATMOSPHERES

6.1 Introduction

Exoplanet transmission spectra that display subdued molecular features and scattering slopes are seen across a wide swath of planet types, from Super Earths to hot Jupiters (e.g., Sing et al., 2016; Crossfield and Kreidberg, 2017). Aerosols have been used to interpret these observations, but their origins and composition are uncertain. In general, it has been suggested that hazes composed of small (< 0.1 microns) spherical particles, possibly stemming from photochemistry, produce the slopes in the optical and NIR regions of transmission spectra, while condensation clouds with larger spherical particles (1 micron) flatten spectra across all wavelengths (e.g. Barstow et al. 2017).

Photochemical hazes have been observed on many solar system bodies, including sulfuric acid aerosols in the upper haze of Venus, stratospheric sulfate aerosols on Earth (e.g., Lazrus and Gandrud, 1974; Turco et al., 1982), and hydrocarbon hazes on the giant planets (e.g., Wong et al., 2003; Koskinen et al., 2016), Titan (e.g., Rannou et al., 2010), Pluto (e.g., Gladstone et al., 2016), and Triton (e.g., Hillier et al., 1991). While some of these hazes are made up of spherical particles (e.g. Kawabata et al. 1980), others are composed of fractal aggregates - loose collections of smaller "monomers" that are highly porous and irregular in shape described by (e.g., Forrest and Witten, 1979; Sorensen and Roberts, 1997):

$$N = k_o(\frac{R}{r_m})^{D_f} \tag{6.1}$$

where R represents the radius of the fractal aggregate that is composed of N monomers, each of a radius r_m . The structural coefficient, k_o , is a prefactor that affects the fractal scaling relationship and the description of the particles' radiative properties. We assume k_o to be of order unity, as previous works have also done (e.g., Westetal.,1991; Wolfetal.,2010). D_f is the fractal dimension of the aggregate, which describes the porosity of the fractal. Zhang et al. (2013) investigated stratospheric aerosols on Jupiter using multiple-phase-angle images from the Cassini Imaging Science Subsystem (ISS) and ground-based near infrared (NIR) spectra. Stratospheric haze at 10-50 mbar, depending on latitude, was found to

be composed of fractal aggregate particles consisting of a thousand 10-nm sized monomers. At Titan, Tomasko et al. (2008) analyzed measurements from Huygens' Descent Imager/Spectral Radiometer (DISR). The aerosols' vertical distribution, phase function, and single scattering albedo were determined by multi-directional measurements from the UV photometers, and the single-scattering phase function of the aerosols between 30 and 80 km were found to be consistent with fractal aggregates. In the lower 30 km of Titan's atmosphere, the wavelength dependence decreased compared to that at higher altitudes, suggesting that the aerosols continued to grow with decreasing altitude. Robinson et al. (2014) analyzed spectral observations at Titan made by the Cassini spacecraft, and found that the aerosol distribution reached unit optical depth at pressures less than 0.1-10 mbar, depending on wavelength, which is comparable to the pressures probed by exoplanet transmission spectra. Gao et al. (2017a) compared numerical models of both spherical and aggregate hazes to New Horizons observations of UV extinction in Pluto's atmosphere. They determined that Pluto's photochemical hazes are composed primarily of fractal aggregate particles, though spherical particles may also be present, as inferred from forward scattering observations (Cheng et al. 2017).

Since fractal aggregates are common in solar system hazes, it is possible that exoplanet hazes may be similar. Kopparla et al. (2016), for example, examined the effects of aggregate hazes on the polarization of reflected light from giant exoplanets. However, they assumed a simplified haze layer in their model. Hazes, and aerosols in general, are controlled by microphysical processes that sculpt their particle size and spatial distributions, but haze models that have considered microphysical processes in the context of exoplanets have mainly examined the effect of spherical haze particles. Lavvas and Koskinen (2017) applied a 1D aerosol microphysics model to produce aerosol distributions on HD 209458b and HD 189733b. The aerosol distribution was found to depend on the particle composition, photochemical production rate, and atmospheric mixing. Soot aerosols were found to match the primary transit observations of HD 189733b. Morley et al. (2013) calculated the vertical profile of hydrocarbons in the atmosphere of GJ 1214b to derive haze particle distributions that could match the observed flat spectra. Particle sizes of 0.01-0.25 μm were found to best match the data, but condensation clouds were also considered. Kawashima and Ikoma (2018) developed a numerical model to simulate the production, growth, and settling of hydrocarbon haze particles on warm exoplanets (<1000 K). The size distribution of haze particles was fairly broad, and they concluded that the breadth of observed exoplanet spectra could be caused by variations in the production rate

of haze monomers due to the varying UV irradiation intensity of the host stars.

In this study, we apply an aerosol microphysics model that considers transport and coagulation over a multidimensional phase space to present a comprehensive analysis of haze opacity in giant exoplanet atmospheres. Specifically, this is the first study to consider the microphysics of aggregate haze particles in exoplanet atmospheres. We also apply our model to the super-Earth GJ 1214b, which has been observed extensively using space- and ground-based observatories, (e.g. Gillon et al., 2014, Kreidberg et al., 2014, Bean et al., 2010), and many observations reported flat spectra. Kawashima and Ikoma (2018) modeled spherical haze particles in the atmosphere of GJ 1214b but required a haze forming efficiency that was orders of magnitude greater than that of Titan in order to produce a flat spectrum, while at low haze forming efficiencies a sloped spectrum at optical wavelengths was produced due to haze scattering, with spectral absorption features of molecular species visible at longer wavelengths. Since spherical hazes did not fit the observations well when considering a haze forming efficiency comparable to that in the solar system, we consider the effect of aggregate hazes on GJ 1214b's transmission spectra.

We describe our methodology in section 2. In section 3, we analyze the effect of varying haze particle shape, monomer production rate, eddy diffusion coefficient, and monomer size on particle size distributions and haze opacity. In section 4, we discuss the impact of our assumptions and the implications of our results on transmission spectra of giant exoplanets and GJ 1214b. We present our conclusions in Section 5.

6.2 Model

We calculate the equilibrium haze particle size distribution using the 1-D Community Aerosol and Radiation Model for Atmospheres (CARMA; Turco et al., 1979; Toon et al., 1988; Jacobson and Turco, 1994; Ackerman et al. 1995; Bardeen et al., 2008; Wolf and Toon, 2010). CARMA solves the continuity equation of aerosol particles that experience production via particle nucleation, growth via condensation and coagulation, loss via evaporation, and transport. We follow the methodology outlined in Gao et al. (2017a) for Pluto hazes to simulate haze distributions in exoplanet atmospheres, where nucleation, condensation, and evaporation were ignored due to the low volatility of the haze material and the uncertain chemical pathway leading to haze formation. The change with time of haze particle number density,

$n_p(z)$, in the pth mass bin at altitude z is given by:

$$\frac{\partial n_p}{\partial t} = \frac{1}{2}\sum_{i=1}^{i=p-1} K_{i,p-i} n_i n_{p-i} - n_p \sum_{i=1}^{i=N} K_{i,p} n_i - \frac{1}{z^2}\frac{\partial (z^2 \Phi)}{\partial z} + \delta_{p,1}\delta_{z,z_{top}} P \qquad (6.2)$$

where $K_{i,j}$ is the Brownian coagulation kernel between particles in mass bins i and j and P is the production rate of the minimum mass particles at the top of the atmosphere, as represented by the Kronecker deltas, which specify that production only occurs at 1 microbar at the top of the atmosphere. The first term on the right hand side of Eq. (2) represents the increase in n_p due to the coagulation of smaller particles with total mass equal to that of particles in the pth mass bin; the second term represents the decrease in n_p due to coagulation of particles in the pth mass bin with other particles to generate more massive particles; and the third term represents vertical transport with Φ as the particle flux, defined as:

$$\Phi = -w_{sed} n - K_{zz} n \frac{\partial (n_p/n)}{\partial z} \qquad (6.3)$$

with w_{sed} as the sedimentation velocity, $\frac{\partial (n_p/n)}{\partial z}$ as the gradient in mixing ratio of the haze particles, and K_{zz} as the eddy diffusion coefficient. Note that all variables in Eq. (3) are functions of z. We refer the reader to the appendix of Gao et al. (2018a) for a full description of w_{sed} and $K_{i,j}$.

Each mass bin corresponds to particle masses twice that of the previous bin. We use 47 bins in our model, with the mass in the first bin corresponding to two monomers in the aggregate case and an equivalent mass in the spheres case. We assume a zero concentration lower boundary condition at 10 bars to simulate loss by thermal decomposition. The haze material mass density is taken to be 1 g/cm3, which is typical of organics including both hydrocarbon soots (e.g., Maricq et al., 2004; Rissler et al., 2013) and tholins (e.g., Trainer et al., 2006; Horst and Tolbert, 2013). The fractal dimension of aggregate particles is assumed to vary with the number of monomers per aggregate, as shown in Fig. 6.1, following the parametrization of Wolf and Toon (2010),where the smallest aggregates, with only two monomers, have a D_f of 1.5. Small aggregates have a low fractal dimension. This corresponds to "chain growth," in which monomers coagulate to form linear chain-like structures. As particles grow larger (1000 monomers), they restructure and collapse into more compact arrangements, resulting in a higher fractal dimension. We set D_f to a constant 2.4 for particles with more than 2000 monomers, an extrapolation of the parameterization of Wolf and Toon (2010) to larger aggregates than they considered.

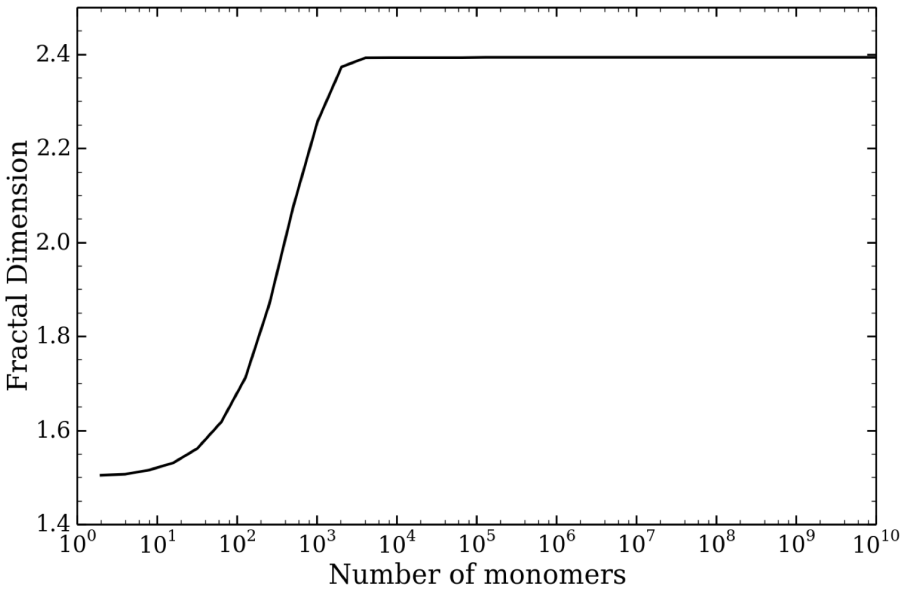

Figure 6.1: Variation of aggregate fractal dimension as a function of the number of monomers in the aggregate.

We consider haze particles composed of hydrocarbon soots, which are likely to survive in hot and warm giant exoplanet atmospheres due to their low volatility at high temperatures, and we use the refractive indices of soot that are presented by Lavvas and Koskinen (2017). As an alternative, we also consider hazes composed of tholins, which have been treated as a proxy for low temperature organic hazes on Titan and Pluto (Khare et al. 1984). As shown in Fig. 6.2, while the refractive indices of soots are smoothly varying, that of tholins show features at 3 and 6.5 microns, and are lower in value overall. In section 4.2, we compare the effect of tholin and soot hazes on hazy transmission spectra.

The optical properties of spherical particles are computed using the Mie scattering code of Grainger et al. (2004), and that of aggregate particles are computed following the methodology of Rannou et al. (1997). The nadir optical depth is defined as:

$$\tau_{nadir,z}(\lambda, z) = \sum_{i=1}^{z} \sigma_{ext}(\lambda, i) n_p \tag{6.4}$$

where σ_{ext} is the extinction cross section, further defined for spheres as:

$$\sigma_{ext} = Q_e \pi r_p^2 \tag{6.5}$$

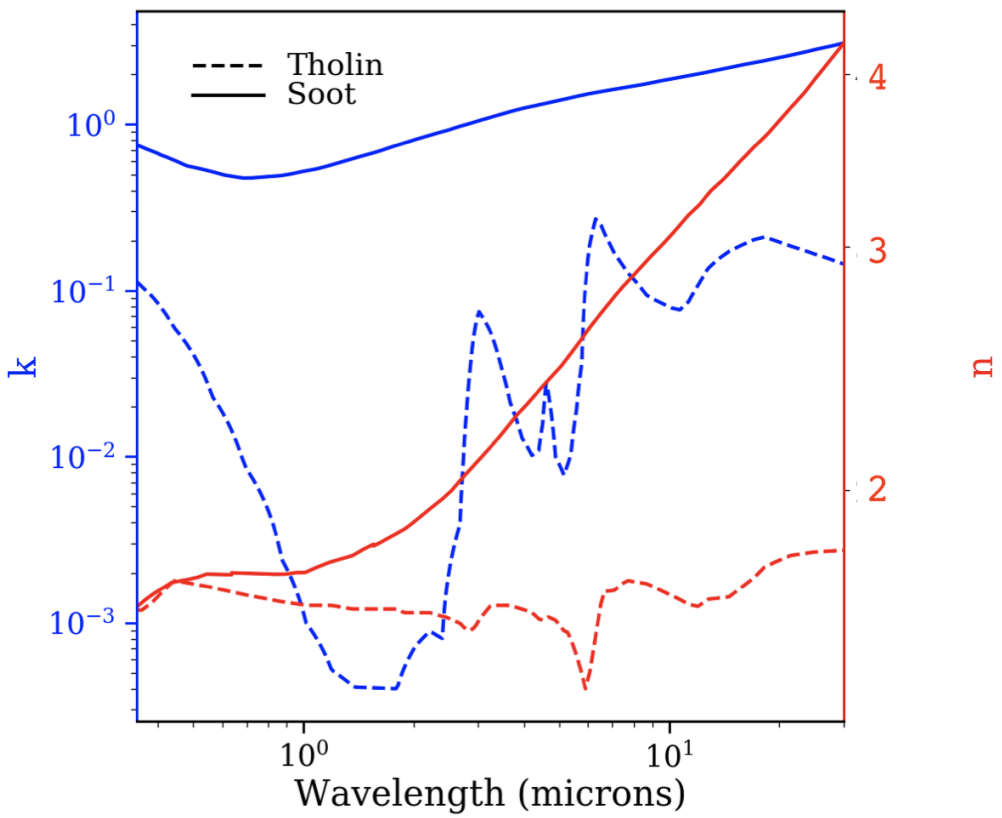

Figure 6.2: Real (n, red) and imaginary (k, blue) refractive indices of tholins (dashed) and soots (solid line).

where Q_e is the extinction coefficient. For aggregates, Rannou et al. (1997) treats each monomer as a Mie sphere, and the fractal structure (equation 1) allows for a description of the relative position between monomers in the aggregate. The scattered fields for each monomer are all summed, while taking into account the phase difference of the incident radiation on each spherical monomer as well as the scattered field due to the spacing of monomers. The monomers' relative positions and scattering terms can yield intensities, from which the cross sections are derived. We refer the reader to the Appendix of Rannou et al. (1997) for greater detail regarding this calculation.

We vary the monomer radius (r_m), eddy diffusion coefficient (K_{zz}), and production rate of haze particles at the top of the atmosphere at 1 microbar to determine their effects on haze opacity. We consider the following evenly log-spaced values: column mass production rate equivalent to $10^8, 10^9, 10^{10}, 10^{11}$ methane molecules $cm^{-2}s^{-1}$ (mass flux of 2.55 x 10^{-15} to 2.55 x 10^{-12} g $cm^{-2}s^{-1}$, K_{zz} of $10^8, 10^9, 10^{10} cm^2 s^{-1}$

and monomer size of 1 and 10nm. The production rate of photochemical aerosols is highly uncertain, but exoplanets can potentially have higher production rates than those seen on Titan (Horst et al., 2018), which has an estimated haze mass production rate of 0.5-2 x 10^{-14} g $cm^2 s^{-1}$ (McKay et al. 2001). Our investigated range of values is within those calculated by Lavvas and Koskinen (2017) with a photochemical model. Similarly, the value of K_{zz} is uncertain. Previous studies of exoplanet atmospheres considered values from 10^6 to $10^{10} cm^2 s^{-1}$ (e.g., Kawashima and Ikoma et al., 2018; Lavvas and Koskinen, 2017; Kopparapu et al., 2012, Miguel et al., 2014, Venot et al., 2015, Barman et al., 2015). The range of monomer sizes we consider also spans values used by previous studies. Gladstone et al. (2016) analyzed Rayleigh scattering observations to conclude that monomer sizes of 10 nm are expected at Pluto. Gao et al. (2017a) considered monomer sizes of 5 and 10 nm in their modeling study of Pluto's haze, and both Lavvas and Koskinen (2017) and Kawashima and Ikoma (2018) used 1 nm monomers for their exoplanet aerosol modeling work. Larger monomers (50 nm) have been considered for Titan, Jupiter, and additional modeling works (e.g., Tomasko et al. 2008; West Smith, 1991; Trainer et al. 2006; Wolf Toon, 2010), as well as produced in laboratory simulations (e.g., He et al., 2018), but we will primarily use the smaller monomer sizes so as to facilitate comparisons to previous exoplanet modeling studies.

We generate temperature-pressure profiles for solar metallicity giant exoplanets orbiting a Sun-like star using a 1D radiative-convective model (e.g., McKay et al., 1989; Marley et al., 1996) that has been previously applied to both hazy and clear atmospheres of solar system bodies, exoplanets, and brown dwarfs (e.g., Marley et al., 1999; Fortney et al., 2008; Saumon Marley 2008). We vary the distance from the host star (0.05 and 0.20 AU) to obtain two T-P profiles spanning 400-1750 K, which are shown in Figure 6.3. The planet's internal temperature is calculated using the results of Thorngren et al. (2018), which uses Bayesian inference and current observations of hot Jupiters to tie internal temperatures to their equilibrium temperatures. Unlike previous studies (e.g., Kawashima and Ikoma, 2018; Lavvas and Koskinen, 2017), our study does not consider photochemistry. Therefore, temperature affects only coagulation and sedimentation rates, as well as the amplitude of spectral features in the transmission spectra due to scale height differences. Photochemical pathways should differ between the 0.05 AU and 0.2 AU cases, as the carbon reservoir at high altitudes for the former is CO while that of the latter is methane (Figure 6.3). Recent laboratory work from Horst et al. (2018) showed that the rate of photochemical haze production for a high metallicity atmosphere

devoid of methane could reach 31% of that of Titan due to the presence of CO. This suggests that CO can replace methane as a progenitor of aerosols, though whether this is applicable to solar metallicity atmospheres is unknown. We investigate the differences in photochemical pathways by considering production rates that vary by several orders of magnitude. An alternative to carbon-based aerosols is the sulfur-based hazes originating from H_2S photochemistry (Zahnle et al., 2016), but they tend to emerge at lower temperatures than those considered here (Gao et al., 2017b).

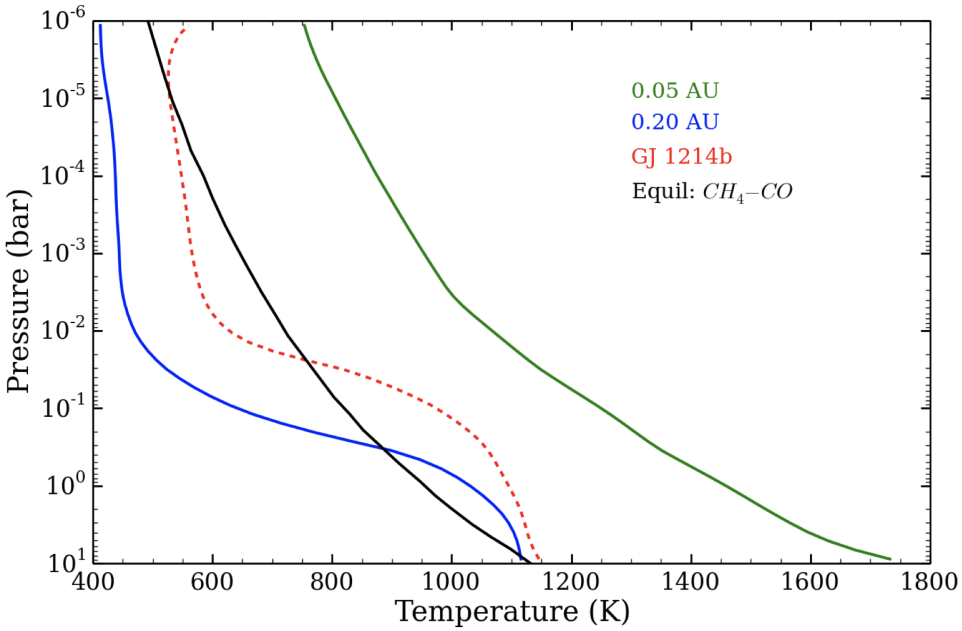

Figure 6.3: Temperature-pressure profiles of exoplanets at 0.05 AU (green) and 0.20 AU (blue) away from their host star, as well as GJ 1214b (dashed red). The chemical equilibrium $[CH_4]$=[CO] curve for a solar metallicity atmosphere is shown in black.

We use the same radiative-convective model to generate a TP profile for GJ 1214b, assuming 100x solar metallicity. As in Morley et al. (2013, 2015), we use k-coefficients for a 50x solar metallicity atmosphere multiplied by 2 for the molecular opacity. For the Kzz profile, we consider the parameterization specific to the 100 x solar metallicity GJ 1214b case from Charnay et al. (2015), given by:

$$K_{zz} = 3x10^7 P^{-0.4} \tag{6.6}$$

with P in bars and K_{zz} in cgs units. We consider a column rate of production of 1 nm monomers limited by the diffusion flux of methane into the upper atmosphere,

$$P(z) = nK_{zz}\frac{df}{dz} \tag{6.7}$$

with an atmospheric number density n and an eddy diffusivity K_{zz} at the top of the atmosphere (1 microbar). The methane mixing ratio gradient $\frac{df}{dz}$ is computed assuming total methane photolysis within a scale height (220 km) above 1 microbar. We calculate the methane mixing ratio at 1 microbar assuming thermochemical equilibrium using the Chemical Equilibrium with Applications code (Gordon and McBride, 1994), yielding 30 ppm. This results in a mass production rate equivalent to $1.3 \times 10^1 1 CH_4$ molecules $cm^{-2}s^{-1}$. Note that this value is much smaller than that of Kawashima and Ikoma (2018), who assumed a photon-limited production rate that scaled with lyman alpha flux.

6.3 Results

Size Distributions

Scattering efficiency depends on the particle size relative to the wavelength of light, and therefore the size distributions of haze particles are critical in determining the spectral response. Here, size distributions for aggregate and spherical particles are compared, while varying monomer size, production rate, and the eddy diffusion coefficient. Throughout the atmosphere, aggregate haze particles tend to be larger. This is due to aggregate particles having an irregular shape with a greater cross sectional area than spherical particles of the same mass. This larger cross section allows for an increased number of regions for particles to collide and stick, in comparison to spherical particles. This dependence of coagulation on particle shape is demonstrated by the spatial and size distributions shown in Fig. 6.4. Aggregate haze particles coagulate to produce a broad distribution centered at a few microns and extending beyond 10 microns, while coagulation of spherical haze particles results in a narrower distribution centered at sizes 0.3 micron and extending out to only 1 micron.

The difference between the two particle types is further demonstrated by comparing the size distributions explicitly in Fig. 6.5. The aggregate and spherical size distributions peak at 2.5 and 0.16 microns, respectively. Due to their greater sizes, it is expected that aggregate particles obscure observations at longer wavelengths more effectively than spherical particles.

The size distributions are altered by variations in the production rate, eddy diffusion coefficient, and monomer size. An increased production rate allows for more

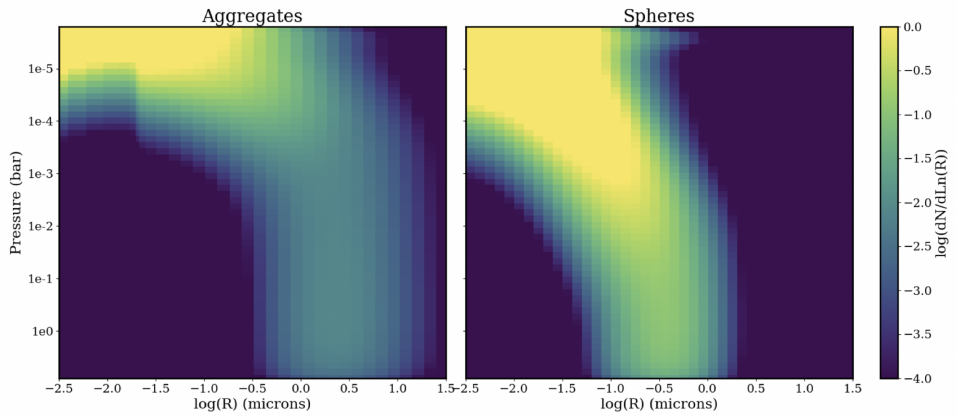

Figure 6.4: Color map of particle size distributions with respect to atmospheric pressure for aggregate particles (left) and spherical particles (right). Parameters were chosen to maximize the haze mass loading, with a mass production rate equivalent to 1011 methane molecules cm-2s-1 (maximum), an eddy diffusion coefficient of 108 cm2s-1 (minimum), and a monomer size of 1 nm (minimum).

particles to collide and stick together, resulting in the formation of larger particles. As shown by Fig. 6.6, the enhanced production rate yields size distributions that peak at radii 24 and 8 times larger for aggregate and spherical particles, respectively. Aggregate haze particles respond to changes in production rate more significantly than spherical haze particles. This is due to their larger cross sections and correspondingly increased collision frequency.

Increasing K_{zz} increases the rate of vertical transport of the haze particles, by definition. Allowing the particles to be transported through the atmosphere faster provides decreased time for collisions and coagulation, and this therefore results in smaller particles, as shown in Fig. 6.6. At a sufficiently high K_{zz}, the haze particles stay small such that no separate coagulation size mode forms.

Monomer size influences the aggregate size distributions due to porosity effects, and the difference in shape of the aggregate distribution is due to the fixed N versus D_f relationship, given by Figure 6.1. As shown in Fig. 6.6, the aggregate size distributions peak at 2.5 and 0.77 microns for rm of 1 and 10 nm, respectively. On the other hand, spherical particles are by definition not porous and their size distributions do not significantly respond to variations in monomer radius. For spherical particles, increasing the monomer size only increases the initial particle size, allowing larger particles to exist at lower pressures, though in lower number densities. Larger particles higher in the atmosphere have different coagulation rates

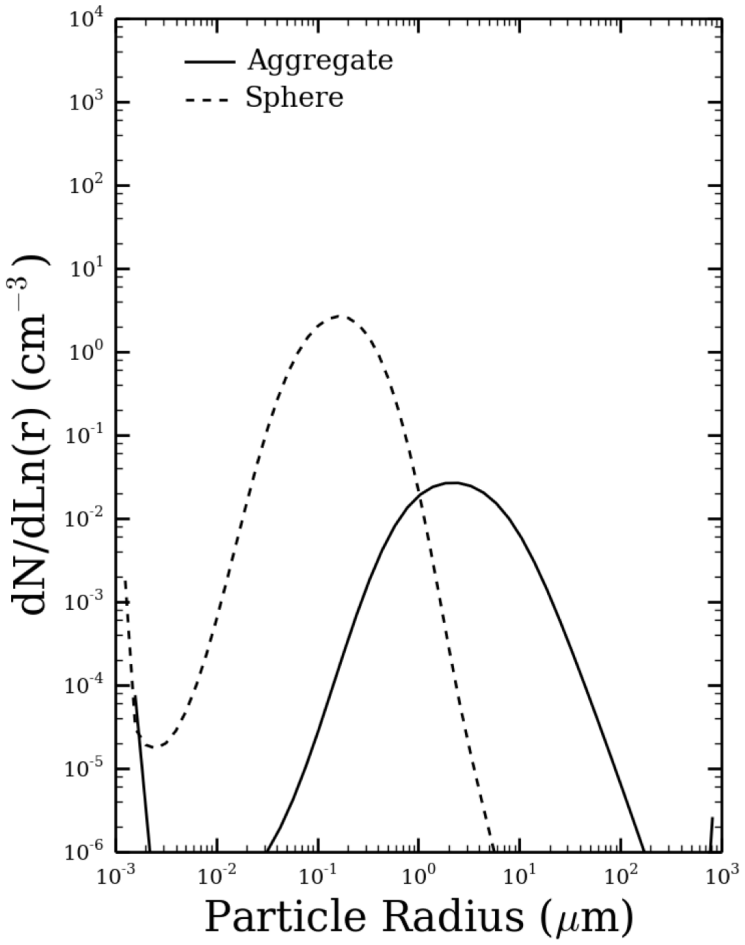

Figure 6.5: Size distributions for spherical (dashed) and aggregate (solid) particles. Parameters were chosen to maximize the haze mass loading, with a mass production rate equivalent to 1011 methane molecules cm-2s-1 (maximum), an eddy diffusion coefficient of 108 cm2s-1 (minimum), and a monomer size of 1 nm (minimum).

than had they been produced a few scale heights down. This yields slightly offset size distributions for different monomer sizes, as demonstrated in Fig. 6.6.

Optical Depth

We first calculate the optical depth at each altitude layer. The nadir optical depth at a given pressure level is then calculated by summing the optical depths of the layers above, given by:

$$\tau_{nadir,i}(\lambda) = \sum_{i=1}^{n} \tau_n(\lambda) \tag{6.8}$$

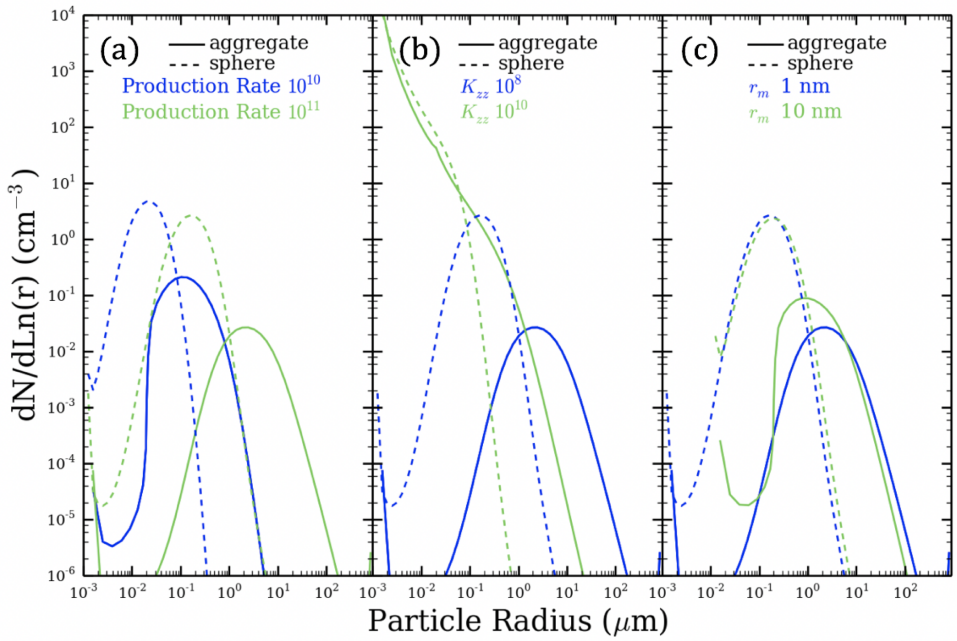

Figure 6.6: Size distributions are compared at 2.8 mbar (in the middle of our model atmosphere) for spherical and aggregate particles, while varying (a) production rate, (b) diffusion coefficient, and (c) monomer size. Aggregate and spherical haze particles are shown in solid and dashed profiles respectively. Green profiles represent the lower value for the varied parameter and blue represents the greater value. The following parameters were used in each figure: (a) $K_{zz} = 10^8 cm^2 s^{-1}$ and rm = 1 nm, (b) mass production rate equivalent to 10^{11} methane molecules $cm^{-2}s^{-1}$ and rm=1 nm, (c) mass production rate equivalent to 10^{11} methane molecules $cm^{-2}s^{-1}$ and $K_{zz} = 10^8 cm^2 s^{-1}$.

Similar to the size distributions, the nadir optical depth is unique to particle shape as well. The wavelength dependence of the spherical haze optical depth is significant, in comparison to that of aggregate hazes, as shown in Fig. 6.7. When wavelength is increased from 0.4 to 30 microns, the nadir optical depth for aggregate particles decreases by a factor of 3 while nadir optical depth for spherical particles decreases by nearly two orders of magnitude, given the same values for the other parameters. Aggregates generally have a greater optical depth than spheres, with the exception of high altitude hazes at a wavelength of 0.4 microns. High in the atmosphere at 10 microbar, spherical particles grow to become moderately opaque at 0.4 microns. By comparison, aggregates grow to larger sizes more quickly, such that, while they can block more light per single particle, their number density is much lower. This allows spheres to be more opaque at 0.4 microns high in the atmosphere. At greater pressures, coagulation of spheres also reduces their number density.

Thus, while the extinction coefficient of spherical particles remains small (2), that of aggregates, computed assuming the cross sectional area of an equivalent-mass sphere, increases (from 12 to 20). The change in both density and extinction coefficient allows aggregates to become more opaque deeper in the atmosphere. At 3 microns, however, spheres have a much lower extinction coefficient (0.2) than aggregates (32) at the top of the atmosphere, and the larger particles of aggregates are more efficient at scattering long wavelengths of light. Hence, at this wavelength, aggregates are more opaque than spheres at all levels of the atmosphere.

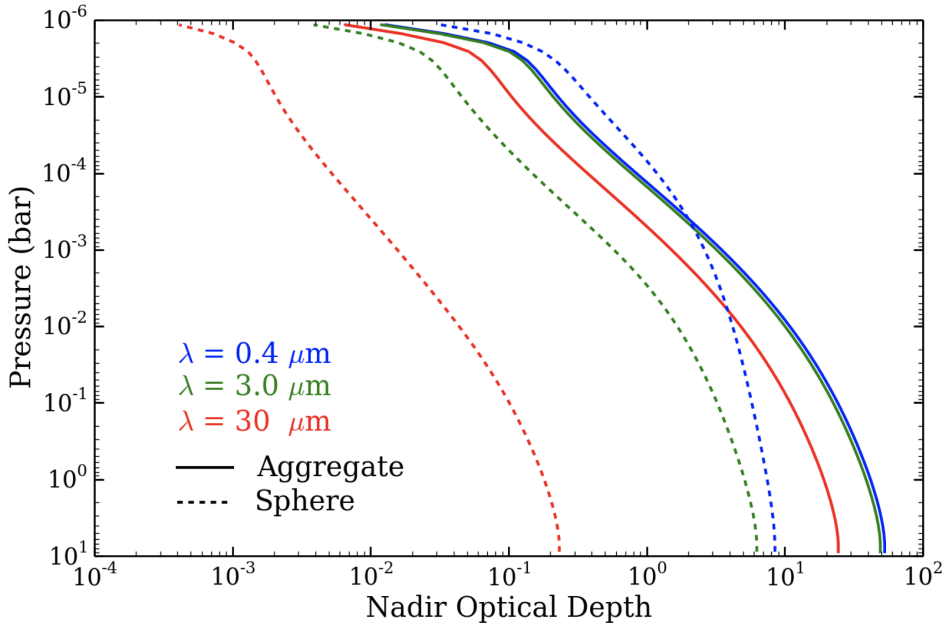

Figure 6.7: Nadir optical depth profiles for aggregate (solid) and spherical (dashed) haze particles at wavelengths of 30 (red), 3 (green), and 0.4 microns (blue). Mass production rate equivalent to 10^{11} methane molecules $cm^{-2}s^{-1}$, eddy diffusion coefficient of $10^{8}cm^{2}s^{-1}$, and monomer radius of 1 nm were used.

The pressure level of unit optical depth as a function of wavelength dictates the maximum depth to which observations may probe, particularly for thermal emission; transmission observations probe lower optical depths. As a result of the difference in the wavelength dependence of optical depth of the two particle shapes, aggregate particles are more efficient at obscuring molecular spectral features at long wavelengths than spherical particles (Fig. 6.8), as aggregate hazes reach unit optical depth higher in the atmosphere and across a broader range of wavelengths. At short wavelengths ($\lambda < 0.5\mu m$) spherical and aggregate hazes reach an optical depth of unity at a comparable pressure level in the atmosphere. For example, in comparing

opacity at 0.35 and 10 microns in Fig. 6.8, unit optical depth occurs 7 scale heights and <1 scale height deeper in the atmosphere for spherical and aggregate hazes respectively.

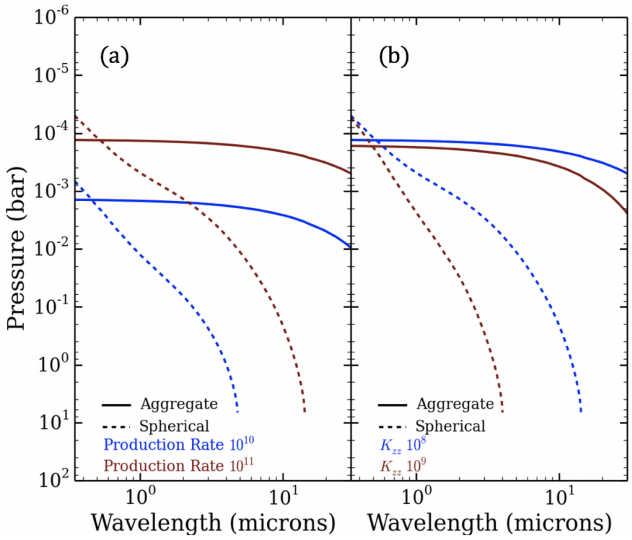

Figure 6.8: Comparison of the pressure levels at which the nadir optical depth reaches unity for aggregate and spherical hazes while varying (a) production rate and (b) eddy diffusion coefficient. The pressure of unit nadir optical depth for aggregate and spherical hazes are depicted by solid and dashed profiles, respectively. Blue profiles correspond to the lower value of the varied parameter, and red profiles correspond to the greater value. The following parameters were used in each figure: (a) $K_{zz} = 10^8 cm^2 s^{-1}$ and $r_m = 1$ nm and (b) mass production rate equivalent to 10^{11} methane molecules $cm^{-2} s^{-1}$ and r_m =1 nm.

Increasing production rate increases the number density of large particles at low pressures and results in optical depth reaching unity higher in the atmosphere. The haze particle sizes at the unit optical depth level does not change significantly, however, so the slopes of the unit optical depth level are not affected (Fig. 6.8). However, increasing the eddy diffusion coefficient results in smaller particles due to faster transport and decreased time for coagulation, resulting in steeper slopes for the unit optical depth level (Fig. 6.8), as smaller particles are less efficient at scattering at longer wavelengths.

Increasing the monomer size from 1 to 10 nm leads to a minor increase in the altitude at which unit optical depth occurs in the atmosphere (Fig. 6.9). For aggregate hazes, the size distribution of haze particles composed of 10 nm monomers peaks at smaller sizes but the distribution is broader. The slope of the unit optical depth level is mainly consistent between the 1 and 10 nm monomer size cases, but unit

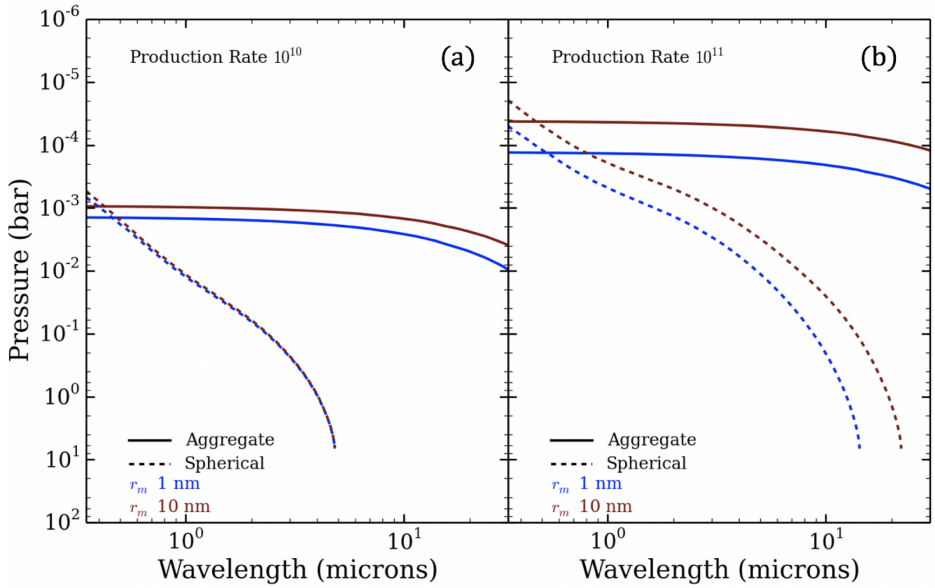

Figure 6.9: Level of unit optical depth with monomer sizes of 1 (blue) and 10 (red) nm for aggregate (solid) and spherical (dashed) haze particles. A production rate of 10^{10} methane molecules $cm^{-2}s^{-1}$ and eddy diffusivity of $10^{8}cm^{2}s^{-1}$ were considered.

optical depth occurs deeper in the atmosphere with 1 nm monomers. This effect may be due to the relationship between N and D_f, in which for a 2 constant N and particle radius, the fractal dimension increases with an increasing monomer size. However, the vertical shift of this level is relatively small, and the uncertainties regarding the relationship between N and D_f likely dominate any conclusions one could make about a difference in haze opacity caused by monomer size. Also, the effect of monomer size on the level of unit optical depth is found to depend on production rate: given P = 10^{10} molecules $cm^{-2}s^{-1}$ (Fig. 6.9), a minor shift in haze opacity between the 1 and 10 nm monomer cases is observed for aggregates and no difference is observed for spherical particles; increasing the production rate to 1011 (Fig 9b) results in a greater shift between the two aggregate cases and causes a shift to develop between the spherical 1 and 10 nm cases. This dependence on production rate exemplifies the effect of the uncertainties regarding N vs D_f, and suggests that monomer size alone may not have a significant effect on haze opacity. We also tested the impact of having 50 nm monomers on haze optical depth and found that it continued the trend seen previously with 1 nm and 10 nm monomers, in that the optical depth increased, and so for clarity we do not include those results here.

It is common for haze particles in planetary atmospheres in the solar system to have a potential charge on their surface, or charge density parameter, of up to 30 $e^{-}\mu m^{-}1$, or 30 electron charges per unit particle radius on a particle's surface (e.g., Borucki et al. 1987; Lavvas et al., 2010; Larson et al. 2015; Gao et al. 2017a). A nonzero charge density parameter can affect coagulation rates and therefore particle size. We therefore considered the effect of varying charge density from 0 to 30 $e^{-}\mu m^{-}1$. For spherical particles, the presence of charge results in slightly smaller particles and decreased opacity at long wavelengths, while for aggregates the effect was insignificant, as shown in Fig. 6.10. Despite the larger size of aggregate particles, we surmise that the corresponding coagulation rate is sufficiently high that charge effects become negligible. We consider zero charge density for all other results in this study.

Several cases produced optically thin hazes that never reached unit nadir optical depth in the atmosphere, such as hazes yielding from mass production rates $\leq 10^{9}$ methane molecules $cm^{-2}s^{-1}$ and Kzz = 10^{10} $cm^{-2}s^{-1}$. Transits probe slant optical depths and may detect opacity not viewed from the top down. This is shown in the generated transmission spectra in section 4.1.

Application to GJ 1214b

Similar to the results shown in our giant exoplanet cases, size distributions of aggregate hazes in the atmosphere of GJ 1214b extend to larger particle sizes than that of spherical hazes, while a greater production rate leads to larger particles for both aggregate and spherical hazes, as shown in Fig. 6.11. Likewise, the depth of unit nadir optical depth is less wavelength dependent for aggregate than spherical hazes, and a greater production rate produces hazes of unit optical depth significantly higher in the atmosphere, as shown in Fig. 6.11. From these results, it is clear that aggregate and spherical hazes would have significantly different effects on the transmission spectrum of GJ 1214b.

6.4 Discussion

Transmission Spectra of Warm Giant Exoplanets and GJ 1214b

Since photochemical hazes can dominate spectra of exoplanet atmospheres, we follow the methodology of Fortney et al. (2003, 2010) to generate synthetic transmission spectra to explore the variety of observations possible given the parameter space we have considered in this study. We find that aggregate hazes can generate flat spectra, similar to condensate clouds, since aggregate hazes allow for larger

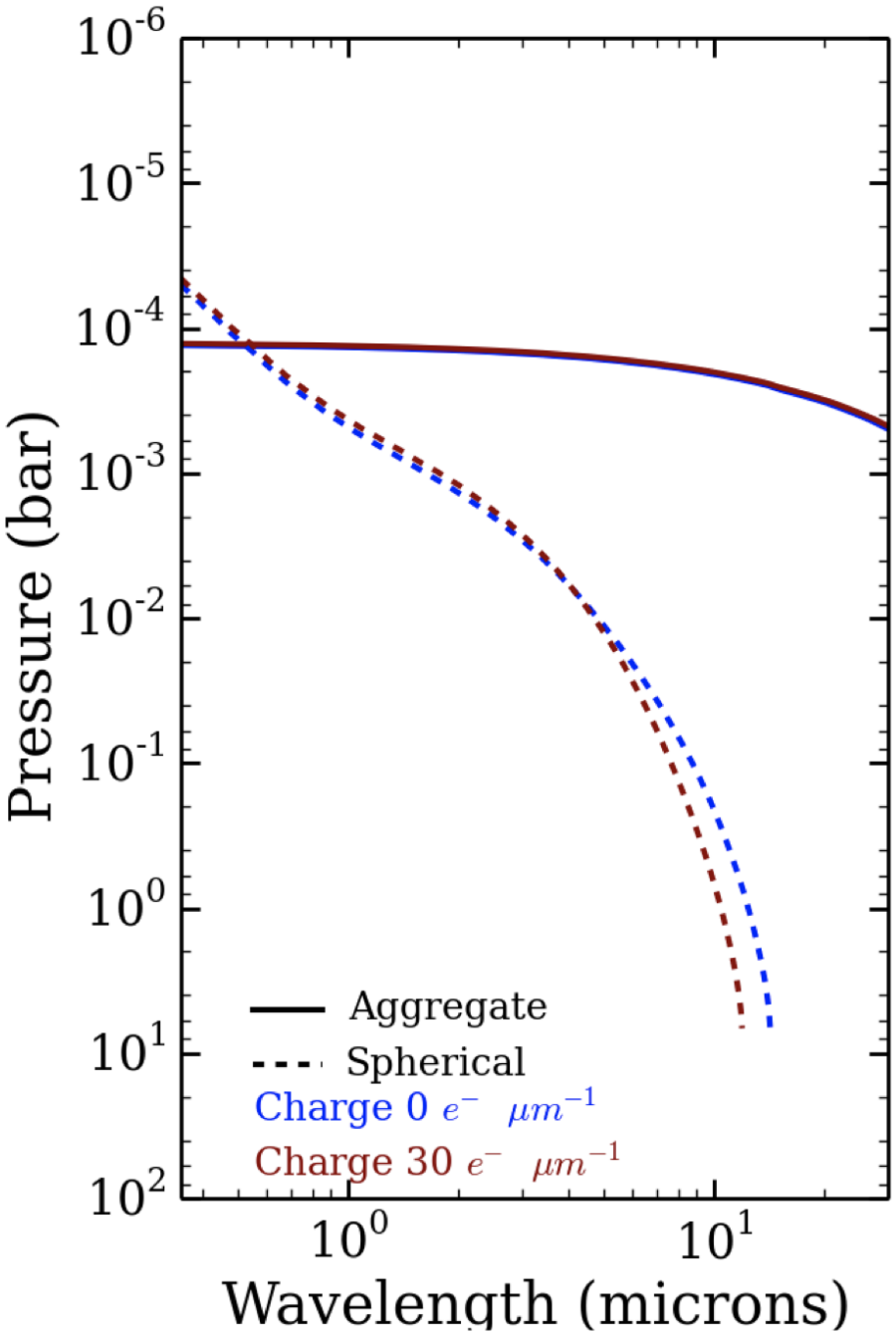

Figure 6.10: Comparison of the pressure level at which unit optical depth occurs when charge is varied from 0 $e^-\mu m^-1$ (blue) to 30 $e^-\mu m^-1$ (red) for both aggregate (solid) and spherical (dashed) haze particles. The following parameters are used to generate these profiles: mass production rate equivalent to 10^{11} methane molecules $cm^{-2}s^{-1}$, eddy diffusion coefficient of $10^8 cm^{-2}s^{-1}$, and monomer size of 1 nm.

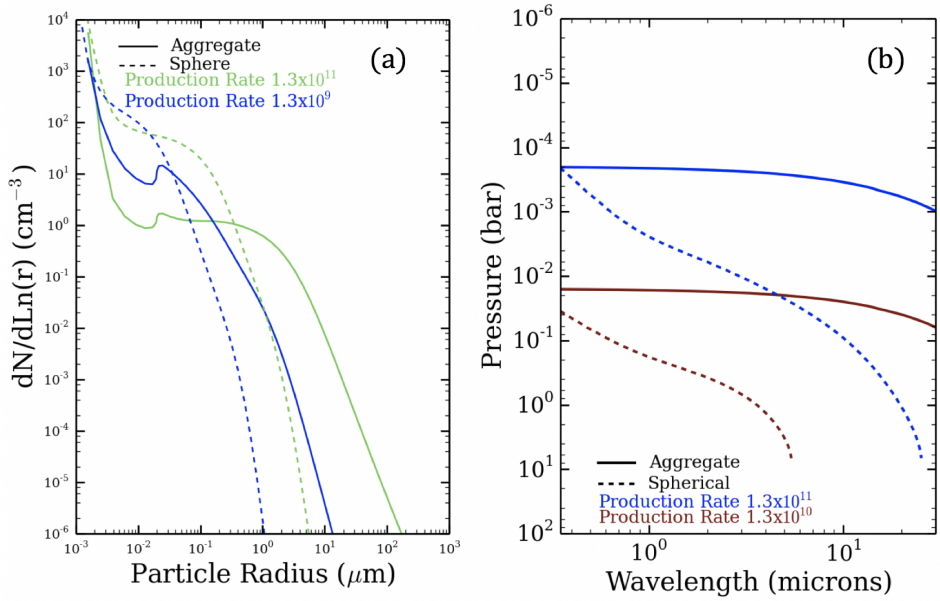

Figure 6.11: (a) Particle size distributions for GJ 1214b with aggregate (solid) and spherical (dashed) hazes. A mass production rate equivalent to 1.3×10^{11} (green) and 1.3×10^{9} molecules $cm^{-2}s^{-1}$ (blue) were considered. (b) The depth of unit nadir optical depth of GJ 1214b for aggregate (solid) and spherical (dashed) hazes. A mass production rate equivalent to 1.3×10^{11} (blue) and 1.3×10^{10} molecules $cm^{-2}s^{-1}$ (red) were considered.

particles to form. By contrast, we are unable to produce flat spectra with spherical haze particles despite the large range in the values considered for production rate, eddy diffusivity, and monomer radius. For example, in Fig. 6.12, high production rate ($10^{1}1$ molecules $cm^{-2}s^{-1}$) and low eddy diffusivity ($10^{8}cm^{2}s^{-1}$) results in high opacity hazes for both aggregate and spherical haze particles. The spectra with aggregate haze particles are nearly flat across all wavelengths, while the spectra with spherical haze particles are sloped. In hazy conditions, spherical haze particles can obscure most molecular spectral features at wavelengths shorter than 1 micron, but with increasing wavelength, spectral features become more distinct.

The effect of varying eddy diffusivity and production rate on transmission spectra mirrors that on the unit optical depth pressure level. Smaller molecular features are produced with greater production rates and lower eddy diffusivity values due to increased haze opacity. In contrast, varying monomer size results in the opposite effect in transmission as in the nadir view. This is caused by the different regions probed by the two viewing geometries, as well as the more complicated relationship between monomer size and haze opacity, as shown in Fig 13. 1 nm monomer cases

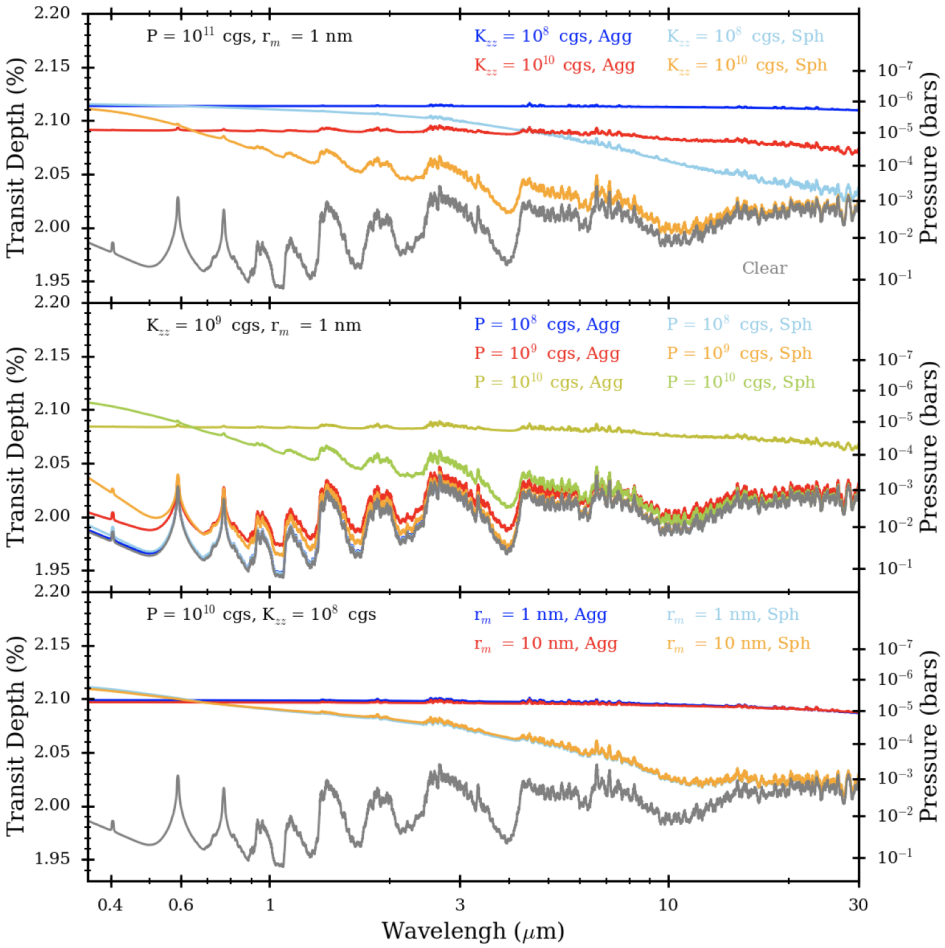

Figure 6.12: Computed transmission spectra for the 0.05 AU atmosphere with hazes considering: (a) K_{zz} of 10^8 (blue and light blue) and $10^{10} cm^2 s^{-1}$ (red and orange) for aggregate (blue and red) and spherical (light blue, orange) hazes. Mass production rate equivalent to 10^{11} methane molecules $cm^{-2}s^{-1}$ and r_m = 1 nm are used. (b) Mass production rates equivalent to 10^8 (blue and light blue), 10^9 (red and orange), and 10^{10} (yellow and green) methane molecules $cm^{-2}s^{-1}$ are considered for aggregate (blue, red, and yellow) and spherical (light blue, orange, and green) haze particles. K_{zz} =$10^9 cm^2 s^{-1}$ and r_m = 1 nm are used. (c) Monomer radii of 1 (blue and light blue) and 10 nm (red and orange) are considered for aggregate (blue and red) and spherical (light blue and orange) haze particles. Mass production rate equivalent to 10^{10} methane molecules $cm^{-2}s^{-1}$ and K_{zz} of 10^8 $cm^2 s^{-1}$ are used. The transmission spectrum of the clear atmosphere is shown in grey.

show a jump in opacity at the top of the atmosphere before a more gradual increase at higher pressures, while 10 nm monomer cases show a more smooth increase in optical depth. The "jump" for 1 nm monomer cases likely arises due to the forced constant mass flux at the top of the atmosphere, which causes 1 nm monomer haze

particles to be more numerous there. Since the coagulation rate is proportional to the square of the number density, 1 nm monomer cases (and the equivalent cases for spherical particles) coagulate faster at the top of the atmosphere, producing larger particles that increase haze opacity. Lower in the atmosphere, farther away from the haze production site, coagulation reaches equilibrium, allowing size distributions and haze opacity to become consistent across monomer radius (as observed for the lower production rate, spherical haze case in Fig. 6.13). Greater production rates exaggerate the difference between coagulation rates at the top of the atmosphere between the 1 and 10 nm monomer cases.

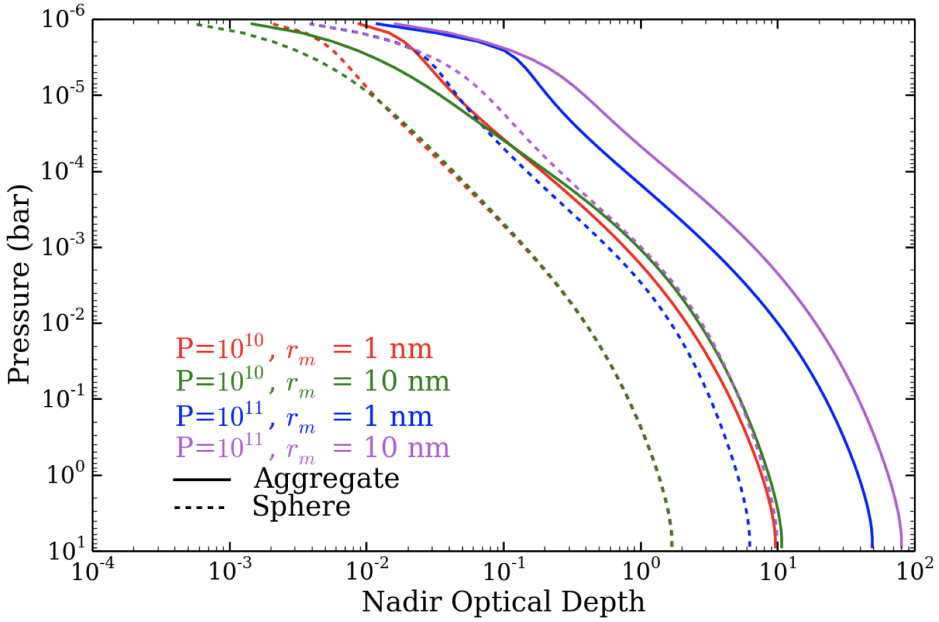

Figure 6.13: Effect of monomer radius on haze opacity depends on production rate and pressure. The nadir optical depth of aggregate (solid) and spherical (dashed) hazes are shown, and production rates of 10^{10} (red and green) and 10^{11} (blue and purple) methane molecules $cm^{-2}s^{-1}$ and monomer radii of 1 (red and blue) and 10 (green and purple) nm are considered.

It is evident that transmission spectra could be highly sensitive to haze properties. For example, increasing the production rate in Fig. 6.12 from 10^8 and 10^9 molecules $cm^{-2}s^{-1}$ does not significantly change the prominence of molecular spectral features. However, increasing the production rate another order of magnitude, from 10^9 to 10^{10} molecules $cm^{-2}s^{-1}$ results in very hazy conditions, with minimal spectral features. Since the production rate is a poorly constrained parameter for exoplanets (as discussed in Section 1), this sensitivity emphasizes the breadth of observations possible within this parameter space, as discussed by Kawashima and Ikoma (2018).

Spherical and aggregate hazes do not significantly differ across atmospheric temperature profiles with a fixed production rate, eddy diffusivity, and monomer radius. The obscuration of molecular features is comparable for planets at 0.05 AU and 0.20 AU as shown in Fig. 6.14, with the main difference due to the significantly different scale heights between the two cases. Note that we do not consider photochemistry or atmospheric dynamics in our model, so production rate and eddy diffusivity are not affected. Instead, only the temperature responses of transport and coagulation rates are considered.

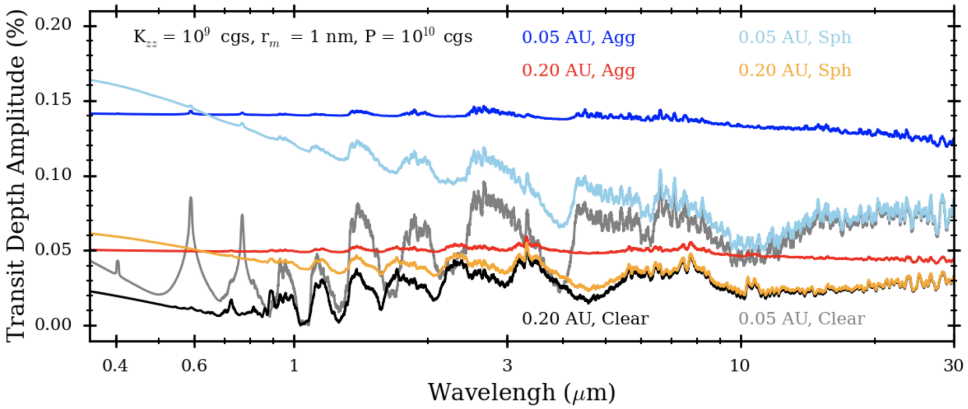

Figure 6.14: Transmission spectra models for planets at 0.05 AU (blue and light blue) and 0.20 AU (red and orange) with aggregate (blue and red) and spherical (light blue and orange) haze particles. The following parameters were considered: $K_{zz} = 10^9 cm^2 s^{-1}$, mass production rate equivalent to 10^{10} methane molecules $cm^{-2}s^{-1}$ and r_m = 1 nm. The minimum transit depth value of the clear cases was subtracted from the spectra in order to compare the two atmospheres across different planetary radii.

In order to investigate the effect of aggregate and spherical hazes on the transmission spectra of GJ 1214b, we generate synthetic spectra of the case discussed in section 3.3 with the diffusion limited mass production rate equivalent to 1.3 x 10^{11} methane molecules $cm^{-2}s^{-1}$. Comparing these models to observations from HST WFC3 (Kreidberg et al., 2014) and Spitzer (Gillon et al., 2014) yields a reduced chi squared of 1.58 for the aggregate haze case and 7.29 for the spherical haze case. These results are shown in Fig. 6.15. For reference, a flat spectrum results in a reduced chi squared of 1.64 (Gao et al. 2018b). The aggregate haze case fits the observations better than a flat spectrum due to CO_2 absorption at 4.5 microns in the former case coinciding with an increased transit depth measured in the Spitzer 4.5 micron band. The spherical haze case does not fit the data at all due to the pronounced scattering slope across the entire wavelength range presented. Note

that the water feature at 1.4 microns is more pronounced in our aggregate haze model spectra than in the data, suggesting that a slightly higher haze opacity may better fit the data there. This could be achieved with contributions to the haze mass production rate from CO and N_2, which are more abundant than CH_4 by several orders of magnitude in a 100 x solar metallicity atmosphere. Also, the K_{zz} profile is a model prediction, and slightly lower values could also contribute to higher haze opacity.

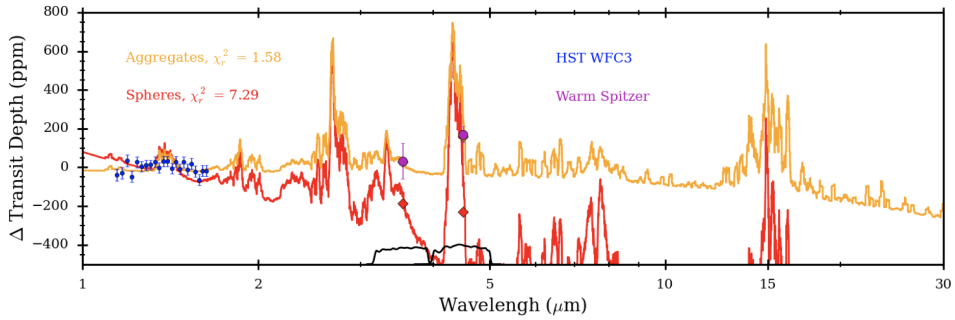

Figure 6.15: Synthetic spectra of GJ 1214b with aggregate (orange) and spherical (red) hazes compared to HST WFC3 and Spitzer observations (blue and magenta; Kreidberg et al., 2014; Gillon et al., 2014). A production rate of 1.3×10^{11} molecules $cm^{-2}s^{-1}$ and 1 nm monomers were considered. The Spitzer filter responses are shown at the bottom of the plot. The Spitzer observations overlay the model values in the Spitzer bands for the aggregate case.

Comparing our GJ 1214b results with previous efforts to fit the observations using microphysical models demonstrates the value in considering aggregate hazes. Kawashima Ikoma (2018) were able to produce relatively flat transmission spectra using spherical haze particles and reasonable Kzz values only when the haze production efficiency was several orders of magnitude greater than that of Titan. Gao et al. (2018b) were able to produce transmission spectra that fit the HST WFC3 and Spitzer points using spherical KCl cloud particles only when the Kzz was 1-2 orders of magnitudes greater than those predicted by Charney et al. (2015). Ohno Okuzumi (2018) considered the Kzz profile from Charnay et al. (2015) and spherical KCl cloud particles but were unable to reproduce the cloud top pressures retrieved by Kreidberg et al. (2014) unless the atmosphere was dominated by metals and the cloud particles were porous. However, we note that, even though we are able to reproduce the data with both reasonable Kzz values and haze production rates, there exist large uncertainties in haze optical and material properties and photochemical networks that could impact our results.

Tholin Hazes

Photochemical hydrocarbon hazes can have compositions other than soots. For example, hazes at Titan and Pluto have been modeled as tholins (e.g., Gao et al., 2017a). We apply tholin refractive indices to our haze particle distributions and find that their opacity is comparable but less than that of soot hazes, as shown by the synthetic spectra in Fig 16. This is understandable since the imaginary refractive index of tholins is much smaller than that of soots (Fig 2). Unique from soots, tholins have spectral features in the infrared. The most prominent spectral feature occurs at 6.5 microns and is visible for the spherical case due to the small size of the particles. Tholin hazes are nearly indistinguishable from soot hazes for the aggregate case, as aggregate particles are sufficiently large (e.g. $r > 6.5/2\pi$) and compact in our parameterization of fractal dimension that the spectral feature is muted.

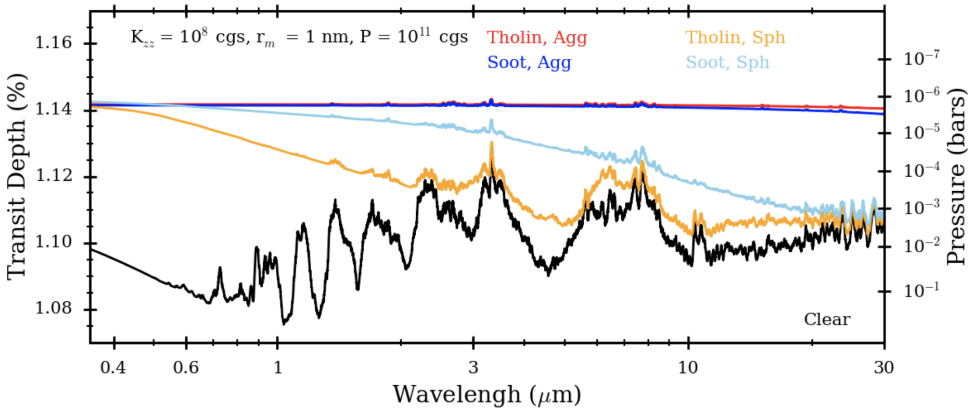

Figure 6.16: Synthetic spectra of the 0.2 AU atmosphere. Clear conditions are shown in black. Tholin aggregate hazes (red), soot aggregate hazes (blue), tholin spherical hazes (yellow), and soot spherical hazes (light blue) are considered. Kzz = $10^8 cm^2 s^{-1}$, r_m = 1 nm, and P = 10^{11} methane molecules $cm^{-2} s^{-1}$ are used to generate these haze cases.

Restructuring of Aggregates in Warm Atmospheres

While aggregate particles are common in solar system atmospheres, it is critical to consider whether they may be restructured or destroyed in the warmer atmospheric conditions considered in this study. We investigate this question by comparing the effective collisional energies of aggregates in our work to the critical energies for aggregate restructuring computed in Dominik Tielens (1997), which includes the following restructuring mechanisms: sticking of aggregates without visible restructuring; losing monomers upon collision; maximum compression; and catastrophic

destruction. A collision is considered to cause "catastrophic destruction" if the colliding aggregates are broken into monomers or very small fragments. The effective collision energy E_{ff} is defined as:

$$E_{eff} = \frac{1}{2} M v_{col}^2 \tag{6.9}$$

with an effective mass M given by $M^{-1} = M_1^{-1} + M_2^{-1}$ where M_1 and M_2 are the masses of the colliding aggregates. We set the colliding velocity to the relative thermal velocity of the aggregates in the atmosphere, as with Lavvas and Koskinen (2017):

$$v_{col} = \sqrt{\frac{8kT}{\pi M}} \tag{6.10}$$

Combining Eqs 7 and 8, we find that E_{eff} is only dependent on temperature. The rolling and breaking critical energies are given by $logE_{crit} = Alog(R) + B$ with an effective radius R given by $R^{-1} = R_1^{-1} + R_2^{-1}$ where R_1 and R_2 are the radii of the monomers. A and B are the constants depending on the material, and for this analysis, we consider the values for graphite and polystyrene given by Dominik Tielens (1997) since these materials are composed of carbon and hydrogen, similar to the haze composition we consider. The critical energies for graphite are defined as:

$$logE_{roll,G} = log(R) - 4.65$$
$$logE_{break,G} = \frac{4}{3} log(R) - 2.40$$

The critical energies for polystyrene are defined as:

$$logE_{roll,P} = log(R) - 5.45$$
$$logE_{break,P} = \frac{4}{3} log(R) - 3.47$$

By comparing the temperatures corresponding to the critical energies to 1750 K (T_{max}), the maximum temperature reached in our model atmospheres (Fig. 6.3), we can assess whether collisions of aggregates lead to any significant restructuring. Table 1 shows the results of this comparison, and reveals that aggregate particles do not undergo restructuring in the atmospheric temperatures considered. While the

	Critical energy	r_m = 1 nm	r_m = 3 nm	r_m = 10 nm
sticking without visible restructuring	$E_{eff} < 5E_{roll}$	$T_G = 31850\ K$ $T_P = 5050\ K$	$T_G = 99560\ K$ $T_P = 15150\ K$	$T_G = 318530\ K$ $T_P = 50480\ K$
losing monomers upon collision	$E_{eff} > 3n_c E_{break}$	$T_G = 12520\ K$ $T_P = 1070\ K$	$T_G = 54170\ K$ $T_P = 4610\ K$	$T_G = 269750\ K$ $T_P = 22960\ K$
maximum compression	$E_{eff} = 1n_c\, E_{roll}$	$T_G = 6371\ K$ $T_P = 1010\ K$	$T_G = 19112\ K$ $T_P = 3029\ K$	$T_G = 63706\ K$ $T_P = 10997\ K$
catastrophic destruction	$E_{eff} > 10n_c E_{break}$	$T_G = 41740\ K$ $T_P = 3550\ K$	$T_G = 180580\ K$ $T_P = 15370\ K$	$T_G = 899160\ K$ $T_P = 76530\ K$

Figure 6.17: Critical temperatures at which graphite (T_G) and polystyrene (T_P) aggregates composed of 1 nm, 3 nm, or 10 nm monomers begin to undergo their corresponding restructuring mechanism. Critical temperatures are derived from critical energies, assuming n_c = 1(or a single contact point within an aggregate).

critical temperatures for the conditions of "losing monomers upon collision" and "maximum compression" for the rm = 1 nm, polystyrene cases exceed T_{max} , this is only for 1 contact (n_c = 1), or an aggregate composed of only 2 monomers. For both cases, T_{max} is less than a factor of two greater than the critical temperatures, demonstrating that for aggregates composed of three or more monomers ($n_c \geq 2$), the critical temperature will exceed T_{max}. The relationship between this critical temperature and the number of monomers in an aggregate is shown in Fig. 6.17, and it is clear that for more than 2 monomers, the temperatures considered in our models are cooler than that for maximum compression. Therefore, only small aggregates at very high temperatures may possibly undergo restructuring due to collisions. Also, the critical temperatures are much greater for graphite than for polystyrene, and neither of these compositions are fully representative of the hazes considered here.

While our atmospheric conditions appear to prevent the structures of the aggregates from being significantly affected by collisions, the methodology of Dominik Tielens (1997) did not consider gas drag. Kataoka et al. (2013) demonstrated that gas drag acting on an aggregate may result in greater compaction than that resulting from collisions. Therefore, we suggest that gas drag may compress larger aggregate particles, allowing for the evolution in D_f that we have 2 assumed in Fig. 6.1.

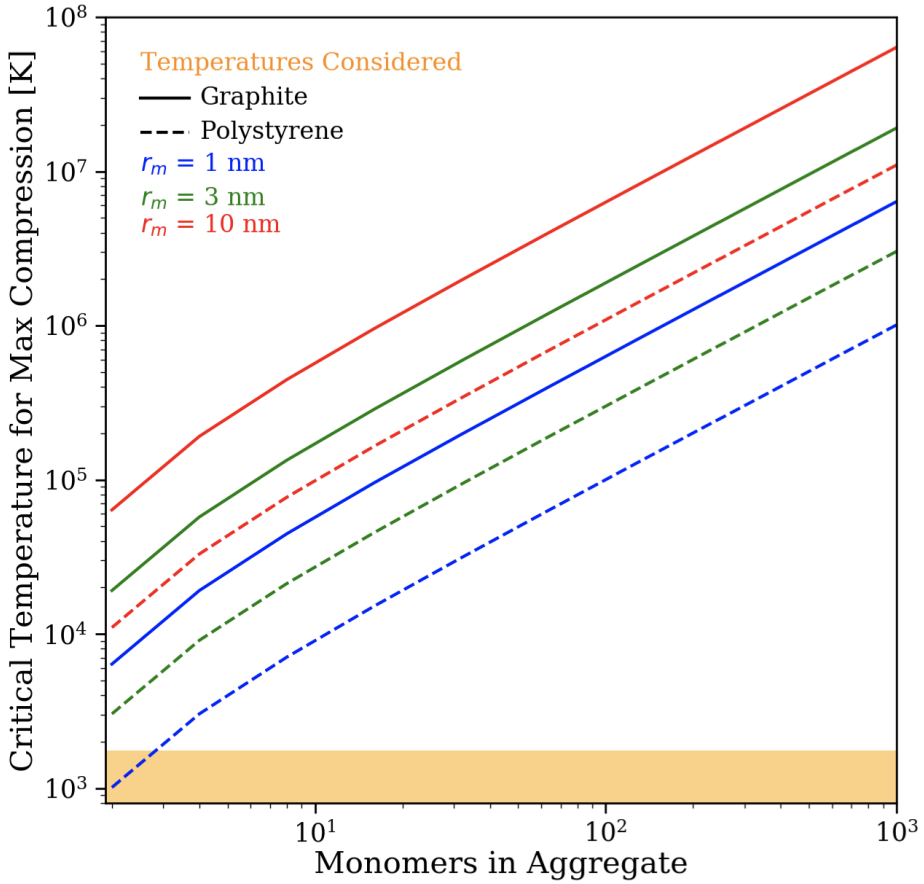

Figure 6.18: Critical temperature for maximum compression as a function of the number of monomers in an aggregate particle. Graphite (solid) and polystyrene (dashed) materials are considered, with monomer radii of 1 nm (blue), 3 nm (green), and 10 nm (red). The range of temperatures considered in our model atmospheres is shown in orange.

Haze Production Assumptions

In this study, we assumed that the haze particles are sufficiently nonvolatile that they do not grow by condensation. This is consistent with the low volatility of soots as indicated by their condensation curves shown in Lavvas Koskinen (2017). Nucleation is assumed to occur above 1 microbar to form the initial monomers, which is where previous studies have found maximum haze precursor production to occur (e.g., Zahnle et al., 2016; Morley et al., 2013, 2015; Lavvas and Koskinen, 2017; Kawashima and Ikoma, 2018).

Despite our results, hazes composed of aggregate particles do not intrinsically produce flat spectra. By comparing the effective optical depth of aggregate and

spherical particles, Wolf and Toon (2010) determined that the spectral behavior of tholin aggregate particles are more sloped compared to equivalent-mass spherical particles in an early earth-type atmosphere. Robinson et al. (2014) found significant wavelength dependence in Titan's haze opacity in transmission, with a slope rising towards shorter wavelengths, even though the haze is composed of tholin aggregates with characteristic particle sizes of 1-2 microns. We provide two possible explanations for differences between these previous studies and our work. First, the different spectral behavior of the imaginary refractive index of tholins are shown in Figure 6.16 to produce more sloped spectra, at least for spherical particles, compared to the spectra produced by haze with the imaginary refractive index of soots. Second, the particle size distributions of Titan's aggregate haze are different from those of our work. For example, we can compare our size distributions (Figure 6.4) to those of Lavvas et al. (2010) at pressures probed by transmission spectra. From Robinson et al. (2014) we know transmission spectra of Titan probe altitudes from 100-300 km, while for the P=1e11, Kzz=1e8, and rm=1 nm case the pressures probed in Figure 6.12 is 2e-6 bar. Lavvas et al. (2010) showed through microphysical simulations that the haze particle size distribution at 100-300 km altitude in Titan's atmosphere is bimodal, with a large population centered near 0.01 microns and a second narrow distribution centered near 1 micron. In contrast, our particle size distribution shows a tail of slightly larger particles, extending to a few microns, and abundant particles between 0.1-0.5 microns, which are lacking in the results of Lavvas et al. (2010). Our greater number density of larger particles likely contributes to the greater opacity at long wavelengths and the flattened spectra compared to the results of Robinson et al. (2014), and shows that the atmospheres in which hazes develop play an important role in determining their spectral behavior.

We have only considered hazes formed from hydrocarbon chemistry, but Zahnle et al. (2016) showed the significance of sulfur chemistry on the production of photochemical hazes. They found that the free radicals that result from sulfur photochemistry can divert carbon into the stronger bonds of CO and CO_2 rather than the weaker bonds of hydrocarbons. While Horst et al. (2018) found that CO can spur haze production under certain conditions, interference from sulfur chemistry may affect the aerosol production rate. Photochemical sulfur hazes can also provide significant opacity to obscure molecular spectral features for planets with effective temperatures < 750 K.

Variations in the optical constants of our considered haze materials would affect our

computed haze optical depths and synthetic spectra. For example, Mahjoub et al. (2012) found tholin optical properties to be dependent on the methane concentration of the gas from which the tholins are produced, while Tran et al. (2003) identified minimal dependence on the ratio of methane, ethylene, acetylene, cyanoacetylene, hydrogen, and nitrogen. Instead, hazes produced via photochemistry versus plasma discharge were found to have distinct imaginary refractive indices. Imanaka et al. (2004) found that both the chemical composition and optical properties of tholins produced were dependent on the pressure at which they were deposited. In the context of exoplanets, He et al. (2018) identified that large particle color variations in organic haze material occurred for different temperatures when varying metallicity from 100x to 10000x solar in an exoplanet atmosphere analog. Changes to the imaginary refractive index would affect the slope at shorter wavelengths for the relatively large particles in our work, as shown by the difference between soots and tholins in Figure 6.16, while differences in the specific spectral response of the material would affect haze spectral features at wavelengths longer than the radius of the haze particles.

Our model ignored photochemistry when varying production rate and K_{zz}, but previous studies have found that these parameters do not behave independently. The parent molecules of the hazes (including CH_4 and CO), as well as haze precursors like more complex hydrocarbon molecules and nitriles are also transported via diffusion. Thus, a high K_{zz} could quickly deplete the upper atmosphere of haze precursors, resulting in decreased haze production. On the other hand, faster upwelling of haze parent molecules could lead to increased haze production. For example, Lavvas and Koskinen (2017) found that increasing eddy diffusivity by an order of magnitude increased mass fluxes of major compounds generated by photolysis at HD 189733b by up to 3 orders of magnitude, while HD 209458b experienced no change in mass flux. However, Zahnle et al. (2016) found that strong vertical mixing creates a more oxidized environment in the upper atmosphere, resulting in lower production rates of haze precursors. Hence, eddy diffusivity and production rate are not independent parameters, but their dependency is complex.

6.5 Conclusions

Numerous studies have suggested photochemical hazes as an interpretation of exoplanet transmission spectra that show an upward slope towards shorter wavelengths and weak molecular features. Previous works have largely considered hazes composed of spherical particles on exoplanets, while both spherical and aggregate haze

particles have been inferred to exist in solar system atmospheres. We used a 1D aerosol microphysics model to investigate the effects of aggregate and spherical haze particles on exoplanet spectra while varying haze production rate, strength of atmospheric mixing, initial haze particle mass, and atmospheric thermal profile. Our results showed that:

- For any given set of parameter values, aggregate haze particles grow to larger sizes than spherical haze particles due to the larger collisional cross section per unit mass of aggregates and the resulting increase in collisional frequency.
- Aggregate haze opacity is gray in the optical and NIR, while spherical haze opacity displays a scattering slope towards shorter wavelengths. Therefore, in high haze opacity cases, aggregate hazes could obscure molecular features in transmission across a wide range of optical and infrared wavelengths, while spherical hazes mostly dominate the optical wavelengths only. We note however that this result is dependent on assumptions of material optical properties and the porosity of the aggregates.
- Increasing haze production rates and decreasing atmospheric mixing rates increased haze opacity at all considered wavelengths due to increased particle number densities, particle radii, or both.
- The effect of monomer radius on haze opacity depends on a myriad of factors including production rate, and changes depending on whether it is viewed in nadir geometry or transmission due to variability in haze opacity with pressure level.

Given reasonable ranges of parameter values, both spherical and aggregate hazes were able to produce a continuum of clear-to-featureless transmission spectra, with spherical hazes generating almost exclusively sloped spectra, and aggregate hazes generating almost exclusively flat spectra, mimicking the effects of condensation clouds. By considering aggregate haze particles, we are able to interpret the flat transmission spectrum of GJ 1214b without the need for extremely high haze production rates or eddy diffusivities, showing the value in taking into account more complex hazes beyond the simple spherical assumption. Our ability to produce differently shaped haze spectra (sloped and flat), as well as the sensitivity of the spectra to uncertain parameters such as production rate suggests the need to better constrain haze properties in exoplanet atmospheres to understand their thermal structure and

composition. Additionally, any spectral features from haze particles (e.g., tholins) would be useful in providing size constraints on haze particles; though aggregate particles may be too large and/or compact for spectral features at wavelengths <10 microns to be seen.

Chapter 7

SPATIALLY RESOLVED MODELING OF OPTICAL ALBEDOS FOR A SAMPLE OF SIX HOT JUPITERS

7.1 Introduction

Transiting short period gas giant planets, or 'hot Jupiters', are among the most favorable targets for atmospheric characterization studies. By observing the decrease in optical flux when the planet passes behind the host star (secondary eclipse), we can measure the optical dayside albedos for these tidally locked planets. Most of these albedo measurements have come from space telescopes observing in broad optical bandpasses (e.g. Rowe et al., 2008; Kipping and Bakos, 2011; Brice-Olivier Demory, Sara Seager, et al., 2011; Brice-Olivier Demory, de Wit, et al., 2013; Coughlin and Lopez-Morales, 2012; Parviainen, Deeg, and Belmonte, 2013; Angerhausen et al., 2014; von Paris et al., 2016; Niraula et al., 2018). The hot Jupiter HD 189733b is currently the only planet with a spectroscopically resolved reflected light measurement (Evans et al., 2013, geometric albedo of 0.40 ± 0.12 at $290 - 450$ nm and < 0.12 at $450 - 570$ nm). WASP-12b and WASP-43b were also observed with optical spectrographs on *HST*, but both observations resulted in non-detections (Bell et al., 2017; Fraine et al., 2021, geometric albedos < 0.06). These spectroscopic albedo measurements are invaluable for constraining the nature of the scattering particles in the atmospheres of these planets (e.g. Barstow et al., 2014).

Theoretical models predict that variations in hot Jupiter optical albedos should primarily be driven by the presence or absence of high altitude aerosols, which are expected to scatter incident starlight (e.g. S. Seager, Whitney, and Sasselov, 2000; A. Burrows, Ibgui, and I. Hubeny, 2008). Cloud-free atmosphere models for hot Jupiters generally predict dayside albedos of less than 0.1 (S. Seager, Whitney, and Sasselov, 2000), but the observed optical geometric albedo measurements published to date span a wide range of values, with the brightest planets exhibiting albedos as high as 0.3 (e.g. Heng and Brice-Olivier Demory, 2013; Niraula et al., 2018). In the solar system, the presence of water clouds increases Earth's geometric albedo to approximately 0.37 (e.g. Goode et al., 2001), while ammonia clouds in Jupiter's atmosphere contribute to its geometric albedo of approximately 0.5 (e.g. Mark S. Marley, Gelino, et al., 1999). For the same reason, models suggest that the presence

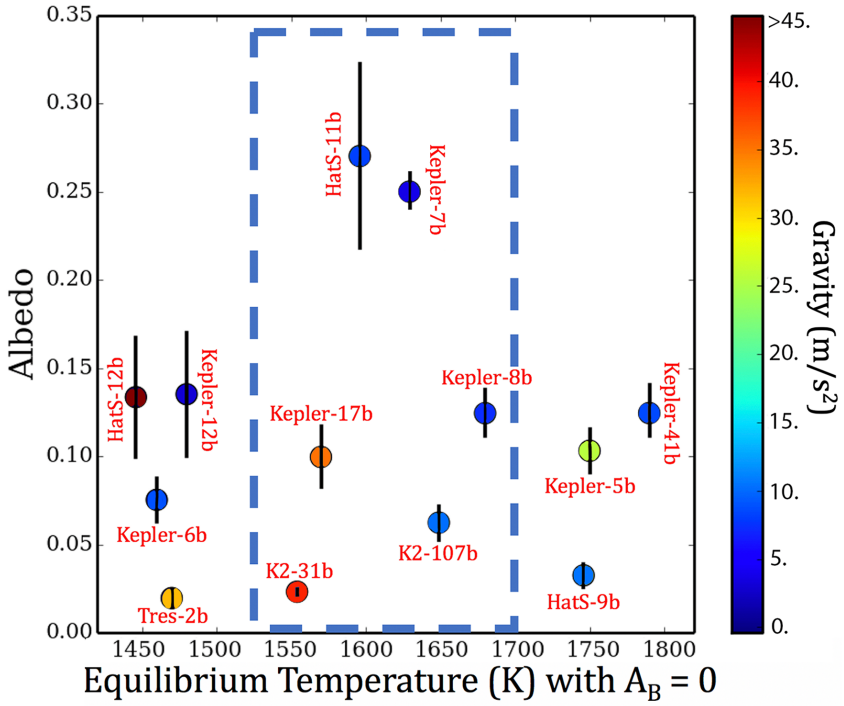

Figure 7.1: Optical geometric albedo measurements for a sample of hot Jupiters observed in the *Kepler* bandpass; at these temperatures thermal emission is negligible for planets with cloudy skies and the measured secondary eclipse depth is dominated by reflected light. The equilibrium temperature is calculated assuming a Bond albedo of zero and efficient day-night circulation. The planet colors vary as a function of surface gravity. The dashed box indicates the temperature range considered in this study. Measurements are drawn from Jonathan J. Fortney et al. (2011), Desert et al. (2011), Barclay et al. (2012), Esteves, De Mooij, and Jayawardhana (2013), Shporer and Hu (2015), Niraula et al. (2018), and Heng, Morris, and Kitzmann (2021).

of reflective condensates such as Mg_2SiO_4 or $MgSiO_3$ in hot Jupiter atmospheres can increase their albedos to values as high as 0.5 (Vivien Parmentier, Jonathan J. Fortney, et al., 2016; Vivien Parmentier, Adam P. Showman, and Jonathan J. Fortney, 2021; M. T. Roman et al., 2021). Unlike brown dwarfs, whose cloud distributions and optical depths correlate closely with their equilibrium temperatures (e.g. Kirkpatrick, 2005; Mark S. Marley, Didier Saumon, and Goldblatt, 2010), hot Jupiter albedos can vary by as much as an order of magnitude within a relatively narrow range of equilibrium temperatures (Figure 7.1). This suggests that individual planets with similar equilibrium temperatures may exhibit diverse cloud properties.

Hot Jupiters are expected to be tidally locked as a result of their short orbital periods, which can lead to significant day-night temperature gradients (e.g. Guillot and

A. P. Showman, 2002). This inhomogneous temperature structure affects the cloud distribution, and 3D atmospheric circulation models predict that hot Jupiters should host spatially inhomogenous clouds over a wide range of equilibrium temperatures (e.g. Vivien Parmentier, Jonathan J. Fortney, et al., 2016; Vivien Parmentier, Adam P. Showman, and Jonathan J. Fortney, 2021; M. T. Roman et al., 2021). Furthermore, there is direct observational evidence for inhomogeneous cloud structures stemming from reflected-light phase curves (e.g., Brice-Olivier Demory, de Wit, et al., 2013). To date, three of the four planets with observed reflected-light phase curves appear to have patchy clouds (Desert et al., 2011; Brice-Olivier Demory, de Wit, et al., 2013; Angerhausen et al., 2014; Esteves, De Mooij, and Jayawardhana, 2015; Shporer and Hu, 2015; von Paris et al., 2016; Niraula et al., 2018, also see Figure 7.1). Kepler-7b, -12b, and -41b all appear to have patchy clouds that are preferentially concentrated in the western (dawn) hemisphere, causing the peak of the phase curve to occur after the secondary eclipse (Shporer and Hu, 2015). Observations of the fourth planet, TrES-2b, indicate that it is uniformly dark ($A_s < 0.03$, which is equivalent to $A_g < 0.02$ for a Lambertian sphere, where A_s is the spherical albedo and A_g is the geometric albedo) at all phases (von Paris et al., 2016). These studies demonstrate that if we wish to explain the observed planet-to-planet variations in the measured dayside optical albedos of hot Jupiters, we must utilize 3D models capable of capturing the spatially varying cloud structure.

While an increasing number of studies are using general circulation models (GCMs) to predict cloud patterns, these have either focused on individual planets (e.g. Webber et al., 2015; Lee, Ch. Helling, and Dobbs-Dixon, 2015; Oreshenko, Heng, and Brice-Oliver Demory, 2016; Christiane Helling, Iro, et al., 2019; Christiane Helling, 2019; Christiane Helling, Kawashima, Y., et al., 2020; Lines, Mayne, Boutle, et al., 2018; Lines, Mayne, Manners, et al., 2019; M. Roman and Rauscher, 2019) or generic grids of models (e.g. Vivien Parmentier, Jonathan J. Fortney, et al., 2016; Vivien Parmentier, Adam P. Showman, and Jonathan J. Fortney, 2021; M. T. Roman et al., 2021). Of these listed studies, only five (Webber et al., 2015; Oreshenko, Heng, and Brice-Oliver Demory, 2016; Vivien Parmentier, Jonathan J. Fortney, et al., 2016; Vivien Parmentier, Adam P. Showman, and Jonathan J. Fortney, 2021; M. T. Roman et al., 2021) use their models to calculate predicted albedos in the *Kepler* bandpass. The question of why individual planets with similar equilibrium temperatures would exhibit widely varying cloud properties therefore remains largely unexplored in the literature.

Table 1
Properties of our Planet Sample

Planet	M_P (M_J)	R_P (R_J)	$T_{eq}(K)$[a]	g ($m\ s^{-2}$)	a (au)	Period (days)	Measured A_g	Reference[b]
K2-31b	1.77	1.06	1550	39.07	0.022	1.26	0.023 ± 0.002	1,**9**
Kepler-17b	2.45	1.31	1570	35.41	0.026	1.49	0.099 ± 0.017	2,**3**
HATS-11b	0.85	1.51	1560	7.97	0.051	3.62	0.270 ± 0.052	4,5,**9**
Kepler-7b	0.45	1.65	1630	4.16	0.062	4.89	0.25 ± 0.01	6,**8**
K2-107b	0.84	1.44	1650	10.26	0.048	3.31	0.062 ± 0.010	5,7,**9**
Kepler-8b	0.60	1.41	1680	7.32	0.047	3.85	0.124 ± 0.013	6,**10**

Notes. (1) Grziwa et al. (2016), (2) Desert et al. (2011), (3) Bonomo et al. (2017), (4) Bayliss et al. (2018), (5) Livingston et al. (2018), (6) Esteves et al. (2015), (7) Eigmuller et al. (2017), (8) Heng et al. (2021), (9) Niraula et al. (2018), (10) Esteves et al. (2013).
[a] Calculated assuming a Bond albedo of zero and efficient day–night recirculation.
[b] Reference to geometric albedo measurement is bolded for each row.

Modeling the 3D structure of clouds can be computationally demanding, especially given the large number of parameters that must be considered (including but not limited to the particle number density and size distribution, spatial extent of the clouds, location of the cloud decks, number and composition of cloud species, and coupled radiative feedback). In examining the body of published studies that use GCMs to predict hot Jupiter dayside albedos, we find that all of these studies make simplifying assumptions in order to conserve run time and numerical complexity. Oreshenko, Heng, and Brice-Oliver Demory (2016), for example, determined the locations of clouds by comparing the 3D thermal structure from a GCM with relevant condensation curves, but assumed a fixed particle size and local condensation only (i.e., they neglected vertical mixing) for the cloud layers. In Vivien Parmentier, Jonathan J. Fortney, et al. (2016), cloud distributions were determined using the completed temperature structure calculated by a non-gray cloud-free GCM, with a cloud-top minimum pressure fixed at 1 microbar. In Vivien Parmentier, Adam P. Showman, and Jonathan J. Fortney (2021), cloud layers were also calculated using the thermal structure output from a GCM, but the prescribed vertical extent is limited by temperatures within the extent of 200 mbar to 1 μbar. M. Roman and Rauscher, 2019 and M. T. Roman et al., 2021 differ significantly from the Parmentier models. In the former, cloud distributions were determined at each timestep in a double-grey GCM which included radiative feedback. They included extended clouds which form when the temperature-pressure profile permits, but are forced to taper off at pressures between 0.3 mbar and 0.057 mbar. They also consider compact cases with varied optical thickness where the clouds are truncated and tapered off after approximately one scale height regardless of where their base forms. In M. T. Roman et al., 2021, they also consider a more extensive grid of planet models, while also varying cloud compositions, densities, and vertical extents. All of the studies listed above assumed homogeneous condensation, allowing them to treat each individual cloud species separately. Although there are studies in the literature that have combined GCMs with microphysical cloud models (e.g., Lee, Ch. Helling,

and Dobbs-Dixon, 2015; Lines, Mayne, Boutle, et al., 2018; Christiane Helling, Iro, et al., 2019; Christiane Helling, 2019; Christiane Helling, Kawashima, Y., et al., 2020), these models focused on individual planets and were limited in their albedo predictions in the *Kepler* bandpass. Although there are studies in the literature that have combined GCMs with microphysical cloud models (e.g., Lee, Ch. Helling, and Dobbs-Dixon, 2015; Lines, Mayne, Boutle, et al., 2018; Christiane Helling, Iro, et al., 2019; Christiane Helling, 2019; Christiane Helling, Kawashima, Y., et al., 2020), these models focused on individual planets and were limited in their albedo predictions in the *Kepler* bandpass.

In this study, we utilize a suite of models to investigate the role of patchy clouds over a sample of six individual hot Jupiters, chosen due to their diverse observed albedos over a narrow range of equilibrium temperatures. In §7.2, we describe our sample selection and summarize our modeling approach. We use 3D GCMs to derive the thermal structure and eddy diffusion coefficients (K_{zz}). We then use `Virga`, a phase equilibrium cloud code, to make detailed maps of cloud structure over the dayside of each planet. We use `PICASO`, a radiative transfer program, to calculate the corresponding geometric albedo maps and hemisphere-integrated dayside albedos. We also consider a microphysical code, `CARMA`, which enables us to take a closer look at the role of nucleation, condensation, and sedimentation in shaping the distribution of dayside clouds.

In §7.3 we compare our predicted dayside-integrated optical albedos with observations of the six planets of interest. We then investigate the relative importance of various model assumptions, such as equilibrium condensation versus kinetic condensation, by comparing the `Virga` results with the `CARMA` results. Finally, we discuss the implications of our results in §7.4 and present our conclusions in §7.5.

7.2 Methods

Planet Sample

In this study we focus on planets with equilibrium temperatures (T_{eq}, calculated assuming an albedo of zero and efficient day-night recirculation) between 1550 – 1700 K. For planets in this relatively narrow temperature range, we expect that reflective silicate clouds should dominate the optical dayside albedos (e.g. Vivien Parmentier, Jonathan J. Fortney, et al., 2016; Powell, Zhang, et al., 2018; Vivien Parmentier, Adam P. Showman, and Jonathan J. Fortney, 2021; Gao, Thorngren, et al., 2020; M. T. Roman et al., 2021). This temperature range contains some of the most re-

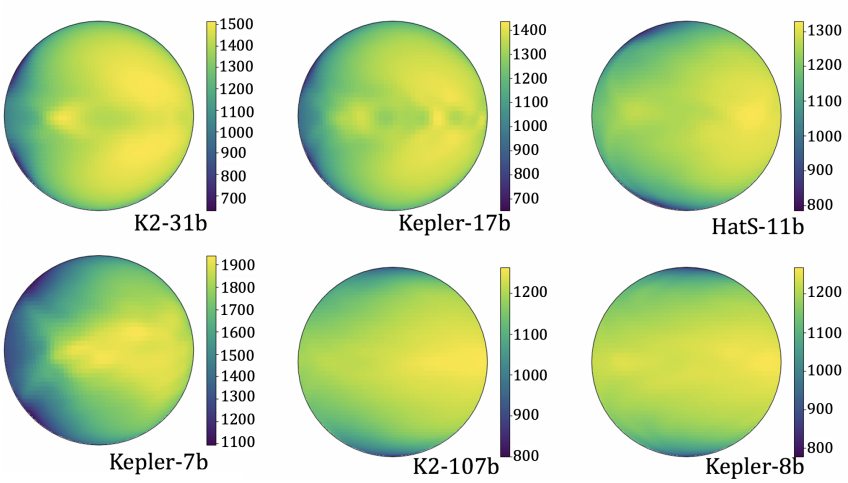

Figure 7.2: Map of the dayside temperatures (in Kelvin) of each planet at 1 mbar, roughly the pressure of unit optical depth in a clear atmosphere in the *Kepler* bandpass. Each planet is given a unique scale for the color bar to best match the relevant temperature range.

flective hot Jupiters observed to date, including Kepler-7b (Brice-Olivier Demory, de Wit, et al., 2013; Heng, Morris, and Kitzmann, 2021) and HATS-11b (Niraula et al., 2018). Note that two observed geometric albedos have been reported for Kepler-7b, and from here on we consider the most recent value from Heng, Morris, and Kitzmann (2021). It also includes three moderately reflective hot Jupiters (Kepler-8b, Kepler-17b, and K2-107b; Esteves, De Mooij, and Jayawardhana, 2013; Desert et al., 2011; Niraula et al., 2018) and one very dark hot Jupiter (K2-31b; Niraula et al., 2018). Previous studies (e.g., Brice-Olivier Demory, de Wit, et al., 2013) have concluded that planets with these equilibrium temperatures should have negligible amounts of thermal emission in the *Kepler* bandpass. We checked this by using `PICASO` to compute the predicted thermal emission for each of the six planets in our sample and found a contribution of 2 ppm or less. This is significantly smaller than the uncertainties on the secondary eclipse depths used to calculate the geometric albedos for these planets. Hence, throughout this paper we ignore the thermal contribution to the measured secondary eclipse depth in the *Kepler* bandpass.

In this study we present a GCM tailored to each of the six individual planets, which we use to predict planet-to-planet variations in cloud coverage and dayside albedo in the optical *Kepler* band. These planets sample a range of surface gravities, allowing us to investigate its effect on the planet's thermal structure, cloud distributions, and optical albedo. We summarize the physical and orbital properties of each system in

Table 1.

Modeling Atmospheric Circulation with the SPARC/MITgcm

We model each planet's clear-sky (cloud-free) 3D thermal structure and atmospheric circulation with the Substellar and Planetary Radiation and Circulation (SPARC) model, which couples the GCM maintained at the Massachusetts Institute of Technology (the MITgcm; Adcrot et al., 2004) with a plane-parallel, two-stream version of the multi-stream radiation code as described in Mark S. Marley, Gelino, et al. (1999). The MITgcm solves the 3D primitive equations on a staggered Arakawa C grid (Arakawa, Williams, and Inagaki, 1977) with the finite-volume method. The equations are discretized on a 128×64 cubed-sphere grid with 53 vertical layers extending from 200 bars at the bottom boundary to 20 μbar at the top boundary. A horizontal fourth-order Shapiro filter is used to smooth horizontal noise. We let each model run for a simulated 1000+ Earth days so as to reach quasi-steady state equilibrium.

The radiative transfer scheme solves the two-stream radiative transfer equations using the correlated-k method (Goody et al., 1989; Mark S. Marley, Gelino, et al., 1999) over 11 spectral bins (T. Kataria et al., 2013). This coupling allows for the self-consistent calculation of the heating and cooling rates of the atmosphere with latitude, longitude and pressure. At each grid point, the radiative transfer scheme calculates the upward and downward fluxes at each pressure layer, which are used to update the heating/cooling rates. These rates are used by the MITgcm to update the wind and temperature fields. Opacities are computed at each pressure-temperature point assuming chemical and thermodynamic equilibrium, using the solar photospheric elemental abundances of Lodders (2003). We interpolate across the PHOENIX stellar atmosphere models to generate an input spectrum for each host star. The SPARC/MITgcm has been successfully utilized for a series of hot Jupiter studies (e.g. Adam P. Showman, Jonathan J. Fortney, et al., 2009; Adam P. Showman and Kaspi, 2013; Adam P. Showman, Lewis, and Jonathan J. Fortney, 2015; T. Kataria et al., 2013; Tiffany Kataria, Adam P. Showman, et al., 2015; Tiffany Kataria, David K. Sing, et al., 2016; Vivien Parmentier, Adam P. Showman, and Lian, 2013; Lewis et al., 2014), and we refer the reader to Tiffany Kataria, David K. Sing, et al. (2016) for further details. Figure 7.2 shows the resulting thermal structure for each of the six planets in our sample at 1 mbar (approximately the level of unit optical depth for clear skies).

Computing Equilibrium Condensate Clouds with `Virga`

We use the thermal structure and vertical mixing rates from the SPARC/MITgcm model as inputs to `Virga` (N. Batalha, caoimherooney11, and sagnickm, 2020)[1], an open-source code that calculates phase equilibrium cloud distributions. The cloud parameterization used in this code is described in Andrew S Ackerman and Mark S Marley (2001) and has been used for 1D model studies across a wide range of exoplanets and brown dwarfs (e.g. J. J. Fortney et al., 2006; Mark S. Marley, Didier Saumon, and Goldblatt, 2010; Caroline V Morley et al., 2015). This parametric approach also allows us to sample the 3D cloud structure at a much higher spatial resolution than for our microphysical models.

We calculate K_{zz} profiles from the root-mean-square (rms) vertical velocities derived from global horizontal averages at a given pressure level from the GCMs by assuming $K_{zz} = w(z)L(z)$, where $w(z)$ is the horizontally averaged global rms vertical velocity from the GCM simulations, $L(z)$ is approximated as the atmospheric pressure scale height $H(z)$ (but could be a fraction of $H(z)$; see Smith, 1998), and z is altitude. Moses et al. (2011) note that this is only an estimate; a better approach would involve calculating K_{zz} from the eddy vertical velocity times the eddy displacement, but this information is not readily obtainable from the GCMs; this could be resolved by adding passive tracers to future GCM models. Our treatment may overestimate K_{zz} in the ∼10–200 bar radiative region, where the vertical motion often consists of small-scale wave oscillations.

We reduce the spatial resolution of our longitude and latitude grid from 128×65 to 10×10 by binning the pressure-temperature profiles and corresponding Kzz profiles prior to running Virga. We retain the original 53 pressure levels in the rebinned grid. This binning has a negligible effect on our calculation of the phase-integrated albedo and significantly reduces computation time. We bin using the area mean with angles from the Chebyshev-Gauss integration method that vary as a function of planetary latitude and longitude.

In `Virga` the molar mixing ratio of the condensed phase, q_c, is calculated by solving the equation:

$$-K_{zz}\frac{\partial q_t}{\partial z} - f_{sed}\omega_* q_c = 0 \tag{7.1}$$

[1] Code and documentation available at https://natashabatalha.github.io/virga/

where q_t is the total mixing ratio (condensed and vapor phases), ω_* is the convective velocity scale, and f_{sed} is defined as the ratio of the mass-weighted droplet sedimentation velocity to the convective velocity, ω_*. The product $f_{sed}\omega_*$ describes an average sedimentation velocity for the condensate, which offsets turbulent mixing. We refer the reader to Andrew S Ackerman and Mark S Marley (2001) for more details regarding the equations that govern `Virga`.

In Eq. 7.1, f_{sed} is the only parameter that cannot be calculated directly from the models. We therefore treat it as a tunable parameter and explore a range of possible values. Models with larger values of f_{sed} will have high rates of sedimentation, concentrating the condensing species in the lower atmosphere. Conversely, models with smaller values of f_{sed} will have much slower sedimentation rates, allowing cloud particles to remain lofted higher in the atmosphere. For each planet, we run a suite of `Virga` models with f_{sed} values of 0.03, 0.1, 0.3, 1.0, 3.0, and 6.0. This range is motivated by comparisons to observational data, which suggest that f_{sed} can be as small as 0.01 for super Earths (Caroline V Morley et al., 2015) or as large as 2-5 for some gas giants and brown dwarfs (Skemer et al., 2016; MacDonald et al., 2018; D. Saumon and M. S. Marley, 2008). For Jupiter's ammonia clouds, an f_{sed} of ~2 appears to provide the best match to observations (Andrew S Ackerman and Mark S Marley, 2001). We therefore conclude that our chosen list of values spans a representative range for this parameter.

Computing Microphysical Clouds with `CARMA`

In addition to the parametric model described above, we also utilize the Community Aerosol and Radiation Model for Atmospheres (`CARMA`), a more computationally demanding microphysical cloud formation model. `CARMA` calculates the equilibrium cloud particle size distribution by solving the 1D discretized continuity equation for aerosol particles that experience vertical transport due to sedimentation and eddy diffusion and production and loss due to particle nucleation (homogeneous and heterogeneous), condensation, evaporation, and coagulation. `CARMA` has been previously used to investigate condensate cloud formation on Earth (e.g., Andrew S. Ackerman, Owen B. Toon, and Peter V. Hobbs, 1993; Andrew S Ackerman, Owen B Toon, and Peter V Hobbs, 1995; Jensen and O. B. Toon, 1994), Venus (e.g. James, O. Toon, and Schubert, 1997; McGouldrick and Owen B. Toon, 2007; Gao, Zhang, et al., 2014), Mars (e.g. Colaprete, Owen B. Toon, and Magalhães, 1999), and exoplanets (e.g., Gao, Mark S. Marley, and Andrew S. Ackerman, 2018; Gao, Thorngren, et al., 2020; Powell, Louden, et al., 2019). `CARMA` has also

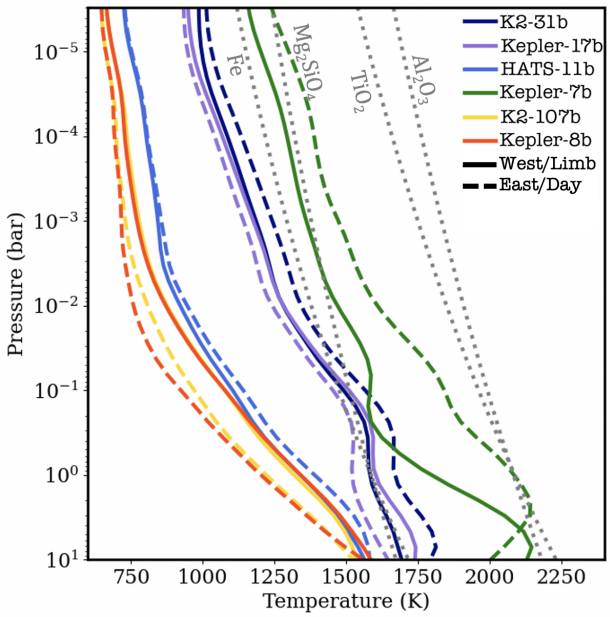

Figure 7.3: Condensation curves (dashed grey) of Fe, Al_2O_3, TiO_2, and Mg_2SiO_4 clouds compared with the two-zone model averaged temperature profiles (see §7.3). Dayside (solid) and western limb (dashed) are shown for each planet: K2-107b (yellow), Kepler-8b (orange), HATS-11b (black), K2-31b (navy), Kepler-17b (purple), and Kepler-7b (green).

been used to model photochemical hazes on Titan (O. Toon et al., 1992), Pluto (Gao, Fan, et al., 2017), ancient Earth (Wolf and Owen B. Toon, 2010), and warm Jupiters (Adams et al., 2019). In order to make our use of `CARMA` computationally tractable, we divide each planet into two zones and calculate averaged temperature and K_{zz} profiles for each zone as described in §7.3 (see also Figure 7.3). We do not consider photochemical hazes here, as the planets in our sample lie above the temperature range where these hazes are expected to form (Lodders and Fegley, 2002; Kawashima and Ikoma, 2019; Gao, Thorngren, et al., 2020).

In the `CARMA` model, the formation of condensate clouds begins with either homogeneous or heterogeneous nucleation. Cloud particles undergo homogeneous nucleation when stable clusters of condensate molecules form and grow directly from the vapor. The rate is controlled by the material properties of the condensate, such as its molecular weight and surface energy, and the flux of molecules to the cluster, which depends on the abundance of condensate vapor. Under the same supersaturation and local temperature, high surface energy and molecular weight materials tend to nucleate more slowly than low surface energy and low molecular weight materials. Unlike homogeneous nucleation, heterogeneous nucleation in-

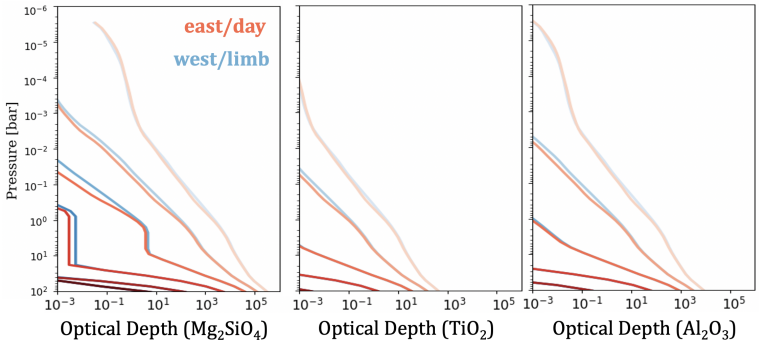

Figure 7.4: Nadir optical depths (integrated over the Kepler bandpass) for three condensate species in our `Virga` model of K2-107b. From left to right: Mg_2SiO_4, TiO_2, Al_2O_3. Each panel shows two representative grid points: black corresponds to a western grid point centered at −60 W, 8 N and red corresponds to a dayside gridpoint centered at 42 E, 8 N. The value of f_{sed}, which ranges from 0.03 to 6.0, is indicated by the shading of each line, where the lightest shades correspond to the smallest values and darkest shades represent the largest values of f_{sed}.

volves the formation of stable clusters on condensation nuclei, or foreign surfaces, which are provided by other aerosol particles in the atmosphere. The size and abundance of these particles strongly impact the rate of heterogeneous nucleation. The nucleation rate is also dependent on the interaction between the condensate and the surface, characterized by the contact angle between the surface and the condensate cluster, the energy needed by a condensate molecule to desorb from the surface, and the oscillation frequency of the condensate molecule on the surface, which is related to the desorption energy (Pruppacher and Klett, 1978).

Unlike in `Virga`, which assumes a log-normal particle size distribution, particle size distributions in `CARMA` are resolved using mass bins and can change over time via condensation, evaporation, and coagulation. The former two rates are dependent on the flux of condensate molecules and the rate at which particles may conduct away the latent heat released upon condensation. Coagulation, or growth via physically sticking upon the collision of particles, is also considered. Each mass bin corresponds to particle masses twice that of the previous bin. We use 65 bins in our model, with the mass in the first bin corresponding to particles with radii of 0.1 nm for all species.

Cloud Compositions

For the `Virga` cloud modeling in this study, we are only interested in cloud species that are expected to be abundant in these atmospheres and which condense at

relatively low pressures (approximately 1 bar). We identify three cloud species that are likely to be important based on comparing the species' condensation curves to the planets' temperature pressure profiles (Figure 7.3; also see Andrew S Ackerman and Mark S Marley, 2001; Caroline V. Morley, Jonathan J. Fortney, Mark S. Marley, et al., 2012): Mg_2SiO_4, Al_2O_3, and TiO_2. This assumes that all SiO goes into Mg_2SiO_4 rather than SiO_2 or $MgSiO_3$. The inclusion of SiO_2 would require a different modeling framework including kinetic condensation. We plot the optical depths in the Kepler bandpass (shown in Figure 7.6) for these species as a function of pressure as computed by `Virga` at a representative location on the planet K2-107b in Figure 7.4. Although some previous studies of spatially inhomogeneous cloud formation in hot Jupiters also included sulfide clouds (e.g. Vivien Parmentier, Jonathan J. Fortney, et al., 2016), recent microphysical cloud models (Powell, Louden, et al., 2019; Gao, Thorngren, et al., 2020) indicate that the high surface energy of sulfide condensates makes homogeneous nucleation unlikely. This conclusion is in good agreement with observational data indicating that the observed cloud opacity for more moderately irradiated hot Jupiters is well-matched by models without sulfide condensates (e.g. Chachan, Knutson, et al., 2019; Gao, Thorngren, et al., 2020). We therefore exclude sulfide condensates from our `Virga` models. Fe is also a potentially important condensate, but like the sulfides previous microphysical modeling suggested that Fe cloud formation proceeds slowly due to Fe's high surface energy (Gao, Thorngren, et al., 2020). On the other hand, Fe has been considered a major cloud component in many previous works (M. S. Marley et al., 2013; Christiane Helling, Dehn, et al., 2008; M. Marley and Robinson, 2015; Jonathan J. Fortney, 2005; Sudarsky, Adam Burrows, and Ivan Hubeny, 2003). Therefore, while our nominal `Virga` models will not include Fe, we will consider another set of simulations where Fe is included to explore its impact on our predicted albedos.

For the `CARMA` simulations in this study, we use the same model setup as in Gao, Thorngren, et al. (2020) where clouds of TiO_2, Al_2O_3, Fe, Mg_2SiO_4, Cr, MnS, Na_2S, ZnS, and KCl are allowed to form. However, as previously discussed, in practice only Mg_2SiO_4, Al_2O_3, and TiO_2 form in any significant abundance. Of these three species, Mg_2SiO_4 is particularly unlikely to undergo homogeneous nucleation, as it is not abundant in the vapor phase. Instead, it is the product of a thermochemical reaction between Mg, SiO, and H_2O (e.g. Visscher, Lodders, and Fegley, 2010). Similarly, Al_2O_3 does not exist in the gaseous phase as other aluminum oxide species will be more stable (e.g. Patzer et al., 2005). As in Gao, Thorngren, et al. (2020), we

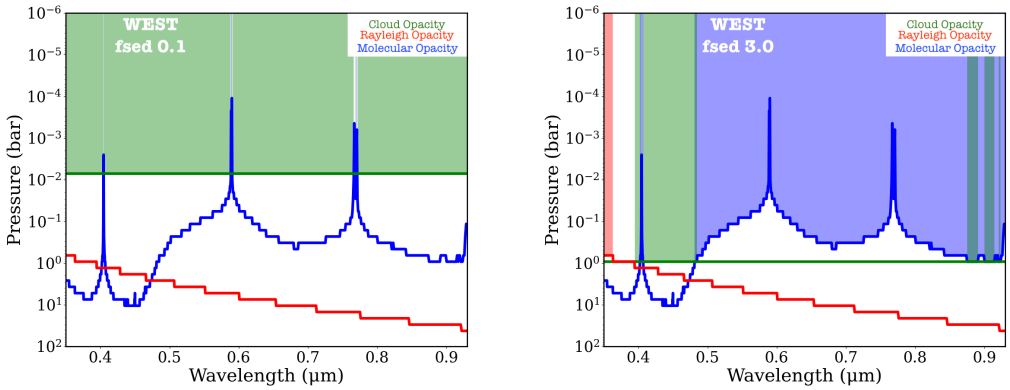

Figure 7.5: Pressure level (bar) of unit optical depth for Rayleigh scattering (pink), cloud opacity (green), and molecular opacity (black) as a function of wavelength for a single grid point (−60 W, 8 N) in the `Virga` model of hot Jupiter K2-107b. f_{sed} of 0.1 is shown on the left and 3.0 on the right. The shaded regions indicate the dominant opacity source as a function of wavelength. This is the same grid point shown in Figure 7.4.

allow these two species to heterogeneously nucleate on homogeneously nucleated TiO_2 seeds. Though Fe is permitted to both homogeneously and heterogeneously nucleate (on TiO_2 seeds), the high surface of Fe prevents significant Fe cloud formation.

Computing Optical Albedos with `PICASO`

We use the outputs from the cloud codes `Virga` and `CARMA` to calculate the single scattering albedos, asymmetry parameters, and optical depths for each pressure layer at each location in the atmosphere assuming Mie scattering. We then convert these quantities into wavelength-dependent albedos using The Planetary Intensity Code for Atmospheric Scattering Observations (`PICASO`; N. E. Batalha et al., 2019). This code is governed by the radiative transfer equation:

$$I(\tau_i, \mu) = I(\tau_{i+1}, \mu) \exp(\frac{\delta\tau_i}{\mu}) - \int_0^{\delta\tau_i} S(\tau'\mu) \exp(-\frac{\tau}{\mu}) d\tau'/\mu \tag{7.2}$$

where $I(\tau_i, \mu)$ is the azimuthally averaged intensity emerging from the top of a layer i with opacity τ_i and outgoing angle μ. $I(\tau_{i+1}) \exp(\frac{\delta\tau_i}{\mu})$ is the incident intensity at the lower boundary of the layer attenuated by the optical depth within the layer $\delta\tau$, and $S(\tau', \mu)$ is the source function integrated over all layers. The source function

has two components: single scattered and multiple scattered radiation integrated over all diffuse angles:

$$S(\tau', \mu) = \frac{\omega}{4\pi} F_o P_{single}(\mu, -\mu_o) \exp(-\frac{\tau'}{\mu_s}) + \frac{\omega}{2} \int_{-1}^{1} I(\tau', \mu') P_{multi}(\mu, \mu') d\mu', \tag{7.3}$$

where ω is the single scattering albedo and F_o is the incident flux. P_{multi} and P_{single} describe the phase function of the multiple and single scattering, respectively. P_{single} is an opacity weighted combination of the Rayleigh phase function and a two-term Henyey Greenstein phase function. P_{multi} requires integration over all diffuse angles, for which `PICASO` uses a $N = 2$ Legendre expansion. This approximation alone is inadequate to represent cases with high rates of forward scattering, so `PICASO` implements the delta-Eddington approximation to scale g, ω, and τ to more accurately capture the forward scattering peak.

`PICASO` considers the extinction from three opacity sources in order to calculate the geometric albedo as a function of wavelength: molecular absorption, Rayleigh scattering, and scattering by clouds. We show a representative calculation of these three opacity sources as a function of wavelength in Figure 7.5. To describe the phase-dependence, `PICASO` computes the emergent intensity from the disk at multiple plane-parallel facets, where each has its own incident and outgoing angles. `PICASO` uses the Chebyshev-Gauss integration method to integrate over all emergent intensities. We integrate the wavelength-dependent geometric albedo over the *Kepler* response function for each point in our 10×10 grid and then integrate again over the dayside hemisphere in order to obtain a geometric albedo that we can compare with the *Kepler* measurements. We have run sensitivity tests that demonstrate a higher resolution grid (20×20 grid) yields comparable results.

Effect of Simplifying Model Assumptions

In this study we do not consider radiative feedback from clouds, which might affect our albedo predictions. Clouds can alter the planet's global thermal structure in several ways. First, they can reduce the amount of heating on the dayside by increasing the planet's Bond albedo. Second, they can suppress cooling on the nightside by preventing the re-radiation of infrared light to space. Vivien Parmentier, Adam P. Showman, and Jonathan J. Fortney, 2021 and M. T. Roman et al., 2021 ran grids of 3D GCM models incorporating radiative feedback from clouds spanning

a range of incident fluxes. They found that the presence of reflective clouds on the dayside resulted in lower global temperatures, while the presence of nightside clouds inhibited cooling, causing a 100 – 200 K global increase in temperature. With the possible exception of Kepler-7b (see §7.4), we expect that such shifts in temperature would not substantially alter the pressures of the cloud decks or reduce their horizontal extent for the planets examined here.

We also note that in this study, our 3D atmospheric circulation models are decoupled from our cloud models. While this does enable more flexibility in exploring different cloud species and sedimentation parameters in both `Virga` and `CARMA`, cloud formation and transport is ultimately a coupled process between advection, radiation, and chemistry. Previous studies that couple cloud microphysical models and atmospheric circulation models (e.g., Lee, Ch. Helling, and Dobbs-Dixon, 2015; Lines, Mayne, Boutle, et al., 2018) suggest that zonal (east/west) and/or meridional (north-south) transport of cloud particles from colder regions of the atmosphere could lead to high cloud particle number densities, even on the hotter dayside, which could in turn enable more cloud nucleation and growth. These processes will only affect our dayside albedo predictions if the planet in question has large dayside temperature (and hence albedo) gradients with longitude or latitude. We revisit both of these assumptions (radiative feedback and cloud microphysics coupled to circulation) in §7.4, where we discuss their implications for individual planets in light of our model results.

7.3 Results

The SPARC/MITgcm models indicate that the day-night temperature contrasts for the six planets in our sample vary in magnitude (Figure 7.2). As expected, the hottest region on the day side in all six models is located to the east of the substellar point. This shift is caused by eastward equatorial winds, which transport heat to the planet's nightside (e.g., Adam P. Showman, Tan, and V. Parmentier, 2020, and references therein).

Kepler-7b has the largest thermal gradient of all the planets in our sample, followed by K2-31b and Kepler-17b; this is because the former has a relatively low surface gravity (approximately 4 m/s^2) and the latter two have the shortest orbital periods in the sample

Kepler-7b has the largest thermal gradient of all the planets in our sample, followed by K2-31b and Kepler-17b; this is because the former has a relatively low surface

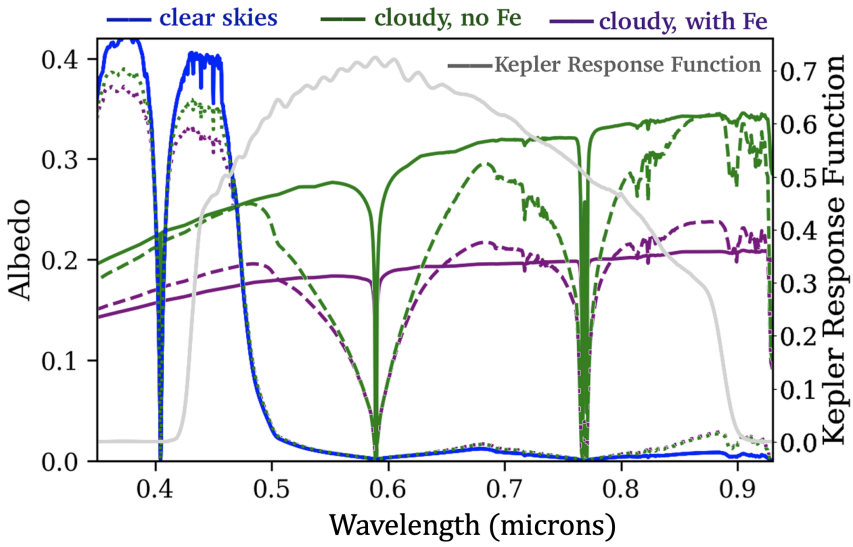

Figure 7.6: Hemisphere-averaged albedo of K2-107b as a function of wavelength for a clear atmosphere (black) and cloudy atmospheres of varying f_{sed} values (green; 0.03 as a solid line, 0.1 as a dashed line, and 0.3 as a dotted line). Cloudy atmospheres including Fe condensates are shown in purple. All cloud distributions are computed using `Virga`. The *Kepler* response function is overplotted in grey.

gravity (approximately 4 m/s^2) and the latter two have the shortest orbital periods in the sample. Our models indicate that Kepler-7b is also warmer at depth than the other planets in this sample. This is expected, as Kepler-7b has the lowest surface gravity of the six planets and under hydrostatic equilibrium the gradient of temperature with respect to pressure is related to the inverse of the surface gravity (e.g., Gao, Mark S. Marley, and Andrew S. Ackerman, 2018).

`Virga` Model Results

In order to determine the effect of the clouds on the albedo, we must first calculate their vertical extent at each location in our model grid. In our `Virga` equilibrium cloud models, the vertical extend of the clouds is controlled by our choice of f_{sed}. Taking K2-107b as a representative example, Figure 7.4 indicates that Mg_2SiO_4 clouds reach a unit optical depth near 1 mbar for the lowest f_{sed} value, 0.03, and near 50 mbar for f_{sed} = 0.1. These clouds will only contribute to the albedo at wavelengths where they reach optical depth unity at lower pressures than Rayleigh scattering or molecular opacity (Figure 7.5). This means that clouds will have a greater effect at wavelengths where the combined molecular and Rayleigh scattering opacity is lower. We show the effect of varying f_{sed} on the wavelength-dependent albedo of K2-107b in Figure 7.6. As f_{sed} decreases and the clouds extend to lower

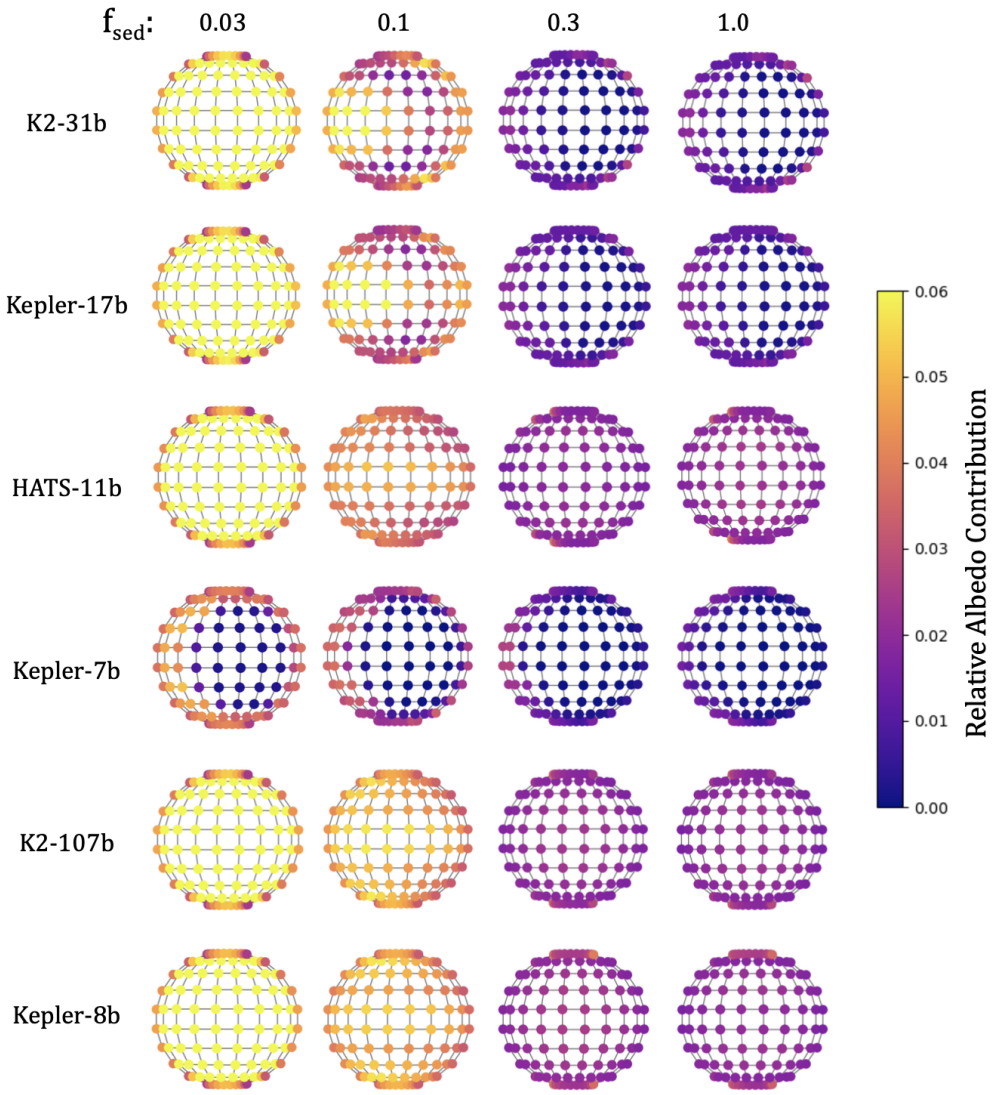

Figure 7.7: Relative dayside albedo contribution at each grid point including appropriate geometric weights. Planets are sorted by increasing equilibrium temperature from top to bottom, and sorted by increasing f_{sed} (0.03, 0.1, 0.3, and 1.0) from left to right. We omit f_{sed} values of 3.0 and 6.0 from the figure, as the clouds in these models reside below the level of unit molecular albedo, and thus the albedo remains roughly unchanged compared to the f_{sed} = 1.0 case. The relative albedo contributions are all smaller than the face-integrated albedo by roughly a factor of π; summing over the points yields the integrated albedo. The models include three cloud species: Mg_2SiO_4, Al_2O_3, and TiO_2.

Table 2. Hemisphere-Averaged Albedos from `Virga` Models as a Function of f_{sed}[a]

Planet	Measured	Clear	0.03	0.1	0.3	1.0	3.0	6.0	0.1, with Fe
K2-31b	0.023±0.002	0.015	0.404	0.123	**0.023**	0.015	0.015	0.015	0.115
Kepler-17b	0.099±0.017	0.017	0.416	**0.131**	0.023	0.017	0.017	0.017	0.125
HATS-11b	0.270±0.052	0.066	**0.301**	0.127	0.060	0.066	0.066	0.066	0.127
Kepler-7b	0.194±0.013	0.009	**0.064**	0.034	0.015	0.010	0.009	0.009	0.030
K2-107b	0.062±0.010	0.065	0.333	0.154	**0.063**	0.065	0.065	0.065	0.134
Kepler-8b	0.124±0.013	0.069	0.319	**0.151**	0.063	0.070	0.070	0.070	0.151

[a]Bolded values indicate the simulated `Virga` albedo that best matches the *Kepler* eclipse observations.

pressures, the cloud opacity contributes most to the overall albedo for an increasingly large fraction of the *Kepler* bandpass.

We next examine how the contribution of clouds to the band-integrated albedo varies across the dayside atmosphere. In Figure 7.7, we show the 10×10 grid of albedos in the *Kepler* bandpass for each planet as a function of f_{sed}. We find that the three planets with the greatest temperature variation as a function of longitude (Kepler-7b, K2-31b and Kepler-17b) also have relatively large albedo variations across their dayside atmospheres for low to intermediate f_{sed} values. Once f_{sed} increases above 0.3, the clouds remain confined below the optical depth unity level of molecular absorbers, such that the presence or absence of clouds does not affect the observed albedo. These three planets appear brighter on their western limbs than in the east, in good agreement with the albedo maps derived from the *Kepler* phase curve for Kepler-7b (Brice-Olivier Demory, de Wit, et al., 2013) and other planets with comparable equilibrium temperatures (Shporer and Hu, 2015). In contrast to these three planets, HATS-11b, K2-107b, and Kepler-8b all appear to have fairly homogeneous albedos, as expected based on their more homogeneous thermal structures.

Lastly, we compare the hemisphere-averaged dayside albedo in the *Kepler* bandpass as a function of f_{sed} to the measured dayside albedo for each planet (Figure 7.8). We find that K2-31b and K2-107b are best described by models with large values of f_{sed} or (equivalently) clear atmospheres, indicating that any reflective clouds present in these atmospheres do not extend above the level of unit molecular opacity. Kepler-17b and Kepler-8b are best-matched by models with intermediate f_{sed} values, implying that their albedos are moderately enhanced by cloud opacity. HATS-11b is best matched by models with low f_{sed} values, corresponding to a high, vertically extended reflective cloud layer spanning a wide range of longitudes. No f_{sed} value is able to reproduce the high observed albedo for Kepler-7b, which our models indicate is too warm for bright Mg_2SiO_4 clouds to form over much of the day side.

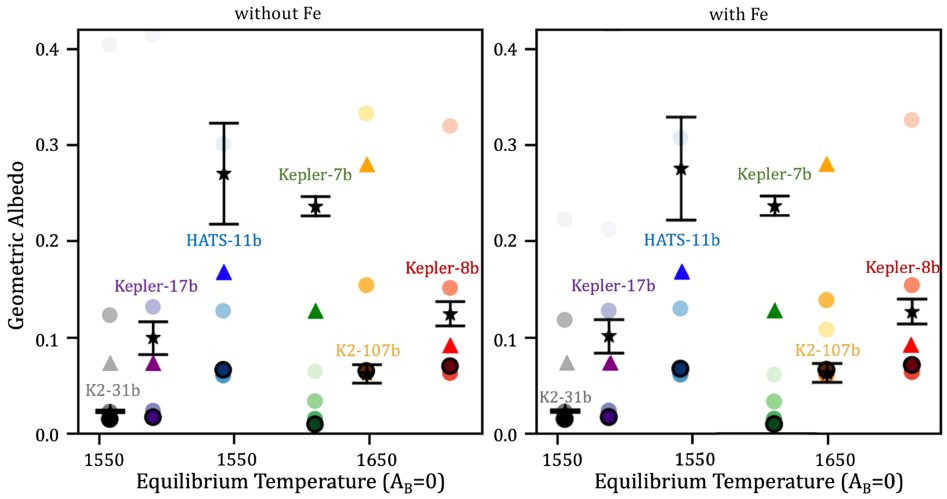

Figure 7.8: Geometric albedo predictions in the *Kepler* optical bandpass compared with published albedo measurements as a function of equilibrium temperature. Albedo predictions from the full-resolution `Virga` models are shown as circles where the shading indicates the f_{sed} value, going from 0.03 (light) to 6.0 (dark). *Kepler* albedo measurements are shown as stars while the predicted albedos from the two-zone CARMA models are shown as triangles. Left panel excludes Fe in `Virga` calculations, while the right panel includes Fe condensates.

Instead, our models indicate that the dayside of Kepler-7b is dominated by deep Al_2O_3 clouds at pressures of around a bar. The addition of iron clouds do not greatly change our results except for decreasing the albedos of low f_{sed} models, as iron clouds sink below the photosphere for higher f_{sed}'s. We list the observed albedos and the predicted albedos as a function of f_{sed} in Table 7.3. We find that the hemisphere-integrated albedo over the *Kepler* bandpass is very sensitive to the assumed value of f_{sed}.

Comparison to `CARMA` Microphysical Models

We find that dayside albedos can vary significantly depending on the assumed sedimentation efficiency (e.g., Figure 7.7). We therefore use these maps to divide each planet into two zones, and then utilize the more computationally demanding `CARMA` microphysical cloud model to solve for the vertical extent of the clouds and corresponding albedo in each zone.

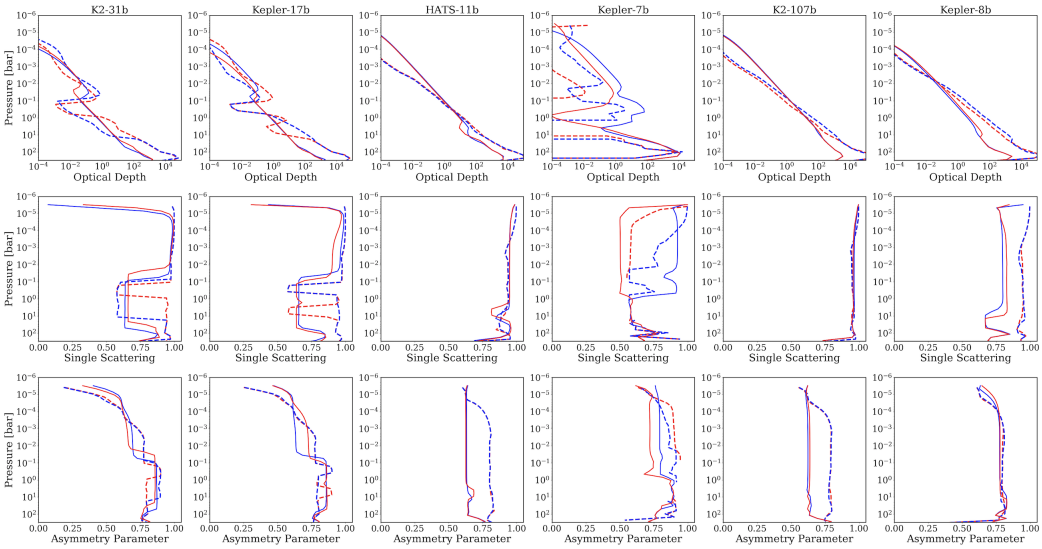

Figure 7.9: Optical depth (left), single scattering albedo (center), and asymmetry parameter (right) as a function of pressure for the two-zone `Virga` (dashed; f_{sed} fixed to 0.1) and `CARMA` (solid) models, calculated by dividing the dayside hemisphere into a dayside (red) and western (black) zone (see §7.3). Each row corresponds to a different planet, sorted left-to-right by increasing equilibrium temperature.

Our `Virga` albedo maps indicate that a subset of the planets in our sample are likely to have spatially inhomogenous Mg_2SiO_4 clouds located near their western limbs. Although it would be computationally prohibitive to run a separate `CARMA` model for each point in the 10×10 grid, we can nonetheless capture this cloud structure using a more computationally tractable two-zone model. We define a threshold value in longitude for each planet based on the albedo distributions found by `Virga` as shown in Figure 7.7 and in Table 7.3. We determine the longitude range defining the two zones (a western zone and a dayside zone) as the division that yields the greatest difference in albedo at mid-latitudes as determined from the `Virga` albedo maps. Occasionally the western zone includes a limb region in the east; see Table 7.3 for a list of the zone definitions for each planet. The resulting zonally-averaged pressure-temperature profiles are plotted in Figure 7.3. We run a separate `CARMA` model for each zone, and also run `Virga` models for the same zones in order to facilitate comparisons between the two models. In the discussion below, we limit our comparisons to these two-zone `Virga` models unless otherwise noted.

When comparing the two models, it is important to note that they predict distinct particle compositions. While `Virga` assumes that particles nucleate homogeneously, `CARMA` predicts that the Mg_2SiO_4 condensates will nucleate heterogeneously onto

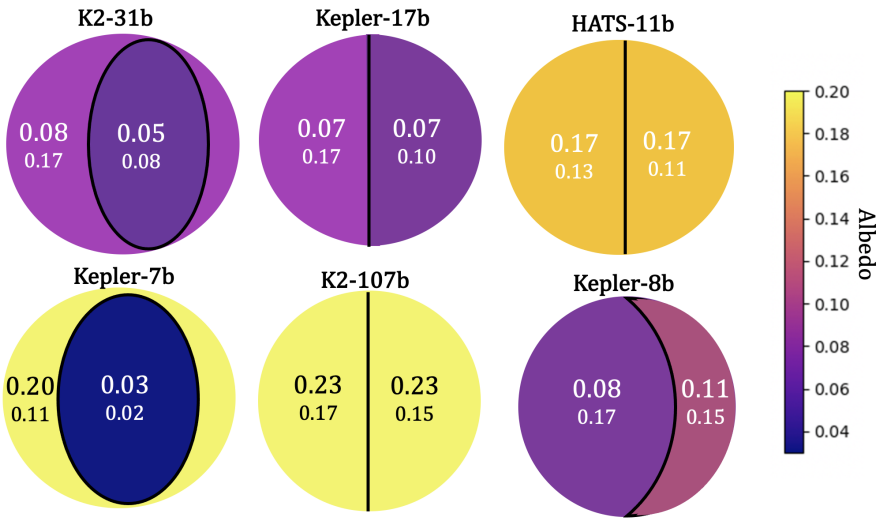

Figure 7.10: Dayside and western zone albedos from the CARMA models integrated over the *Kepler* bandpass. Virga model albedos with f_{sed} equal to 0.1 are listed below for comparison. Both sets of models are calculated in two zonally averaged regions, defined in Table 7.3. Planets are sorted from left to right and top to bottom by increasing equilibrium temperature.

TiO_2 cores (see §7.2). We find that accounting for this TiO_2 core when we calculate the single scattering albedos for the Mg_2SiO_4 particles in our CARMA models results in a lower single scattering albedo than when we repeat the calculation for pure Mg_2SiO_4 particles, which return single scattering albedo profiles of greater than 0.96. For comparison, we refer the reader to Figure 7.9; a single value for single scattering albedo is not representative of heterogeneous particles, which are sensitive to the core mass fraction of TiO_2. However, even after accounting for this effect we find that the species-averaged single scattering albedo shown in Figure 7.9 for our CARMA models with heterogeneous particles is still comparable to the Virga models with f_{sed} equal to 0.1 (Figure 7.10).

When we calculate the hemisphere-integrated albedos for these planets from the CARMA models we find that they generally lie within the range of Virga predictions for varying f_{sed} (see Figure 7.8 and Table 7.3). In Figure 7.8, we show the hemisphere-integrated albedos from the full-resolution Virga model from §7.2 rather than the two-zone model discussed in this section.

We find that K2-107b and HATS-11b appear to have the brightest hemisphere-integrated CARMA albedos, with values consistent with those of the lowest f_{sed} (0.03 – 0.1) Virga models. Kepler-8b, Kepler-17b, and K2-31b have somewhat

Table 3. Hemisphere-Averaged Dayside Albedos from CARMA Models

Planet	Measured	Clear	West	Day	Day Zone[1]	Integrated
K2-31b	0.023±0.002	0.015	0.085	0.054	$[-17°W, 51°E]$	0.073
Kepler-17b	0.099±0.017	0.017	0.074	0.069	$[0°E, 90°E]$	0.073
HATS-11B	0.270±0.052	0.066	0.169	0.165	$[51°E, 90°E]$	0.168
Kepler-7b	0.194±0.013	0.009	0.199	0.034	$[-38°W, 51°E]$	0.128
K2-107b	0.062±0.010	0.065	0.233	0.229	$[51°E, 90°E]$	0.280
Kepler-8b	0.124±0.013	0.069	0.082	0.109	$[51°E, 90°E]$	0.092

[1] Eastern/day zone boundaries are listed in the table. The western/limb zone is defined as the region excluded by the dayside definition.

lower predicted CARMA albedos, more comparable to the f_{sed} of 0.3 Virga models. Kepler-7b is a notable exception, as our CARMA model predicts an albedo that is higher than that of the smallest f_{sed} Virga model.

7.4 Discussion

Comparison to Previous Modeling Efforts

We can compare our results to generic grids of cloudy GCM models in the published literature. First, we note that our GCM outputs for Kepler-7b roughly agree with those shown in Oreshenko, Heng, and Brice-Oliver Demory (2016), and the general distribution of our silicate and corundum clouds agrees with the modeling results of M. Roman and Rauscher (2019).

M. T. Roman et al. (2021) investigated planetary albedos using a grid of GCMs with varying irradiation temperature and surface gravity. The closest equivalent models in their grid are for a planet with an irradiation temperature of either 2500 K (equilibrium temperature of 1500 K) or 2750 K (equilibrium temperature of 1700 K) and a surface gravity of 10 m/s^2. We compare to their nucleation-limited models, which also exclude iron and sulfide condensates.

The models presented in M. T. Roman et al. (2021) assume a fixed pressure-dependent particle size for the clouds, with a size of 0.1 μm at the top of the atmosphere that increases exponentially with increasing pressure for pressures greater than 10 mbar. Since their equilibrium cloud models do not solve for the vertical extent of the cloud layers, they present two cases corresponding to compact (cloud tops limited to 1.4 scale heights above the cloud base) and vertically extended (cloud top pressure of 0.1 mbar) cloud layers. Unlike our models, they account for radiative feedback from these clouds when solving for the temperature structure of the atmosphere. These models indicate that compact cloud layers will result in relatively low and uniform dayside albedos, in good agreement with our results (Figure 7.7). Their vertically extended cloud models exhibit a range of optical spherical albedos

between 0.2 – 0.3, with lower values for the higher temperature model as the reflective silicate clouds become increasingly confined to the cooler western region of the atmosphere. This also agrees with the qualitative picture from our models, which span an equivalent range of albedos. They conclude that their optical albedos for the nucleation-limited case are dominated by silicate cloud particles, consistent with our conclusions here.

Vivien Parmentier, Jonathan J. Fortney, et al. (2016) and Vivien Parmentier, Adam P. Showman, and Jonathan J. Fortney (2021) considered GCMs spanning a wide range of equilibrium temperatures. In Vivien Parmentier, Jonathan J. Fortney, et al., 2016, the clouds are post-processed (i.e., they do not include cloud radiative feedback in the GCM models), and they model the condensation of a wide range of cloud species. These models predict that $MgSiO_3$ and $CaTiO_3$ clouds should dominate the dayside optical albedo for planets with equilibrium temperatures between 1500 – 1700 K. In Vivien Parmentier, Adam P. Showman, and Jonathan J. Fortney, 2021 they incorporate cloud radiative feedback for the condensation of a single cloud species, MnS, but the treatment of silicate clouds is similar to Vivien Parmentier, Jonathan J. Fortney, et al. (2016). For that reason, we focus on Vivien Parmentier, Jonathan J. Fortney, et al., 2016 for our comparison. In this study they assume a small fixed particle size distribution centered at 0.1 μm and a cloud top pressure of 1 microbar, which yields geometric albedos greater than 0.5 in the *Kepler* bandpass for planets of approximately 1500 K equilibrium temperature. This value is much higher than both our albedos and those reported by M. T. Roman et al., 2021, and is most likely due to the very low cloud top pressure assumed in these models. They invoke a cold trap for silicates to reduce the albedo, while we predict that changing the cloud vertical extent can achieve a similar difference in observable albedo.

Comparison to Published Kepler Albedos

Our results show that, with the exception of Kepler-7b, it is possible to match the observed optical geometric albedos for all of the planets in our sample using either `Virga` or `CARMA` models. However, no single model (`Virga` at a fixed f_{sed} or `CARMA`) can explain the observed albedos of all six planets. Although the albedo predictions from the `CARMA` models are broadly consistent with those of the `Virga` models, neither model is able to reproduce or explain the observed planet-to-planet variations in dayside albedo. This suggests that accounting for differences in equilibrium temperature, host star spectral type, surface gravity, and rotation rate alone are not sufficient to capture the observed diversity of hot Jupiter albedos in

this temperature range. We discuss our results in more detail on a planet-by-planet basis below.

Kepler-7b: Spatially Resolved Clouds

Our `CARMA` and `Virga` models both indicate that Kepler-7b's relatively bright dayside albedo is dominated by reflection from the region near the western limb, in good agreement with spatially resolved albedo constraints from phase curve observations (Brice-Olivier Demory, de Wit, et al., 2013; Heng, Morris, and Kitzmann, 2021). This underscores the importance of using spatially resolved cloud models for tidally locked hot Jupiters. We note that there is some tension between our model predictions and the observational data, as fits to Kepler-7b's optical phase curve indicate that the bright reflective western zone extends as far as 10 ± 6 west of the substellar point (Muñoz and Isaak, 2015; Heng, Morris, and Kitzmann, 2021). Our `Virga` models predict that the atmosphere will only be cool enough for Mg_2SiO_4 clouds to condense in the two westernmost longitude bins (extending from the terminator to approximately 38 west of the substellar point; see Figure 7.7 and Table 7.3). This is likely why our models under-predict Kepler-7b's optical geometric albedo.

We consider two possible explanations for this discrepancy. Zonal transport of cloud particles from the western limb region could increase the albedo in adjacent longitudes where the atmosphere is otherwise too warm for them to condense (see §7.2). However, our models for Kepler-7b prefer small cloud particles with a large vertical extent; these small particles might have a relatively short lifetime in the hotter substellar region of the dayside atmosphere. Instead, perhaps small particles transported meridionally could nucleate and grow in bands at high latitudes (Lines, Mayne, Boutle, et al., 2018). Ultimately, this planet would be an interesting test case for microphysical transport models (e.g., Lee, Ch. Helling, and Dobbs-Dixon, 2015; Lines, Mayne, Boutle, et al., 2018), which can explicitly quantify the timescales of these processes and predict the resulting horizontal distribution of cloud particles.

Alternatively, if Kepler-7b's dayside is cooler than predicted by our GCM, Mg_2SiO_4 would be able to condense over a wider range of longitudes. Our GCMs do not account for reflectivity from clouds when calculating the effect of incident starlight on the dayside atmosphere; this effect might reduce the magnitude of dayside heating and result in globally lower temperatures (Lines, Mayne, Boutle, et al., 2018; M. Roman and Rauscher, 2019; M. T. Roman et al., 2021). However, if the clouds extend over a significant fraction of the planet's nightside it could result in net

global warming, as they would act to reduce the amount of energy that can be radiated to space in this region (M. Roman and Rauscher, 2019; M. T. Roman et al., 2021; Vivien Parmentier, Adam P. Showman, and Jonathan J. Fortney, 2021). For Kepler-7b, whose clouds extend over much of the western hemisphere, it is unclear which of these two competing effects would dominate. These explanations assume that the dayside coverage area is the most significant limiting factor on the brightness of the dayside-integrated albedo. However, it is also important to consider factors that might increase the brightness of the cloudy region, including a larger vertical extent for the clouds or brighter cloud particles. We discuss how porous particles may increase HATS-11b's dayside albedo in Section 4.2.3; this same explanation might also apply to Kepler-7b..

K2-31b and K2-107b Do Not Host High Altitude Reflective Cloud Layers

The observed albedos of K2-31b and K2-107b are relatively low, and are well-matched by `Virga` models with clear skies and/or deep clouds (i.e., those with opacities dominated by molecular absorption). For K2-31b, the contribution of clouds to the albedo is negligible for f_{sed} of 0.3 and larger. For K2-107b, we obtain a comparable result for f_{sed} of 1.0 and larger. This suggests that both of these planets may have relatively efficient sedimentation (deep clouds), or alternatively that they have relatively little condensable material in their atmospheres (perhaps corresponding to a relatively low atmospheric metallicity). If the lack of clouds is due to efficient sedimentation, this would appear to contradict predictions from our microphysical `CARMA` models, which track the sedimentation of cloud particles explicitly and predict albedos that are a factor of two or more higher than the observed values for these two planets.

Our `CARMA` models utilize vertical mixing rates calculated from our GCMs. If these mixing rates are overestimates of the true values, we might expect any clouds near the day-night terminator on these planets to also be relatively compact. If this is the case, the transmission spectra of these two planets should show relatively strong absorption features. Although K2-31b has a high surface gravity and is therefore a more challenging target for transmission spectroscopy, K2-107b might be accessible to future space telescopes like *JWST*. More broadly, the sedimentation rates calculated from GCMs and `CARMA` could be tested with comparisons to transmission spectra from ongoing surveys (David K Sing et al., 2016; Crossfield and Kreidberg, 2017; Fu et al., 2017). If `CARMA` models underestimate the sedimentation

efficiency for other planets, the disagreement should be detectable in these data, which are very sensitive to the vertical distribution of cloud particles near the limb. To date, most planets appear to be well-matched by `CARMA` model predictions (e.g. Chachan, Jontof-Hutter, et al., 2020; Gao, Thorngren, et al., 2020), indicating that such model-data disagreements may be relatively rare.

HATS-11b, K2-31b, and K2-107b Have Reflective Dayside Clouds

The measured *Kepler* albedo for HATS-11b (0.27 ± 0.05) is brighter than that of Kepler-7b, in good agreement with our model predictions. This planet is cooler than Kepler-7b, with a smaller day-night temperature gradient. As a result, our models predict a global reflective dayside cloud layer for small f_{sed} values, and our hemisphere-integrated `Virga` albedo for the f_{sed} of 0.03 model is within 1σ of the measured value. This is an unusually small value of f_{sed}, compared to the other planets' best-fit value, while more typical values of 0.1 and larger underestimate the observation. The `CARMA` model albedo is somewhat lower, but is still within 2σ of the observed value. If we wish to adapt our models to better match this planet's high dayside albedo, it likely would require increasing the predicted cloud opacity, such as by increasing the porosity of the cloud particles (Samra, Helling, Ch., and Min, M., 2020). Although increasing the atmospheric metallicity might also increase the cloud opacity, published models for other planets indicate that there is not a simple scaling between these two quantities (e.g. Caroline V. Morley, Jonathan J. Fortney, Kempton, et al., 2013; Gao, Mark S. Marley, and Andrew S. Ackerman, 2018), and increasing the metallicity will also affect the global thermal structure (e.g. Tiffany Kataria, Adam P. Showman, et al., 2015).

Our model predictions for Kepler-17b and Kepler-8b are also in reasonable agreement with the observed albedos. In both cases, an $f_{sed} = 0.1$ `Virga` model slightly overestimates the albedo while our `CARMA` model slightly underestimates the albedo. This may indicate that moderately bright/cloudy worlds have moderate sedimentation efficiencies. For Kepler-8b, both `CARMA` and `Virga` models predict that the planet will have relatively uniform cloud coverage in both latitude and longitude; we therefore do not need to consider further spatial variations in cloud number density and particle size. For Kepler-17b, the $f_{sed} = 0.1$ `Virga` model predicts an albedo gradient across the dayside atmosphere, but this gradient appears to be localized near the equatorial (low latitude) region of the atmosphere. Our `CARMA` model predicts a relatively uniform albedo across the two zones, but this may be biased by our

inability to resolve latitudinal gradients in the simplified two-zone model.

7.5 Conclusions

Optical secondary eclipse measurements made by *Kepler* reveal a wide range of geometric albedos for hot Jupiters with equilibrium temperatures between 1550-1700 K. We combine 3D general circulation models with both equilibrium (`Virga`) and microphysical (`CARMA`) cloud models to explore whether 3D effects can explain these observations. We find that the predicted albedos from our `Virga` models are very sensitive to the assumed sedimentation efficiency (f_{sed}). We can compare these albedo predictions to results from our `CARMA` model, which use mixing rates calculated from the GCM models to predict the vertical extent and particle size distributions of the clouds. We find that while the hemisphere-integrated `CARMA` albedos generally agree with the range of albedos predicted by `Virga`, there is no single f_{sed} value that consistently matches the `CARMA` predictions.

When we compare these model predictions to the measured *Kepler* albedos for each of the six planets in our sample, we find that the albedos of K2-31b and K2-107b are best matched by models that are either cloud-free or have very deep compact cloud layers (large f_{sed} values). Kepler-8b and Kepler-17b's optical albedos can be matched by moderately cloudy models (f_{sed} greater than 0.3). Both `Virga` and `CARMA` tend to under-predict the dayside albedos of the two most reflective planets in our sample, HATS-11b and Kepler-7b, which are best matched by `Virga` models with reflective Mg_2SiO_4 clouds extending to very low pressures (f_{sed} = 0.03); our `CARMA` model for HATS-11b predicts a slightly lower albedo value than the brightest `Virga` model, while our `CARMA` model for Kepler-7b predicts a slightly higher albedo value than `Virga`. Although HATS-11b has relatively uniform cloud coverage across the dayside, it is possible that other factors (such as a low particle porosity) might increase the dayside cloud opacity beyond the values predicted by our models.

Our models predict that the observed albedo of Kepler-7b should be lower than that of HATS-11b, in good agreement with the observations. Although a bright reflective cloud layer forms in the westernmost region of the dayside atmosphere, most dayside longitudes in Kepler-7b's atmosphere are too warm for Mg_2SiO_4 to condense, resulting in a lower hemisphere-averaged dayside albedo. Empirical constraints on the horizontal extent of the western cloudy region from phase curve observations indicate that it extends farther east than predicted by our models,

hinting that a more detailed study of the planet that couples cloud microphysics and dynamics is required.

We conclude that the sample of optical albedos measured by *Kepler* represents a rich source of information for 3D cloud models, and that there is no single explanation for the observed diversity of albedos for the planets considered in this study. Future studies leveraging the large sample of transmission spectra of hot Jupiters could provide complementary constraints on the typical sedimentation efficiencies their atmospheres, while additional complementary modeling studies exploring the coupled effects of atmospheric dynamics and cloud microphysics, as well as an exploration of the micro-porosity of cloud particles, would help to further illuminate the relative importance of these processes in explaining the high albedos of the brightest planets in our sample.

References

Ackerman, Andrew S and Mark S Marley (2001). "Precipitating Condensation Clouds in Substellar Atmospheres". In: *The Astrophysical Journal* 556.2. DOI: 10.1086/321540.

Ackerman, Andrew S, Owen B Toon, and Peter V Hobbs (1995). "A model for particle microphysics, turbulent mixing, and radiative transfer in the stratocumulus-topped marine boundary layer and comparisons with measurements". In: *Journal of the atmospheric sciences* 52.8, pp. 1204–1236. DOI: 10.1175/1520-0469(1995)052<1204:AMFPMT>2.0.CO;2.

– (1993). "Dissipation of Marine Stratiform Clouds and Collapse of the Marine Boundary Layer Due to the Depletion of Cloud Condensation Nuclei by Clouds". In: *Science* 262.5131, pp. 226–229. ISSN: 0036-8075. DOI: 10.1126/science.262.5131.226. eprint: https://science.sciencemag.org/content/262/5131/226.full.pdf. URL: https://science.sciencemag.org/content/262/5131/226.

Adams, Danica et al. (2019). "Aggregate Hazes in Exoplanet Atmospheres". In: *The Astrophysical Journal* 874.1.
D.J.A. ran the microphysical model CARMA and computed the optical properties of haze particles. P.G. provided assistance to D.J.A. in these models and computed the synthetic spectra. D.J.A drafted the initial manuscript, and all authors provided revisions., p. 61. DOI: 10.3847/1538-4357/ab074c.

Adcrot, Alistair et al. (2004). "Implementation of an Atmosphere Ocean General Circulation Model on the Expanded Spherical Cube". In: *Monthly Weather Review* 132. DOI: 10.1175/MWR2823.1.

Angerhausen, Daniel et al. (2014). "Occultation Spectrophotometry of Extrasolar Planets with SOFIA". In: *Formation, Detection, and Characterization of Extra-*

solar Habitable Planets, Proceedings of the International Astronomical Union, IAU Symposium 293. DOI: 10.1017/S1743921313013343.

Arakawa, E. T., M. W. Williams, and T. Inagaki (1977). "Optical properties of arc-evaporated carbon films between 0.6 and 3.8 eV". In: *Journal of Applied Physics* 48.7, pp. 3176–3177. DOI: 10.1063/1.324057.

Barclay, Thomas et al. (Nov. 2012). "PHOTOMETRICALLY DERIVED MASSES AND RADII OF THE PLANET AND STAR IN THE TrES-2 SYSTEM". In: *The Astrophysical Journal* 761.1, p. 53. DOI: 10.1088/0004-637x/761/1/53. URL: https://doi.org/10.1088/0004-637x/761/1/53.

Barstow, J. K. et al. (2014). "Clouds on the Hot Jupiter HD189733b: Constraints from the Reflection Spectrum". In: *The Astrophysical Journal* 786. DOI: 10.1088/0004-637X/786/2/154.

Batalha, Natasha, caoimherooney11, and sagnickm (Apr. 2020). *natashabatalha/virga: Initial Release*. Version v0.0. DOI: 10.5281/zenodo.3759888. URL: https://doi.org/10.5281/zenodo.3759888.

Batalha, Natasha E. et al. (June 2019). "Exoplanet Reflected-light Spectroscopy with PICASO". In: 878.1, 70, p. 70. DOI: 10.3847/1538-4357/ab1b51. arXiv: 1904.09355 [astro-ph.EP].

Bell, Taylor J. et al. (Sept. 2017). "The Very Low Albedo of WASP-12b from Spectral Eclipse Observations with Hubble". In: *The Astrophysical Journal* 847.1, p. L2. DOI: 10.3847/2041-8213/aa876c. URL: https://doi.org/10.3847/2041-8213/aa876c.

Burrows, A., L. Ibgui, and I. Hubeny (2008). "Optical Albedo Theory of Strongly Irradiated Giant Planets: The Case of HD 209458b". In: *The Astrophysical Journal* 682. DOI: 10.1086/589824.

Chachan, Yayaati, Daniel Jontof-Hutter, et al. (Nov. 2020). "A Featureless Infrared Transmission Spectrum for the Super-puff Planet Kepler-79d". In: 160.5, 201, p. 201. DOI: 10.3847/1538-3881/abb23a. arXiv: 2008.05480 [astro-ph.EP].

Chachan, Yayaati, Heather A. Knutson, et al. (Nov. 2019). "A Hubble PanCET Study of HAT-P-11b: A Cloudy Neptune with a Low Atmospheric Metallicity". In: *The Astronomical Journal* 158.6, p. 244. DOI: 10.3847/1538-3881/ab4e9a. URL: https://doi.org/10.3847/1538-3881/ab4e9a.

Colaprete, Anthony, Owen B. Toon, and Julio A. Magalhães (1999). "Cloud formation under Mars Pathfinder conditions". In: *Journal of Geophysical Research: Planets* 104.E4, pp. 9043–9053. DOI: https://doi.org/10.1029/1998JE900018. eprint: https://agupubs.onlinelibrary.wiley.com/doi/pdf/10.1029/1998JE900018. URL: https://agupubs.onlinelibrary.wiley.com/doi/abs/10.1029/1998JE900018.

Coughlin, J and M Lopez-Morales (2012). "A Uniform Search for Secondary Eclipses of Hot Jupiters in Kepler Q2 Light Curves". In: *The Astrophysical Journal* 143. DOI: 10.1088/0004-6256/143/2/39.

Crossfield, I. J. M. and L. Kreidberg (2017). "Trends in Atmospheric Properties of Neptune-size Exoplanets". In: *The Astronomical Journal* 154.6. DOI: 10.3847/1538-3881/aa9279.

Demory, Brice-Olivier, Julien de Wit, et al. (2013). "Inference of Inhomogeneous Clouds in an Exoplanet Atmosphere". In: *The Astrophysical Journal Letters* 776. DOI: 10.1088/2041-8205/776/2/L25.

Demory, Brice-Olivier, Sara Seager, et al. (2011). "The High Albedo of the Hot Jupiter Kepler-7b". In: *The Astrophysical Journal* 735. DOI: 10.1088/2041-8205/735/1/L12.

Desert, Jean-Michel et al. (2011). "The Atmospheres of the Hot Jupiters Kepler-5b and Kepler-6b Observed during Occultations with Warm Spitzer and Kepler". In: *The Astrophysical Journal Supplement* 197. DOI: 10.1088/0067-0049/197/1/11.

Esteves, Lisa J., Ernst J. W. De Mooij, and Ray Jayawardhana (2013). "Optical Phase Curves of Kepler Exoplanets". In: *The Astrophysical Journal* 772. DOI: 10.1088/0004-637X/772/1/51.

– (2015). "Changing Phases of Alien Worlds: Probing Atmospheres of Kepler Planets with High-precision Photometry". In: *The Astrophysical Journal* 804. DOI: 10.1088/0004-637X/804/2/150.

Evans, Thomas M. et al. (2013). "The Deep Blue Color of HD 189733b: Albedo Measurements with Hubble Space Telescope/Space Telescope Imaging Spectrograph at Visible Wavelengths". In: *The Astrophysical Journal Letters* 772. DOI: 10.1088/2041-8205/772/2/L16.

Fortney, J. J. et al. (Nov. 2006). "The Influence of Atmospheric Dynamics on the Infrared Spectra and Light Curves of Hot Jupiters". In: *The Astrophysical Journal* 652.1, pp. 746–757. DOI: 10.1086/508442. URL: https://doi.org/10.1086/508442.

Fortney, Jonathan J. (Dec. 2005). "The effect of condensates on the characterization of transiting planet atmospheres with transmission spectroscopy". In: *Monthly Notices of the Royal Astronomical Society* 364.2, pp. 649–653. ISSN: 0035-8711. DOI: 10.1111/j.1365-2966.2005.09587.x. eprint: https://academic.oup.com/mnras/article-pdf/364/2/649/18662777/364-2-649.pdf. URL: https://doi.org/10.1111/j.1365-2966.2005.09587.x.

Fortney, Jonathan J. et al. (Oct. 2011). "DISCOVERY AND ATMOSPHERIC CHARACTERIZATION OF GIANT PLANET KEPLER-12b: AN INFLATED RADIUS OUTLIER". In: *The Astrophysical Journal Supplement Series* 197.1, p. 9. DOI: 10.1088/0067-0049/197/1/9. URL: https://doi.org/10.1088/0067-0049/197/1/9.

Fraine, Jonathan et al. (2021). *The Dark World: A Tale of WASP-43b in Reflected Light with HST WFC3/UVIS*. arXiv: 2103.16676 [astro-ph.EP].

Fu, Guangwei et al. (Oct. 2017). "Statistical Analysis of Hubble /WFC3 Transit Spectroscopy of Extrasolar Planets". In: *The Astrophysical Journal* 847.2, p. L22. DOI: 10.3847/2041-8213/aa8e40. URL: https://doi.org/10.3847/2041-8213/aa8e40.

Gao, Peter, Siteng Fan, et al. (2017). "Constraints on the microphysics of Pluto's photochemical haze from New Horizons observations". In: *Icarus* 287. Special Issue: The Pluto System, pp. 116–123. ISSN: 0019-1035. DOI: https://doi.org/10.1016/j.icarus.2016.09.030.

Gao, Peter, Mark S. Marley, and Andrew S. Ackerman (Mar. 2018). "Sedimentation Efficiency of Condensation Clouds in Substellar Atmospheres". In: *The Astrophysical Journal* 855.2, p. 86. DOI: 10.3847/1538-4357/aab0a1. URL: https://doi.org/10.3847/1538-4357/aab0a1.

Gao, Peter, Daniel P Thorngren, et al. (2020). "Aerosol composition of hot giant exoplanets dominated by silicates and hydrocarbon hazes". In: *Nature Astronomy* 4.10, pp. 951–956. DOI: 10.1038/s41550-020-1114-3.

Gao, Peter, Xi Zhang, et al. (2014). "Bimodal distribution of sulfuric acid aerosols in the upper haze of Venus". In: *Icarus* 231, pp. 83–98. ISSN: 0019-1035. DOI: https://doi.org/10.1016/j.icarus.2013.10.013. URL: https://www.sciencedirect.com/science/article/pii/S0019103513004326.

Goode, P. R. et al. (2001). "Earthshine observations of the Earth's reflectance". In: *Geophysical Research Letters* 28.9, pp. 1671–1674. DOI: https://doi.org/10.1029/2000GL012580.

Goody, Richard et al. (1989). "The correlated-k method for radiation calculations in nonhomogeneous atmospheres". In: *Journal of Quantitative Spectroscopy and Radiative Transfer* 42.6, pp. 539–550. ISSN: 0022-4073. DOI: https://doi.org/10.1016/0022-4073(89)90044-7.

Guillot, T. and A. P. Showman (2002). "Evolution of 51 Pegasus b-like Planets". In: *Astronomy and Astrophysics* 385. DOI: 10.1051/0004-6361:20011624.

Helling, Christiane (2019). "Exoplanet Clouds". In: *Annual Review of Earth and Planetary Sciences* 47. DOI: 10.1146/annurev-earth-053018-060401.

Helling, Christiane, Matthias Dehn, et al. (Feb. 2008). "Consistent Simulations of Substellar Atmospheres and Nonequilibrium Dust Cloud Formation". In: *The Astrophysical Journal* 675.2, pp. L105–L108. DOI: 10.1086/533462. URL: https://doi.org/10.1086/533462.

Helling, Christiane, N. Iro, et al. (2019). "Understanding the atmospheric properties and chemical composition of the ultra-hot Jupiter HAT-P-7b. I. Cloud and chemistry mapping". In: *Astronomy and Astrophysics* 631. DOI: 10.1051/0004-6361/201935771.

Helling, Christiane, Kawashima, Y., et al. (2020). "Mineral cloud and hydrocarbon haze particles in the atmosphere of the hot Jupiter JWST target WASP-43b". In: *A&A* 641, A178. DOI: 10.1051/0004-6361/202037633. URL: https://doi.org/10.1051/0004-6361/202037633.

Heng, Kevin and Brice-Olivier Demory (Oct. 2013). "UNDERSTANDING TRENDS ASSOCIATED WITH CLOUDS IN IRRADIATED EXOPLANETS". In: *The Astrophysical Journal* 777.2, p. 100. DOI: 10.1088/0004-637x/777/2/100. URL: https://doi.org/10.1088/0004-637x/777/2/100.

Heng, Kevin, Brett Morris, and Daniel Kitzmann (2021). "Closed-formed ab initio solutions of geometric albedos and reflected light phase curves of exoplanets". In: *arXiv*. DOI: arXiv:2103.02673.

James, E.P., O.B. Toon, and G. Schubert (1997). "A Numerical Microphysical Model of the Condensational Venus Cloud". In: *Icarus* 129.1, pp. 147–171. ISSN: 0019-1035. DOI: https://doi.org/10.1006/icar.1997.5763. URL: https://www.sciencedirect.com/science/article/pii/S0019103597957638.

Jensen, E. J. and O. B. Toon (1994). "Ice nucleation in the upper troposphere: Sensitivity to aerosol number density, temperature, and cooling rate". In: *Geophysical Research Letters* 21.18, pp. 2019–2022. DOI: https://doi.org/10.1029/94GL01287. eprint: https://agupubs.onlinelibrary.wiley.com/doi/pdf/10.1029/94GL01287. URL: https://agupubs.onlinelibrary.wiley.com/doi/abs/10.1029/94GL01287.

Kataria, T. et al. (Mar. 2013). "THREE-DIMENSIONAL ATMOSPHERIC CIRCULATION OF HOT JUPITERS ON HIGHLY ECCENTRIC ORBITS". In: *The Astrophysical Journal* 767.1, p. 76. DOI: 10.1088/0004-637x/767/1/76. URL: https://doi.org/10.1088/0004-637x/767/1/76.

Kataria, Tiffany, Adam P. Showman, et al. (Mar. 2015). "THE ATMOSPHERIC CIRCULATION OF THE HOT JUPITER WASP-43b: COMPARING THREE-DIMENSIONAL MODELS TO SPECTROPHOTOMETRIC DATA". In: *The Astrophysical Journal* 801.2, p. 86. DOI: 10.1088/0004-637x/801/2/86. URL: https://doi.org/10.1088/0004-637x/801/2/86.

Kataria, Tiffany, David K. Sing, et al. (Apr. 2016). "THE ATMOSPHERIC CIRCULATION OF A NINE-HOT-JUPITER SAMPLE: PROBING CIRCULATION AND CHEMISTRY OVER A WIDE PHASE SPACE". In: *The Astrophysical Journal* 821.1, p. 9. DOI: 10.3847/0004-637x/821/1/9. URL: https://doi.org/10.3847/0004-637x/821/1/9.

Kawashima, Yui and Masahiro Ikoma (May 2019). "Theoretical Transmission Spectra of Exoplanet Atmospheres with Hydrocarbon Haze: Effect of Creation, Growth, and Settling of Haze Particles. II. Dependence on UV Irradiation Intensity, Metallicity, C/O Ratio, Eddy Diffusion Coefficient, and Temperature". In: *The Astrophysical Journal* 877.2, p. 109. DOI: 10.3847/1538-4357/ab1b1d. URL: https://doi.org/10.3847/1538-4357/ab1b1d.

Kipping, David and Gaspar Bakos (2011). "Analysis of Kepler's Short-cadence Photometry for TrES-2b". In: *The Astrophysical Journal* 733. DOI: 10.1088/0004-637X/733/1/336.

Kirkpatrick, J. D. (2005). "New Spectral Types L and T". In: *Annual Review of Astronomy and Astrophysics* 43. DOI: 10.1146/annurev.astro.42.053102.134017.

Lee, G., Ch. Helling, and D. Dobbs-Dixon I. aand Juncher (2015). "Modelling the local and global cloud formation on HD 189733b". In: *Astronomy and Astrophysics* 580. DOI: 10.1051/0004-6361/201525982.

Lewis, Nikole K. et al. (Oct. 2014). "ATMOSPHERIC CIRCULATION OF ECCENTRIC HOT JUPITER HAT-P-2B". In: *The Astrophysical Journal* 795.2, p. 150. DOI: 10.1088/0004-637x/795/2/150. URL: https://doi.org/10.1088/0004-637x/795/2/150.

Lines, S., N. J. Mayne, I. A. Boutle, et al. (2018). "Simulating the cloudy atmospheres of HD 209458b ad HD 189733b with the 3D Met Office Unified Model". In: *Astronomy and Astrophysics* 615. DOI: 10.1051/0004-6361/201732278.

Lines, S., N. J. Mayne, J. Manners, et al. (2019). "Overcast on Osiris: 3D radiative-hydrodynamical simulations of a cloudy hot Jupiter using the parametrized, phase-equilibrium cloud formation code EDDYSED". In: *Monthly Notices of the Royal Astronomical Society* 488. DOI: 10.1093/mnras/stz1788.

Lodders, Katharina (2003). "Solar System Abundances and Condensation Temperatures of the Elements". In: *The Astrophysical Journal* 591 (2), pp. 1220–1247. DOI: 10.1086/375492.

Lodders, Katharina and Bruce Fegley (2002). "Atmospheric Chemistry in Giant Planets, Brown Dwarfs, and Low-Mass Dwarf Stars: I. Carbon, Nitrogen, and Oxygen". In: *Icarus* 155.2, pp. 393–424. ISSN: 0019-1035. DOI: https://doi.org/10.1006/icar.2001.6740. URL: https://www.sciencedirect.com/science/article/pii/S0019103501967405.

MacDonald, Ryan J. et al. (May 2018). "Exploring H_2O Prominence in Reflection Spectra of Cool Giant Planets". In: 858.2, 69, p. 69. DOI: 10.3847/1538-4357/aabb05. arXiv: 1804.00662 [astro-ph.EP].

Marley, M. S. et al. (2013). "Clouds and Hazes in Exoplanet Atmospheres". In: *Comparative Climatology of Terrestrial Planets*. Ed. by Stephen J. Mackwell et al., p. 367. DOI: 10.2458/azu_uapress_9780816530595-ch15.

Marley, M.S. and T.D. Robinson (2015). "On the Cool Side: Modeling the Atmospheres of Brown Dwarfs and Giant Planets". In: *Annual Review of Astronomy and Astrophysics* 53.1, pp. 279–323. DOI: 10.1146/annurev-astro-082214-122522. eprint: https://doi.org/10.1146/annurev-astro-082214-122522. URL: https://doi.org/10.1146/annurev-astro-082214-122522.

Marley, Mark S., Christopher Gelino, et al. (1999). “Reflected Spectra and Albedos of Extrasolar Giant Planets I. Clear and Cloudy Atmospheres”. In: *The Astrophysical Journal* 513.2, pp. 879–893. DOI: 10.1086/306881.

Marley, Mark S., Didier Saumon, and Colin Goldblatt (2010). “A Patchy Cloud Model for the L to T Dwarf Transition”. In: *The Astrophysical Journal Letters* 723. DOI: 10.1088/2041-8205/723/1/L117.

McGouldrick, Kevin and Owen B. Toon (2007). “An investigation of possible causes of the holes in the condensational Venus cloud using a microphysical cloud model with a radiative-dynamical feedback”. In: *Icarus* 191.1, pp. 1–24. ISSN: 0019-1035. DOI: https://doi.org/10.1016/j.icarus.2007.04.007. URL: https://www.sciencedirect.com/science/article/pii/S0019103507001649.

Morley, Caroline V et al. (2015). “Thermal emission and reflected light spectra of super Earths with flat transmission spectra”. In: *The Astrophysical Journal* 815.2. DOI: 10.1088/0004-637X/815/2/110.

Morley, Caroline V., Jonathan J. Fortney, Eliza M. R. Kempton, et al. (2013). “Quantitatively Assessing the Role of Clouds in the Transmission Spectrum of GJ 1214b”. In: *The Astrophysical Journal* 775.1. DOI: 10.1088/0004-637X/775/1/33.

Morley, Caroline V., Jonathan J. Fortney, Mark S. Marley, et al. (Aug. 2012). “NEGLECTED CLOUDS IN T AND Y DWARF ATMOSPHERES”. In: *The Astrophysical Journal* 756.2, p. 172. DOI: 10.1088/0004-637x/756/2/172. URL: https://doi.org/10.1088/0004-637x/756/2/172.

Muñoz, Antonio Garcıa and Kate G. Isaak (2015). “Probing exoplanet clouds with optical phase curves”. In: *Proceedings of the National Academy of Sciences* 112.44, pp. 13461–13466. ISSN: 0027-8424. DOI: 10.1073/pnas.1509135112. eprint: https://www.pnas.org/content/112/44/13461.full.pdf. URL: https://www.pnas.org/content/112/44/13461.

Niraula, Prajwal et al. (2018). “Discovery of Six Optical Phase Curves with K2”. In: *arXiv preprint arXiv:1812.09227*.

Oreshenko, Maria, Kevin Heng, and Brice-Oliver Demory (2016). “Optical Phase Curves ass Diagnosticsc for Aerosol Composition in Exoplanetary Atmospheres”. In: *Monthly Notices of the Royal Astronomical Society* 457. DOI: 10.1093/mnras/stw133.

Parmentier, Vivien, Jonathan J. Fortney, et al. (2016). “Transitions in the Cloud Composition of Hot Jupiters”. In: *The Astrophysical Journal* 828. DOI: 10.3847/0004-637X/828/1/22.

Parmentier, Vivien, Adam P. Showman, and Jonathan J. Fortney (Jan. 2021). “The cloudy shape of hot Jupiter thermal phase curves”. In: 501.1, pp. 78–108. DOI: 10.1093/mnras/staa3418. arXiv: 2010.06934 [astro-ph.EP].

Parmentier, Vivien, Adam P. Showman, and Yuan Lian (2013). "3D mixing in hot Jupiters atmospheres - I. Application to the day/night cold trap in HD 209458b". In: *A&A* 558, A91. DOI: 10.1051/0004-6361/201321132. URL: https://doi.org/10.1051/0004-6361/201321132.

Parviainen, H, H. J. Deeg, and J. A. Belmonte (2013). "Secondary eclipses in the CoRoT light curves. A homogeneous search based on Bayesian model selection". In: *Astronomy & Astrophysics* 550. DOI: 10.1051/0004-6361/201220081.

Patzer, A. et al. (2005). "A density functional study of small AlxOy (x,y=1-4) clusters and their thermodynamic properties". In: *The European Physical Journal D - Atomic, Molecular, Optical and Plasma Physics* 32. DOI: 10.1140/epjd/e2005-00026-8.

Powell, Diana, Tom Louden, et al. (Dec. 2019). "Transit Signatures of Inhomogeneous Clouds on Hot Jupiters: Insights from Microphysical Cloud Modeling". In: *The Astrophysical Journal* 887.2, p. 170. DOI: 10.3847/1538-4357/ab55d9. URL: https://doi.org/10.3847/1538-4357/ab55d9.

Powell, Diana, Xi Zhang, et al. (June 2018). "Formation of Silicate and Titanium Clouds on Hot Jupiters". In: *The Astrophysical Journal* 860.1, p. 18. DOI: 10.3847/1538-4357/aac215. URL: https://doi.org/10.3847/1538-4357/aac215.

Pruppacher, Hans R. and James D. Klett (1978). "Homogeneous Nucleation". In: *Microphysics of Clouds and Precipitation*. Dordrecht: Springer Netherlands, pp. 162–182. ISBN: 978-94-009-9905-3. DOI: 10.1007/978-94-009-9905-3_7. URL: https://doi.org/10.1007/978-94-009-9905-3_7.

Roman, Michael and Emily Rauscher (2019). "Modeled Temperature-dependent Clouds with Radiative Feedback in Hot Jupiter Atmospheres". In: *The Astrophysical Journal* 872. DOI: 10.3847/1538-4357/aafdb5.

Roman, Michael T. et al. (Feb. 2021). "Clouds in Three-dimensional Models of Hot Jupiters over a Wide Range of Temperatures. I. Thermal Structures and Broadband Phase-curve Predictions". In: 908.1, 101, p. 101. DOI: 10.3847/1538-4357/abd549. arXiv: 2010.06936 [astro-ph.EP].

Rowe, Jason et al. (2008). "The Very Low Albedo of an Extrasolar Planet: MOST Space-based Photometry of HD 209458". In: *The Astrophysical Journal* 689. DOI: 10.1086/591835.

Samra, D., Helling, Ch., and Min, M. (2020). "Mineral snowflakes on exoplanets and brown dwarfs - Effects of micro-porosity, size distributions, and particle shape". In: *A&A* 639, A107. DOI: 10.1051/0004-6361/202037553. URL: https://doi.org/10.1051/0004-6361/202037553.

Saumon, D. and M. S. Marley (2008). "The evolution of L and T dwarfs in color-magnitude diagrams". In: *The Astrophysical Journal* 689.2, pp. 1327–1344. DOI: 10.1086/592734.

Seager, S., B. A. Whitney, and D. D. Sasselov (2000). "Photometric Light Curves and Polarization of Close-in Extrasolar Giant Planets". In: *The Astrophysical Journal* 540. DOI: 10.1086/309292.

Showman, Adam P., Jonathan J. Fortney, et al. (June 2009). "ATMOSPHERIC CIRCULATION OF HOT JUPITERS: COUPLED RADIATIVE-DYNAMICAL GENERAL CIRCULATION MODEL SIMULATIONS OF HD 189733b and HD 209458b". In: *The Astrophysical Journal* 699.1, pp. 564–584. DOI: 10.1088/0004-637x/699/1/564. URL: https://doi.org/10.1088/0004-637x/699/1/564.

Showman, Adam P. and Yohai Kaspi (Oct. 2013). "ATMOSPHERIC DYNAMICS OF BROWN DWARFS AND DIRECTLY IMAGED GIANT PLANETS". In: *The Astrophysical Journal* 776.2, p. 85. DOI: 10.1088/0004-637x/776/2/85. URL: https://doi.org/10.1088/0004-637x/776/2/85.

Showman, Adam P., Nikole K. Lewis, and Jonathan J. Fortney (Mar. 2015). "THREE-DIMENSIONAL ATMOSPHERIC CIRCULATION OF WARM AND HOT JUPITERS: EFFECTS OF ORBITAL DISTANCE, ROTATION PERIOD, AND NONSYNCHRONOUS ROTATION". In: *The Astrophysical Journal* 801.2, p. 95. DOI: 10.1088/0004-637x/801/2/95. URL: https://doi.org/10.1088/0004-637x/801/2/95.

Showman, Adam P., X. Tan, and V. Parmentier (2020). "Atmospheric Dynamics of Hot Giant Planets and Brown Dwarfs". In: *Space Science Reviews* 216. DOI: 10.1007/s11214-020-00758-8.

Shporer, Avi and Renyu Hu (2015). "Studying Atmosphere-dominated Hot Jupiter Kepler Phase Curves: Evidence that Inhomogeneous Atmospheric Reflection is Common". In: *The Astronomical Journal* 150. DOI: 10.1088/0004-6256/150/4/112.

Sing, David K et al. (2016). "A continuum from clear to cloudy hot- Jupiter exoplanets without primordial water depletion". In: *Nature* 529.7584, pp. 59–62. DOI: 10.1038/nature16068.

Skemer, Andrew J. et al. (Feb. 2016). "The LEECH Exoplanet Imaging Survey: Characterization of the Coldest Directly Imaged Exoplanet, GJ 504 b, and Evidence for Superstellar Metallicity". In: 817.2, 166, p. 166. DOI: 10.3847/0004-637X/817/2/166. arXiv: 1511.09183 [astro-ph.EP].

Smith, Michael D. (1998). "Estimation of a Length Scale to Use with the Quench Level Approximation for Obtaining Chemical Abundances". In: *Icarus* 132.1, pp. 176–184. ISSN: 0019-1035. DOI: https://doi.org/10.1006/icar.1997.5886. URL: https://www.sciencedirect.com/science/article/pii/S0019103597958863.

Sudarsky, David, Adam Burrows, and Ivan Hubeny (May 2003). "Theoretical Spectra and Atmospheres of Extrasolar Giant Planets". In: *The Astrophysical Journal*

588.2, pp. 1121–1148. DOI: 10.1086/374331. URL: https://doi.org/10.1086/374331.

Toon, O.B. et al. (1992). "A physical model of Titan's aerosols". In: *Icarus* 95.1, pp. 24–53. ISSN: 0019-1035. DOI: https://doi.org/10.1016/0019-1035(92)90188-D.

Visscher, Channon, Katharina Lodders, and Bruce Fegley (May 2010). "ATMOSPHERIC CHEMISTRY IN GIANT PLANETS, BROWN DWARFS, AND LOW-MASS DWARF STARS. III. IRON, MAGNESIUM, AND SILICON". In: *The Astrophysical Journal* 716.2, pp. 1060–1075. DOI: 10.1088/0004-637x/716/2/1060. URL: https://doi.org/10.1088/0004-637x/716/2/1060.

von Paris, P. et al. (2016). "Inferring heat recirculation and albedo for exoplanetary atmospheres: Comparing optical phase curves and secondary eclipse data". In: *Astronomy & Astrophysics* 587. DOI: 10.1051/0004-6361/201526297.

Webber, Matthew W. et al. (2015). "Effect of Longitude-dependent Cloud Coverage on Exoplanet Visible Wavelength Reflected-light Phase Curves". In: *The Astrophysical Journal* 804. DOI: 10.1088/0004-637X/804/2/94.

Wolf, Eric T. and Owen B. Toon (2010). "Fractal organic hazes provided an ultraviolet shield for early earth". In: *Science* 328.5983, pp. 1266–1268. DOI: 10.1126/science.1183260.

Chapter 8

CONCLUSION

In this thesis, I investigated the evolution of Mars's chemistry and climate, predicted the prebiotic chemistry at exoplanets with reduced atmospheres, and interpreted observations of exoplanets. Going forward, I aim to continue developing these three approaches and synthesize towards a single theme: "What worlds may have been habitable at a time during their geologic histories?"

It is likely Mars may have been habitable early on. Geologic evidence for large volumes of flowing liquid water on its surface suggests a more habitable climate, and the preserved volatiles in the Martian soil is telling of prebiotic chemistry including an early nitrogen cycle. In Chapter 2, I investigated how the loss of Mars' atmosphere and surface liquid water influenced its atmospheric chemistry and climate through time. Crustal hydration, or the loss of liquid water to the crust largely to oxidize surface Fe(II), sourced a large hydrogen flux which may have sustained large H_2 concentrations for up to 10^7 years during the Noachian. During cooler eras, reduced iron exposed to the atmosphere may have slowly encouraged a sink of atmospheric oxidants, driving the early Mars atmosphere towards a reduced state with a bulk composition dominated by CO instead of CO_2. My past and current research into Mars' evolution and habitability throughout its geologic history has laid the groundwork for my new conjecture, which my proposed postdoctoral work will investigate: I predict that Mars' atmospheric chemistry may not have always been in steady state, meaning my past results may describe end-of-range cases. Instead, Mars' atmosphere may have alternated between highly oxidized (CO_2 background, oxygen rich and hydrogen depleted) and highly reduced environments (H_2 rich, oxygen depleted, potentially a CO background) on potentially shorter timescales than steady state. In the future, it will be helpful to implement a coupled photochemical and climate model in order to investigate whether how quickly the chemistry and climate could respond to geologic events. These models could then be coupled to an aqueous model to make comparisons to the soil record, similar to the investigations of Mars nitrate which I carried out in Chapters 3 and 4.

Because of its unique and accessible geological record, Mars arguably serves as a Rosetta Stone for the study of the evolution and habitability of planets in our

Solar System (including Earth) and exoplanets. Going forward, the James Webb Space Telescope will soon make measurements of the atmospheres of rocky worlds, some of which may be earth- and Mars- like. JWST will observe many closely orbiting super-Earths, which are thought to have initially formed with thick, puffy, hydrogen-rich envelopes (i.e., 'sub-Neptunes') which were then lost to space. Once basic parameters of these atmospheres are known (including temperature and bulk composition), I aim to extend our understanding of Mars to interpret the evolution of these worlds' atmospheres and climates, and if applicable also examine the potential for prebiotic chemistry. I aim to use the same photochemical model KINETICS to explain the presence of any species observed which may be photochemically derived, and if applicable, I will inform input fluxes from volcanism and/or lightning at the boundary conditions by approximating local thermochemical equilibrium with the model CEA. Extending from my past exoplanet works which explained measurements of warm and hot gas giants, I aim to implement a similar suite of models to interpret spectral observations of smaller rocky worlds. The parametrized cloud model, Virga, and microphysical aerosol model, CARMA, will both be useful in inferring the presence of hazes derived from methane photolysis and the presence of water clouds and thereby a hydr ologic cycle, as well as interpreting the effect of these aerosols in spectral observations. The radiative transfer model, Picaso, will be useful in producing synthetic spectra for predictions of future observations, as well as for conducting atmospheric retrievals.

Future space missions will soon contribute to these goals. The Mars Sample Return (MSR) will provide isotopic measurements in soil measurements, including nitrate and sulfate. Isotopic measurements of the former will help constrain the formation period and mechanism. Meanwhile, Sulfur-Mass Independent Fractionation (S-MIF) on Earth occurs both biotically and abiotically (such as photolysis and thermochemical sulfate reduction). Measurements of non-zero S-MIF have been made at Mars (Tomkins and al., 2020), but not all S isotopes have been measured. MSR will improve measurements of S-MIF at Mars, allowing the Mars community to interpret this signal as an ancient biosignature.

In summary, extended goals include building on the findings and methods presented in this thesis to: [I] improve on understanding Mars' chemical evolution through time and [II] extend that understanding to decipher the evolution and habitability of other worlds through time.